

THERMAL TIDES IN THE ATMOSPHERE OF VENUS

Thesis by

Judith Burt Pechmann

In Partial Fulfillment of the Requirements

For the Degree of

Doctor of Philosophy

California Institute of Technology, Pasadena, California

1983

(Submitted May 20, 1983)

To my husband, Jim,
and to my mother.

ACKNOWLEDGMENTS

I am most grateful to my thesis advisor, Andrew Ingersoll, for suggesting the topic of this thesis and providing much needed advice and inspiration throughout its development.

I thank Lee Elson for supplying me with all the information I needed concerning the Pioneer Venus OIR data. I also thank Lee and Rich Zurek for many helpful discussions on tides and atmospheric science in general. Special credit is due to Arthur Raefsky who wrote the first draft of the computer code for the LPE model and who taught me everything I know about finite elements. Thanks to A.N. Staniforth for providing a copy of the nonlinear GCM on which our model is based.

My fellow graduate students and the planetary science faculty have made Caltech a pleasant and rewarding place to learn and do research. I am grateful to them all.

The encouragement and advice of Joe Veverka were largely responsible for my decision to pursue a career in planetary science. His support has meant a great deal to me throughout the years.

I owe more than I can say to my husband, Jim, for his love, patience, and unflagging belief that someday I would finish this thesis.

I thank all my fellow inhabitants of Ingersoll Ranch Estates, including the non-humans, for their friendship and for providing a rural atmosphere in the middle of Pasadena.

The completion of this thesis would not have been possible without the efforts of Shirley Taylor, Kay Campbell, and Donna Lathrop, who did the typing.

The support of an NSF graduate research fellowship during my first three years at Caltech is gratefully acknowledged. This research was funded by NASA grant NAGW-58.

ABSTRACT

The daily variation in the absorption of sunlight by the atmosphere provides the forcing for thermal tides. In this thesis the response of the Venus atmosphere as a function of height and latitude to the diurnal and semidiurnal components of the forcing is calculated using a linearized primitive equation model. We specify the atmospheric mean state using data from the Pioneer Venus probes and orbiter, and solve for the first order tidal perturbation. Our forcing function is based on data returned by the solar flux radiometer on the Pioneer Venus sounder probe. The perturbation variables are discretized horizontally by spherical harmonics and vertically by finite elements. A semi-implicit time-stepping algorithm is used.

The model results for Venus thermal tides are in agreement with the solar-fixed component of diurnal and semidiurnal brightness temperature fluctuations determined from Pioneer Venus orbiter infrared radiometer (OIR) data. Contrary to the prediction of classical tidal theory, the observed semidiurnal brightness temperature maxima occur before the forcing maxima from about 60 to 80 km. In the model, this phase lead is due to a long vertical wavelength (~30 km) from the cloud tops to 80 km. Also, the data unexpectedly show that the semidiurnal amplitude is larger than the diurnal over much of the region observed, even though the diurnal forcing is about twice as great. The model's diurnal temperature amplitude is larger than that observed in the brightness temperature. However, convolution with the OIR weighting functions results in model brightness temperature amplitudes which are

as small as the observed values because the vertical wavelength of the diurnal tide is shorter than the width of the weighting functions.

The success of the model increases our confidence in our knowledge of the mean state of the Venus atmosphere and provides us with the opportunity to determine the importance of energy and angular momentum transport by the tides. The zonally averaged vertically integrated tidal energy flux is significant compared to the zonally averaged imbalance in incoming solar radiation and outgoing infrared radiation from equatorial to mid-latitudes. However, the tides do not in general tend to reduce the imbalance by transporting heat poleward. The mean meridional circulation driven by this imbalance and the tidal energy flux consists of stacked direct and indirect Hadley cells. The angular momentum transport is upward and poleward in the direct cells. Since the transport is not upward at all altitudes, some other processes must be involved in maintaining the large shear in the mean zonal wind. The vertical transport by the tides is small compared to that of the mean circulation. However, the tides do transport a significant amount of angular momentum equatorward from mid-latitudes.

TABLE OF CONTENTS

	Page
Acknowledgments	iii
Abstract	v
Chapter 1. Introduction	1
1.1 Thermal Tides and the Venus Atmosphere	1
1.2 Thermal Tides on the Terrestrial Planets	8
1.3 Summary of Methods and Organization	15
Chapter 2. Numerical Modeling of Atmospheric Thermal Tides . . .	17
2.1 Introduction	17
2.2 The Linearized Primitive Equation Model	19
2.2.1 Basic Equations and Linearization	19
2.2.2 Discretization in Time	27
2.2.3 Horizontal Discretization	29
2.2.4 Vertical Discretization	32
2.2.5 Method of Solution	36
2.3 Terrestrial Thermal Tides	42
2.4 The Gravity Wave Model	66
2.5 Conservation of Energy	73
Chapter 3. The Basic State of the Venus Atmosphere	83
3.1 Introduction	83
3.2 The Static Stability	85
3.3 The Zonal Wind	102
3.4 The Sponge Layer	111
3.5 Tidal Forcing	116
Chapter 4. Results of the Venus Tidal Calculations	125
4.1 Introduction	125
4.2 Comparison of Model Tides with Observations	128

4.2.1	The OIR Data	128
4.2.2	Model Brightness Temperatures	131
4.2.3	Semidiurnal Temperature Variations	143
4.2.4	Diurnal Temperature Variations - Amplitude	156
4.2.5	Diurnal Temperature Variations - Phase	160
4.2.6	Channel 1 Results	162
4.2.7	Other Pioneer Venus Observations	162
4.3	Weighting Functions and Cloud Parameters	171
4.4	Convergence and Spatial Resolution	182
4.5	Sensitivity to the Basic State and Forcing Parameters	213
4.6	Second Order Calculations	245
References	281

CHAPTER 1

INTRODUCTION

1.1 Thermal Tides and the Venus Atmosphere

Atmospheric thermal tides are planetary scale waves forced by the variation in absorption of solar radiation from day to night. In order to determine their vertical and horizontal structure correctly, the mean thermal and dynamic state of the atmosphere must be known as well as the absorption of solar radiation as a function of height and solar zenith angle. Data from ground-based observations, the Mariner 10 fly-by, the Venera spacecraft, and the Pioneer Venus orbiter and probes have provided our considerable but still incomplete knowledge of these parameters for Venus. In this thesis, a model is developed which uses these data to calculate the vertical and horizontal structure of Venus atmospheric thermal tides. The mean state of the atmosphere is adjusted, within the range allowed by the data, until the calculated tidal structure is consistent with available data on the tides. The tidal data consist of the diurnal and semidiurnal amplitude and phase of the brightness temperatures observed by the Pioneer Venus orbiter infrared radiometer and by ground-based observations. From this structure an estimate is made of the contributions of the tides to the transport of energy from the equator to the pole and to the maintenance of the shear in the mean retrograde zonal wind.

The dominant feature of Venus atmospheric dynamics is the variation of the mean zonal wind with height. Near the surface the atmosphere corotates with the solid planet which has a sidereal period

of 243 days, while at the cloud tops, about 65 km above the surface, the atmosphere rotates with approximately a 4 day period. The direction of the rotation throughout the atmosphere is retrograde. How this global atmospheric super-rotation is maintained is the major unsolved question in the study of the Venus atmosphere general circulation. In the absence of some process which supplies retrograde angular momentum to the upper atmosphere, frictional drag would decrease the mean shear until the atmosphere corotated with the planet at all altitudes. This process consists of some combination of the mean meridional circulation and atmospheric eddies (Schubert, 1982). Eddies are motions whose average with respect to time and longitude is zero; thermal tides are a type of eddy.

On Venus, as on the Earth, the solar energy absorbed near the equator, averaged with respect to longitude, is greater than the energy lost by infrared radiation to space (Tomasko et al., 1980b). At the poles the opposite is true. Thus, on a global scale, the atmospheric circulation must transport energy from the equator to the pole. On Venus this transport is most likely accomplished by a mean meridional circulation of the Hadley cell type (Schubert, 1982). However, eddies, including the tides, may also transport significant amounts of energy across latitude circles.

All types of atmospheric eddies on Venus should be considered in terms of their angular momentum and energy transports to determine their significance on a global scale. There are many types besides the tides which may be important. Some of these are reviewed below.

On the Earth the temperature gradient between the equator and

the poles drives unstable baroclinic waves which are the dominant eddies at terrestrial mid-latitudes. The baroclinic waves tend to reduce the temperature gradient by transporting heat poleward. On Venus the criteria for baroclinic instability are met only in a thin layer in the clouds (Young, 1981). In this layer baroclinic waves may be important, but whether they transport significant amounts of energy and momentum is unknown.

If the vertical temperature gradient exceeds the adiabatic lapse rate then the atmosphere is unstable to convection which efficiently transports heat vertically. Cellular structures present in Pioneer Venus and Mariner 10 ultraviolet pictures indicate that convection is probably present near Venus' cloud tops, particularly near the subsolar point (Murray et al., 1974; Rossow et al., 1980).

Barotropic instability may occur in the presence of strong latitudinal shear in the mean zonal angular velocity. The cloud top winds on Venus seem to oscillate between a state of barotropic stability and instability. During the Pioneer Venus primary and extended missions the atmosphere was at times in nearly solid body rotation while at other times an unstable midlatitude jet was present (Rossow et al., 1980; Rossow and Kinsella, 1982). When the jet becomes unstable it may be destroyed by barotropic eddies which redistribute angular momentum but not heat. However, these eddies have not yet been observed.

There is a good deal of evidence for stable waves or eddies on Venus. In ultraviolet pictures of the planet the dominant dark horizontal 'Y' pattern is a planetary scale wave which propagates with a phase speed close to the 4-day atmospheric rotation at the cloud tops

and is longitudinal wavenumber 1 (Dolfus, 1975; Murray et al., 1974; Belton et al., 1976; Rossow et al., 1980). It has been suggested by Covey (1982) that this wave is a preferential response of the atmosphere at this wavenumber and frequency. Forcing could exist over a broad range of frequencies due to convection near the subsolar point, small scale shear instability in the zonal flow, or turbulence arising from the breaking of small scale gravity waves.

Bow shaped features and circumequatorial belts seen in the UV pictures are probably also examples of wave activity (Murray et al., 1974; Rossow et al., 1980). These features are localized in a small region and only intermittently present. The turbulence inferred to be present in the statically stable regions above and below the clouds from radio scintillation measurements is possibly due to small scale gravity waves (Woo et al., 1980). These waves could be important if they exhibit some coherence on a global scale.

Inadequate information hinders the determination of the energy and momentum transports by the eddies described above. The presence of eddies driven by baroclinic and barotropic instabilities has only been suggested by theory. The presence of stable waves has been determined, but usually there is insufficient data to calculate the magnitude of the energy and momentum transported by them.

The situation for the thermal tides is somewhat better. We use the data on the forcing and the mean state of the atmosphere to calculate the tidal perturbations in temperature and wind velocity. We require the model results to be consistent with the available tidal data. From the perturbations we calculate the transports of energy and

angular momentum.

Since the tides are forced by longitudinal instead of latitudinal variations in solar energy absorption, the direction of their latitudinal energy transport is not necessarily poleward. If the magnitude of the tidal transport is comparable to the imbalance in solar and infrared energy fluxes, then the tidal transport cannot be ignored regardless of its direction.

The tides may contribute to the maintenance of the atmospheric super-rotation by transporting angular momentum upward in the mean, thus offsetting downward transport due to friction. Upward transport exists at all altitudes and latitudes where there is a positive correlation between the tidal perturbation in the upward vertical velocity and the tidal perturbation in the retrograde zonal wind. The tides may also supply angular momentum to the atmosphere by means of the solar gravitational torque on the semidiurnal tidal perturbation in atmospheric mass (Gold and Soter, 1971). We have not determined the solar torque. It is proportional to the surface pressure oscillation which is sensitive to the forcing and thermal structure near the ground. These parameters are not well known at low altitudes. In this thesis we assume the maintenance of the zonal wind shear requires upward transport of angular momentum. However, if the solar torque is significant and in the proper direction, this may not be necessary at all altitudes.

As mentioned earlier, Hadley cells may be important in transporting energy from the equator to the poles. Vertical and latitudinal shear in the mean zonal wind may be created by these cells because along with energy they transport angular momentum. A Hadley

cell transports zonal angular momentum upward because rising motions occur at the equator where the angular momentum is greater than at the poles where sinking motions occur. Hadley cells also transport angular momentum poleward, so a process which balances this latitudinal transport is required to prevent equatorial deceleration of the mean zonal wind. It has been proposed that in the Venus atmosphere there are Hadley cells near the ground and in the cloud layer, separated by an indirect cell in a stable layer below the clouds (Kalnay de Rivas, 1973, 1975; Schubert et al., 1980; Rossow, 1983; Schubert, 1982). Some observational evidence, that is, poleward winds at the cloud tops, supports the presence of the cloud layer Hadley cell (Limaye and Suomi, 1981; Rossow et al., 1980).

In this thesis we have calculated the mean meridional circulation forced by the latitudinal radiative imbalance neglecting eddy energy transport except for that due to the tides. The latitudinal tidal energy transport is significant compared to the radiative imbalance, but does not in general tend to offset it. The tides transport energy from mid-latitudes towards the equator and poles. Our calculations of the mean meridional circulation are basically consistent with the stacked Hadley cell circulation described above. The angular momentum transport in the direct Hadley cells is upward and poleward. However, some other process must transport angular momentum upward in the region of the indirect cell. The vertical transport of angular momentum by the tides is of variable sign with altitude. Thus, the tides do not provide the missing link. However, the tides do transport a significant amount of angular momentum equatorward from mid-latitudes,

so they may be important in balancing the poleward transport by the Hadley cells.

1.2 Thermal Tides on the Terrestrial Planets

A very thorough review of the data relevant to earth thermal tides is given in Chapman and Lindzen (1970). Most of the data consist of time series of the values of meteorological variables taken at ground level. Measurements of surface pressure are the most commonly analyzed to determine tidal components. Wind and temperature data have been analyzed at some localities. In the equatorial region the tidal signal is immediately apparent in the pressure record as shown in Figure 1.1 at Batavia. There is a semidiurnal oscillation with peak-to-peak amplitude of about 2 mb. The amplitude and phase of this oscillation is remarkably steady with time. The amplitude of the diurnal oscillation is about half as great. At mid-latitudes the pressure variation is dominated by large scale weather systems which have a period of several days. For example, see the curve for Potsdam in Figure 1.1. However, by harmonic analysis the tidal components can be determined. The semidiurnal pressure variation has peak-to-peak amplitude of about 1 mb and, again, the diurnal variation is less by a factor of two. Since the diurnal component of the variation in solar radiation is about twice as great as the semidiurnal, and the surface temperature follows this pattern, the relative amplitudes in the pressure variation are just about opposite to that expected.

The first attempt to explain this phenomenon was made by Lord Kelvin (1882) who suggested that the semidiurnal period was close to resonance with a free oscillation of the atmosphere. This theory could not be proved or disproved until the vertical temperature profile was more accurately known. It wasn't until the 1950's that measurements by

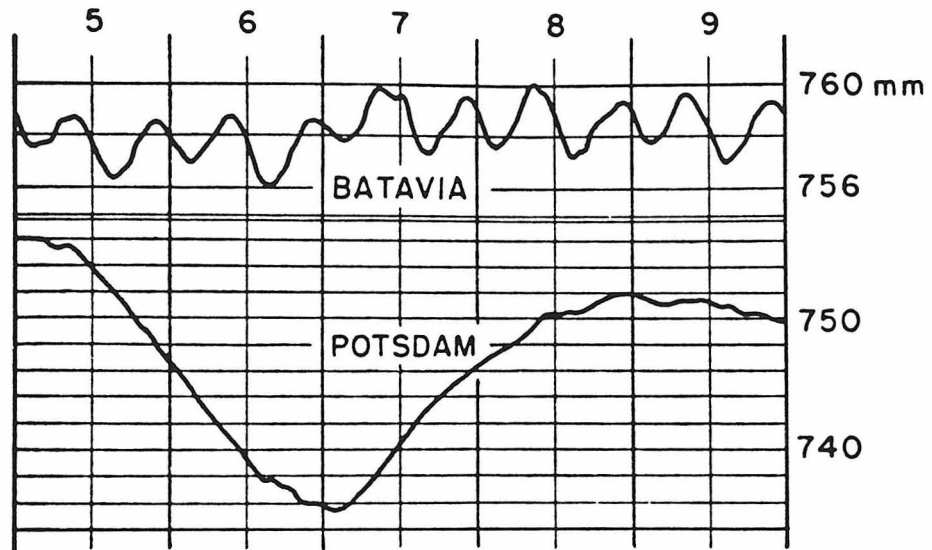


Fig. 1.1 - Surface pressure variations at Batavia (6°S) and Potsdam (52°N) during November 1919. Data from Bartels (1928). This figure is from Chapman and Lindzen (1970).

rockets proved that the resonance theory was false. Up until that time the only thermal forcing considered for the tides was upward eddy conduction of heat from the ground. The calculated semidiurnal pressure response to this forcing was much less than observed. When it became clear that the response could not be enhanced by resonance, other sources of excitation were investigated. It was found that absorption of radiation in the atmosphere could explain the semidiurnal pressure variation. One-third of the response is due to absorption by water vapor near the ground (Siebert, 1961), and the other two-thirds is due to absorption by ozone near 50 km (Butler and Small, 1963; Lindzen, 1968). The calculated phase agrees well with that observed. Since the diurnal forcing due to atmospheric absorption is larger than the semidiurnal, the problem of the relative amplitudes remained. Lindzen (1967) showed that most of the diurnal forcing goes into a trapped oscillation which cannot propagate away from the region of excitation. He also showed, as suggested by Butler and Small (1963), that the main propagating diurnal wave has a very short wavelength and is subject to destructive interference when the forcing extends over a thick layer as is the case with ozone. Thus, very little of the diurnal response reaches the ground.

Chapman and Lindzen (1970) also review work done on determining the tidal fields above the ground. The main sources of data are balloon soundings up to 30 km, rocket soundings from 30 to 60 km, and tracking of meteor trails at 80-115 km. These data are limited, but tidal components of the meridional wind have been estimated at various sites. The diurnal oscillation grows with height until it is the major

dynamical feature in the upper atmosphere. Lindzen's calculations agree with the observed diurnal amplitude and phase up to about 100 km. The large diurnal response is due to the effects of local heating and an upward propagating wave excited by the water vapor absorption which occurs in a thin layer.

On Mars the forcing for thermal tides depends on the variable opacity of the atmosphere. When the atmosphere is clear, most of the incoming solar radiation reaches the ground; there is very little absorption in the atmosphere. During a global dust storm the atmosphere absorbs more radiation, thus raising the level of the forcing. This elevated forcing is analogous to that caused by the ozone layer on the Earth (Zurek, 1980).

Data on Martian thermal tides consist of the diurnal and semidiurnal components of the surface pressure oscillation at the two Viking landing sites. When the atmosphere is clear, the diurnal and semidiurnal amplitudes are nearly the same; however, during global dust storms the semidiurnal oscillation is dominant at the Lander 1 site (Leovy and Zurek, 1979). Raising the level of the forcing and increasing the depth of the layer over which it occurs has the same effect on Mars of suppressing the diurnal surface pressure variation as it has on the Earth (Zurek, 1981). The semidiurnal oscillation is weaker at the Lander 2 site due to the superposition of latitudinal modes with equal but opposite amplitudes (Zurek, 1981). During the global dust storms both the diurnal and semidiurnal tides are enhanced relative to the clear atmosphere case. In fact, the tidal surface winds may be strong enough to play a role in sustaining the storms by raising

dust from the surface (Zurek, 1976).

Because of the large amplitude of Martian topography, horizontal variations in the mean surface pressure cannot be neglected if a quantitatively accurate solution for Martian tides is desired (Zurek, 1976). The topography also distorts the tidal forcing field in a clear atmosphere because the forcing per unit mass is larger over high elevations.

On Venus, data on the tides comes from infrared remote sensing of temperatures at the cloud tops and above. Ground-based observations of thermal emission from the clouds indicate a semidiurnal brightness temperature oscillation larger than the diurnal (Diner et al., 1982). The semidiurnal maxima occur in the morning and post-sunset quadrants. The Pioneer Venus orbiter infrared radiometer (OIR) confirms the ground-based observations and provides information on the vertical structure up to 100 km above the surface (Taylor et al., 1980; Elson, 1982). Except in the highest channel of the radiometer, the semidiurnal tide is larger, and its phase varies slowly with height.

On Venus, most of the absorption of solar energy takes place in the clouds, so the forcing region is above the ground and extended in height, just as on the Earth and on Mars during global dust storms. According to our calculations, the diurnal tide has a shorter vertical wavelength than the semidiurnal. The combination of the forcing distribution and the short diurnal wavelength appear to play a role in attenuating the diurnal tide. However, a much stronger effect is due to a bias in the measurements towards longer vertical scales. We find that the model diurnal tidal temperature amplitude is greater than or equal

to the semidiurnal in the region observed by the OIR. However, after convolving the model temperatures with the OIR weighting functions we arrive at model brightness temperature amplitudes which are consistent with the observed values. The weighting functions are wider than the diurnal wavelength so much cancellation occurs. The model also accurately predicts the phase of the semidiurnal brightness temperature variation. The phase does not change rapidly with height because of the long semidiurnal vertical wavelength (~ 30 km). Above 90 km the tide in the model is damped so that the phase in both the diurnal and semidiurnal tide does not change with height. Thus, convolving the model temperature with the highest OIR weighting function results in model brightness temperature amplitudes where the diurnal is larger than the semidiurnal, which agrees with the data.

The amplitude and phase of the semidiurnal surface pressure oscillation is of special interest on Venus because it determines the solar gravitational torque on the atmosphere. This torque may act to accelerate the atmospheric rotation and/or maintain the rotation of the planet (Gold and Soter, 1971; Dobrovolskis, 1978). Our results are consistent with Dobrovolskis' in that we find that the surface pressure oscillation generated by the heating in the clouds is smaller than that generated by local heating at the ground, even though the cloud level heating is about 30 times greater. This is contrary to the case on Earth and Mars where an elevated forcing region enhances the surface pressure semidiurnal tidal response. The reason this enhancement does not occur on Venus may have to do with the difference in diurnal period between the upper and lower atmosphere (Dobrovolskis, 1976; Ingersoll

and Dobrovolskis, 1978). We have not been able to accurately determine the magnitude of the torque on the atmosphere because the solution near the ground is ill constrained, as discussed in the previous section.

1.3 Summary of Methods and Organization

On the Earth the tidal problem is separable in height and latitude because the atmosphere is assumed to rotate uniformly with height. The latitude structure may be determined analytically and the vertical structure by solving an ordinary differential equation. On Venus the tidal problem is nonseparable because the shear in the mean zonal wind cannot be neglected.

To solve for Venus thermal tides, we have developed a linearized primitive equation model based on the nonlinear general circulation model of Staniforth and Daley (1977). To linearize, each variable in the nonlinear model is expressed as a sum of a zeroth order basic state term and a first order tidal perturbation. Second order terms are then neglected. The basic state terms must be specified as input parameters and represent the average of each variable with respect to time and longitude. The tidal perturbations are expanded in terms of spherical harmonics. The vertical coordinate is discretized using a finite element formulation. The equations are discretized in time using a semi-implicit algorithm. To solve for the tidal structure we begin with arbitrary initial conditions and integrate in time. The free modes excited by the initial conditions are suppressed by allowing the amplitude of the forcing to increase with time. The time dependence of the forced solution is proportional to that of the forcing, so it increases relative to the free modes. The integration continues until the free modes are negligible.

The development of the model and convergence scheme is discussed more fully in Chapter 2. Also in Chapter 2 we test the model by

reproducing the terrestrial tidal solution. The full model is too expensive to run for many cases so we have also developed a simpler gravity wave model to obtain an approximate solution for the vertical structure of the tides. The assumptions made in developing the gravity wave model are discussed in Chapter 2. Finally, in Chapter 2 the conservation of energy in the model is considered.

In Chapter 3 we discuss the basic state of the Venus atmosphere and the tidal forcing, and in Chapter 4, the results of the tidal calculations. The sources of data for the basic state are the Pioneer Venus orbiter and probes, the Mariner 10 fly-by, the Venera spacecraft, and ground-based observations. The model input is required to be consistent with these data while the model output must agree with the observations of the tides made by the Pioneer Venus OIR and by ground-based observations. Since our basic state and forcing provide input and output which satisfy these requirements, our confidence in their validity in actually representing average conditions is increased. The tides are a global scale phenomenon which would not be accurately modeled if the basic state were contaminated by anomalous local or temporal perturbations. In Chapter 4 we discuss the agreement of the calculation with available tidal data, the adequacy of the spatial resolution and convergence, the sensitivity to the basic state and forcing parameters, and the calculation of energy and angular momentum fluxes by the tides and the mean meridional circulation.

CHAPTER TWO

NUMERICAL MODELING OF ATMOSPHERIC THERMAL TIDES

2.1 Introduction

In this chapter we describe the development of our numerical model. The purpose of this model is to calculate the response of the atmosphere to periodic forcing. In the case of atmospheric tides the forcing is due to the longitudinal variation in absorption of sunlight. The response is governed by the equations of motion, the thermodynamic equation, and the continuity equation. In the most general form currently used in meteorology, these equations are called the primitive equations. In deriving the primitive equations it is assumed that the atmosphere is a perfect gas, that it is always in local thermodynamic equilibrium, that it is thin compared to the radius of the planet, and that the hydrostatic approximation holds. It is also assumed that the planet is a sphere. For the purpose of calculating atmospheric tides we make one further very important assumption: we express all tidal fields as small perturbations from a basic or mean state which is steady in time and independent of longitude. When we neglect all terms which are second order or higher in the perturbations, the equations become linear. Therefore, we call our model a linearized primitive equation (LPE) model.

Several further assumptions which are valid for the Earth, but not for Venus, lead to a set of equations which are separable in height and latitude. The equation for the latitudinal structure can then be solved analytically, and the solution for the vertical structure only requires integrating an ordinary differential equation. Topography can

be ignored on both planets. However, the key assumption in obtaining separability is that the basic flow consists only of a zonal wind which is constant with height. On Venus we still assume that the mean meridional wind is zero, but the mean zonal wind varies from near 0 m/s at the ground to about 100 m/s in the clouds. This differential rotation cannot be ignored. Thus, we need a three-dimensional numerical model to solve correctly for Venus thermal tides. The three dimensions are height, latitude, and time.

In Section 2.2 we describe our primitive equation model which is based on the model of Staniforth and Daley (1977). We discuss the linearization, the numerical procedures, treatment of the boundary conditions, the time-stepping algorithm, the convergence scheme, and other relevant topics. Sections 2.2.1 through 2.2.4 are a straightforward application of Staniforth and Daley (1977) to the tidal problem. Section 2.2.5 is a major departure from Staniforth and Daley (1977) and gives a method of finding the forced tidal solution starting from arbitrary initial conditions. We then show in Section 2.3 that our model can reproduce the classical solution for Earth tides. In section 2.4, we present our two-dimensional equivalent gravity wave model which we use to solve for the approximate vertical structure. The gravity wave model is useful for running large numbers of cases cheaply. We have used it extensively in testing our numerical algorithm for solving for the vertical structure and in sensitivity studies. The sensitivity studies are presented in a later chapter. Finally, in section 2.5 we discuss the performance of our model in terms of energy conservation.

2.2 The Linearized Primitive Equation Model

2.2.1 Basic Equations and Linearization

The primitive equation model of Staniforth and Daley (1977), referred to hereafter as SD, is discretized using finite elements in the vertical dimension and spherical harmonics in the horizontal. Both these discretization methods are Galerkin, i.e., dependent variables are represented as sums over spatial basis functions. In Galerkin methods the error introduced by discretization is orthogonal to the basis functions. Thus, nonlinear computational instability cannot arise from the spatial grid, at least (Staniforth and Daley, 1977). The time discretization is not Galerkin, but it is semi-implicit which means that certain terms are evaluated implicitly, i.e., as a mean of their values at the past and future time steps instead of at the present time step. The terms which are evaluated implicitly are those which control the propagation of gravity waves. This has the effect of stabilizing the model with respect to short period gravity waves so that a longer time step may be taken (Robert et al., 1972).

Following SD we start with the primitive equations in sigma coordinates. The vertical coordinate is $\sigma = p/p_s$, where p is pressure and p_s is the surface pressure. In sigma coordinates the ground is at $\sigma = 1$ allowing the boundary condition there to be easily imposed in an accurate form. The price for simplifying the boundary condition is paid in the appearance of numerous terms involving $q = \ln p_s$. The equations are:

$$\zeta_t = -\vec{\nabla} \cdot [(\zeta + f)\vec{V}] - \hat{k} \cdot \vec{\nabla} \times (RT \vec{\nabla} q + \sigma \vec{V}_\sigma) \quad (2.1)$$

$$D_t = \hat{k} \cdot \vec{\nabla} \times [(\zeta + f)\vec{V}] - \vec{\nabla} \cdot (RT \vec{\nabla} q + \sigma \vec{V}_\sigma) - \nabla^2 (\Phi + 1/2 V^2) \quad (2.2)$$

$$T_t = -\vec{V} \cdot \vec{\nabla} T + \sigma \dot{\gamma} - (RT/c_p)(D + \sigma \dot{\sigma}) \quad (2.3)$$

$$q_t = -D - \sigma \dot{\sigma} - \vec{V} \cdot \vec{\nabla} q \quad (2.4)$$

$$\sigma \dot{\Phi}_\sigma = -RT \quad (2.5)$$

where $t = \text{time}$, $\vec{V} = \text{horizontal velocity vector}$, $\hat{k} = \text{unit vertical vector}$, $R = \text{gas constant}$, $c_p = \text{specific heat at constant pressure}$, $\gamma = \text{static stability} = RT/c_p \sigma - \partial T/\partial \sigma$, $\dot{\sigma} = \text{vertical motion in sigma coordinates}$, and $f = \text{the Coriolis parameter}$. A subscript means differentiation with respect to that variable. The primary dependent variables are $\zeta = \hat{k} \cdot \vec{\nabla} \times \vec{V} = \text{vertical component of vorticity}$, $D = \vec{\nabla} \cdot \vec{V} = \text{horizontal divergence}$, $T = \text{temperature}$, $q = \ln p_s$, and $\Phi = \text{geopotential}$. Equations (2.1) and (2.2) are the equations of motion, (2.3) is the thermodynamic equation, (2.4) is the continuity equation, and (2.5) is the hydrostatic equation. We use the equations of motion in their vorticity and divergence forms because these are more suited to a spectral, i.e., spherical harmonic, representation and to a semi-implicit time-stepping algorithm (Hoskins and Simmons, 1975). We follow SD for several more steps before linearizing.

Equations (2.1)-(2.5) as they stand are not well-posed since we have five dependent variables : ζ , D , T , Φ , and $\dot{\sigma}$, which are functions of latitude, longitude, and σ , plus q which is a function of latitude

and longitude only. However, we now introduce the vertical boundary conditions

$$\dot{\sigma} = 0 \quad \text{at} \quad \sigma = 1 \quad \text{and} \quad \sigma = 0 . \quad (2.6)$$

These can be used to derive a diagnostic equation for σ . First, we define for any function, F ,

$$\hat{F}^\sigma = \int_\sigma^1 F d\sigma; \quad \hat{F} = \hat{F}^0 = \int_0^1 F d\sigma .$$

By integrating the continuity equation, (2.4), from 0 to σ and applying the lower boundary condition we obtain:

$$\dot{\sigma} = -\sigma q_t + \hat{D}^\sigma - \hat{D} + \hat{V}^\sigma \cdot \vec{\nabla}_q - \hat{V} \cdot \vec{\nabla}_q .$$

Next we integrate (2.4) from 0 to 1 and apply the boundary conditions to obtain

$$q_t = -\hat{D} - \hat{V} \cdot \vec{\nabla}_q \quad (2.7)$$

which we use to eliminate q_t in the expression for σ .

Thus,

$$\dot{\sigma} = (\sigma - 1)(\hat{D} + \hat{V} \cdot \vec{\nabla}_q) + \hat{D}^\sigma + \hat{V}^\sigma \cdot \vec{\nabla}_q . \quad (2.8)$$

Since Φ is unbounded as $\sigma \rightarrow 0$, it is inconvenient to use it in the numerical model. We therefore use the hydrostatic equation, (2.5), to eliminate Φ . We also introduce a new variable

$$W = - \int_0^\sigma D d\sigma = \hat{D}^\sigma - \hat{D} \quad (2.9)$$

Thus,

$$D = - \partial W / \partial \sigma . \quad (2.10)$$

By differentiating (2.2) with respect to σ we obtain

$$\begin{aligned} \sigma W_{\sigma \sigma t} = & -\sigma \{ \hat{\mathbf{k}} \cdot \vec{\nabla} \times (\zeta + \mathbf{f}) \vec{\nabla} - \vec{\nabla} \cdot (RT \vec{\nabla} \mathbf{q} + \delta V_{\sigma}) - \nabla^2 (V^2/2) \}_{\sigma} \\ & - R V^2 T \end{aligned} \quad (2.11)$$

This differentiation raises the order of the system of equations in the vertical dimension so another boundary condition is required. This condition will just be the undifferentiated form, i.e. (2.2), imposed at the lower boundary.

We also rewrite (2.3) and (2.7) in terms of W :

$$T_t = -\vec{\nabla} \cdot \vec{\nabla} T + \delta \gamma + (RT/c_p) (W^s + \vec{\nabla} \cdot \vec{\nabla} \mathbf{q} - \hat{\mathbf{k}} \cdot \vec{\nabla} \mathbf{q}) \quad (2.12)$$

$$q_t = W^s - \hat{\mathbf{k}} \cdot \vec{\nabla} \mathbf{q} \quad (2.13)$$

where $W^s = W|_{\sigma=1}$. Thus, the prognostic equations to be used are (2.1), (2.11), (2.12), and (2.13). As a final step before linearization, we bring the terms to be treated implicitly to the left-hand side of the equations and make some more definitions. (2.14)-(2.17) are the nonlinear equations solved by SD.

$$\zeta_t = G \quad (2.14)$$

$$\sigma W_{\sigma \sigma t} + R \nabla^2 (T - \sigma T_{\sigma}^* \mathbf{q}) = \sigma H_{\sigma} \quad (2.15)$$

$$T_t - \sigma T_{\sigma}^* q_t - \gamma^* W = J \quad (2.16)$$

$$q_t - W^s = K \quad (2.17)$$

where

$$G = -\vec{\nabla} \cdot [(\zeta + f)\vec{V}] - \hat{k} \cdot \vec{\nabla} \times (RT\vec{\nabla}_q + \delta\vec{V}_\sigma)$$

$$H = -\hat{k} \cdot \vec{\nabla} \times [(\zeta + f)\vec{V}] + \vec{\nabla} \cdot (R(T - T^*) \vec{\nabla}_q + \delta\vec{V}_\sigma) + \nabla^2 (v^2/2)$$

$$J = \sigma T_\sigma^* \vec{\nabla} \cdot \vec{\nabla}_q - \vec{\nabla} \cdot \vec{\nabla} T + \delta\gamma - (W - \sigma W^s) \gamma^* + [R(T - T^*)/c_p] W^s \\ + (RT/c_p) (\vec{\nabla} \cdot \vec{\nabla}_q - \hat{k} \cdot \vec{\nabla}_q)$$

$$K = -\hat{k} \cdot \vec{\nabla}_q$$

In the above $T^*(\sigma)$ = the global mean temperature profile and $\gamma^*(\sigma)$ = the global mean static stability profile.

To linearize we express all dependent variables as a sum of a zeroth-order basic state component plus a first-order perturbation. For example,

$$T(\sigma, \lambda, \phi, t) = T^*(\sigma) + T_1(\sigma, \lambda) + T'(\sigma, \lambda, \phi, t)$$

where λ is latitude and ϕ is longitude. To be consistent with SD we have broken up our basic state temperature into a global mean profile, $T^*(\sigma)$, and a latitudinally varying component, $T_1(\sigma, \lambda)$.

For the zonal wind, which is parallel to latitude circles, u , we have

$$u = a \cos \lambda \Omega(\sigma, \lambda) + u'(\sigma, \lambda, \phi, t)$$

where Ω is the basic state rotation and a is the radius of the planet. If the atmosphere is in solid body rotation at each level, Ω will be a function of σ only. This is the case in our standard basic state. The

basic state meridional wind, which is parallel to meridians, is zero so

$$v = v'(\sigma, \lambda, \phi, t) .$$

From these expressions for u and v we see that

$$D^* = \vec{\nabla} \cdot \vec{V}^* = \frac{1}{a \cos \lambda} \frac{\partial}{\partial \phi} [a \cos \lambda \Omega] = 0$$

where a superscript $*$ denotes a basic state quantity. Thus, $W^* = 0$.

$$\text{However, } \zeta^* = \hat{k} \cdot \vec{\nabla} \times \vec{V}^* = \frac{-1}{\cos \lambda} \frac{\partial}{\partial \lambda} (\cos^2 \lambda \Omega) .$$

All horizontal derivatives will be taken in spherical coordinates as above. A mean surface pressure which varies with latitude represents zonally averaged topography. Recall that $q = \ln p_s$. Thus, we allow q^* to depend on λ in our general model development, although our standard basic state has constant q^* . From the above basic state expressions and equation (2.8) it follows that $\sigma^* = 0$.

The linearized equations are obtained by substituting expressions for the basic state plus perturbation quantities into the equations and keeping only terms which are first order in the perturbations. These terms contain a perturbation quantity either by itself, multiplied by a basic state quantity, or multiplied by a constant. Terms which contain multiplications of two or more perturbation quantities are neglected. Terms that only involve the basic state are assumed to balance. Only equation (2.15) contains basic state terms. The equation which is derived by balancing the basic state terms in (2.15) is called the thermal wind equation for cyclostrophic balance. It can be used in determining the basic state as described in Chapter 3.

The terms on the left-hand side of (2.14)-(2.17) are already linear, so the main work in linearization comes in finding G' , H' , J' , and K' . We obtain

$$G' = -\Omega \frac{\partial \zeta'}{\partial \phi} - (\zeta^* + f) D' - \frac{v'}{a} \frac{\partial}{\partial \lambda} (\zeta^* + f) + \frac{R}{a^2} \frac{\partial T_1}{\partial \lambda} \frac{1}{\cos \lambda} \frac{\partial q'}{\partial \phi}$$

$$- \frac{R}{a^2} \frac{\partial T'}{\cos \lambda} \frac{\partial q^*}{\partial \phi} + \frac{1}{\cos \lambda} \frac{\partial}{\partial \lambda} (\cos^2 \lambda \delta' \frac{\partial \Omega}{\partial \sigma})$$

$$H' = -(\zeta^* + f) \zeta' + \frac{u'}{a} \frac{\partial}{\partial \lambda} (\zeta^* + f) + \frac{1}{\cos \lambda} \frac{\partial}{\partial \lambda} (\zeta' \cos^2 \lambda \Omega)$$

$$+ RT_1 \nabla^2 q' + \frac{R}{a^2} \frac{\partial T_1}{\partial \lambda} \frac{\partial q'}{\partial \lambda} + \frac{\partial \Omega}{\partial \sigma} \frac{\partial \sigma'}{\partial \phi} + \nabla^2 u' a \cos \lambda \Omega$$

$$+ \frac{1}{a^2} \frac{\partial}{\cos \lambda} (RT' \cos \lambda \partial q^* / \partial \lambda)$$

$$J' = \sigma \hat{\Omega} T_\sigma^* \frac{\partial q'}{\partial \phi} + \sigma T_\sigma^* \frac{\hat{v}'}{a} \frac{\partial q^*}{\partial \lambda} - \frac{v'}{a} \frac{\partial T_1}{\partial \lambda} - \Omega \frac{\partial T'}{\partial \phi} + \sigma' (\gamma^* + \gamma_1)$$

$$- (W' - \sigma W^{s'}) \gamma^* - \frac{RT_1}{c_p} \hat{D}' + \frac{R(T^* + T_1)}{c_p} (\Omega - \hat{\Omega}) \frac{\partial q'}{\partial \phi}$$

$$+ \frac{R(T^* + T_1)}{c_p} \frac{(v' - \hat{v}')}{a} \frac{\partial q^*}{\partial \lambda}$$

$$K' = -\hat{\Omega} \frac{\partial q'}{\partial \phi} + \frac{\hat{v}'}{a} \frac{\partial q^*}{\partial \lambda}$$

In the linearized equations we include, as first-order quantities, the thermal forcing, Q' , and dissipation in the form of Rayleigh friction and Newtonian cooling. The forcing and dissipation terms are not included in SD, but since we require them, we will carry them through the rest of the derivation. The linearized equations are:

$$\zeta'_t + \zeta'/\tau_R = G' \quad (2.18)$$

$$\sigma W'_{\sigma\sigma t} + \sigma (W'_{\sigma}/\tau_R)_{\sigma} + R\nabla^2 (T' - \sigma T'_{\sigma} q') = \sigma H'_{\sigma} \quad (2.19)$$

$$T'_t - \sigma T'_{\sigma} q'_t + T'/\tau_N - \sigma T'_{\sigma} q'/\tau_N - \gamma^* W' = J' + Q' \quad (2.20)$$

$$q'_t - W^s' = K' \quad (2.21)$$

where τ_R and τ_N are the time constants of Rayleigh friction and Newtonian cooling, respectively.

These dissipation terms are used to form a sponge layer in the upper atmosphere which absorbs upward propagating energy. The sponge layer is necessary because the boundary condition $\sigma = 0$ at $\sigma = 0$, when applied in the numerical model, causes spurious reflection of upward propagating waves off the upper boundary. In fact, due to the vertical discretization, it has the same effect as a rigid lid at a finite value of σ (Lindzen et al., 1968; Kirkwood and Derome, 1977). In models of the earth's troposphere a rigid lid boundary condition is usually adequate because the jump in static stability at the tropopause forms a natural 'lid'. Disturbances in the troposphere propagate only weakly into the stratosphere. Venus atmospheric structure is quite different, and waves there may be able to freely propagate upward until damped by nonlinear processes. A rigid lid is inappropriate for the earth's astratosphere as well.

2.2.2 Discretization in Time:

We are now ready to time discretize (2.18) - (2.21). For the implicit terms we use the notation

$$\bar{F}^t = \frac{F|_{t+\Delta t} + F|_{t-\Delta t}}{2}$$

for any function F . Δt is the time step. We evaluate time derivatives by a centered difference. Thus,

$$F_t = \frac{F|_{t+\Delta t} - F|_{t-\Delta t}}{2\Delta t}$$

The time discretized equations are

$$\left(1 + \frac{\Delta t}{\tau_R}\right) \zeta^t = \zeta|_{t-\Delta t} + \Delta t G|_t \quad (2.22)$$

$$\begin{aligned} \sigma \left[\left(1 + \frac{\Delta t}{\tau_R}\right) \bar{w}_\sigma^t \right]_\sigma + R\Delta t \nabla^2 (\bar{T}^t - \sigma T_\sigma^* \bar{q}^t) \\ = \sigma W_{\sigma\sigma} |_{t-\Delta t} + \Delta t \sigma H_\sigma |_t \end{aligned} \quad (2.23)$$

$$\begin{aligned} \left(1 + \frac{\Delta t}{\tau_N}\right) (\bar{T}^t - \sigma T_\sigma^* \bar{q}^t) - \gamma^* \bar{w}^t \\ = (T - \sigma T_\sigma^* q)|_{t-\Delta t} + \Delta t (J + Q)|_t \end{aligned} \quad (2.24)$$

$$\bar{q}^t - \Delta t \bar{w}^t = q|_{t-\Delta t} + \Delta t K|_t \quad (2.25)$$

where we have dropped the primes on the first-order quantities.

A simple example suffices to show why it is necessary to treat the dissipation terms implicitly. Consider the equation

$$F_t + F/\tau = 0$$

Discretized explicitly this equation becomes

$$\frac{F|_{t+\Delta t} - F|_{t-\Delta t}}{2\Delta t} = \frac{-F|_t}{\tau} \quad (2.26)$$

Assume a solution of the form $F = F_0 e^{-\lambda t}$ where λ may be complex. Let $\lambda = \lambda_R + i\lambda_I$. For a stable numerical solution we need $\lambda_R > 0$. Upon substitution of $F_0 e^{-\lambda t}$ into (2.26) we obtain

$$\sinh(\lambda \Delta t) = \Delta t / \tau$$

or

$$\sinh(\lambda_R \Delta t) \cos(\lambda_I \Delta t) = \frac{\Delta t}{\tau}, \quad \cosh(\lambda_R \Delta t) \sin(\lambda_I \Delta t) = 0 \quad (2.27)$$

Since $\cosh x > 0$ for all x , we must have $\lambda_I = n\pi/\Delta t$ to satisfy the second part of (2.27). When n is odd, $\cos(\lambda_I \Delta t) = -1$. Then $\sinh(\lambda_R \Delta t) = -\Delta t/\tau$, which implies $\lambda_R < 0$. Thus, unstable solutions exist for the explicit discretization and will be excited by any numerical noise. On the other hand, if we discretize implicitly, we obtain

$$\frac{F|_{t+\Delta t} - F|_{t-\Delta t}}{2\Delta t} = \frac{-F^t}{\tau}$$

Assuming $F = F_0 e^{-\lambda t}$ we derive

$$\tanh \lambda \Delta t = \Delta t / \tau$$

or

$$\frac{\sinh(2\lambda_R \Delta t)}{\cosh(2\lambda_R \Delta t) + \cos(2\lambda_I \Delta t)} = \frac{\Delta t}{\tau}, \quad \frac{\sin(2\lambda_I \Delta t)}{\cosh(2\lambda_R \Delta t) + \cos(2\lambda_I \Delta t)} = 0 \quad (2.28)$$

To satisfy the second part of (2.28), $\lambda_I = n\pi/2\Delta t$. In this case λ_R will be positive for any n . Although our system of equations is more complicated than this example, the dissipation terms will still be unstable if evaluated explicitly. A similar argument shows that the other implicit terms in (2.22)-(2.25) stabilize short period gravity waves.

2.2.3 Horizontal Discretization

We will now formulate our horizontal discretization in terms of spherical harmonics. Let F' be any perturbation variable except \vec{V}' .

Then

$$F'(\sigma, \lambda, \phi, t) = \sum_{n=m}^N F'_n(\sigma, t) Y_n^m(\lambda, \phi) \quad (2.29)$$

where

$$Y_n^m(\lambda, \phi) = P_n^m(\lambda) e^{im\phi}.$$

P_n^m is the Legendre function of order m and degree n . The dependence on longitude is a simple sinusoid with zonal wavenumber m . This longitude dependence is particularly convenient for the tidal problem since the diurnal fields have $m = 1$, the semidiurnal, $m = 2$, etc. Since we have

linearized about a basic state with no longitudinal dependence, components with different zonal wavenumber will not interact. Therefore, we may solve separately for the various tidal components, which enables us to reduce the horizontal dependence to a single sum over n , as in (2.29), instead of a double sum over m and n . This increases our computational efficiency. Note that we may now use the relations

$$F'_\phi = imF' \quad ; \quad \nabla^2 F' = \sum_n \frac{-n(n+1)}{a^2} F'_n Y_n^m$$

u' and v' may also be expressed in terms of spherical harmonics, but the expansions include terms with horizontal derivatives.

$$u' = \frac{a}{\cos \lambda} \sum_{n=m}^N \left(\frac{im(\partial W_n / \partial \sigma)}{n(n+1)} P_n^m + \zeta_n \frac{(1 - \sin^2 \lambda)}{n(n+1) \cos \lambda} \frac{dP_n^m}{d\lambda} \right)$$

$$v' = \frac{a}{\cos \lambda} \sum_{n=m}^N \left(- \frac{im \zeta_n}{n(n+1)} P_n^m + \frac{(\partial W_n / \partial \sigma)(1 - \sin^2 \lambda)}{n(n+1) \cos \lambda} \frac{dP_n^m}{d\lambda} \right)$$

If we represent all first-order terms in (2.22)-(2.25) in terms of spherical harmonics, first of all we see that we may cancel out $e^{im\phi}$ since it appears in every term. If we then multiply (2.22)-(2.25) by P_n^m and integrate over the sphere we will obtain, by the orthogonality of Legendre functions, a separate system of equations for each n . In what follows, only subscript σ denotes differentiation; other subscripts are constants introduced during discretization.

$$\left(1 + \frac{\Delta t}{\tau_R} \right) \bar{\zeta}_n^t = \zeta_n|_{t-\Delta t} + \Delta t G_n|_t \quad (2.30)$$

$$\begin{aligned} \sigma \left[\left(1 + \frac{\Delta t}{\tau_R} \right) (\bar{W}_n^t)_\sigma \right]_\sigma - R \Delta t \frac{n(n+1)}{a^2} (\bar{T}_n^t - \sigma T_\sigma^* \bar{q}_n^t) \\ = \sigma (\bar{W}_n)_\sigma |_{t-\Delta t} + \Delta t \sigma (H_n)_\sigma |_t \end{aligned} \quad (2.31)$$

$$\begin{aligned} \left(1 + \frac{\Delta t}{\tau_N} \right) (\bar{T}_n^t - \sigma T_\sigma^* \bar{q}_n^t) - \gamma^* \bar{W}_n^t \\ = (\bar{T}_n - \sigma T_\sigma^* \bar{q}_n) |_{t-\Delta t} + \Delta t (J_n + Q_n) |_t \end{aligned} \quad (2.32)$$

$$\bar{q}_n^t - \Delta t \bar{W}_n^{st} = \bar{q}_n |_{t-\Delta t} + \Delta t K_n |_t \quad (2.33)$$

The problem is not completely separated, however, since at each time step G_n , H_n , J_n , and K_n must be evaluated. These terms involve interactions of the perturbations with the basic state. Through these interactions, modes of different n are coupled. The procedure for calculating G_n , H_n , J_n , and K_n is as follows: evaluate all necessary perturbations on a Gaussian grid in $\sin \lambda$; this involves performing the sum in (2.29) for each variable. At each grid point multiply the perturbations by the appropriate basic state quantities; multiply by P_n^m for each n ; do a Gaussian integration over $\sin \lambda$ to obtain G_n , H_n , etc. If a sufficient number of grid points are used, the integration over $\sin \lambda$ will be exact. When n is large, this method is more efficient than representing the basic state quantities in terms of the P_n^m and calculating the interactions from a full correlation matrix.

At each time step, for each n , we must solve (2.30)–(2.33). The problem reduces to an elliptic boundary value problem in \bar{W}_n^t . By eliminating $(\bar{T}_n^t - \sigma T_\sigma^* \bar{q}_n^t)$ from (2.31) and (2.32) we obtain

(2.34)

$$[(1 + \Delta t/\tau_R)(\bar{W}_n^t)_\sigma - \frac{R\gamma^*}{a^2} \frac{(\Delta t)^2}{(1 + \Delta t/\tau_N)} n(n+1)] \bar{W}_n^t = L_n$$

where

$$L_n = \Delta t [(H_n)_\sigma + \frac{R(J_n + Q_n)}{a_2 \sigma} \frac{\Delta t}{(1 + \Delta t/\tau_N)} n(n+1)] \Big|_t$$

$$+ [(W_n)_{\sigma\sigma} + n(n+1) \frac{\Delta t}{(1 + \Delta t/\tau_N)} \frac{1}{\sigma} \frac{R}{a^2} (T_n - \sigma T_\sigma^* q_n)] \Big|_{t-\Delta t}$$

2.2.4 Vertical Discretization:

The above problem will be solved using one-dimensional finite elements in a procedure similar to that used by SD in the nonlinear problem. In finite elements the variables are represented in terms of locally defined basis functions. We will use Chapeau basis functions which are piece-wise linear. The form is illustrated in Figure 2.1. One of these basis functions is centered on each grid point or node. Let $e^i(\sigma)$ be the basis function centered on node i . Then

$$e^i(\sigma) = \begin{cases} (\sigma - \sigma_{i-1})/(\sigma_i - \sigma_{i-1}) & \text{for } \sigma_{i-1} \leq \sigma \leq \sigma_i \\ (\sigma_{i+1} - \sigma)/(\sigma_{i+1} - \sigma_i) & \text{for } \sigma_i \leq \sigma \leq \sigma_{i+1} \\ 0 & \text{otherwise} \end{cases}$$

and, for example, $\bar{W}_n^t = \sum_{i=1}^{NVPTS} (\bar{W}_n^t)_i e^i(\sigma)$. NVPTS is the number of vertical points. $\sigma_1 = 0$ and $\sigma_{NVPTS} = 1$.

At the lower boundary there is a half basis function extending upward into the domain. The upper boundary is difficult to treat

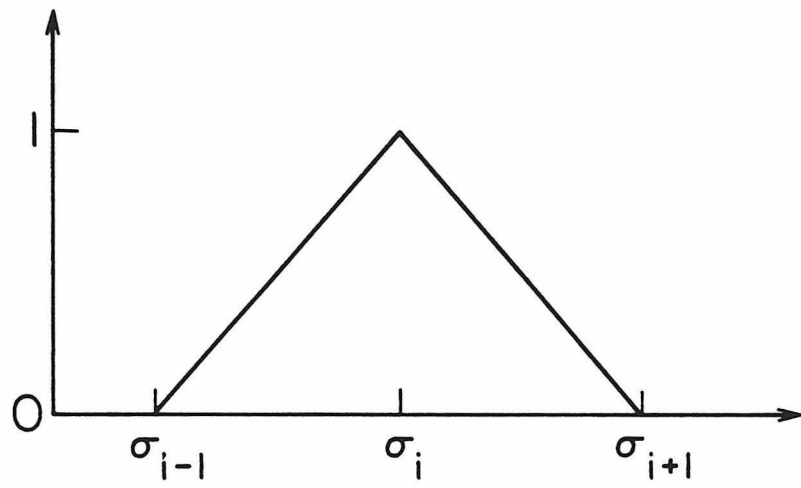


Figure 2.1 Piece-wise linear Chapeau basis function as presented in Staniforth and Daley (1976).

realistically since the governing equations are not valid as $\sigma \rightarrow 0$. SD solve this problem by omitting the half basis function which would extend downward into the domain from the upper boundary. All the variables, except W , are then undefined at the upper boundary. Their values there are not required, however. All we need is the boundary condition on W which follows from equation (2.9).

$$W(0) = 0 \quad \text{Thus, } (W_n)_1 = 0 \quad \text{for all } n.$$

This is automatically satisfied by putting $e^1 = 0$. We follow this procedure, but in our case since the upper boundary is deep in the sponge layer, a realistic treatment of the boundary condition is not crucial.

In terms of the basis functions (2.34) becomes

$$\sum_i \{ [(1 + \Delta t/\tau_R) (\bar{W}_i^t e^i(\sigma)) \sigma] \sigma - \frac{R\gamma^* (\Delta t)^2}{a^2 \sigma (1 + \Delta t/\tau_N)} n(n+1) \bar{W}_i^t e^i(\sigma) \} = L_i e^i(\sigma) \quad (2.35)$$

where we have dropped the subscript n . To obtain a solution for the \bar{W}_i^t , we multiply (2.35) by $e^j(\sigma)$ for all j and integrate from $\sigma = 0$ to $\sigma = 1$. The result is (NVPTS-1) linear equations in (NVPTS-1) unknowns. For each j there will be a contribution from the sum in (2.35) only from the terms $i = j - 1, j, j + 1$, giving us a tridiagonal system. This sparseness of interactions occurs because each basis function only overlaps with its nearest neighbors.

To make the procedure clearer let us examine the first term in (2.35):

where

$$M = \{W_\sigma|_{t-\Delta t} + \Delta t H|_t - \Delta t n(n+1) \frac{RT^*}{a^2} (q|_{t-\Delta t} + \Delta t K|_t)\}|_{\sigma=1}$$

If we combine all the matrices from the left hand side of (2.35) and call the resulting matrix \underline{S} , we obtain

$$\underline{S} \begin{pmatrix} \bar{W}_1^t \\ \bar{W}_2^t \\ \vdots \\ \bar{W}_{NVPTS}^t \end{pmatrix} + (\Delta t)^2 \frac{RT^*}{a^2} n(n+1) \begin{pmatrix} 0 \\ 0 \\ \vdots \\ \bar{W}_{NVPTS}^t \end{pmatrix} = -\underline{A} \begin{pmatrix} 0 \\ L_2 \\ L_3 \\ \vdots \\ L_{NVPTS} \end{pmatrix} + \begin{pmatrix} 0 \\ 0 \\ \vdots \\ 0 \\ M \end{pmatrix}$$

which may be solved for \bar{W}_i^t by Gaussian elimination. The elements of A are given by $\int_0^1 e^i e^j d\sigma$.

$W_i|_{t+\Delta t}$ is then easily obtained from $W_i|_{t-\Delta t}$ and \bar{W}_i^t . The updated values of the other variables, $\zeta_i|_{t+\Delta t}$, $T_i|_{t+\Delta t}$, and $q|_{t+\Delta t}$, can now be obtained from equations (2.30), (2.32), and (2.33) evaluated at each vertical point and each Legendre mode. Recall that the subscript n has been suppressed.

Actually, in the model we do not require $\Delta\sigma$ to be constant. We also break L up into various terms in order to treat derivatives and the vertical dependence of some coefficients more accurately.

2.2.5 Method of Solution:

The discussion of our general numerical model is now complete. Next we apply the model to the specific problem of thermal tides. Since we have a time-stepping model, we need to supply initial conditions, apply the appropriate forcing, and, after integrating forward in time,

arrive at the forced solution. We can't assume that we know very much about the solution, so we must be able to find the forced solution starting from arbitrary initial conditions. Unfortunately, the initial conditions will excite the free modes of the system, some of which may have as large an amplitude as the forced solution, and some of which may even be unstable. Unstable free modes can either arise from actual physical instabilities or from instabilities in the numerical algorithm. (Unstable numerical modes can exist as long as there are explicit terms.) Consider the case where either unstable modes don't exist or their growth rates are much longer than our time integration. The problem of separating the forced solution from the stable free modes still must be solved.

Our first step is to transform to a reference frame in which the tides are steady in time. This is a solar-fixed reference frame, i.e., the line from the center of the sun to the center of Venus is fixed in this frame. As shown in Figure 2.2, the longitude coordinate, ϕ , measures local time instead of longitude fixed with respect to the planet.

In this reference frame the forced tidal solution has no time dependence, while all the free modes oscillate with some finite frequency. Of course, there is one exception -- a free mode with the tidal frequency might exist. Then we would be forcing at a resonance, and a very large tidal amplitude would result. However, we have found no evidence of a resonance in our solutions.

The oscillatory part of the solution can be removed in several ways. Perhaps the most obvious method would be to do a running time

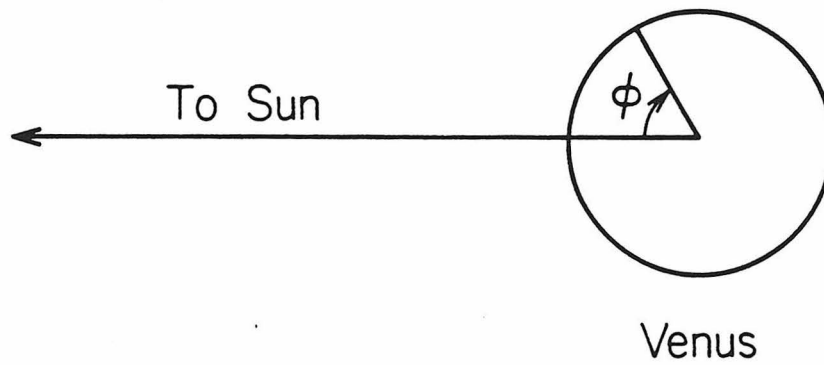


Figure 2.2 Measurement of ϕ , the longitude in a solar fixed reference frame. Venus is viewed from above the north pole; the planet rotates in the direction of increasing ϕ .

average. The averaged amplitude of the oscillations would be inversely proportional to the length of the record, while the steady part would remain constant. However, to avoid aliasing between low frequency free modes and the steady solution, the time integration would have to be at least as long as the period of the lowest frequency mode. Since free modes with very long periods are present, this method requires an unreasonably long time integration. Another alternative would be to damp the free modes by applying large amounts of dissipation at the beginning of the time integration. If the dissipation was then decreased slowly and smoothly, so as not to re-excite the free modes, the undamped, forced solution would slowly emerge. This method was used by Madala et al. (1975) in a numerical model for Earth thermal tides. However, we found that the decrease in dissipation had to be so slow that, again, the time integration was unreasonably long. The problems with both these methods seem to be due to the complexity of the Venus basic state which generates an unruly set of free modes. The simple basic states used for the earth tend to result in better behavior.

Fortunately, we found a method which works. Instead of trying to decrease the amplitude of the free modes, we increase the amplitude of the forced solution as a function of time. This is accomplished by increasing the forcing algebraically in time; the forced response increases proportionately. Since the free modes are only present due to excitation by the initial conditions, they are unaffected by the forcing, and their amplitudes remain constant. We have found that an increase in the forcing which is quadratic in time is sufficient. The

forced response grows rapidly enough so that the free modes are insignificant in comparison after a reasonable number of time-steps.

We can illustrate how this method works in a simple system. Consider the equation

$$\frac{\partial u}{\partial t} + i\omega u = F$$

where F is a constant forcing. The forced, or particular, solution is $u_p = F/i\omega$. There is only one free, or homogeneous, mode in the system, namely, $u_H = Ae^{-i\omega t}$ where A is a free parameter. If we arbitrarily apply the initial condition $u = 0$ at $t = 0$ then

$$u(t) = F/i\omega (1 - e^{-i\omega t})$$

which will never converge to $F/i\omega$. Now consider the equation

$$\frac{\partial v}{\partial t} + i\omega v = Ft$$

The particular solution is $v_p = (F/i\omega)t - F/\omega^2$ while $v_H = Ae^{-i\omega t}$ as before. With the same initial condition, $v = 0$ at $t = 0$, we obtain

$$v(t) = \frac{F}{i\omega} \left(t - \frac{1}{i\omega} (1 - e^{-i\omega t}) \right) .$$

As $t \rightarrow \infty$, v/t approaches $F/i\omega$, the desired forced solution. When the forcing increases linearly, the amplitude of the free mode in v/t is proportional to $1/t$. The method of time averaging described above gives exactly the same result if the averaging is continuous in time.

However, if the above example is done using a discrete time dependence, and the averaging is also done discretely, then increasing the forcing gives faster convergence.

Forcing proportional to more rapidly increasing functions of time may be used. For example:

$$\frac{\partial v}{\partial t} + i\omega v = Ft^2$$

If

$$v = 0 \text{ at } t = 0,$$

then

$$v/t^2 = F/i\omega t^2 \left(t^2 - \frac{2}{i\omega} t - \frac{2}{\omega^2} (1 - e^{-i\omega t}) \right).$$

The stronger decay in the free mode is offset by the presence of the term $2F/i\omega t$ which, although it doesn't oscillate, slows down the convergence. In this simple example little, if anything, is gained by using a t^2 increase. However, in our model where many free modes of different frequencies are present, a t^2 increase in the forcing results in a smoother, more rapid convergence than a linear increase.

For each computer run of the model, initial conditions are required at $t = 0$ and at $t = -\Delta t$ in equations (2.22) - (2.25). The initial conditions we choose are simply to set all perturbation variables equal to zero at these times. For consistency the same initial conditions are used for every run.

A test of the validity of our model in a tidal problem is presented in the next section. We solve for the tidal fields on the earth and compare our results to the classical solution.

2.3 Terrestrial Thermal Tides

The major features of Earth thermal tides can be modeled using classical tidal theory. In the classical theory the equations are separable in height and latitude, and the solution is comparatively easy to obtain. The classical theory is derived from the linearized primitive equations by making some simplifying assumptions. Internal dissipation and topography are ignored, and the basic flow of the atmosphere with respect to the solid planet is set equal to zero. The other basic state variables are functions only of height.

In our model setting the basic flow equal to zero is equivalent to setting Ω , the basic state rotation, equal to $2\pi/P_{\odot}$ where P_{\odot} is the length of a solar day. Ω is not zero because we have transformed to a solar-fixed reference frame. This is different from most meteorological models where the reference frame rotates with the planet. The terms in our model involving Ω are identically the same as those involving $f = 2\Omega \sin \lambda$, the Coriolis parameter, in a rotating frame. Actually, since our frame still rotates with the motion of the planet around the sun, we should retain a Coriolis term, $f_y = 2\Omega_y \sin \lambda$, where $\Omega_y = 2\pi/P_y$. P_y is the length of the year. On a rapidly rotating planet like the earth where the day is much less than the year, f_y may be neglected. We will retain f_y when modeling Venus tides.

We have modeled the earth's diurnal thermal tide using the same basic state and forcing functions as Lindzen (1967), so that our results may be compared to those he obtained using the classical theory. The diurnal tide is modeled using an isothermal atmosphere with $T^* = 260$ K.

The other non-zero basic state quantities required are the static stability, $\gamma^* = RT^*/c_p\sigma$, and $\zeta^* = 2 \Omega \sin \lambda$. In this run we ignored the dependence of c_p on pressure. Since only the latitudinal gradient of the surface pressure enters the equations, the value of q^* need not be specified. The altitude and latitude dependence of the forcing functions is shown in Figure 2.3. The analytic form of these functions is given in Lindzen (1971).

The rest of the model parameters are chosen to provide adequate resolution and convergence. The computer run to calculate the diurnal tide had 100 vertical points equally spaced in $-\ln\sigma$ from $-\ln\sigma = 0$ to 13, 41 more points spaced twice as far apart from $-\ln\sigma = 13$ to 24, plus the point at $\sigma = 0$ for a total of 142 vertical points. The upper boundary of the resolved region was at 183 km. The break in grid spacing was at 101 km. We degraded the resolution above this level to save on computer time. The change in grid spacing does not seem to have affected the results. We used 20 Legendre functions including both those symmetric and asymmetric with respect to the equator and 23 points in the Gaussian latitude grid from equator to pole. The time step was 1 hour, and the number of time steps was 600. For this run we used a linear increase in the forcing. For the sponge layer we set $\tau_R = \tau_N = \tau_0\sigma$ where $\tau_0 = 1.2 \times 10^7$ years. In the lower atmosphere the dissipation will be negligible. At 140 km, $\tau = 43$ days while at 180 km, $\tau = 5$ hrs. Thus, the dissipation becomes really large only in the top few levels.

Our results are compared to Lindzen's (1967) calculations in Figures 2.4-2.15. The diurnal tide shows a great deal of vertical and horizontal structure which is reproduced by our model. We are

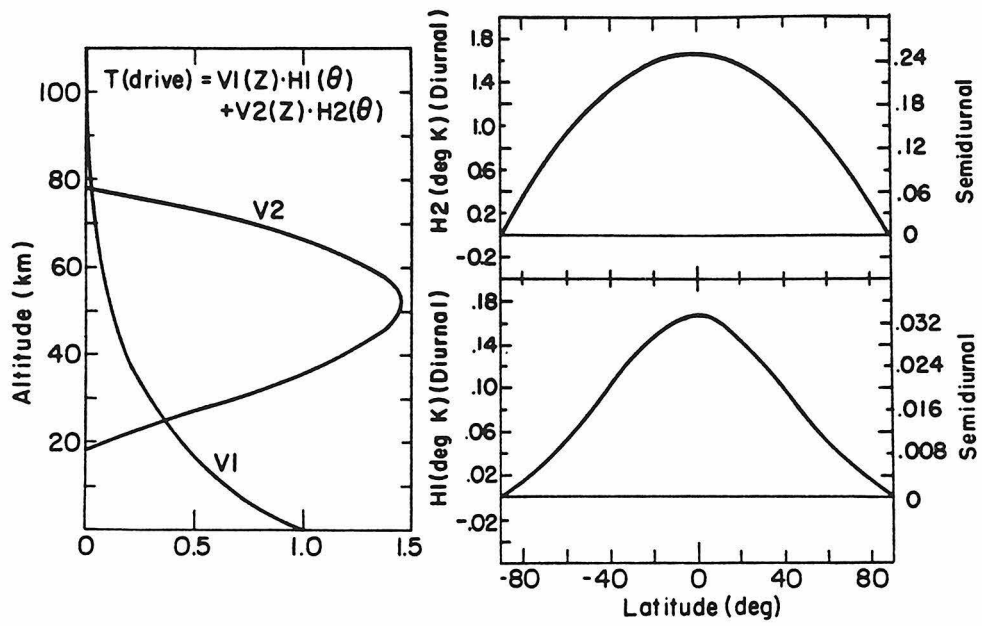


Figure 2.3 Vertical distributions of thermal excitation due to water vapor (V1) and ozone (V2); latitude distributions for water vapor (H1) and ozone (H2). From Chapman and Lindzen (1970).

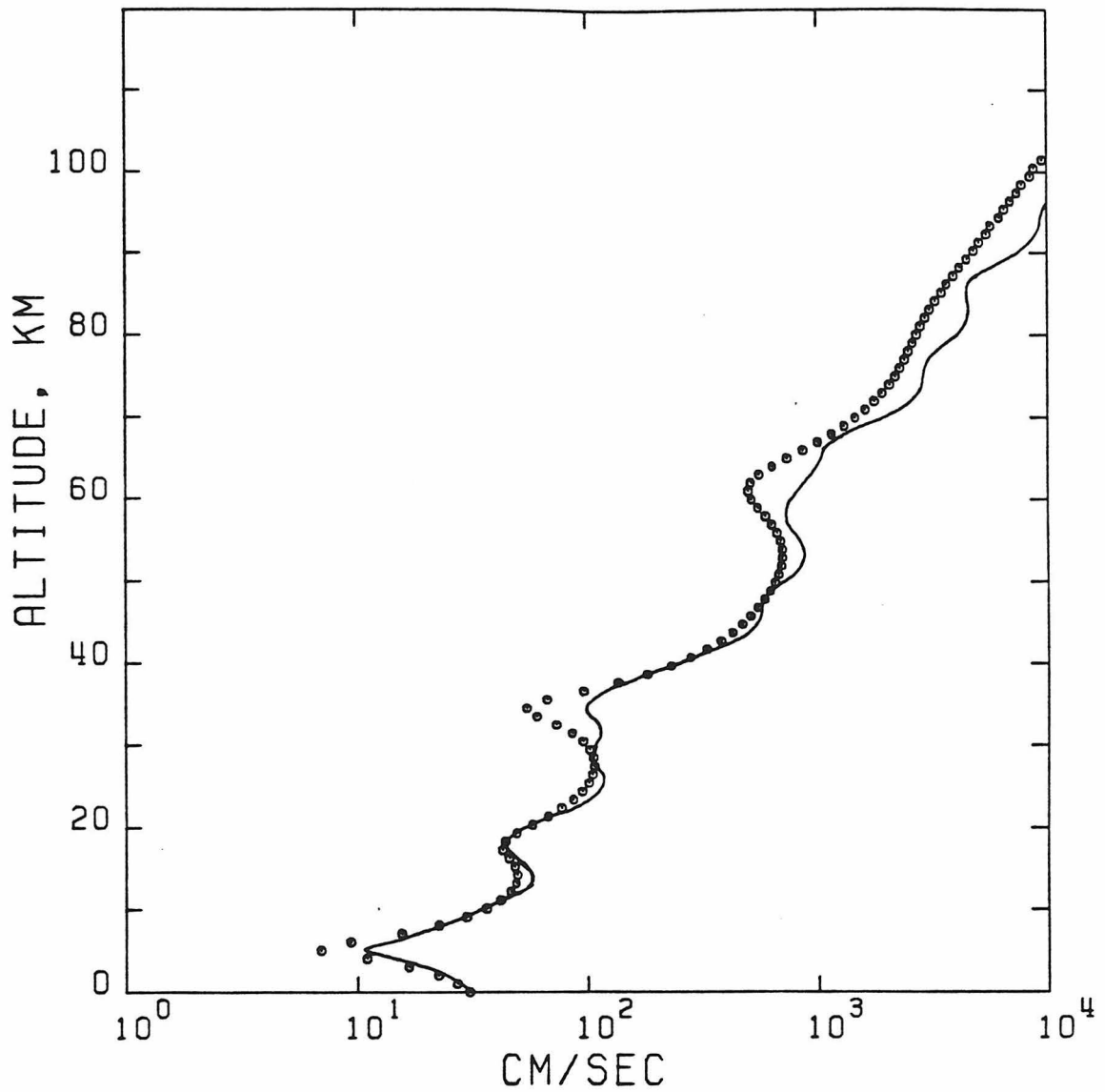
DIURNAL AMPLITUDE OF v AT LATITUDE 15

Figure 2.4 Amplitude of v' for the diurnal terrestrial thermal tide at 15° . The solid curve is the analytic model of Lindzen (1967). The data points are from the LPE model.

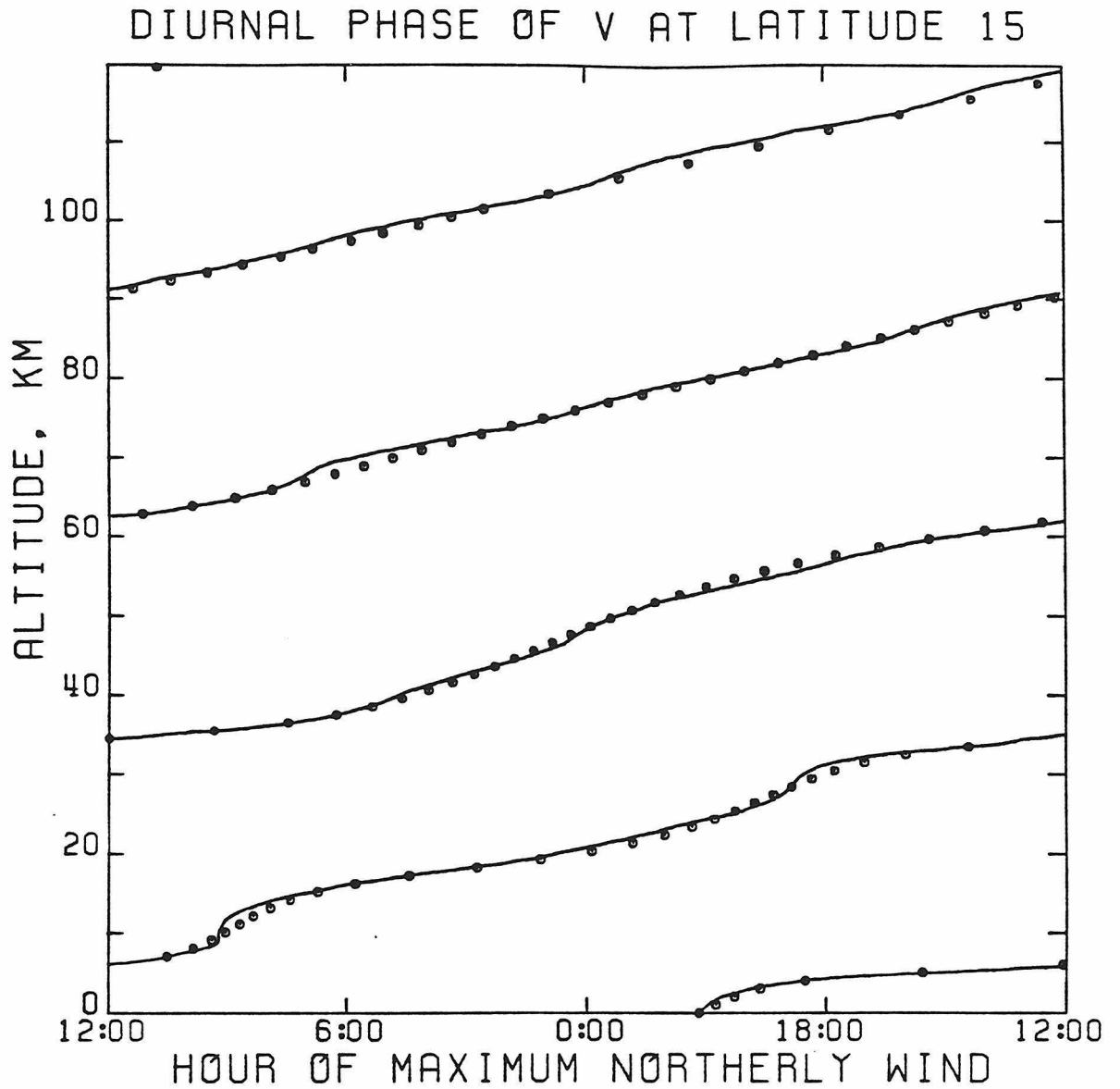


Figure 2.5 Phase of v for the diurnal terrestrial thermal tide at 15° . The solid curve is the analytic model of Lindzen (1967). The data points are from the LPE model.

DIURNAL AMPLITUDE OF U AT LATITUDE 15

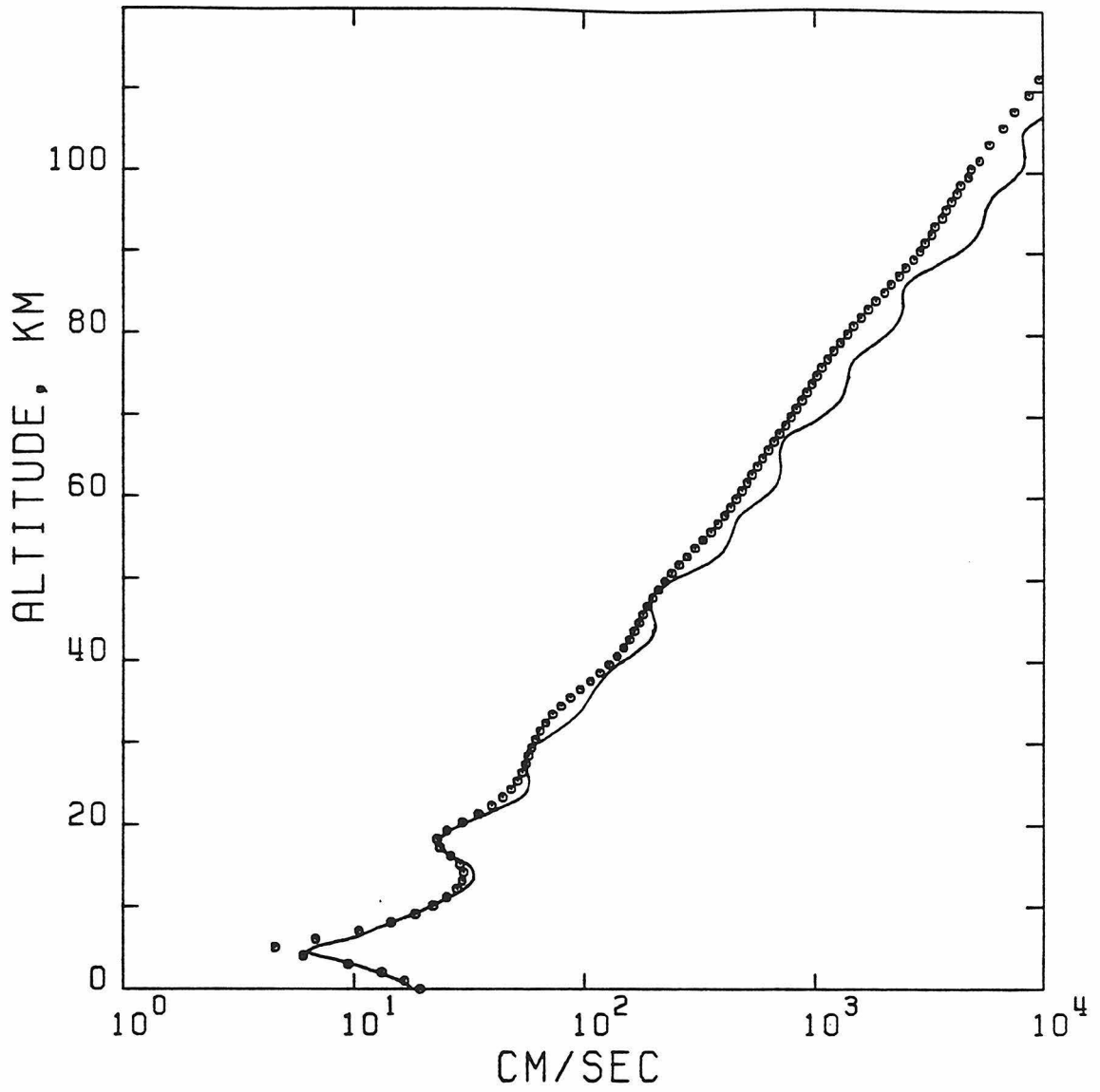


Figure 2.6 Same as Fig. 2.4 for u' .

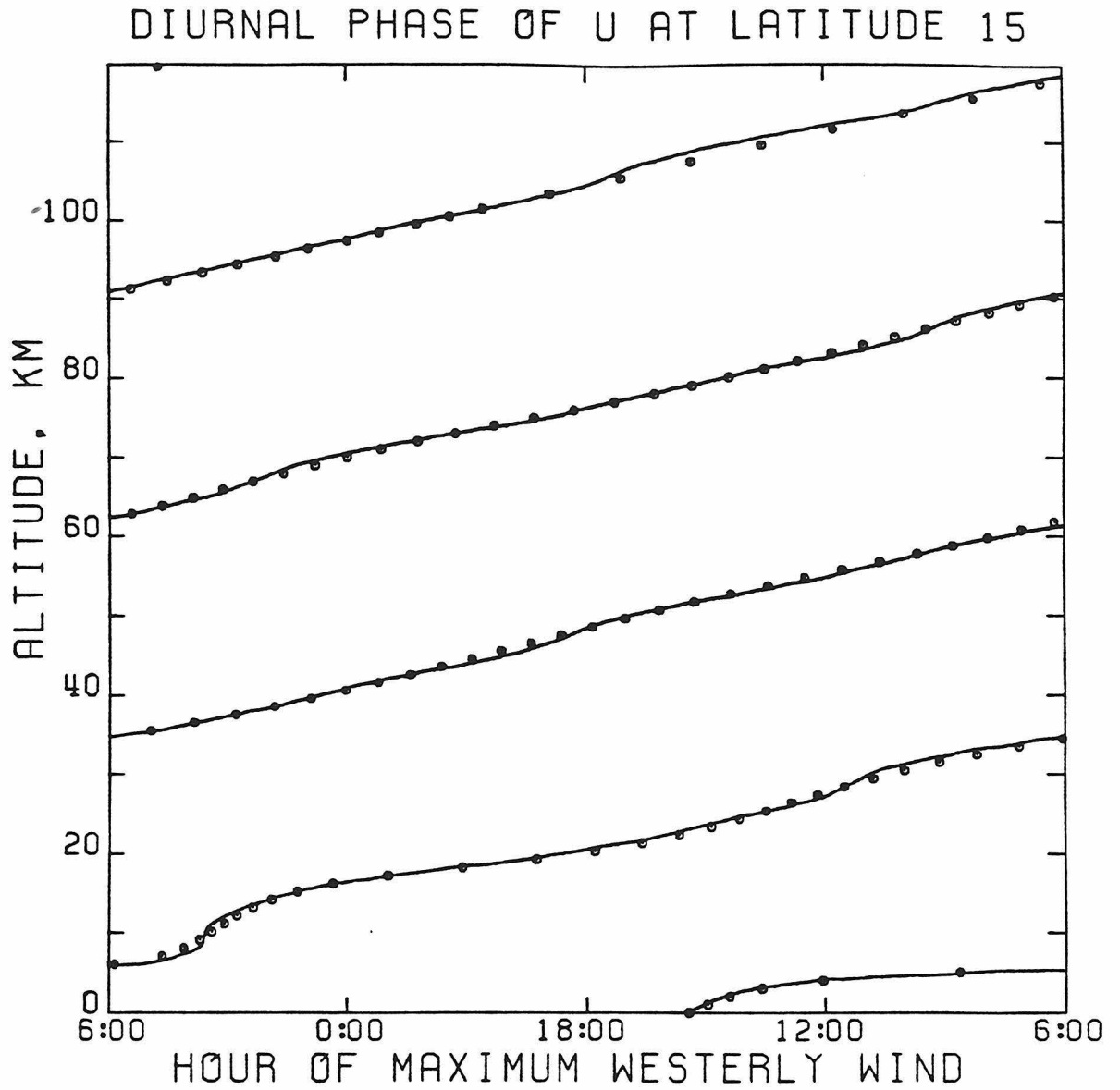


Figure 2.7 Same as Fig. 2.5 for u' .

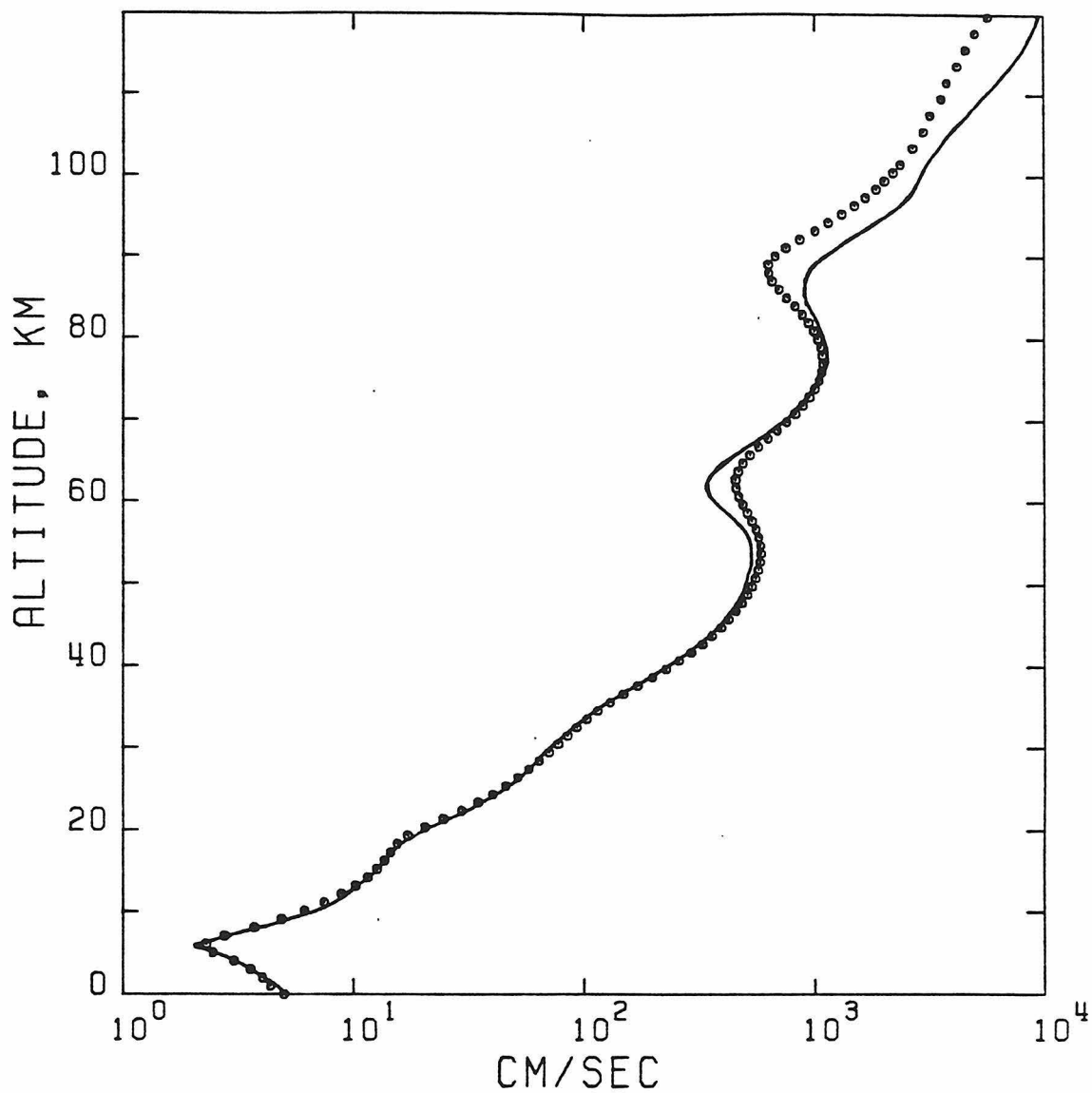
DIURNAL AMPLITUDE OF v AT LATITUDE 45

Figure 2.8 Amplitude of v' for the diurnal terrestrial thermal tide at 45° . The solid curve is the analytic model of Lindzen (1967). The data points are from the LPE model.

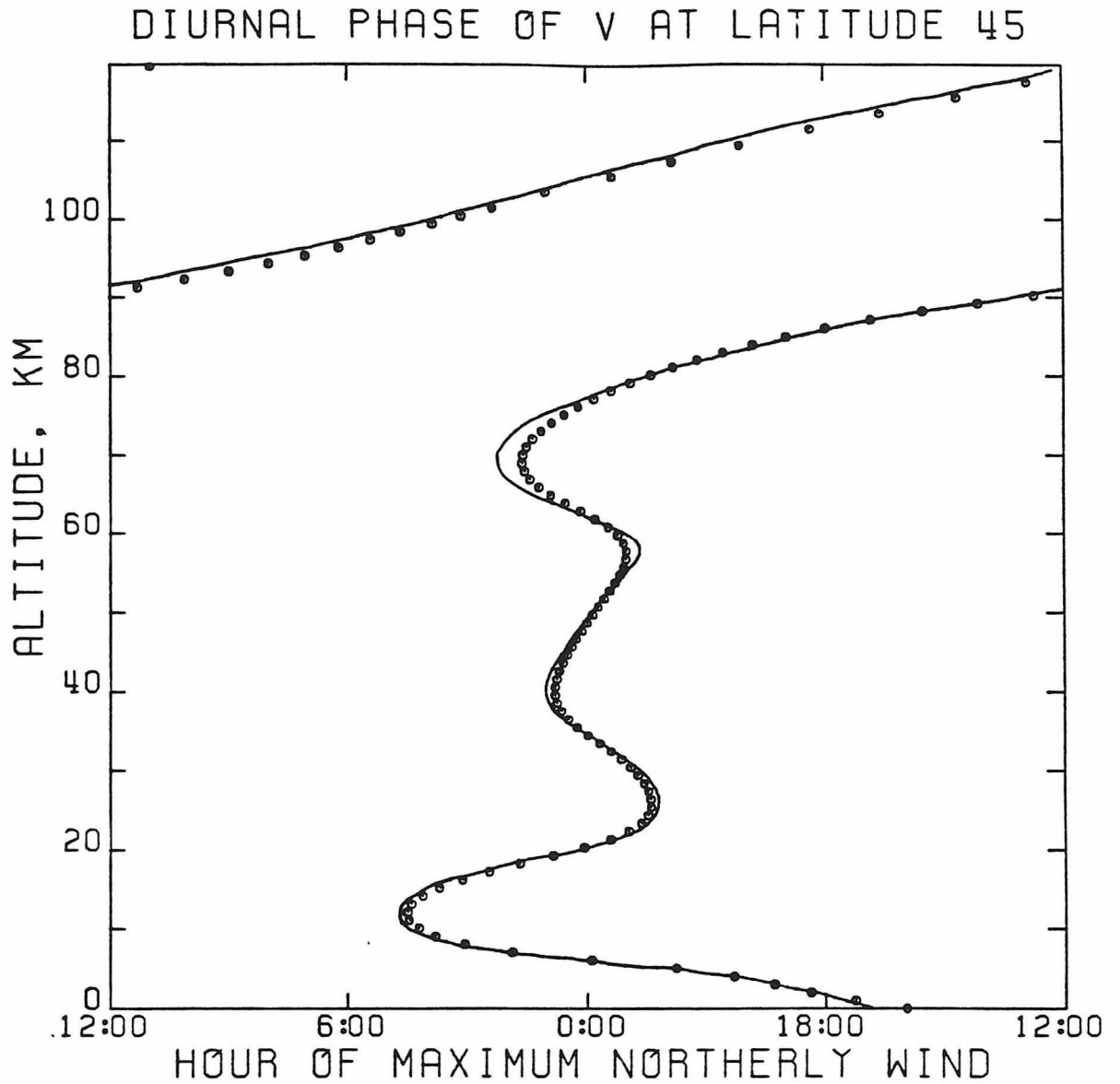
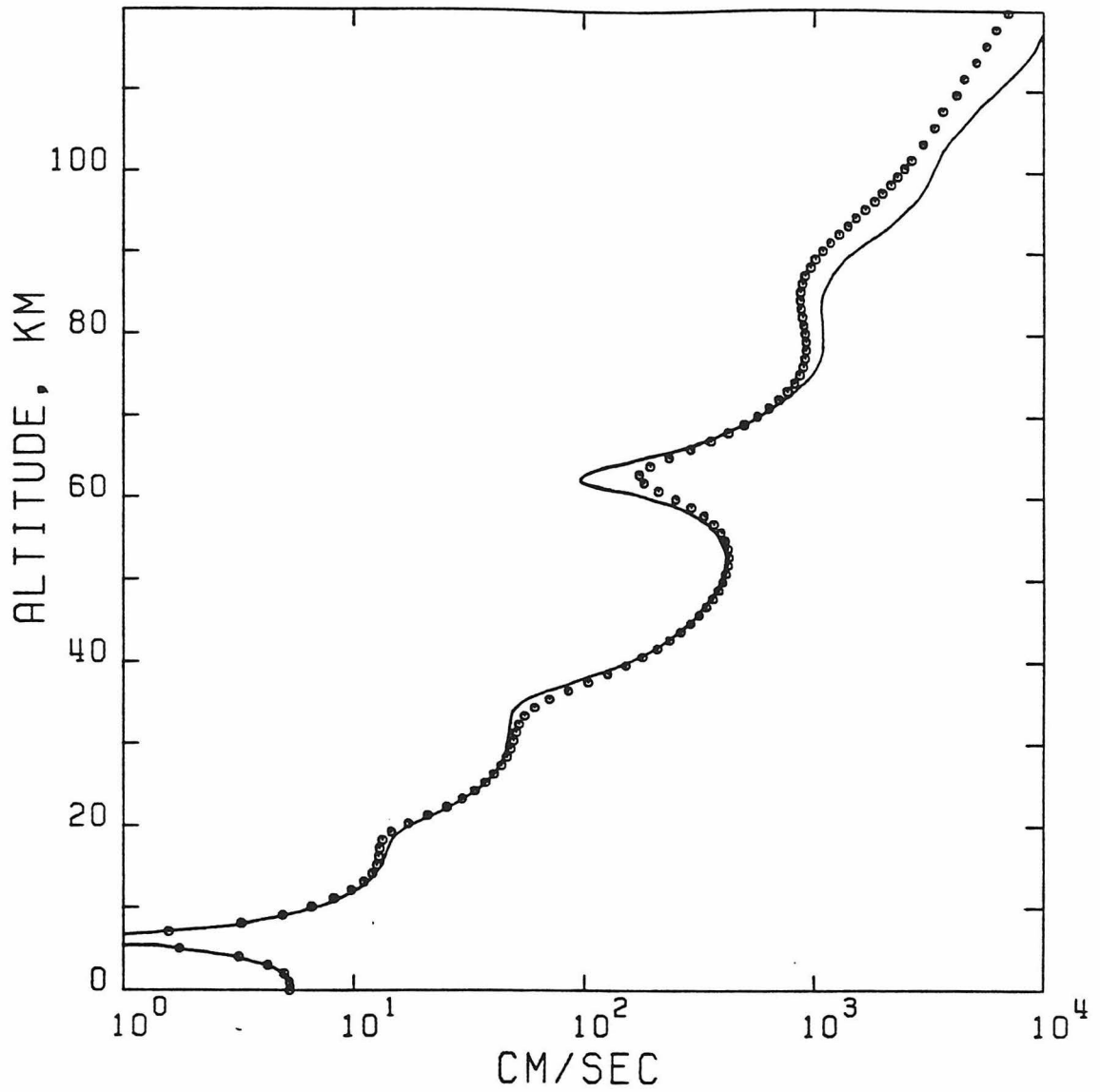


Figure 2.9 Phase of v' for the diurnal terrestrial thermal tide at 45° . The solid curve is the analytic model of Lindzen (1967). The data points are from the LPE model.

DIURNAL AMPLITUDE OF U AT LATITUDE 45

Figure 2.10 Same as Fig. 2.8 for u' .

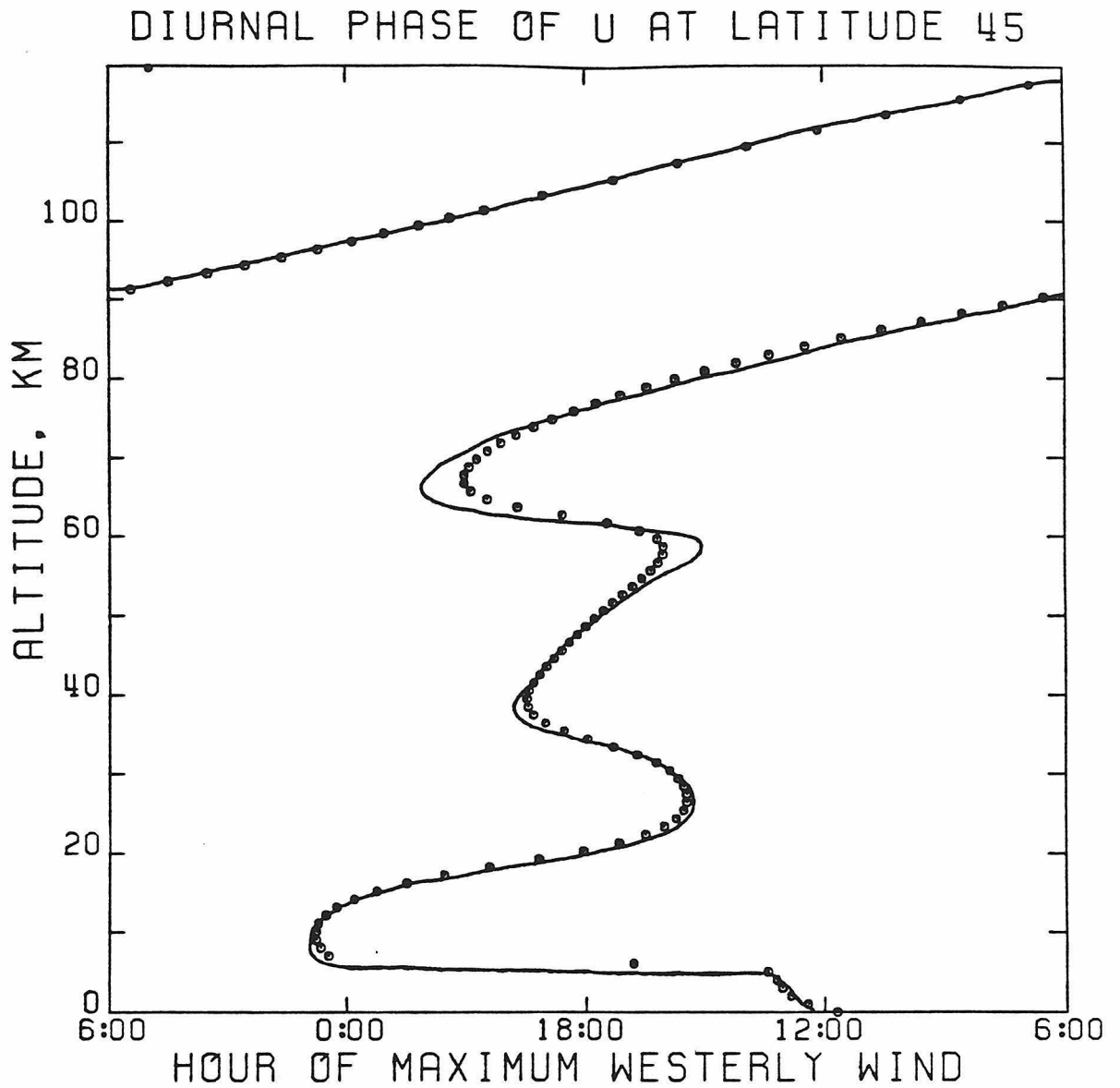


Figure 2.11 Same as Fig. 2.9 for u' .

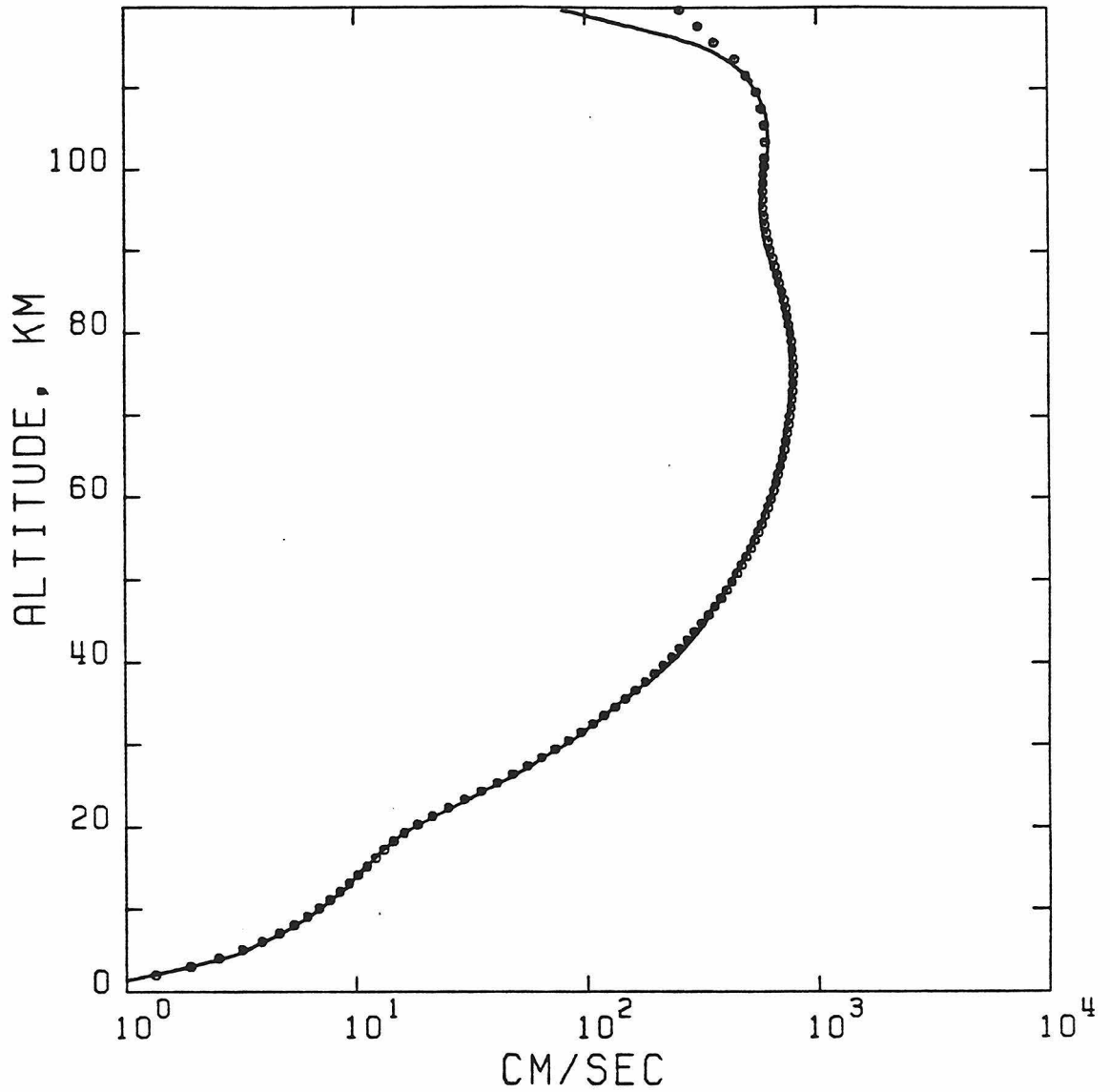
DIURNAL AMPLITUDE OF v AT LATITUDE 75

Figure 2.12 Amplitude of v' for the diurnal terrestrial thermal tide at 75° . The solid curve is the analytic model of Lindzen (1967). The data points are from the LPE model.

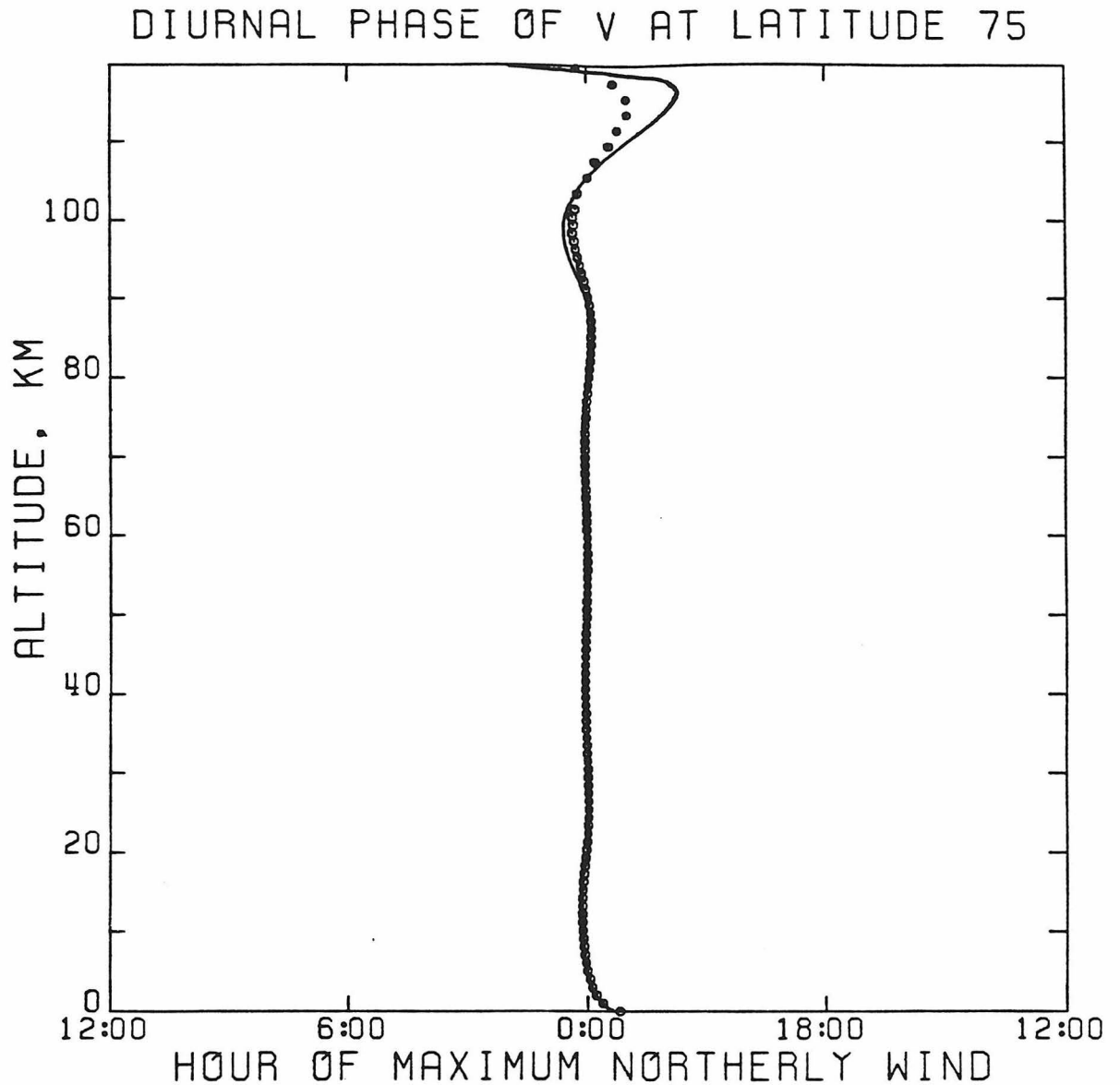


Figure 2.13 Phase of v' for the diurnal terrestrial thermal tide at 75° . The solid curve is the analytic model of Lindzen (1967). The data points are from the LPE model.

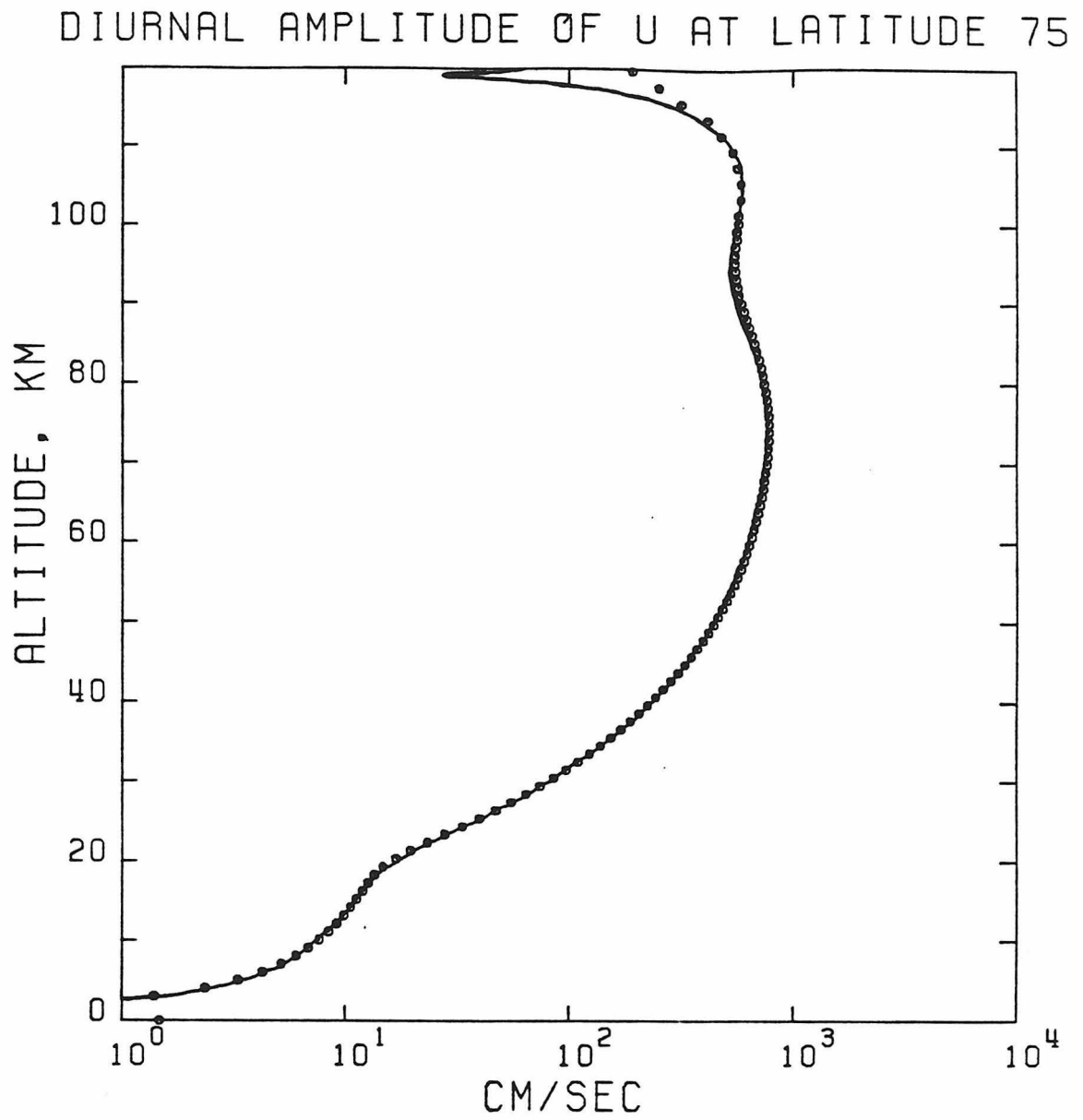


Figure 2.14 Same as Fig. 2.12 for u' .

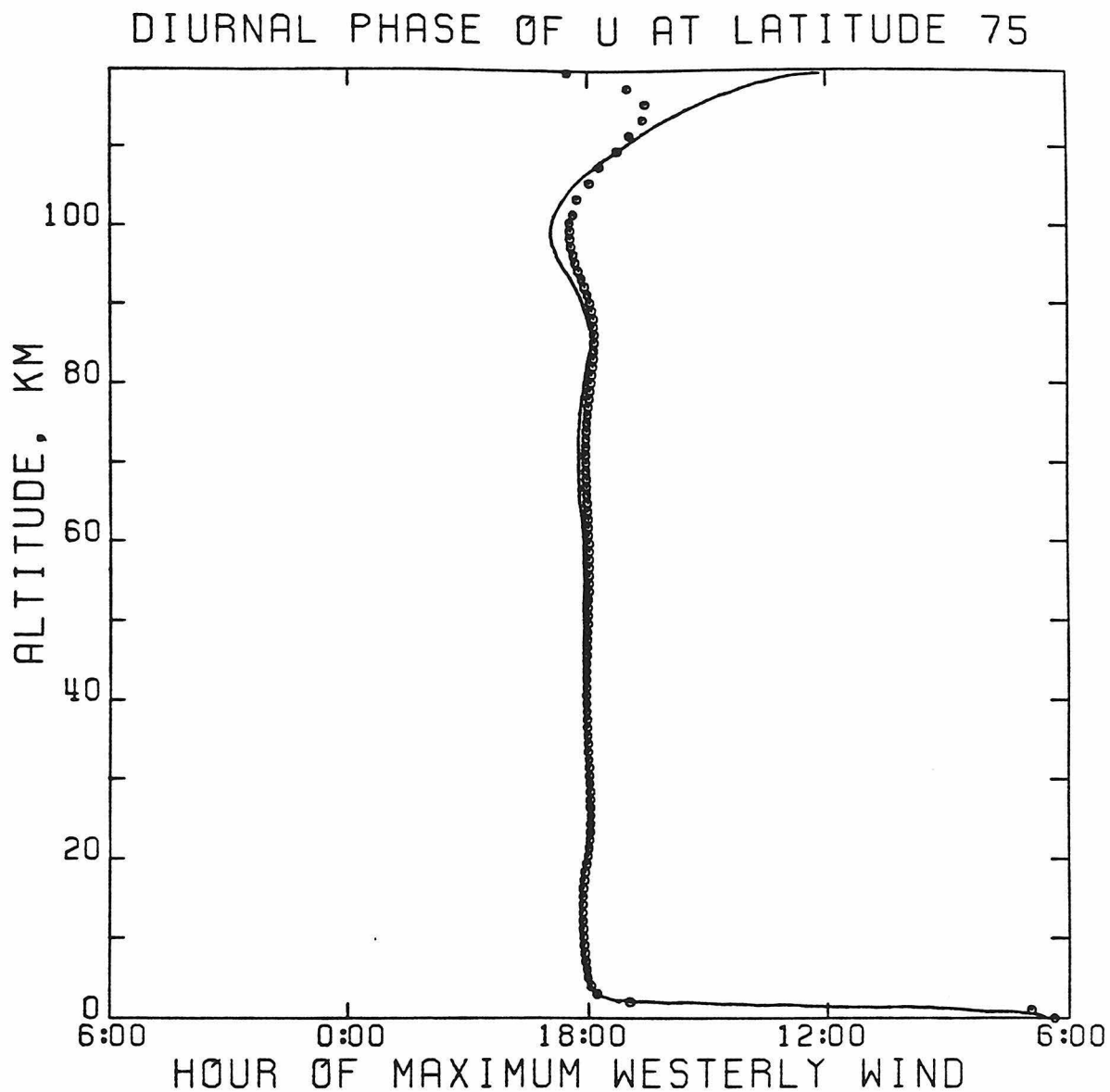


Figure 2.15 Same as Fig. 2.13 for u' .

encouraged by the excellent agreement in the phase at all latitudes. The major discrepancy between our model and Lindzen's is our smaller amplitude above about 80 km at low to mid-latitudes. Our amplitudes may be small due to lack of convergence or the effect of the sponge layer.

At low latitudes the diurnal tide propagates with a wavelength of about 20 km as shown in Figures 2.5 and 2.7. For comparison, a downward propagating wave with a constant wavelength in kilometers, λ , would have the form $Ae^{i2\pi z/\lambda + im\phi}$ where ϕ measures local time in radians from noon. Since $m = 1$, the hour of maximum amplitude would be $h_{\max} = (- (2\pi z/\lambda) + \pi) \cdot 12 \text{ hrs}/\pi$ where h is measured from local midnight. Thus a plot of h_{\max} as a function of z would just be a line of constant slope. Since the range of h is only a day, in such a plot we could break the line and shift it back 24 hours every time it reached the hour plotted on the z axis. The plot would then look very similar to Figures 2.5 and 2.7 except that the phase lines would be perfectly straight and parallel. The wavelength can be determined by measuring the vertical spacing between lines. The phase propagation for this wave is downward which implies upward energy propagation (Holton, 1972). We shall refer to waves whose energy propagation is upward as 'upward propagating.'

As shown in Figures 2.13 and 2.15 the phase at 75° latitude is constant with height. Thus, at high latitudes the diurnal tide does not propagate vertically. It is possible to show that on a rotating plane waves will not propagate vertically if their frequency is less than twice the rotation rate (Eckart, 1960). This result apparently holds

approximately for a rotating sphere although it hasn't been theoretically derived (Chapman and Lindzen, 1970). In the case of a sphere it predicts that the frequency of the wave must be greater than twice the vertical component of the rotation vector for propagation. The frequency of the diurnal tide is Ω so, neglecting the difference between the solar and sidereal day, the diurnal tide should not propagate poleward of 30° if this theory holds. Since there is some propagation at 45° (Figures 2.9 and 2.11) the extrapolation to a sphere isn't completely valid, but qualitatively the diurnal tide propagates at low latitudes and is trapped at high latitudes as predicted. Since the frequency of the semidiurnal tide is 2Ω it will propagate at all latitudes.

Our results for the semidiurnal tide in the meridional velocity are shown in Figures 2.16-2.19. The solid curve is the classical result from Chapman and Lindzen (1970). The temperature profile for this run is shown in Figure 2.20. The semidiurnal tide is more sensitive to the temperature profile so an isothermal atmosphere is not adequate to model it correctly. The forcing functions are the same as those used in the diurnal case with the amplitude appropriately adjusted. The computer run had 72 vertical points, half the resolution of the diurnal case. The upper boundary of the resolved region was at 195 km. We used 14 Legendre functions and 17 Gaussian grid points. The time step was half an hour, and the total number of time steps was 800. The forcing was increased linearly with time. The sponge layer was the same as that used for the diurnal case.

SEMIDIURNAL AMPLITUDE AND PHASE OF V AT LATITUDE 10

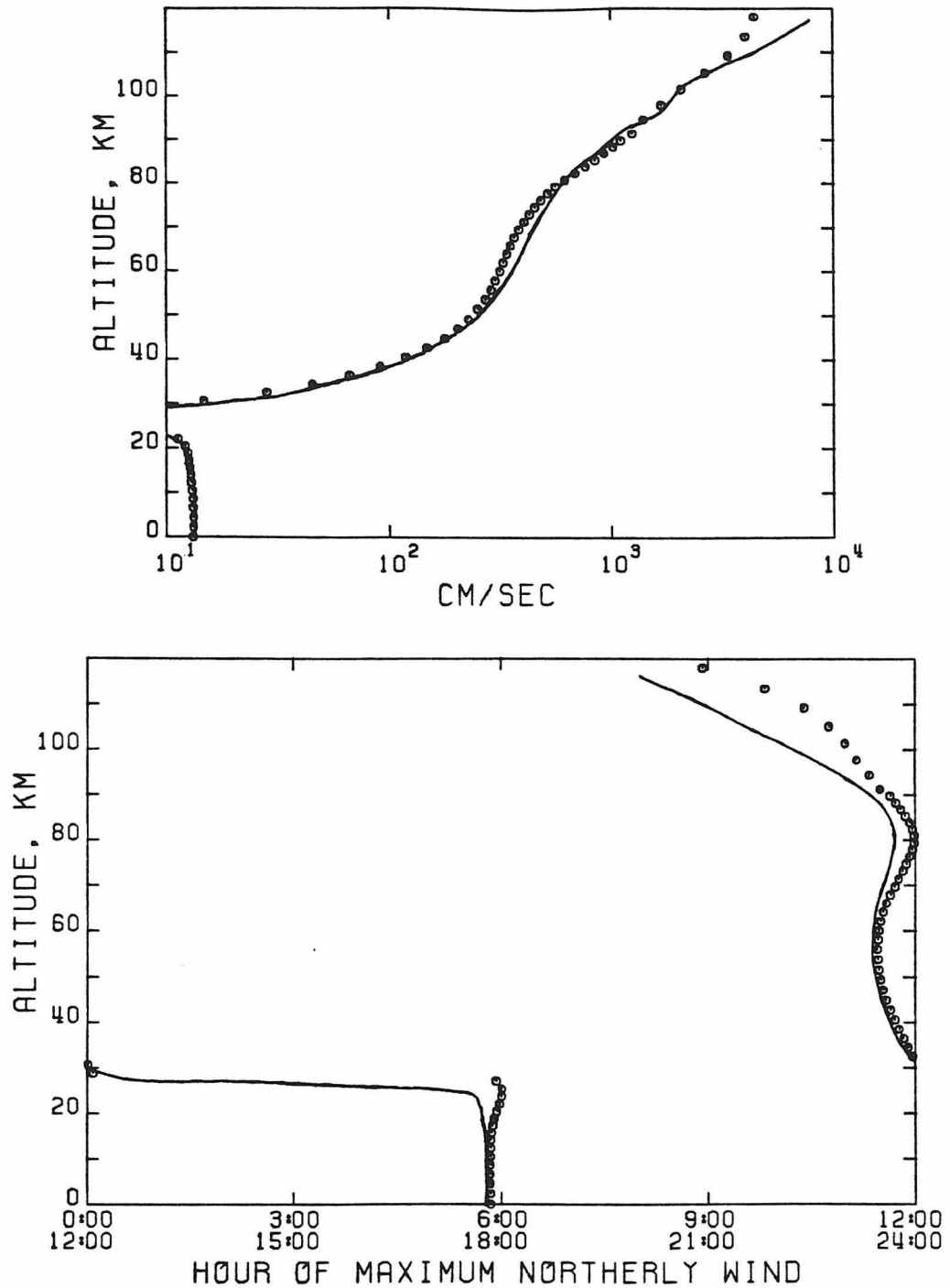
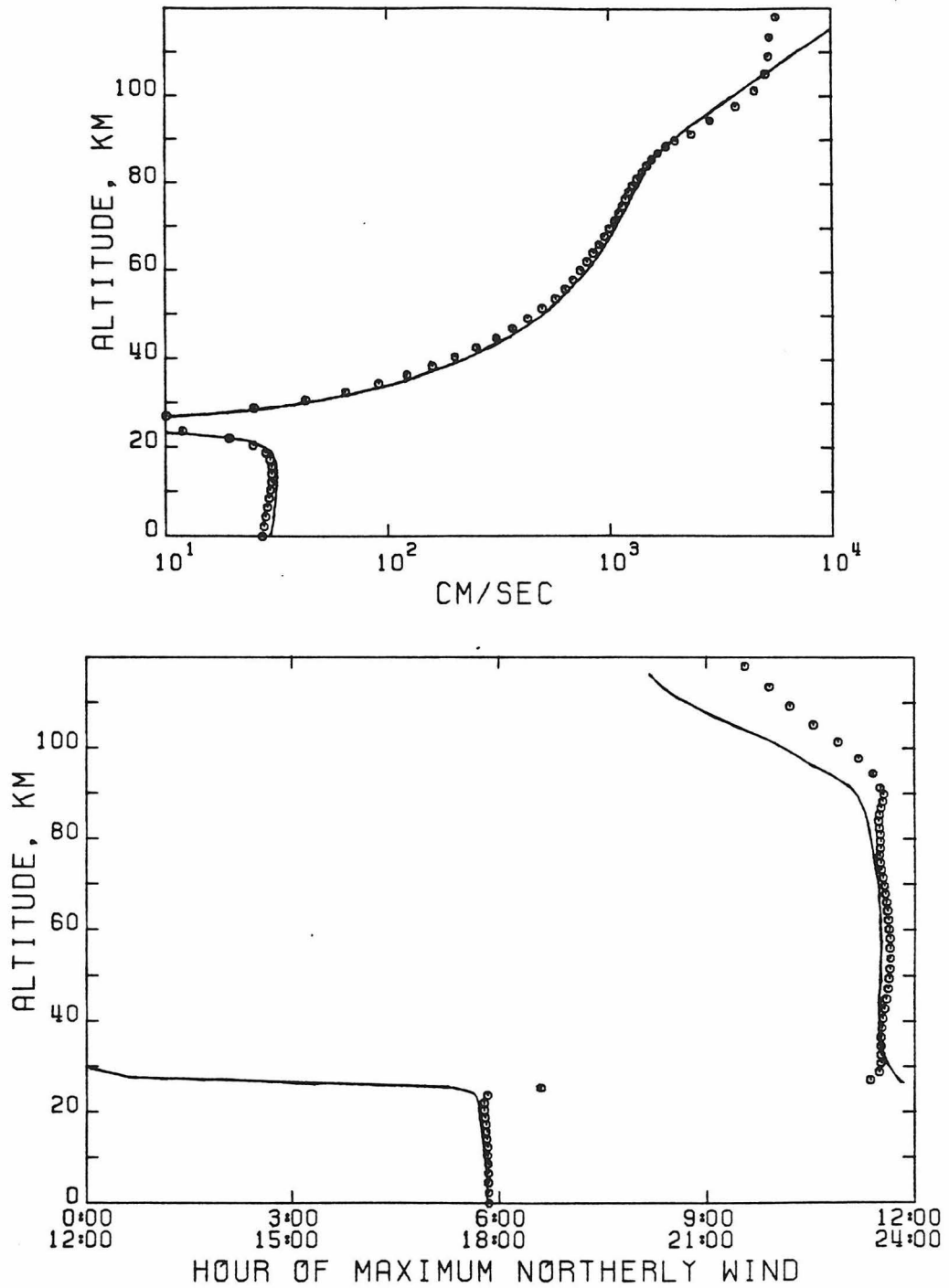
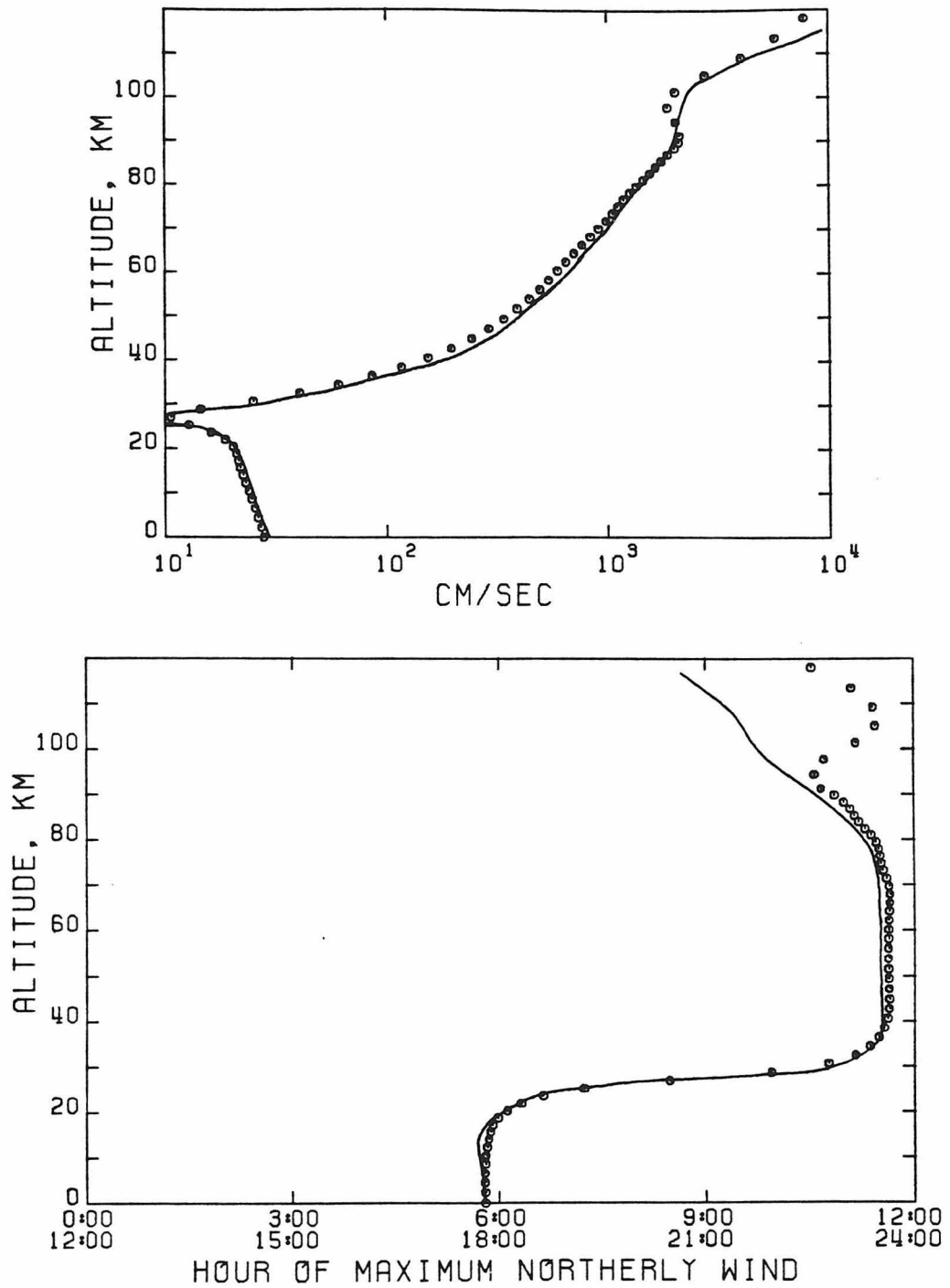


Figure 2.16 Amplitude and phase of v' for the semidiurnal terrestrial thermal tide at 10° according to Chapman and Lindzen's (1970) analytic model (solid curve) and the LPE model (data points).

SEMIDIURNAL AMPLITUDE AND PHASE OF v AT LATITUDE 30Figure 2.17 Same as Fig. 2.16 for v' at 30°.

SEMIDIURNAL AMPLITUDE AND PHASE OF v AT LATITUDE 50Figure 2.18 Same as Fig. 2.16 for v' at 50° .

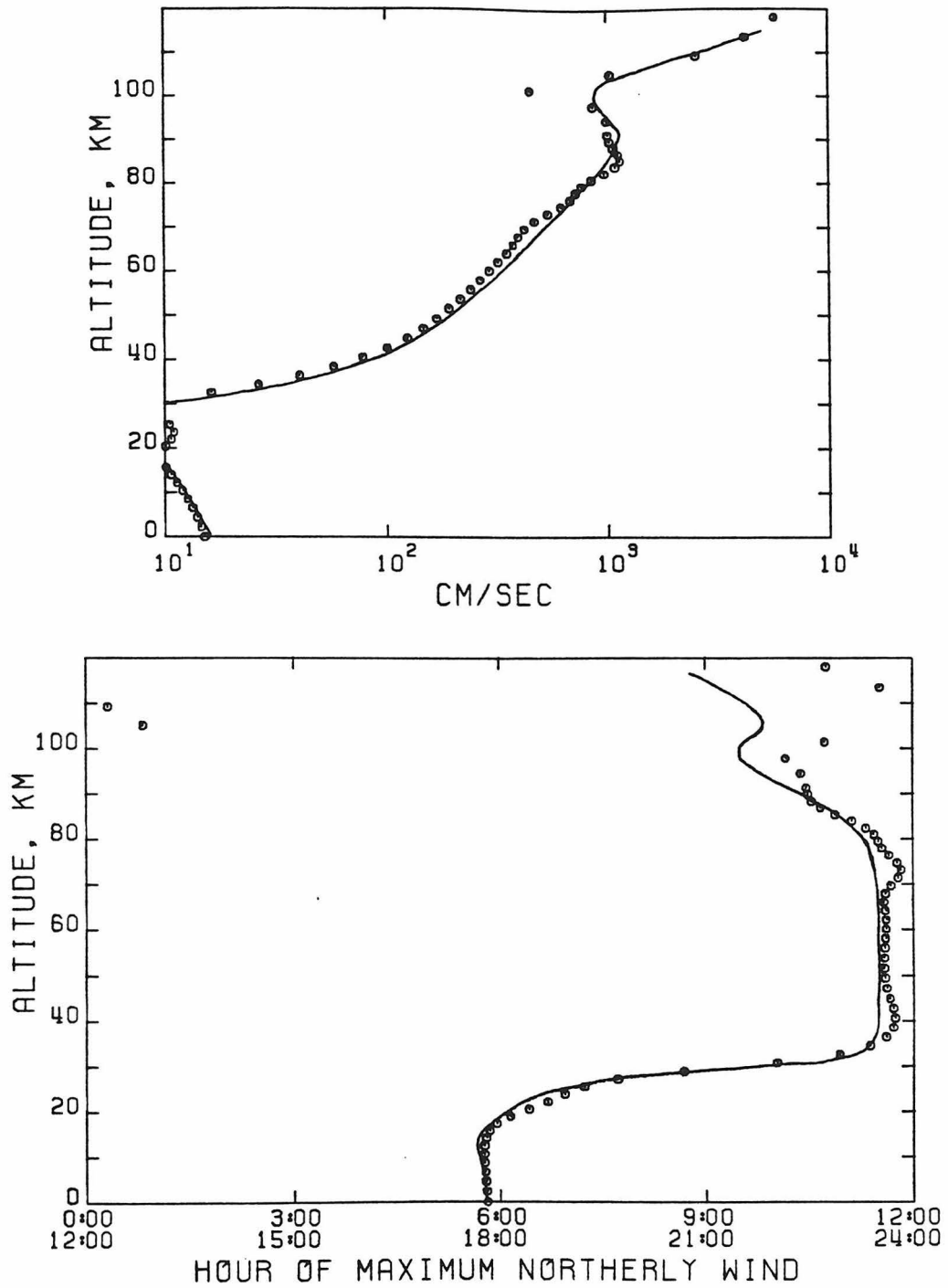
SEMIDIURNAL AMPLITUDE AND PHASE OF v AT LATITUDE 70° 

Figure 2.19 Same as Fig. 2.16 for v' at 70° .

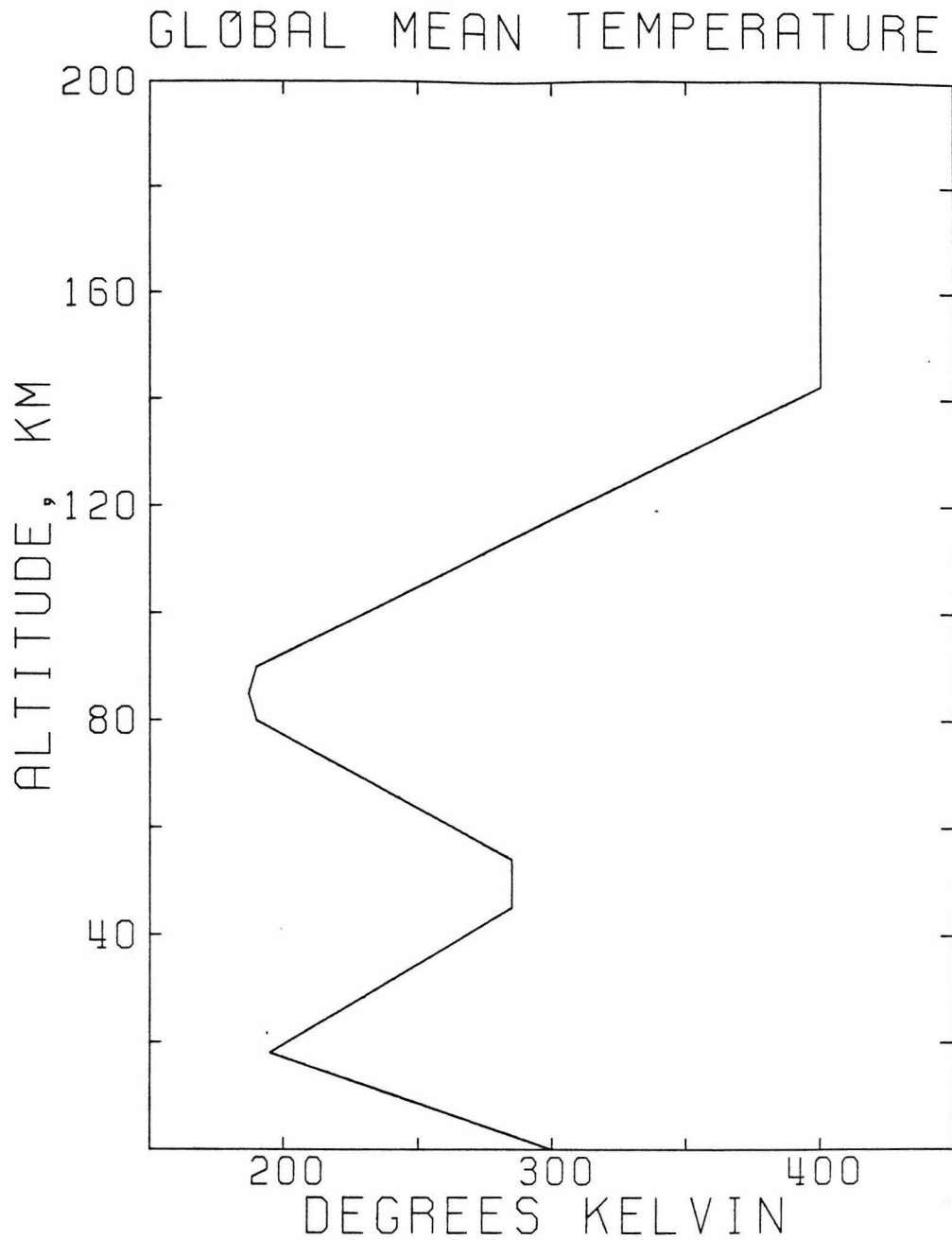


Figure 2.20 Mean temperature profile used in the LPE model for the terrestrial semidiurnal tide. Below 100 km this profile coincides with the standard equatorial profile used in Chapman and Lindzen (1970) for calculating the semidiurnal tide.

Our model agrees more closely with the classical theory for the semidiurnal case than for the diurnal case. This probably is at least partly due to the lack of structure in the semidiurnal tide. The phase plots seem to indicate that it is trapped, although as mentioned above, it should propagate everywhere. In fact, the main semidiurnal mode has a wavelength of about 150 km. Because of this long wavelength, the excitation due to ozone is nearly in phase at each level over the 40 km layer where it is important. This accounts for the large semidiurnal response. Since the level of forcing is well off the ground, between this level and the ground a standing wave will be set up. There are equal upward and downward propagating components in a standing wave so the phase will be constant, giving the appearance of a trapped oscillation. The 180° phase shift at 30 km is just a node in the standing wave. Above the forced layer the wave will propagate upward. This can be seen in the figures above 80 km.

As mentioned earlier in this section, the diurnal tide has a wavelength of less than 40 km so the ozone excitation is subject to destructive interference. Because of this, the water vapor absorption near the ground is the most important forcing for the diurnal tide. Thus, the propagating diurnal mode seen at low latitudes propagates upward from the ground. The standing wave due to the ozone heating is present, but masked because of its small amplitude.

The subject of terrestrial thermal tides was introduced in this section mainly to show how well our results agree with the classical theory. However, the discussion of the nature of the earth's tides was

included in order to make some aspects of tidal solutions more understandable. In the next section the discussion of our gravity wave model also gives us the opportunity to introduce some important features of thermal tides.

2.4 The Gravity Wave Model

Tides belong to a class of atmospheric waves called gravity waves. For these waves the buoyancy associated with adiabatic vertical displacements in a stable atmosphere is the restoring force (Holton, 1972). On a sphere, rotation provides an additional restoring force. However, many characteristics of tides can be investigated using simple gravity wave systems. In this section we will show how the linearized primitive equations can be simplified to represent gravity waves and will relate the simplified equations to tides.

The gravity wave system we will study is two-dimensional in space. The dependence of the perturbations on the horizontal coordinate, x , is assumed to be e^{ikx} where k is constant. We will still use σ as the vertical coordinate. The response as a function of σ is the solution we seek. To represent tides in this two-dimensional system, we identify x with the zonal direction so that the e^{ikx} dependence corresponds to $e^{im\phi}$ in the tides. However, the latitude dependence of the tides must be ignored. This is a serious omission, but there is a fudge factor which may be included that will allow us to solve for the vertical structure exactly when the original tidal equations are separable and will give us an approximate solution when they are not.

The gravity wave equations can be derived from equations (2.18)-(2.21). We will use Cartesian instead of spherical coordinates with $\partial/\partial x \rightarrow ik$ and $\partial/\partial y \rightarrow 0$. The basic state consists of the zonal wind, u^* , and the static stability, γ^* , both of which may depend on height. The basic state temperature is required only at the ground. u^* is related

to Ω by $u^* = a \cos \lambda \Omega$. We will usually use the equatorial value of u^* . As in the tidal problem, we specify u^* such that the waves are steady in our reference frame, and $f = 0$.

With these assumptions we may rewrite equations (2.18)-(2.21);

$$\zeta' = 0 \quad (2.36)$$

$$\begin{aligned} \sigma \left[\left(\frac{\partial}{\partial t} + \frac{1}{\tau_R} \right) W'_\sigma \right]_\sigma - Rk^2 (T' - \sigma T^*_\sigma q') \\ = \sigma (ik\delta' u^*_\sigma - iku^* W'_\sigma)_\sigma \end{aligned} \quad (2.37)$$

$$\begin{aligned} \left(\frac{\partial}{\partial t} + \frac{1}{\tau_N} \right) (T' - \sigma T^*_\sigma q') - \gamma^* W' \\ = -iku^* (T' - \sigma T^*_\sigma q') \end{aligned}$$

$$+ \delta\gamma^* - (W' - \sigma W^{s'}) \gamma^* + \frac{RT^*}{c_p} (ik(u^* - \hat{u}^*)q') + Q' \quad (2.38)$$

$$\frac{\partial q'}{\partial t} - W^{s'} = -iku^* q' \quad (2.39)$$

To solve these equations numerically we follow the procedures outlined in section 2.2 for vertical discretization, time-stepping, initialization, and obtaining the forced solution. Of course, we omit the steps having to do with the spherical harmonic expansion.

The nature of gravity waves can be understood by solving these equations analytically in some simple cases. For example, we put u^* and T^* both equal to constants. Since $\gamma^* = RT^*/c_p \sigma - T^*_\sigma$, for an isothermal

atmosphere $\gamma^* \sigma$ is a constant. Let $S = \gamma^* \sigma$. We will solve for the free mode so $Q' = 0$. We also put the dissipation terms equal to zero. In order to obtain a more general result, we do not specify the steady reference frame. The time dependence is assumed to be $e^{i\nu t}$ where ν is a constant frequency. The equations become:

$$(i\nu + iku^*) \sigma W'_{\sigma\sigma} - Rk^2 (T' - \sigma T^*_\sigma q') = 0 \quad (2.40)$$

$$(i\nu + iku^*) (T' - \sigma T^*_\sigma q') - \frac{S}{\sigma} W' = 0 \quad (2.41)$$

$$(i\nu + iku^*) q' = W^S \quad (2.42)$$

The definition of $\hat{\sigma}$ and \hat{u}^* were used to eliminate the terms on the right hand side of (2.41).

We eliminate the quantity $T' - \sigma T^*_\sigma q'$ from (2.40) and (2.41) to obtain

$$-(\nu + ku^*)^2 \sigma W'_{\sigma\sigma} - Rk^2 \frac{S}{\sigma} W' = 0$$

Compare this equation to (2.34). The terms on the left have the same vertical dependence.

It is convenient to define a new variable $\mathcal{Y} = -\ln \sigma$ and rewrite the above equation in terms of \mathcal{Y} :

$$W'_{\mathcal{Y}\mathcal{Y}} + W'_{\mathcal{Y}} + \frac{SR}{(u^* + \nu/k)^2} W' = 0 \quad (2.43)$$

The solution to this equation is of the form

$$W' = W_{\pm} e^{-z/2} [e^{\pm i\omega z}] e^{i\omega t + ikx}$$

where $\omega = (SR/(u^* + v/k)^2 - 1/4)^{1/2}$.

The relative amounts of W_+ and W_- would be determined by the boundary conditions. If v , k , and ω are positive then the wave with the plus sign has downward phase propagation and upward energy propagation (Holton, 1972).

In this simple case the wavelength is constant with respect to z . Even when S and u^* are functions of height, the wavelength tends to vary more slowly as a function of z than as a function of σ . In fact, we often use the above dispersion relation to estimate ω even when S and u^* are not constant, and the results are fairly accurate. Thus, in our numerical modeling we use grids which are evenly spaced in $-\ln\sigma$ to obtain the most even resolution possible. We also usually plot our results against $-\ln\sigma$.

The amplitude of W' decays exponentially as $e^{-z/2}$ while T' and u' grow exponentially with height as $e^{z/2}$. This behavior is also seen in the tides, although modified by the complexities of the basic state and the forcing. Therefore, we usually plot tidal amplitudes on a log scale.

The relationship of tides to gravity waves can be seen by examining the vertical structure equation which results when the tidal problem is separable, i.e., when Ω is constant. This equation is derived in Chapman and Lindzen (1970); the derivation will not be repeated here. The vertical structure equation in terms of W is

$$\frac{d^2 W_n}{dz^2} + \frac{d W_n}{dz} + \frac{S}{(a\Omega)^2} \frac{\varepsilon_n^m}{4} W_n = 0 \quad (2.44)$$

where $W' = \sum_n W_n(z) \Theta_n^m(\lambda) e^{im\phi}$, and Θ_n^m satisfies $F(\Theta_n^m) = -\varepsilon_n^m \Theta_n^m$ where F is Laplace's tidal operator. In the separable problem the horizontal dependence is naturally expressed in terms of Θ_n^m , the eigenfunctions of F , which are called Hough functions. Laplace's tidal operator depends on the zonal wavenumber, m , and the ratio of the solar to the sidereal day, as well as latitude, so ε_n^m will also depend on m and on this ratio.

The solutions of (2.44) obviously have the same form as the solutions of (2.43). If we put $v = 0$ and $u^* = a\Omega$, then the dispersion relation which results from (2.44) is the same as for the gravity waves with the addition of the $\varepsilon_n^m/4$ factor. If we include this factor in equation (2.37) as follows:

$$\begin{aligned} \sigma \left(\frac{\partial}{\partial t} + \frac{1}{\tau_N} \right) W'_\sigma - Rk^2 \frac{\varepsilon_n^m}{4} (T' - \sigma T'_\sigma q') \\ = \sigma (ik\sigma u_\sigma^* - iku_\sigma^* W'_\sigma) \sigma \end{aligned}$$

then, setting $u^* = a\Omega$, we can use our gravity wave program to solve for the vertical structure associated with any Hough mode. The inclusion of the factor $\varepsilon_n^m/4$ should be thought of as a modification of the value of k^2 . This k^2 came from the horizontal Laplacian. Multiplying it by $\varepsilon_n^m/4$ has the effect of correctly including the latitudinal derivative for a given Hough mode.

When u^* depends on height, strictly speaking, ε_n^m does not exist. However, in order to investigate Venus tides we define an ε_n^m which depends on height. Lindzen (1970) gives a value of ε_n^m for the lowest

diurnal and semidiurnal Hough modes for the Venus rotation rate. We use these values at the ground, assuming the mean zonal wind is zero there. In the clouds the atmosphere rotates with a four day period which is rapid enough so that the Earth value of ε_n^m should be valid. ε_1^m for Earth and Venus rotation rates are given in Table 2.1 for $m=1$ and $m=2$. With the values for these two rotation rates we define a linear dependence of ε_1^m on u^* for $m=1$ and $m=2$. The only way to test this method is to compare results from the gravity wave model to the full model. We have found that the gravity wave results reproduce the general features of the full model solution at low latitudes. The gravity wave solution is not valid at high latitudes because it approximates the vertical structure of the lowest 'Hough mode' which has a low amplitude in the polar region. The gravity wave results will be presented in Chapter 4.

TABLE 2.1

 ϵ_1^2 FOR EARTH AND VENUS ROTATION RATES

	SIDEREAL DAY	SOLAR DAY	ϵ_1^1	ϵ_1^2
Earth	24 hours	24 hours	127.53	11.16
Venus	247 days	117 days	2.13	2.04

2.5 Conservation of Energy

An important characteristic of a dynamical model like ours is its performance in conserving energy. The rate of change of the total perturbation energy, i.e., the kinetic, internal, and gravitational potential energies integrated over the whole atmosphere, should be equal to the rate at which energy is gained or lost by the system. The equation relating these terms is called the energy conservation or energy balance equation. Perturbation energy is gained from the forcing and is lost by dissipation. Perturbation energy may also be gained from or lost to the basic state. This conversion does not violate the assumption that the basic state is constant at zeroth order because the perturbation energy is a second order quantity.

A spurious growth of energy may occur in a numerical model whose spatial discretization is Galerkin because of the presence of explicit terms in the time discretization. The case of the explicit damping term discussed in Section 2.2 demonstrates this growth. In the presence of a numerical instability, the properly time-discretized terms in the energy equation would still balance, but the rate of change of energy would be unphysical. Physical instabilities may also be present and would cause an exponential growth of energy. Since we are looking for a stable, forced solution, these instabilities are also undesirable. Fortunately, since the forcing increases quadratically in our model, we know that the perturbation energy, E , should be proportional to t^4 for large t . Thus, by calculating the rate of change of energy, $\Delta E/\Delta t$, and comparing it to the predicted value, $4E/t$, we can determine how close the entire system

is to convergence. For small t , $\Delta E/\Delta t$ will differ from $4E/t$ because of the importance of free modes and the term in the solution which is linear in time. (See the discussion of convergence near the end of Section 2.2.) $\Delta E/\Delta t$ should approach $4E/t$ as t increases if numerical or physical instabilities are not present.

The equation for the conservation of energy for the full model is very complicated, especially in its discretized form, because of the presence of numerous basic state/perturbation conversion terms and the dependence of the solution on latitude. In this section the energy conservation equation for the gravity wave problem will be derived and discussed. It includes all the major features of the full model's energy balance. An analytic expression for the energy balance will be derived first. A discretized treatment will follow. Hopefully, this discussion of the energy will lead to a clearer understanding of the numerical model.

In the gravity wave problem $\partial W'/\partial \sigma$ is given by iku' . Therefore, $\frac{1}{2k^2} \left| \frac{\partial W'}{\partial \sigma} \right|^2$ is equal to the perturbation kinetic energy per unit mass averaged with respect to x due to horizontal motions. For a column of atmosphere of unit area this component of the energy would be

$$\int_0^{\infty} \frac{1}{2k^2} \left| \frac{\partial W'}{\partial \sigma} \right|^2 \rho dz = \int_0^1 \frac{p_s}{2gk^2} \left| \frac{\partial W'}{\partial \sigma} \right|^2 d\sigma .$$

There is no x dependence. The rate of change of this quantity can be derived from equation (2.37) by multiplying by $\langle W' \rangle / k^2$ and integrating over σ . Angular brackets denote complex conjugate. This notation is used to avoid confusion with the use of $'_*$ for basic state quantities.

The energy form of (2.37) is

$$\begin{aligned} \text{Re } \frac{p_s}{gk^2} \int_0^1 \left\{ \langle W' \rangle \frac{\partial}{\partial t} \frac{\partial^2 W'}{\partial \sigma^2} + \langle W' \rangle \frac{\partial}{\partial \sigma} \left(\frac{1}{\tau_R} \frac{\partial W'}{\partial \sigma} \right) - \frac{Rk^2 \langle W' \rangle}{\sigma} \left(T' - \sigma \frac{\partial T^*}{\partial \sigma} q' \right) \right. \\ \left. = \langle W' \rangle \frac{\partial}{\partial \sigma} \left(ik\hat{\sigma}' \frac{\partial u^*}{\partial \sigma} - iku^* \frac{\partial W'}{\partial \sigma} \right) \right\} d\sigma . \end{aligned}$$

Integration by parts of the terms containing second derivatives with respect to σ yields

$$\begin{aligned} \text{Re } \frac{p_s}{gk^2} \left\{ \int_0^1 \left(\frac{1}{2} \left| \frac{\partial \partial W'}{\partial t \partial \sigma} \right|^2 + \frac{1}{\tau_R} \left| \frac{\partial W'}{\partial \sigma} \right|^2 \right) d\sigma - \left(\langle W' \rangle \left(\frac{\partial \partial W'}{\partial t \partial \sigma} + \frac{1}{\tau_R} \frac{\partial W'}{\partial \sigma} \right) \right) \Big|_{\sigma=1} \right. \\ \left. + \int_0^1 \frac{Rk^2}{\sigma} \langle W' \rangle \Pi' d\sigma = \int_0^1 \left(\frac{\partial \langle W' \rangle}{\partial \sigma} \left(ik\hat{\sigma}' \frac{\partial u^*}{\partial \sigma} - iku^* \left| \frac{\partial W'}{\partial \sigma} \right|^2 \right) \right) d\sigma \right. \\ \left. - \left(\langle W' \rangle \left(ik\hat{\sigma}' \frac{\partial u^*}{\partial \sigma} - iku^* \frac{\partial W'}{\partial \sigma} \right) \right) \Big|_{\sigma=1} \right\} \end{aligned}$$

where $\Pi' = T' - \sigma \frac{\partial T^*}{\partial \sigma} q'$. The boundary terms may be simplified by using the undifferentiated form of (2.37):

$$\frac{\partial}{\partial t} \left(\frac{\partial W'}{\partial \sigma} \right) + \frac{1}{\tau_R} \frac{\partial W'}{\partial \sigma} + iku^* \frac{\partial W'}{\partial \sigma} - ik\hat{\sigma}' \frac{\partial u^*}{\partial \sigma} = -k^2 RT^* q'$$

and the continuity equation:

$$W^{s'} = \frac{\partial q'}{\partial t} + iku^* q'$$

Then the boundary terms become

$$\text{Re} \left\{ (k^2 RT^* q')|_{\sigma=1} \left(\frac{\partial \langle q' \rangle}{\partial t} + ik \hat{u}^* \langle q' \rangle \right) \right\} = \frac{k^2 RT^*|_{\sigma=1}}{2} \frac{\partial |q'|^2}{\partial t}$$

The advection term has no real part. Likewise, the advection term in the main expression has no real part. Finally,

$$\begin{aligned} \frac{p_s}{gk^2} \left\{ \int_0^1 \frac{1}{2} \frac{\partial}{\partial t} \left| \frac{\partial W'}{\partial \sigma} \right|^2 + \frac{k^2 RT^*|_{\sigma=1}}{2} \frac{\partial |q'|^2}{\partial t} + \int_0^1 \frac{1}{\tau_R} \left| \frac{\partial W'}{\partial \sigma} \right|^2 d\sigma \right. \\ \left. + \text{Re} \int_0^1 \frac{Rk^2}{\sigma} \langle W' \rangle \Pi' d\sigma - \text{Re} \int_0^1 ik \hat{\sigma}' \frac{\partial \langle W' \rangle}{\partial \sigma} \frac{\partial u^*}{\partial \sigma} d\sigma = 0 \right\} \quad (2.45) \end{aligned}$$

The first two terms are the rate of change, for a column of unit area, of the perturbation kinetic energy and the part of the perturbation potential energy due to surface pressure changes, respectively, both averaged with respect to x . The third term represents kinetic energy lost to dissipation by Rayleigh friction. The fourth term is a conversion from kinetic to thermal perturbation energy. The last term represents a conversion from perturbation to mean energy or vice versa depending on the sign of the integral.

A similar derivation will convert (2.38) to an equation for the rate of change of perturbation thermal energy. The appropriate quantity to multiply by to get an energy per unit mass is $R \langle \Pi' \rangle / \gamma^* \sigma$. Π' is the temperature on constant pressure surfaces. Besides the fact this quantity has the correct units, it is exactly the quantity needed to multiply the term $\gamma^* W'$ to obtain a conversion term which will cancel the

one in equation (2.45). These terms must cancel because the overall rate of change of perturbation energy should not be affected by conversions between kinetic and thermal perturbation energy. For the thermal energy balance equation we obtain

$$\begin{aligned} \frac{p_s}{g} \operatorname{Re} \int_0^1 \left\{ \frac{1}{2} \frac{R}{\gamma^* \sigma} \frac{\partial}{\partial t} |\pi'|^2 + \frac{1}{\tau_N} \frac{R}{\gamma^* \sigma} |\pi'|^2 - \frac{R}{\sigma} \langle \pi' \rangle W' \right. \\ \left. - ik \frac{\langle \pi' \rangle q'}{\sigma} (\sigma u^* - \hat{u}^* - \hat{u}^{*\sigma}) - \frac{R}{\gamma^* \sigma} \langle \pi' \rangle Q' \right\} d\sigma = 0 \end{aligned} \quad (2.46)$$

The first term is the rate of change of thermal perturbation energy. The second term represents energy lost to dissipation by Newtonian cooling. The third term is the conversion term discussed above. The fourth term represents a conversion between perturbation and mean energy. This term was derived from the terms on the left side of (2.38) using the definition of $\dot{\sigma}'$ and γ^* . The final term is the energy supplied to the system by the forcing. The total perturbation energy balance results from adding (2.45) and (2.46). There is no term involving the rate of change of $\dot{\sigma}'$ because of the hydrostatic assumption. In other words, kinetic energy due to vertical motion is negligible compared with that due to horizontal motion.

The finite element method of vertical discretization is easily modified for energy calculations. For example, consider the term $\frac{\partial}{\partial t} \frac{\partial^2 W'}{\partial \sigma^2}$ which in the energy balance equation becomes $\frac{p_s}{gk^2} \frac{1}{2} \frac{\partial}{\partial t} \int_0^1 \left| \frac{\partial W'}{\partial \sigma} \right|^2 d\sigma$. To vertically discretize this term we express W' in terms of the

To do the discretized energy balance correctly the equations must also be discretized in time as they are to obtain the numerical solution. Thus, we have

$$\begin{aligned} \frac{\partial}{\partial \sigma} \left(1 + \frac{\Delta t}{\tau_R}\right) \frac{\partial}{\partial \sigma} \bar{w}^t - \frac{\partial^2 w|_{t-\Delta t}}{\partial \sigma^2} + ik \Delta t \frac{\partial}{\partial \sigma} \left(u^* \frac{\partial w}{\partial \sigma}\right) \Big|_t + \Delta t ik \frac{\partial}{\partial \sigma} \left(\hat{\sigma}' \frac{\partial u^*}{\partial \sigma}\right) \Big|_t \\ - \frac{\Delta t}{\sigma} Rk^2 \bar{n}^t = 0 \end{aligned} \quad (2.47)$$

and

$$\begin{aligned} \left(1 + \frac{\Delta t}{\tau_N}\right) \bar{n}^t - n|_{t-\Delta t} - \Delta t \gamma^* \bar{w}^t - \gamma^* ik \Delta t q|_t (\sigma u^* - \hat{u}^* + \hat{u}^{*\sigma}) \\ + ik \Delta t u^* n|_{t-\Delta t} - \Delta t Q|_t = 0 \end{aligned} \quad (2.48)$$

To solve this system of equations we eliminate \bar{n}^t from equation (2.47).

This yields:

$$\begin{aligned} \frac{\partial}{\partial \sigma} \left(\left(1 + \frac{\Delta t}{\tau_R}\right) \frac{\partial \bar{w}^t}{\partial \sigma} \right) - \frac{\partial^2 w|_{t-\Delta t}}{\partial \sigma^2} + ik \Delta t \frac{\partial}{\partial \sigma} \left(u^* \frac{\partial w}{\partial \sigma}\right) \Big|_t + \Delta t ik \frac{\partial}{\partial \sigma} \left(\hat{\sigma}' \frac{\partial u^*}{\partial \sigma}\right) \Big|_t \\ - \frac{(\Delta t)^2 Rk^2 \gamma^* \bar{w}^t}{\left(1 + \frac{\Delta t}{\tau_N}\right) \sigma} - L = 0 \end{aligned} \quad (2.49)$$

where

$$\begin{aligned} L = \frac{\Delta t Rk^2}{\left(1 + \frac{\Delta t}{\tau_N}\right) \sigma} \left(n|_{t-\Delta t} - ik \Delta t u^* n|_t + \right. \\ \left. \gamma^* ik \Delta t q|_t (\sigma u^* - \hat{u}^* - \hat{u}^{*\sigma}) + \Delta t Q|_t \right) \end{aligned}$$

To obtain the gravity wave solution (2.49) is vertically discretized by the finite element method and solved for \bar{w}^t . If we multiply the vertically discretized form of (2.49) by $\frac{p_s}{gk^2} \langle \bar{w}^t \rangle^T$ and take the real part, we will obtain the correct discretized energy balance equation analogous to (2.45). Notice that the conversion term analogous to $\text{Re} \int_0^1 \frac{Rk^2}{(\Delta t)^2 Rk^2} \frac{\langle w' \rangle \Pi'}{\sigma} d\sigma$ is made up of two parts, one from $\frac{\gamma^* \bar{w}^t}{(1 + \Delta t/\tau_N)\sigma}$ and one from L . These two terms must be treated in such a way that they will cancel the conversion term in the thermal energy equation or spurious energy will be introduced into the system. The first term in discretized form would be $\frac{p_s}{gk^2} \langle \bar{w}^t \rangle^T \underline{G} \bar{w}^t$ where the elements of \underline{G} are $R(\Delta t)^2 k^2 \int_0^1 \frac{\gamma^* e^{ie^j} d\sigma}{(1 + \Delta t/\tau_N)\sigma}$. Since \bar{w}^t is the dependent variable, the factor

$$\frac{\gamma^*}{(1 + \Delta t/\tau_N)\sigma}$$

must be included in the matrix, \underline{G} .

All the terms involving \bar{w}^t in (2.49) must be written as a matrix with known elements times \bar{w}^t . Since the L term also contributes to the conversion term, for consistency it must be discretized as $\underline{G} \underline{\Lambda}$ where

$$\Lambda_i = \left(\frac{(1 + \Delta t/\tau_N)\sigma L}{Rk^2(\Delta t)^2 \gamma^*} \right)_i$$

Then the conversion term in the kinetic energy balance equation becomes

$$\frac{p_s}{gk^2} \langle \bar{w}^t \rangle^T \underline{G} (\bar{w}^t + \underline{\Lambda}) \quad \text{with} \quad \bar{w}^t + \underline{\Lambda} = \bar{n}^t \cdot \frac{(1 + \Delta t/\tau_N)}{\Delta t \gamma^*}$$

The conversion term in the discretized thermal energy balance equation must have exactly the same form,

$$\frac{p_s}{gk^2} \left(\frac{\langle \bar{n}^t \rangle (1 + \Delta t/\tau_N)}{\Delta t \gamma^*} \right)^T \underline{G} \bar{w}^t$$

Since equation (2.48) does not contain derivatives with respect to σ , it is vertically discretized simply by evaluating it at each grid point. Each term can be thought of as a column vector. To form the energy balance equation we divide (2.48) through by $\gamma^* \Delta t$ and multiply by $\frac{p_s}{gk^2} \left(\langle \bar{\pi}^t \rangle \frac{(1 + \Delta t/\tau_N)^T}{(\Delta t)\gamma^*} \right) \underline{G}$. The conversion terms will cancel, and the other terms will have the correct units.

From the above discussion it is clear that the finite element discretization is closely related to the energy balance equations. For the momentum equation we need only multiply by the proper vector to obtain an expression for the time rate of change of the perturbation kinetic energy which in discretized form is $\frac{p_s}{gk^2} \langle \bar{w}^t \rangle^T \underline{D} (\bar{w}^t - \bar{w}^t / t - \Delta t)$. If the energy balance is not considered, a certain amount of leeway is allowed in the form of the discretized L term. The simplest discretization of this term is $\underline{A} \underline{L}$ where the elements of \underline{A} are $\int_0^1 e^i e^j d\sigma$. This discretization would not conserve energy because the L term is part of the kinetic to thermal energy conversion term. It must be treated in such a way that the sum of it plus the $\gamma^* \bar{w}^t$ term cancels the conversion term in the thermal energy balance equation. The simple discretization was used in some preliminary runs and, as might be expected, it was unstable. The discretized form of the equation for the time rate of change of temperature which is analogous to the one used to solve for the time rate of change of W is $\underline{G} \times (2.48)$. When this equation is multiplied by the proper vector, i.e. $\frac{p_s}{gk^2} \left(\langle \bar{\pi}^t \rangle \frac{(1 + \Delta t/\tau_N)^T}{(\Delta t)\gamma^*} \right)$, the conversion term will exactly balance the one in the kinetic energy

equation. Since each term in equation (2.48) gets multiplied by \underline{G} , it is unnecessary to actually carry out this multiplication in the numerical solution. Equation (2.48) may be evaluated at the grid points.

From the energy balance equation we see why explicit terms may cause trouble in the form of an unphysical growth of energy. Consider the term due to advection: $\text{Re} \int_0^1 \langle W \rangle ik \frac{\partial}{\partial \sigma} (u^* \frac{\partial W}{\partial \sigma}) d\sigma$. This term did not contribute to the analytic energy balance because it had no real part. In discretized form however, we obtain $\text{Re} \frac{p_s}{gk^2} \langle \bar{W}^t \rangle^T \underline{C} \bar{W}|_t$ where the elements of \underline{C} are $ik \Delta t \int_0^1 u^* \frac{\partial e^i}{\partial \sigma} \frac{\partial e^j}{\partial \sigma} d\sigma$. This term will have a real part because $\bar{W}^t \neq W|_t$ except in the special cases where W is constant or linear in time. A feedback effect is possible where a small contribution to the energy from this term causes the solution to grow so that at the next time step the contribution from this term is larger.

The energy balance for the full model is very similar to that of the gravity wave model. The treatment of the conversion terms is exactly the same. Since for the full model $v' \neq 0$, there is a contribution from $|v'|^2$ to the time rate of change of kinetic energy, and since the basic state can depend on latitude there are numerous perturbation/basic state conversion terms involving latitudinal derivatives of the basic state.

CHAPTER 3**THE BASIC STATE OF THE VENUS ATMOSPHERE AND TIDAL FORCING****3.1 Introduction**

Many areas of planetary science have been transformed by a rapidly expanding data base in recent years, and the study of Venus thermal tides is no exception. Before the Pioneer Venus mission speculations about the tides were poorly constrained due to insufficient knowledge of the mean state of the atmosphere, uncertainties about the sources of excitation, and lack of measurements of the tides themselves. However, by the time of the present study, these drawbacks had diminished to the point that it was a challenge to find both model inputs and outputs compatible with the data.

In this chapter we discuss the basic or mean state of the Venus atmosphere and the tidal forcing functions. The basic state is the dynamical and thermal state of the atmosphere averaged with respect to time and longitude. In defining the basic state, forcing functions, and other model parameters, we make extensive use of Pioneer Venus data. Prior to Pioneer Venus, the Venus atmosphere was studied by ground-based observers, the Mariner 10 fly-by, and the Venera probes. Although these provided many useful observations, the Pioneer Venus data set is more complete and well documented. Also, the Pioneer Venus mission has provided a focus for Venus research for the past several years, so it is natural to use the data from this mission as our main source and incorporate other observations only as necessary.

Pioneer Venus, of course, did not provide a complete picture of

the Venus atmosphere. To actually determine the mean state in the lower atmosphere, a long time series of observations would be required at many locations on the planet and at many levels in the atmosphere. The four Pioneer Venus probes provided only an instantaneous view at four locations. However, since there are many similarities from probe to probe, using the probe measurements to determine a basic state is not unreasonable. Measurements from the Pioneer Venus orbiter help determine the basic state in the upper atmosphere. The orbiter measurements give more complete global coverage over a longer time period than the probes, but in general have poorer vertical resolution. There are a few areas where data are almost completely lacking. For example, the zonal wind above the cloud tops has not been directly measured. When model parameters cannot be reliably determined from the data, we choose values which optimize the fit of our computed tidal amplitudes and phases above 70 km to the orbiting infrared radiometer (OIR) tidal data and are consistent with simple models and/or physical intuition.

To specify the basic state we need the zonal mean rotation rate, $\Omega(\sigma, \lambda)$, the global mean static stability, $\gamma^*(\sigma)$, the surface pressure, p_s , and the global mean temperature at some level in the atmosphere. From these quantities we can derive the other necessary basic state quantities. The next two sections deal with $\gamma^*(\sigma)$ and $\Omega(\sigma, \lambda)$ and the quantities derived from them. We also must specify the dissipation time constants, τ_R and τ_N . In the final section of the chapter, the forcing functions are to be discussed.

3.2 The Static Stability

The static stability of the atmosphere is an important parameter in determining the vertical structure of thermal tides as shown in the discussion of gravity waves in section 2.4. Our stability parameter is $\gamma = RT/c_p\sigma - \partial T/\partial\sigma$. The stability is broken up into a global mean and a latitudinally varying part:

$$\gamma(\sigma,\lambda) = \gamma^*(\sigma) + \gamma_1(\sigma,\lambda)$$

γ_1 is derived from the thermal wind equation of cyclostrophic balance and is discussed in the next section. The thermal wind equation relates latitudinal temperature gradients to the vertical shear in the mean zonal wind. γ^* is based on temperature profiles from several Pioneer Venus experiments. Although the raw data are in the form of temperatures, the static stability is the model input. The global mean temperature profile, $T^*(\sigma)$, is calculated numerically from $\gamma^*(\sigma)$. Since the model is more sensitive to the value of γ^* than the value of T^* , calculating γ^* numerically from T^* would introduce more inaccuracies.

From the ground up to 56 km the stability profile is based on measurements made by the atmospheric structure experiment on Pioneer Venus (Sieff et al., 1980). In this experiment simultaneous measurements were made of temperature and pressure as each probe descended. Altitude was determined from the hydrostatic approximation, and the stability was calculated in the form $\Gamma(z) = \Gamma_a + dT/dz$ where Γ_a is the adiabatic lapse rate for a non-ideal gas and z is height in kilometers.

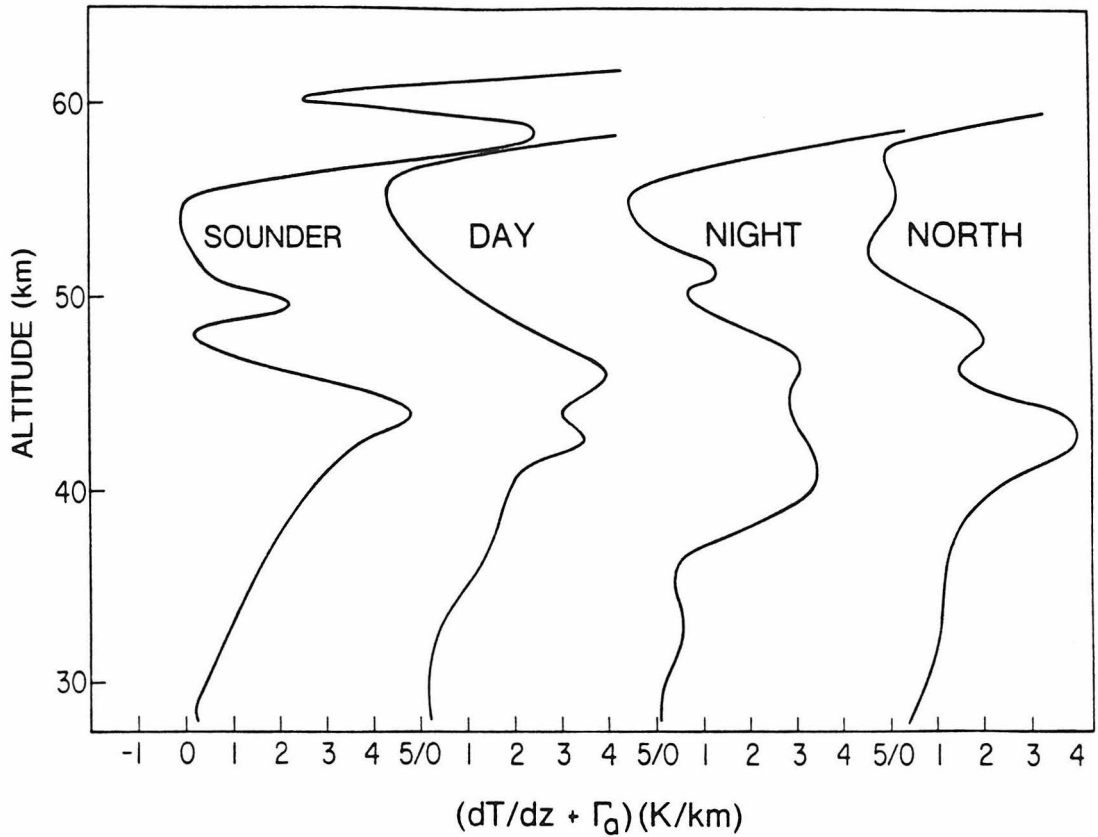


Figure 3.1 Static stability of the atmosphere between 28 and 65 km at the Pioneer Venus probe sites. $\Gamma = -\Gamma_a + dT/dz$ where Γ_a is the adiabatic lapse rate. This figure is taken from Schubert et al. (1980). Γ is based on calculations done by Sieff et al. (1980).

TABLE 3.1
MEASUREMENTS OF STATIC STABILITY
FROM
THE PIONEER VENUS PROBES*

$$\Gamma = \Gamma_a + dT/dz \text{ in K/km}$$

Altitude, km	Sounder	Day	Night	North	Average of four probes
35	1.3	0.9	0.4	1.2	1.0
40	2.7	1.9	3.3	2.1	2.5
42	3.4	2.8	3.3	3.5	3.3
44	4.7	3.1	2.9	3.7	3.6
46	2.7	4.0	3.0	1.5	2.8
48	0.3	2.7	2.2	1.9	1.8
50	2.2	1.3	0.8	1.0	1.3
52	0.3	0.2	1.0	-0.4	0.3
54	-0.1	-0.5	-0.4	-0.2	-0.3
56	2.0	-0.7	0.1	0.0	0.4
58	7.3	4.0	4.2	0.3	4.0

*Probe data are from Figure 12 of Schubert et al. (1980). (Figure 3.6 of this thesis.)

The results from 30 to 60 km are shown in Figure 3.1. The major features seen in the stability profiles of all four probes are: increasing stability above 55 km, an adiabatic region around 55 km, a peak in the stability at 43 km, and decreasing stability below 43 km. To render the data in these profiles useful for our model, values were read off the curves at closely spaced levels, and average values were determined. The probe and average values are given in Table 3.1. The average values are linearly interpolated in z between the given levels to give $\Gamma(z)$ in this region. This profile requires a slight modification before it can be used as model input because negative static stabilities cause instabilities in the model. Therefore at 54 km the value -0.3 K/km is replaced by 0.1 K/km.

The static stability calculated from the probe data below 30 km is shown in Figure 3.2. The temperature sensors on all the probes failed at about 13 km so the stability below that level could not be determined. Below 30 km the lapse rate is close to adiabatic, except that the lowest points show a stable trend. Temperature data from Venera 9 and 10 (Avduevskii et al., 1976) and from the Pioneer Venus small probe net flux radiometer (SNFR) experiment (Suomi et al., 1979) support the existence of a deep stable layer. However, the SNFR temperature sensors also failed at 13 km. The Venera 10 profile returned to adiabatic below 5 km, so the stable region, if it exists, may not extend to the surface. Since theoretical models of the radiative and dynamical state of the deep atmosphere predict an adiabatic profile (Pollack et al., 1980; Stone, 1974), the presence of a stable layer is difficult to explain. In our model we have chosen to

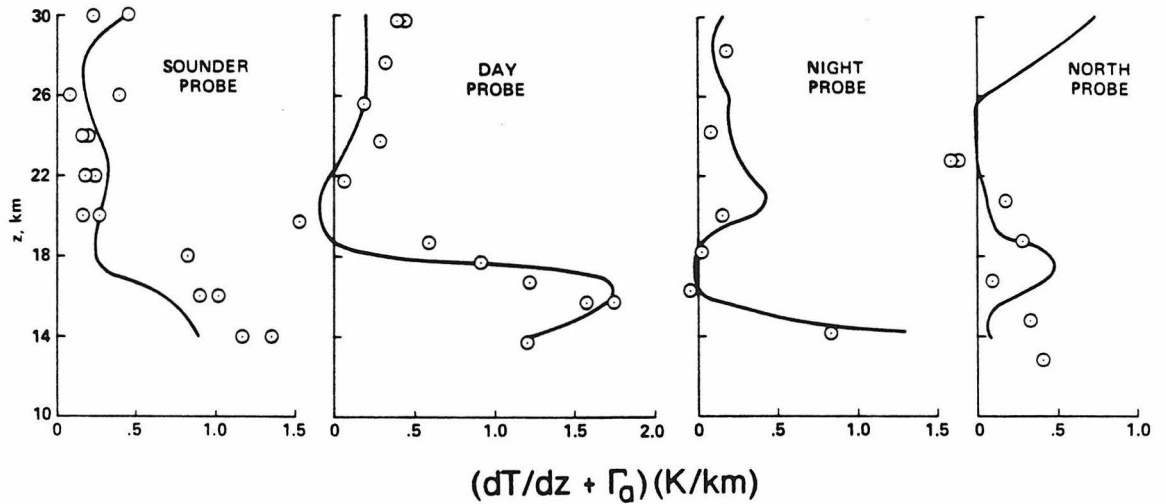


Figure 3.2 Static stability of the atmosphere between about 14 and 30 km at the Pioneer Venus probe sites. The curves are from cubic spline fits to the measured temperature profiles while the points are from graphical estimates of the lapse rate. This figure is from Schubert et al. (1980).

keep a low value of the stability, $\Gamma = 0.05$ K/km, below 30 km. It is more convenient to use a low value of the stability since low stability makes the model converge faster. The effects of the value of the static stability near the ground were investigated using the gravity wave model. They were found to be small in the upper atmosphere. These results are discussed in Chapter 4.

The choice of the stability profile from 55 km to 100 km is of critical importance because the OIR measurements of the tides were made in this region. Temperature profiles from several sources are available above 58 km, from which values for the static stability can be estimated.

The temperature and pressure sensors on the atmospheric structure experiment were not deployed until the probes reached about 65 km altitude. However, above this level temperature profiles were obtained from deceleration and trajectory information (Seiff et al., 1980). These profiles are tabulated in Table VIII of Seiff et al. (1980) for three of the four probes. We used these data to calculate dT/dz for the day and sounder probes. Our values for $\Gamma(z)$ are shown in Figures 3.3 and 3.4. The adiabatic lapse rate for an ideal gas, $\Gamma_a = g/c_p$, was used; this is valid at high altitudes. To get some idea of the validity of our lapse rates, $\Gamma(z)$ was calculated in a similar fashion from the sensor data from the day and sounder probes which are given in Table III of Seiff et al. (1980). Our method is obviously more noisy than that shown in Figure 3.1, but the profile has the correct shape. The average profile given in Table 3.1 is shown for comparison.

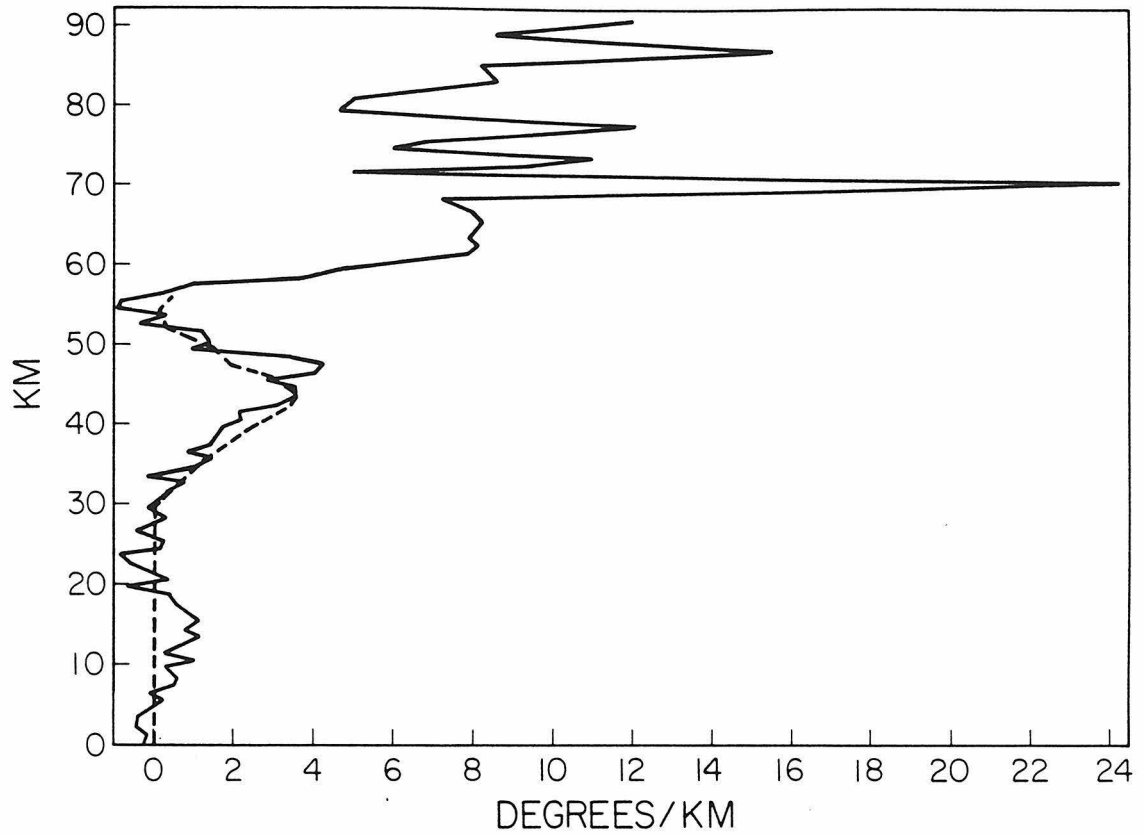


Figure 3.3 The solid curve is an estimate of the static stability, $\Gamma = \Gamma_a + dT/dz$ in degrees/km, of the atmosphere from the day probe temperature profile tabulated in Sieff et al. (1980). The dashed curve is the average profile in Table 3.1 from 30 to 60 km and follows $\Gamma = 0.05$ K/km below 30 km. The agreement of the dashed and solid curves shows the validity of the estimated stability. Above 60 km, this estimate is used to help determine the basis state Γ .

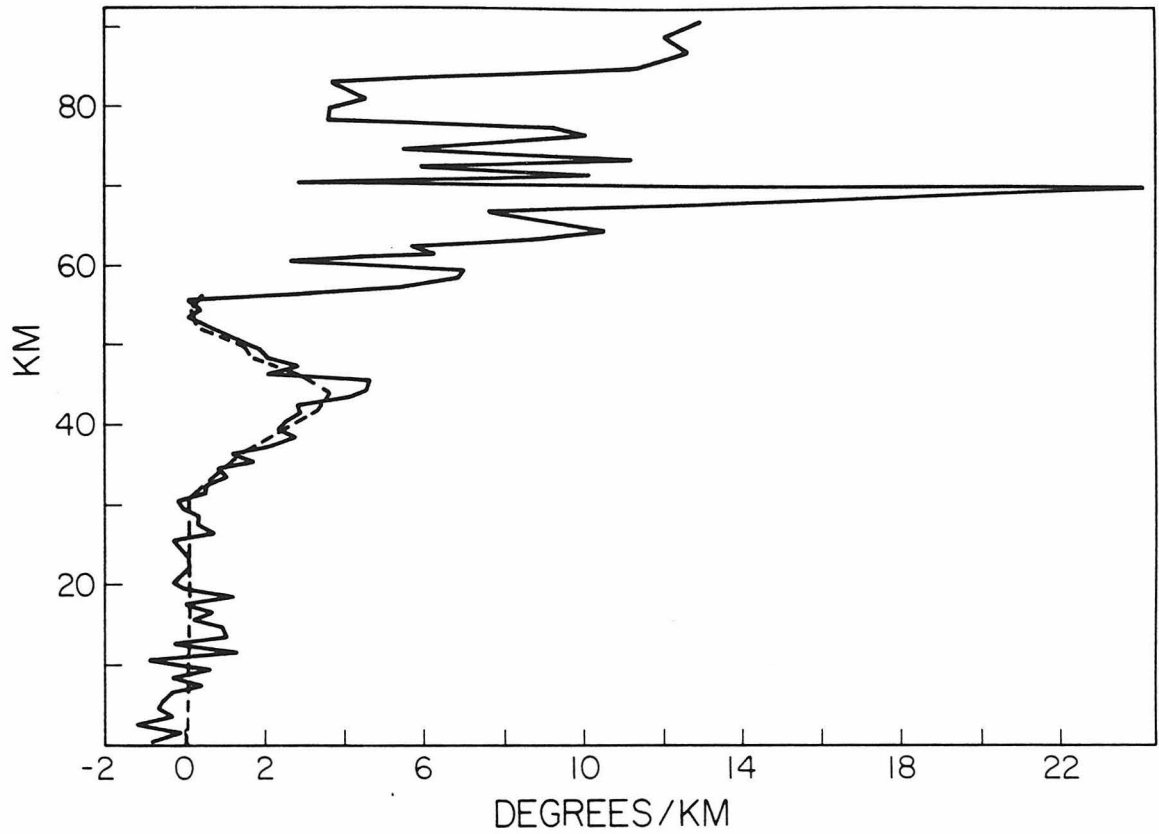


Figure 3.4 Same as Fig. 3.3 for the sounder probe temperature profile tabulated by Sieff et al. (1980).

Above 60 km most of the oscillations are probably noise, but there are two major features which are seen in both probes. At about 70 km there is a narrow peak of very high stability. Since an isothermal region has a Γ of about 12 K/km, this peak indicates the presence of a temperature inversion. The other feature is a broad minimum in the stability centered at about 80 km.

The temperature inversion has been extensively studied by Kliore and Patel (1980) using temperature profiles obtained from Pioneer Venus radio occultations. These profiles cover the 1 bar to 1 mbar region of the atmosphere, i.e., from 50 to 85 km altitude. As latitude increases the inversion becomes deeper, broader, and is centered lower in the atmosphere. We have not obtained the static stability from the radio occultation profiles, but have used them to confirm that the inversion is part of the mean state of the atmosphere. The latitude dependence of the inversion has not been included in our model.

Our final source of information about the static stability above 58 km is OIR retrieved temperature profiles. The OIR measures the radiances in 5 infrared channels. The radiances, the weighting functions for each channel, and a model for the effect of clouds are used in a deconvolution program to obtain a temperature profile. Zonally averaged retrieved temperature profiles (L. Elson and F. Taylor, written communication, 1982) were used to estimate $\Gamma(z)$ for 10° latitude bins centered at 15° , 45° , and 75° as shown in Figure 3.5. In these profiles the minimum at 80 km appears very similar to that seen in the probe data. Since these profiles represent averages over many observations taken at different times and places, this minimum is

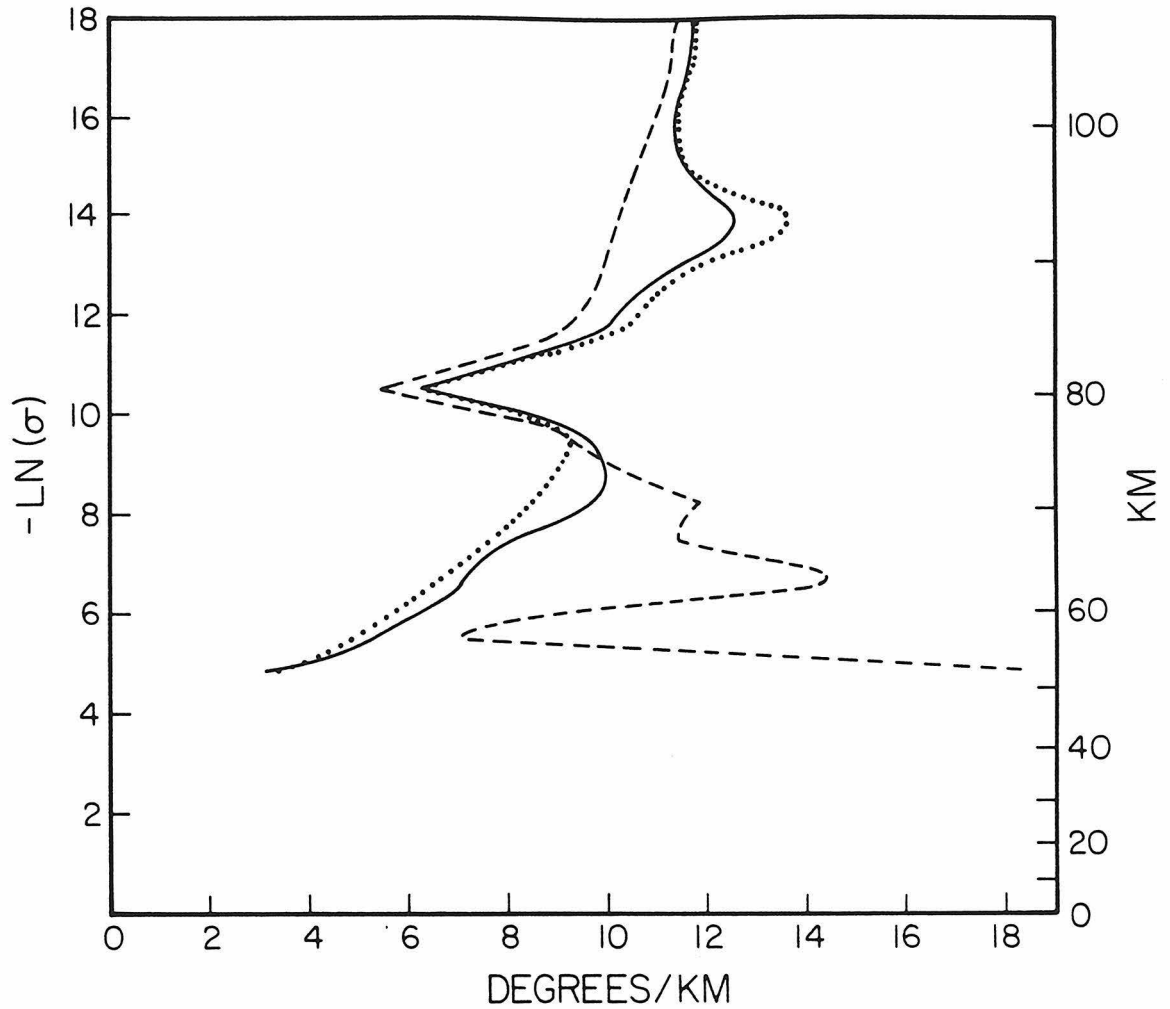


Figure 3.5 $\Gamma(z)$ calculated from OIR zonally averaged retrieved temperature profiles provided by L. Elson and F. Taylor (written communication, 1982). 10° latitude bins were used in the zonal average. The dotted curve is for 10° - 20° , the solid curve for 40° - 50° , and the dashed curve for 70° - 80° .

probably a feature of the basic state. The inversion peak does not show up very prominently in these profiles probably due to lack of vertical resolution.

All the data described above were taken into consideration in constructing our basic state profile of $\Gamma(z)$ shown in Figure 3.6. Below 56 km this profile is the average profile given in Table 3.1 except for the positive stability at 54 km. The stable trend in the lowest 18 km has not been included. Above 56 km the exact values were chosen to give the best agreement with the OIR tidal data. There is a peak in the stability at 70 km and a minimum at 80 km as the data indicate. The narrow inversion layer was omitted since our vertical resolution is insufficient to resolve it. Above 90 km the model atmosphere is isothermal with $T^* = 170$ K. The day and north probe deceleration data show large amplitude temperature waves in this region, but these are likely to be eddies and not representative of the basic state. The average value of the temperature for these probes and the sounder probe is about 170 K.

The static stability input to the model is of the form $\Gamma(z) = g/c_p + \partial T^*/\partial z$. $\Gamma(z)$ is piecewise linear as shown in Figure 3.6. At each σ level of the model $z(\sigma)$ is obtained from the probe data and $\Gamma(\sigma)$ is then specified. $T^*(\sigma)$ is derived by writing $\Gamma(\sigma)$ in the form

$$\Gamma(\sigma) = g/c_p - (g/RT^*) \partial T^*/\partial(\ln\sigma)$$

where we have used the hydrostatic equation $\partial p/\partial z = -pg/RT$. Thus

$$\int_{170 \text{ K}}^{T^*(\sigma)} \frac{dT^*}{T^*} = \int_{\ln \sigma_{\text{top}}}^{\ln \sigma} \left(\frac{R}{c_p} - \frac{R\Gamma}{g} \right) d(\ln \sigma) \quad (3.1)$$

where σ_{top} is the top of the resolved region of the atmosphere in the model. $R = R_g/\mu$ where R_g is the universal gas constant and μ is the mean molecular weight of the Venus atmosphere. The model atmosphere composition is 96% CO_2 and 4% N_2 (Hoffman et al., 1980). The gravitational acceleration, g , is 887 cm/sec^2 .

Since the specific heat per unit mass, c_p , is a function of pressure and temperature the integral in (3.1) cannot be done directly, but must be solved iteratively for a consistent profile of T^* and c_p . The pressure at each level, $p(\sigma)$, is easily obtained provided the basic state surface pressure is known. We use a value of 92.1 bars based on extrapolation of Pioneer Venus probe data to the surface (Sieff et al., 1980). A temperature profile based on day probe data is then used to obtain an initial guess for $c_p(T,p)$. Values for C_p/R , where C_p is the molar specific heat, are taken from the tables of Hilsenrath et al. (1955). These tables cover a pressure range of 0.01 atm to 100 atm and a temperature range of 200 K to 800 K for both CO_2 and N_2 . A two dimensional linear interpolation of the values given in the tables is used to obtain the molar specific heat for both gases for the required temperatures and pressures. In the upper atmosphere where the temperature and pressure lie outside the range of the tables, the value for the lowest temperature and pressure given is used. The values for

the two gases are combined linearly:

$$c_p(T,p) = R \left(0.96 (C_p(T,p)/R_g)_{CO_2} + 0.04 (C_p(T,p)/R_g)_{N_2} \right)$$

Using the initial guess for $c_p(\sigma)$, $T^*(\sigma)$ is calculated from equation (3.1). A new profile, $c_p(\sigma)$, is then obtained from the tables using $T^*(\sigma)$ and the integral is re-evaluated. This process is repeated until the temperature at all levels changes by less than 0.1 K from one iteration to the next. Finally, γ^* is derived from Γ by

$$\gamma^* = RT^*/c_p\sigma - \partial T^*/\partial \sigma = RT^*\Gamma/g\sigma \quad .$$

Profiles for γ^* , T^* , and c_p are shown in Figures 3.7, 3.8, and 3.9.

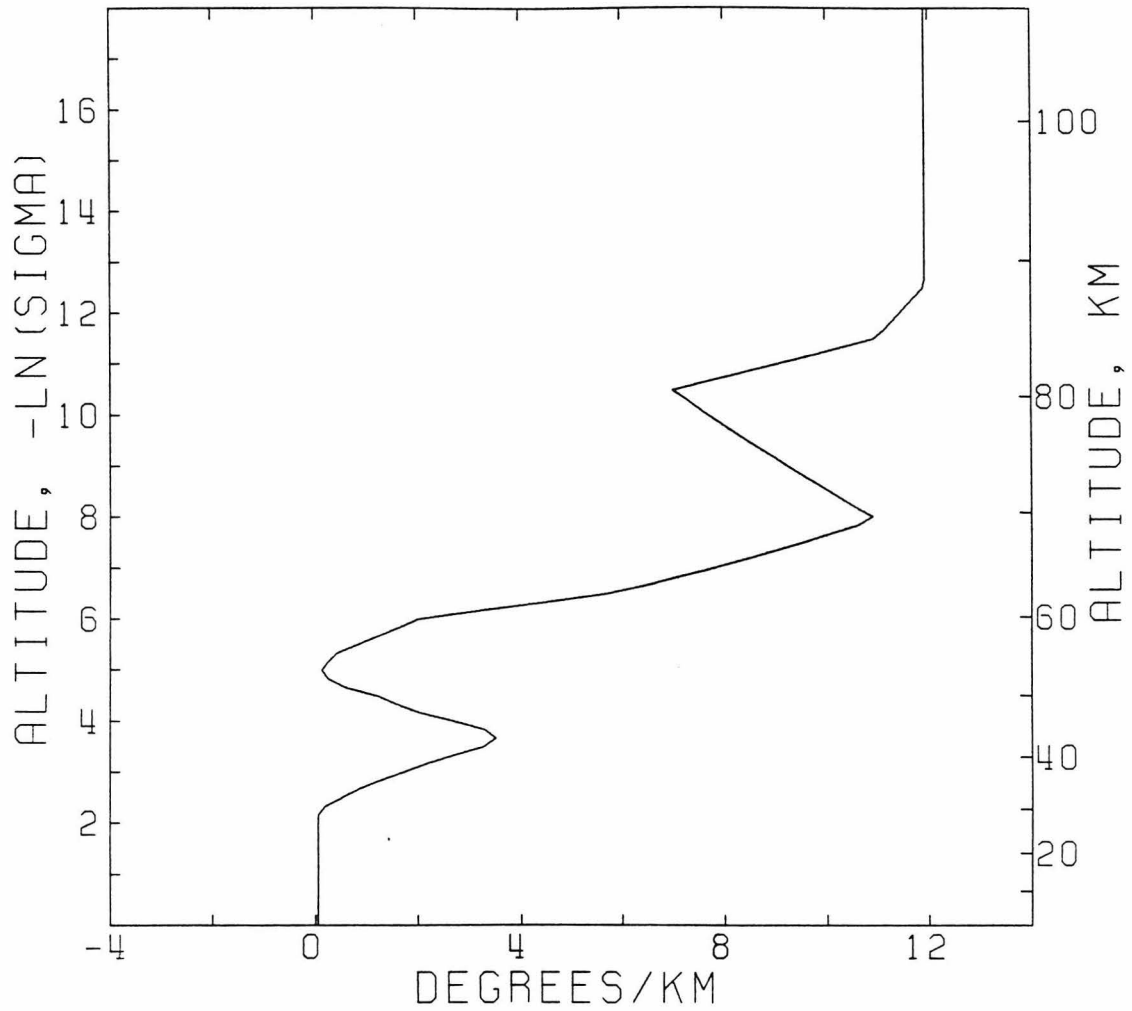


Figure 3.6 The basic state profile $\Gamma(z)$ to be used in all model calculations unless otherwise noted.

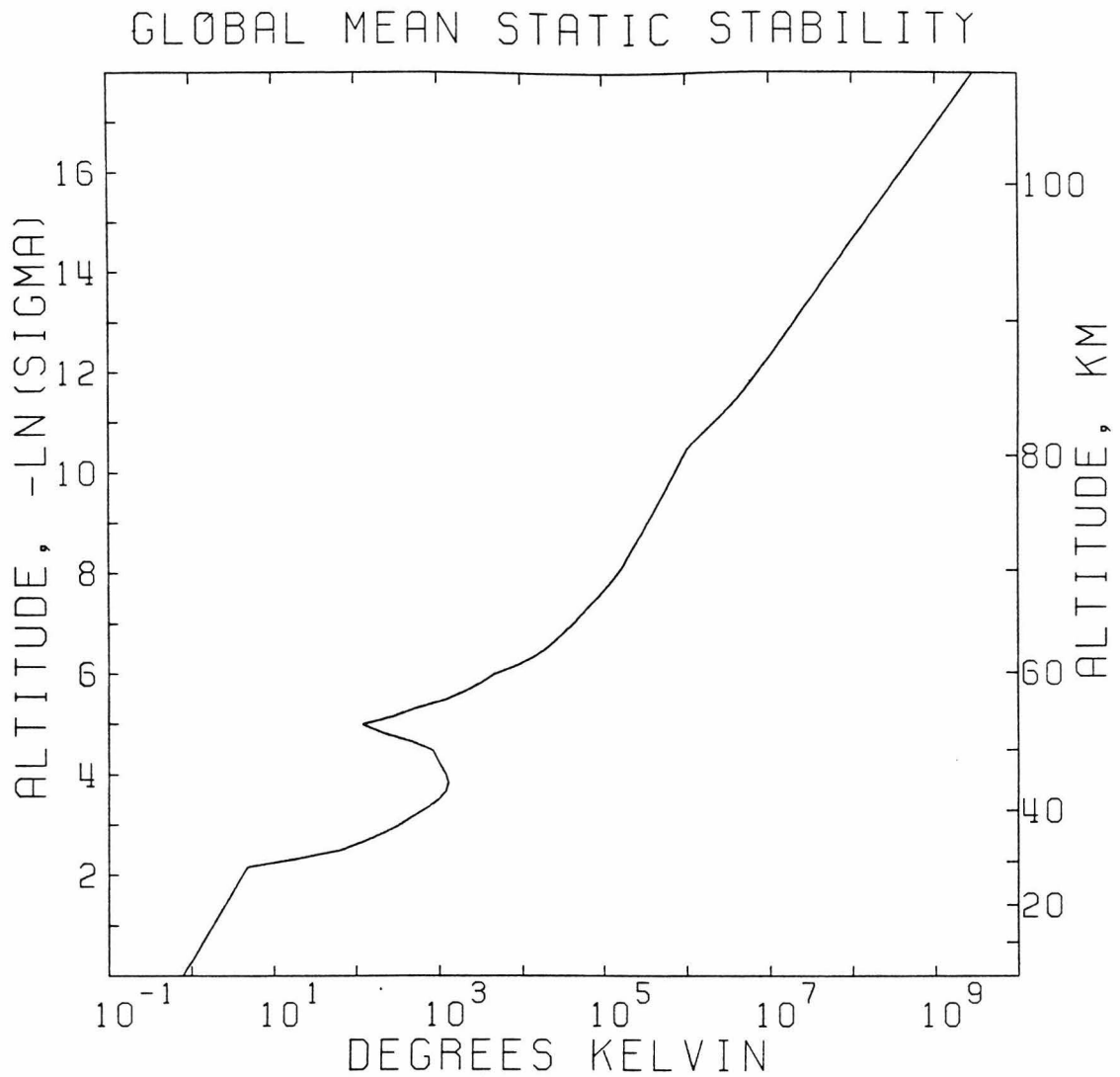


Figure 3.7 The form of the static stability used in the model.
 $\gamma^* = \frac{RT^*}{g\sigma} \Gamma$. This profile will be used in all model calculations unless otherwise noted.

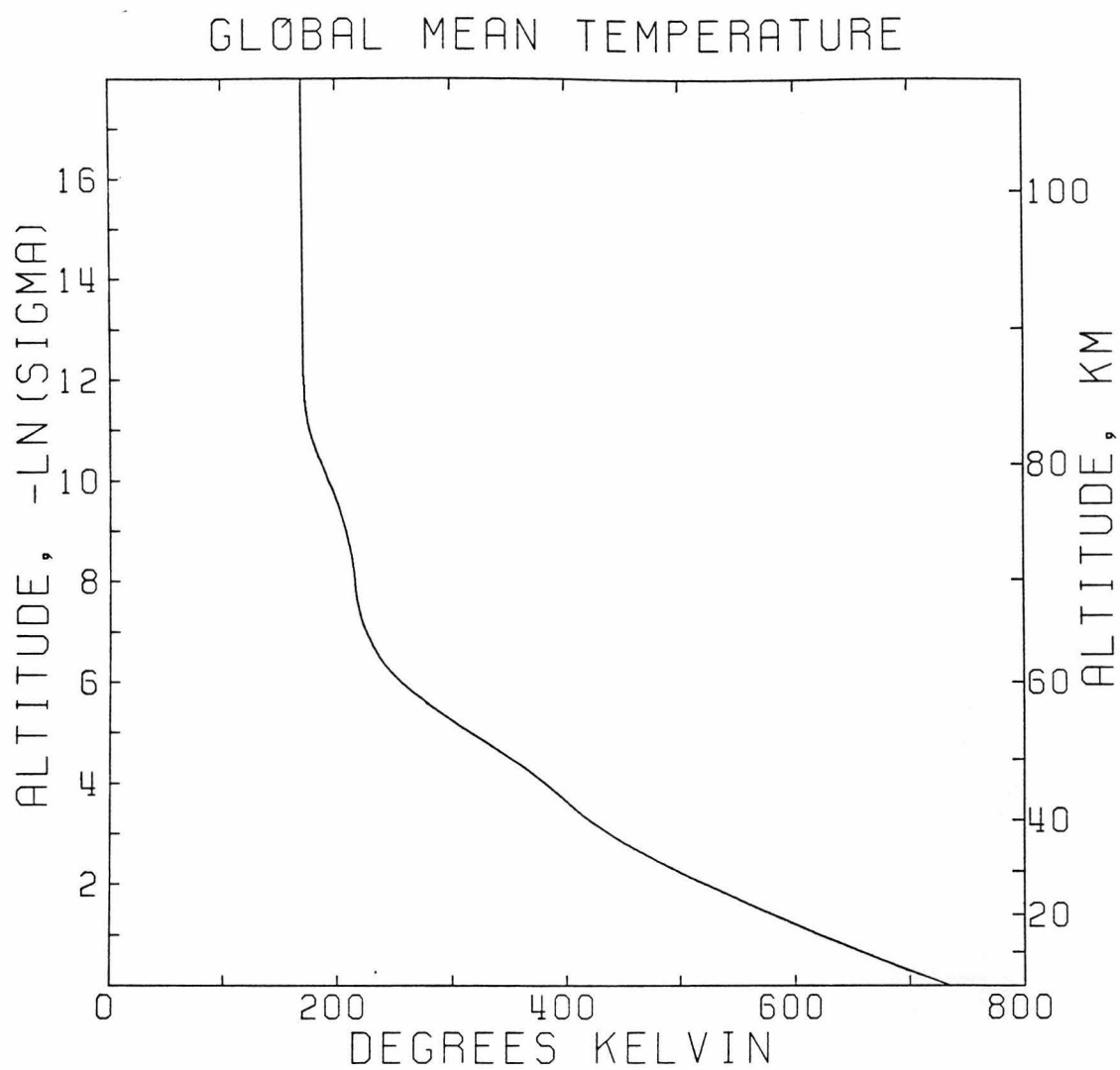


Figure 3.8 The basic state profile of the global mean temperature, $T^*(z)$. This profile will be used in all model calculations unless otherwise noted.

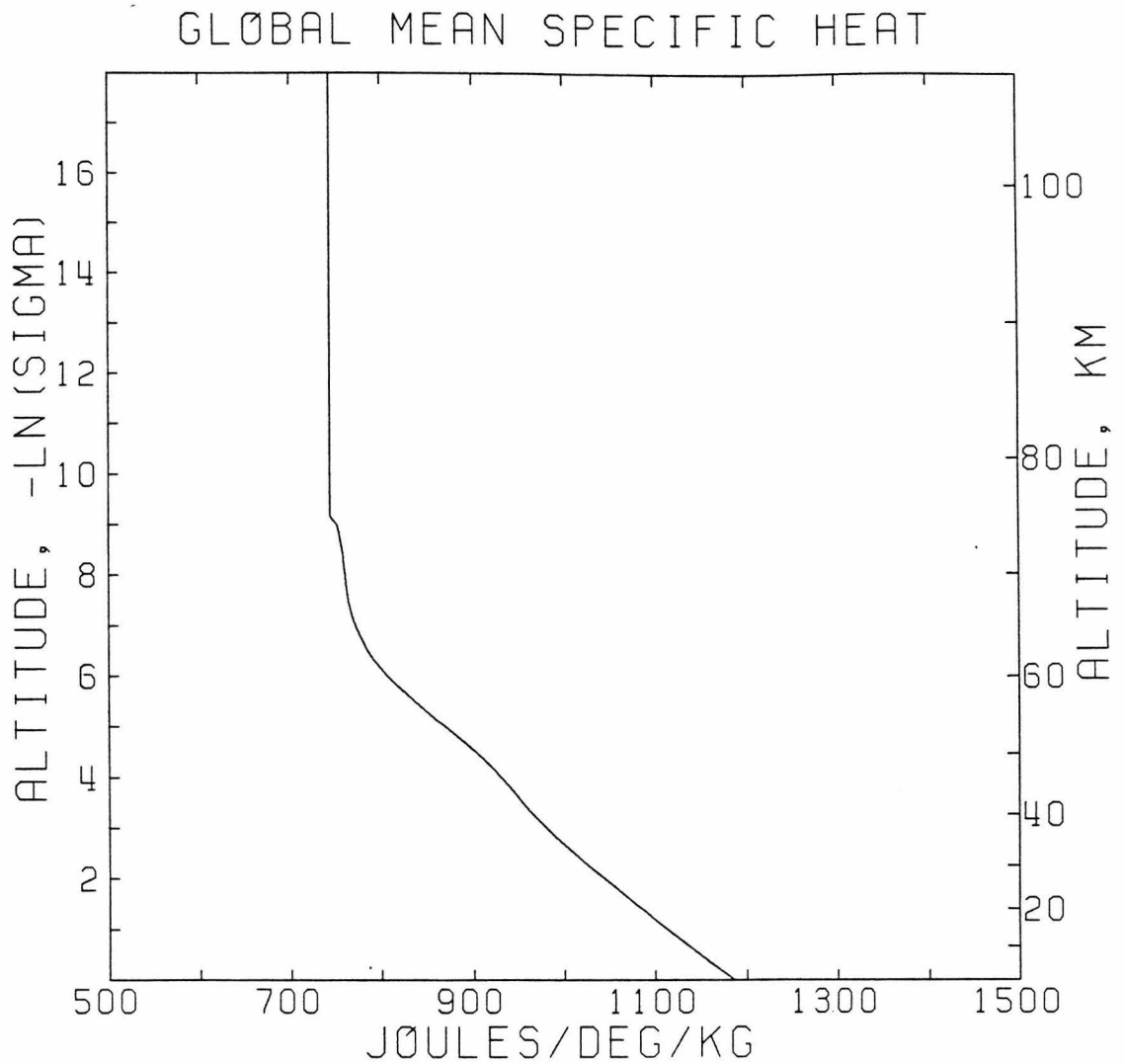


Figure 3.9 The basic state profile of $c_p(z)$, the specific heat at constant pressure. This profile will be used in all model calculations unless otherwise noted.

3.3 The Zonal Wind

The vertical profile of the mean zonal wind is the other major factor in determining the structure of the thermal tides. Our basic state zonal wind profile from the ground up to 60 km is based on the results of the Pioneer Venus differential long baseline interferometry (DLBI) experiment (Counselman et al., 1980). DLBI profiles for the four probes are shown in Figure 3.10. On Venus, due to the retrograde rotation of the atmosphere, a westward zonal wind is defined to be positive. Note that the profiles for the day and night probes are almost identical. These two probes entered at about the same latitude, 30°S , but separated by 100° in longitude. Thus, the similarity in the profiles is considered to be evidence for a lack of major longitudinal variations in the zonal wind below 60 km. The sounder probe profile is similar in shape to the day and night profiles but has higher velocities throughout the region. The difference in velocity is nearly consistent with a state of solid body rotation at each height between the sounder probe at 4°N and the day and night probes at 30°S . These three profiles are characterized by alternating regions of high and low shear. The north probe profile is quite different. The velocities measured at the north probe location, 60°N , are higher at most altitudes than predicted by solid body rotation and the shear increases smoothly from the ground up to 60 km. Our basic state is in solid body rotation and below 60 km is based on the day, night, and sounder measurements. This may have some effect on the validity of our solution in the polar region. The sensitivity of the solution to the zonal wind profile will be investigated in Chapter 4 using the gravity wave program.

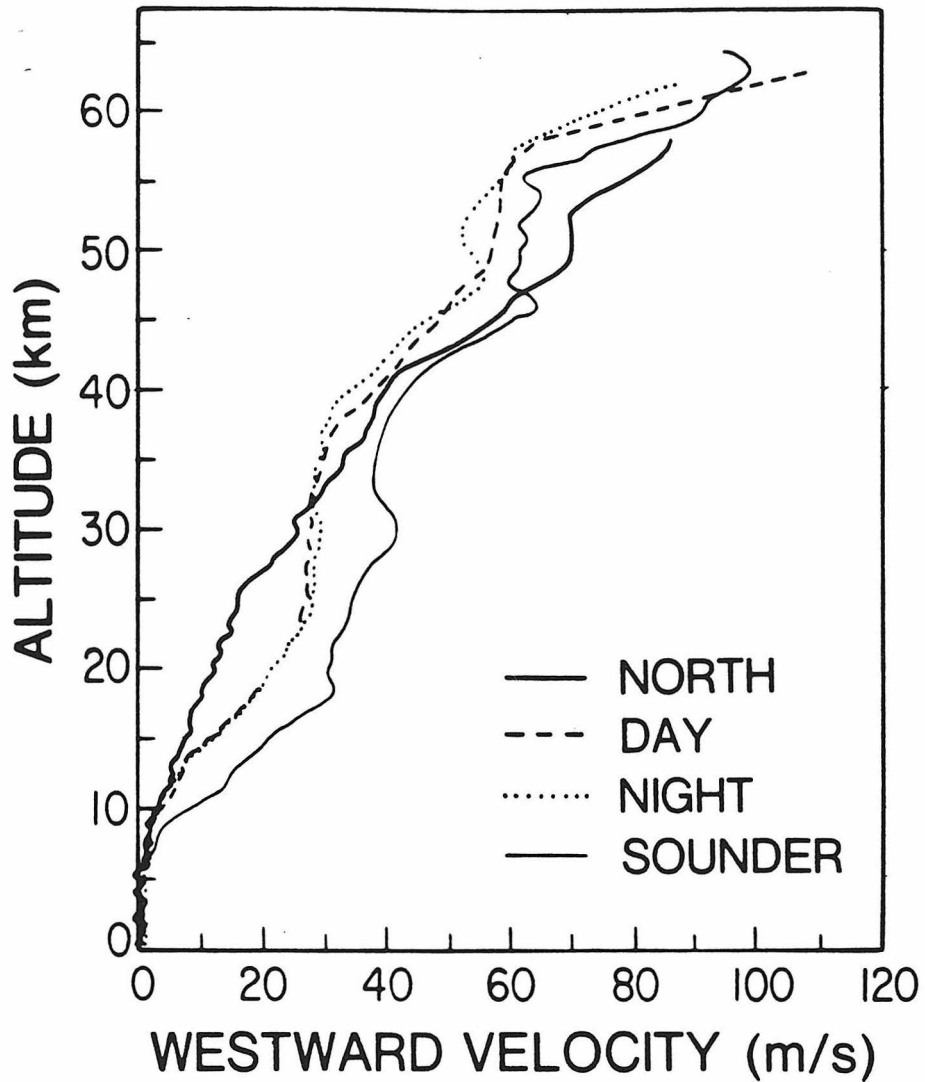


Figure 3.10 The zonal component of the wind velocity vector measured by the DLBI experiment for each of the Pioneer Venus probes. The uncertainties in these profiles are about 1 m/s in velocity and less than 1 km in altitude. This figure is from Schubert et al. (1980), modified from the original in Counselman et al. (1980).

Wind velocity profiles obtained by Doppler tracking of Venera 8, 9, 10, and 12 are compared to the Pioneer Venus DLBI profiles by Schubert et al. (1980). The Venera profiles show a much larger degree of variability and may indicate spatial or temporal changes in the zonal wind.

Above 60 km there are no in situ measurements of wind velocity in the Venus atmosphere. However, there is considerable evidence for equatorial winds on the order of 100 m/s at the cloud top level of about 65 km. Measurements taken by tracking small scale cloud features in Pioneer Venus and Mariner 10 ultraviolet images (Rossow et al., 1980; Limaye and Suomi, 1981) give equatorial winds of about 95 m/s. During the Pioneer Venus primary mission the atmosphere at the cloud tops was nearly in solid body rotation to the limit of the measurements from 60° S to 40° N, but at the time of the Mariner 10 encounter there was a prominent midlatitude jet in each hemisphere. Images taken during the Pioneer Venus extended mission indicate that jets of varying strengths appear and disappear with a time scale of several months and may be present in both, either, or neither hemisphere (Rossow and Kinsella, 1982). It is unclear which situation is more typical of the circulation. Since the OIR tidal results were obtained during the primary mission, the fact that solid body rotation is assumed in our model should lead to consistent model results at least up to 50° latitude. Ground-based observations made by measuring Doppler shifts of spectral lines (Traub and Carelton, 1975) and by heterodyne techniques (Betz et al., 1976, 1977) both support the existence of high retrograde zonal winds at the cloud tops.

It has not been determined how far above the cloud tops the rapid winds extend or what peak value is reached. Our tidal model is quite sensitive to both these parameters. By assuming cyclostrophic balance we can relate latitudinal temperature gradients to vertical shear in the zonal wind (Schubert et al., 1980). Above 70 km temperature measurements made by the OIR and the probes indicate that temperature increases poleward on constant pressure surfaces (Taylor et al., 1980). According to cyclostrophic balance, this implies that the zonal wind will decrease with height. However, the vertical scale of the decrease and the extreme values reached are not well determined, because the mean zonal wind at 70 km is required as a boundary condition.

There is some evidence for non-zero retrograde zonal winds in the atmosphere at about 150 km which is reviewed in Schubert et al. (1980). However, this is above the region of applicability for our tidal model.

Our nominal basic state equatorial zonal wind profile is shown in Figure 3.11. Above 60 km the profile is designed to provide a good fit to the OIR tidal data, keeping in mind that the wind should decrease above 70 km. Below 60 km a smoothed version of the day/night/sounder type profile is used. The smoothing and increased shear in the lowest 10 km were necessary to avoid instabilities in the model. The atmosphere is assumed to be in solid body rotation at each level, i.e., $u^* = a \cos \lambda \Omega(\sigma)$. $\Omega(\sigma)$ is the actual parameter required by the model. Note that in Figure 3.11 the value of u^* is not zero at the ground and does not fall to zero in the upper atmosphere. At these levels the

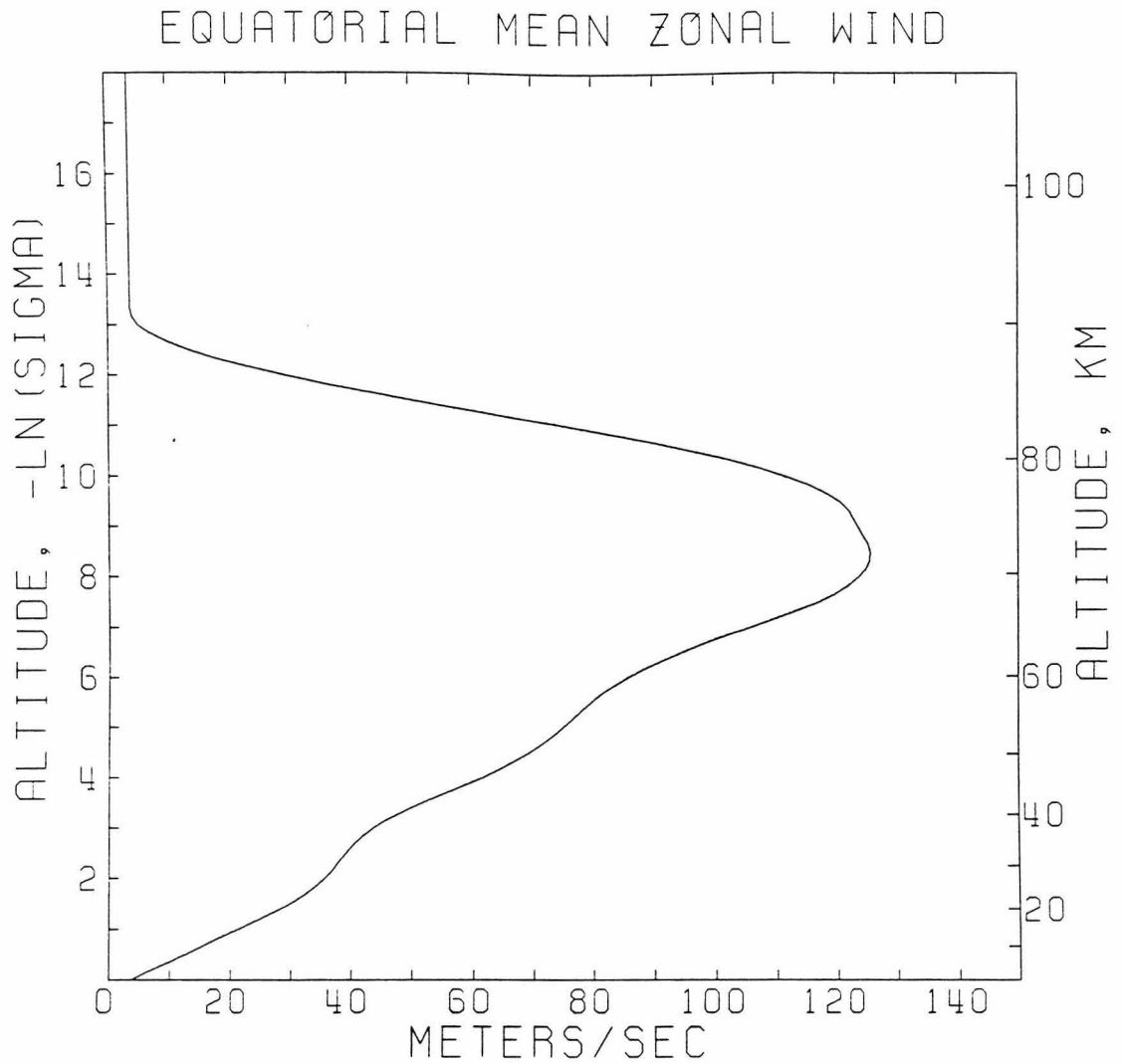


Figure 3.11 The basic state profile of the zonal wind $u^*(z)$. A positive value indicates a westward, i.e., retrograde, rotation. This profile will be used in all model calculations unless otherwise noted.

atmosphere is at rest with respect to the planet, but in the solar-fixed reference frame, Ω , and thus u^* , include a term due to the rotation of Venus.

Once $\Omega(\sigma)$ has been determined at each vertical level in the model, the latitudinally varying part of the mean temperature is determined from the thermal wind equation. Because Venus rotates so slowly, the thermal wind equation is based on cyclostrophic rather than geostrophic balance (Leovy, 1973). The equation can be derived from equation (2.15). In Chapter 2 equation (2.15) was linearized by expressing the variables as sums of a zeroth order basic state term and a first order perturbation term and keeping only first order terms. Assuming that the zeroth order terms balance leads to:

$$\frac{R}{a^2} \frac{\partial}{\cos \lambda} \left[\cos \lambda \frac{\partial T_1}{\partial \lambda} \right] = \sigma \frac{\partial}{\partial \sigma} \left\{ \frac{1}{a \cos \lambda} \frac{\partial}{\partial \lambda} \left[\cos \lambda (\zeta^* + f_y) a \cos \lambda \Omega \right] + \frac{1}{a^2} \frac{\partial}{\cos \lambda} \left[\cos \lambda \frac{\partial}{\partial \lambda} \left(\frac{a^2 \cos^2 \lambda \Omega^2}{2} \right) \right] \right\} \quad (3.2)$$

where $\zeta^* = 2 \sin \lambda \Omega$ and $f_y = 2 \sin \lambda \Omega_y$. $\Omega_y = -2\pi / (225 \text{ earth days})$, the rate of revolution of Venus around the sun. Since we have defined retrograde rotation to be positive, Ω_y is negative. Simplifying the above expression gives

$$\frac{R}{a^2} \frac{\partial T_1}{\partial \lambda} - \sigma \cos \lambda \sin \lambda \frac{\partial (\Omega + \Omega_y)^2}{\partial \sigma} = 0 \quad (3.3)$$

This is the thermal wind equation. Strictly speaking, it should only be applied where Ω is large. Using the requirement that the hemispheric average of T_1 be zero, equation (3.3) may be integrated to yield

$$T_1(\sigma, \lambda) = \frac{2a^2}{R} \sigma (\Omega + \Omega_y) \frac{\partial \Omega}{\partial \sigma} \left(\frac{1}{3} - \frac{\cos^2 \lambda}{2} \right) \quad (3.4)$$

This equation is used in the model to calculate T_1 . The value of T_1 is calculated and stored at every σ -level and every latitude on the Gaussian grid.

T_1 is used to obtain the latitudinally varying part of the static stability, γ_1 . Recall that

$$\gamma(\sigma, \lambda) = \frac{R \cdot (T^* + T_1)}{c_p(p, T^* + T_1) \cdot \sigma} - \frac{\partial (T^* + T_1)}{\partial \sigma}$$

$\gamma^*(\sigma)$ is the horizontal average of γ . The expression used for $\gamma^*(\sigma)$,

$$\gamma^*(\sigma) = \frac{RT^*}{c_p(p, T^*)\sigma} - \frac{\partial T^*}{\partial \sigma}$$

is now seen to be an approximation good to first order in the expansion

$$c_p(p, T^* + T_1) = c_p(p, T^*) + \frac{\partial c_p}{\partial T} \Big|_{T^*} \cdot T_1 + \dots$$

Since c_p does not vary rapidly with T , the error introduced by this

approximation is less than 1 % of γ^* . By definition,

$$\gamma_1 = \gamma - \gamma^* = \frac{R \cdot (T^* + T_1)}{c_p(p, T^* + T_1) \cdot \sigma} - \frac{RT^*}{c_p(p, T^*) \cdot \sigma} - \frac{\partial T_1}{\partial \sigma}$$

In order for the model to be stable, γ must be greater than zero at every (σ, λ) grid point. If γ is found to be less than zero at any point, either the profile of γ^* or Ω must be changed. Regions

where $\frac{\partial^2 \Omega}{\partial \sigma^2}$ is large and/or γ^* is small are the most likely to give trouble. These conditions occur in the cloud layer from 50 to 55 km and in the lowest 30 km of the atmosphere. In order to keep γ greater than zero, the profile of Ω in these regions has been smoothed so that the shear is more uniform than indicated by the day, night, and sounder profiles. However, even with $\frac{\partial \Omega}{\partial (\ln \sigma)}$ constant in the lowest 17 km γ is negative. If γ^* was increased in this region, the rate of convergence would be much slower. Therefore, cyclostrophic balance is not used to obtain T_1 below 17 km. Instead, T_1 is assigned values such that γ is zero at the pole and increases towards the equator. When cyclostrophic balance breaks down, as it may well do when Ω is small, the validity of linearization is in doubt since the imbalance in the zeroth order terms may be as large as terms in the first order equation. However, the solution near the ground is also in doubt because of uncertainty in the forcing and basic state. Obtaining convergence is also a problem. Fortunately, the response near the ground does not significantly affect the upper levels as will be shown in section (4.5).

The profile of Ω is also used to obtain the basic state vorticity at each (σ, λ) grid point. This is simply

$$\zeta^*(\sigma) = 2 \sin \lambda \Omega(\sigma)$$

when Ω does not depend on λ .

3.4 The Sponge Layer

Dissipation was added to the upper levels of our model to absorb upward propagating waves. Without this 'sponge layer' reflections off the upper boundary would be a serious problem. The form of our dissipation terms is very simple as shown in equations (2.18)-(2.21). They give rise, in the absence of other effects, to an exponential decay in any perturbation from the basic state. This form of the damping in the momentum equation is called Rayleigh friction and in the heat equation is called Newtonian cooling.

The physical basis for Newtonian cooling in the upper atmosphere is the damping of temperature perturbations by emission of infrared radiation which escapes to space. Since radiation escapes more readily from the upper levels of the atmosphere, the time required to damp a given perturbation will decrease as the pressure decreases as long as local thermodynamic equilibrium is maintained. A justification for using Newtonian cooling to approximate the cooling-to-space process is given by Pollack and Young (1975). They assumed that the mean state of the upper atmosphere was radiative equilibrium and used a radiative transfer model to calculate the net infrared flux due to arbitrary temperature perturbations, ΔT . Then, at every level they solved $Q = \Delta T / \tau_N$ for τ_N where Q includes the net infrared and solar flux. τ_N was not sensitive to the value of ΔT , so they concluded that using this form of damping with τ_N independent of temperature is not a bad approximation.

The results of several investigations into the infrared radiative cooling are presented in Figure 3.12. In each of these

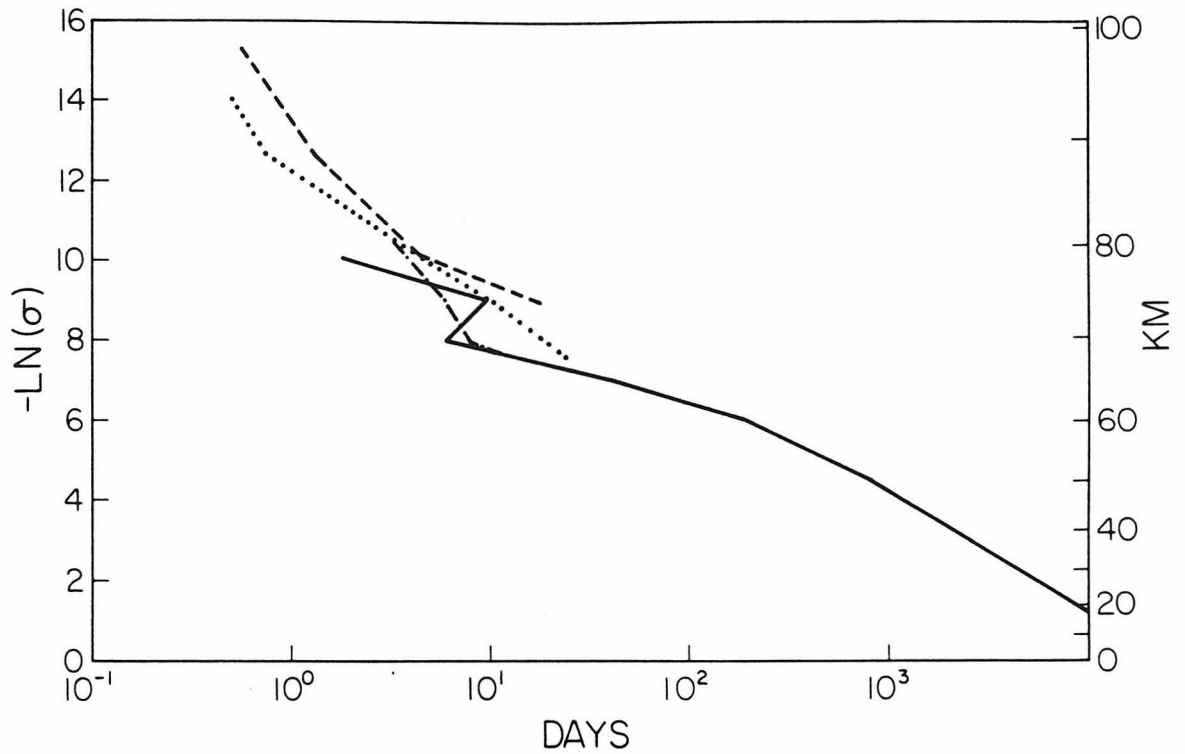


Figure 3.12 The radiative time constant, τ_N , from various sources as described in the text. The solid curve is based on the results of Pollack and Young (1975), the dashed curve on Dickinson (1972), and the dotted and dash/dot curve on D. Crisp (written communication, 1981).

investigations a detailed model of the radiative properties of the atmosphere was constructed and used to derive the time constant in the Newtonian cooling approximation. In the model by Dickinson (1972) only cooling due to 15 μm bands of CO_2 was included, but the calculation was extremely detailed. This model is most likely valid above the clouds where the results of water vapor and aerosols may be neglected. Pollack and Young (1975) included the effects of water vapor and aerosols although, of course, the results depend on their model of cloud structure. In the lower atmosphere, where the mean state of the atmosphere is not radiative equilibrium, ΔT was set equal to the difference between a convectively adjusted profile and the radiative equilibrium profile. Since this ΔT is constant, it naturally leads to a constant τ_N , but what this means for the damping of perturbations is unclear. The values of τ_N derived for the lower atmosphere are extremely long compared to tidal time scales which indicates that there is negligible radiative damping of the tides in this region. The profiles provided by D. Crisp (personal communication, 1981) are for a CO_2 -only model and a CO_2 -plus-cloud model.

Our nominal profile for τ_N is shown in Figure 3.13. It follows Dickinson's curve from 80-100 km and an extrapolation of his curve above that. Below 60 km our curve follows Pollack and Young's model. Between 60 and 80 we smoothly connect the two regions; the result lies along Crisp's CO_2 -only curve. Thus, the damping may be stronger in the cloud region than our profile indicates, and there may be structure in that region that we have neglected. However, the effect of a factor of two or less in τ_N at these levels is not expected to be significant since

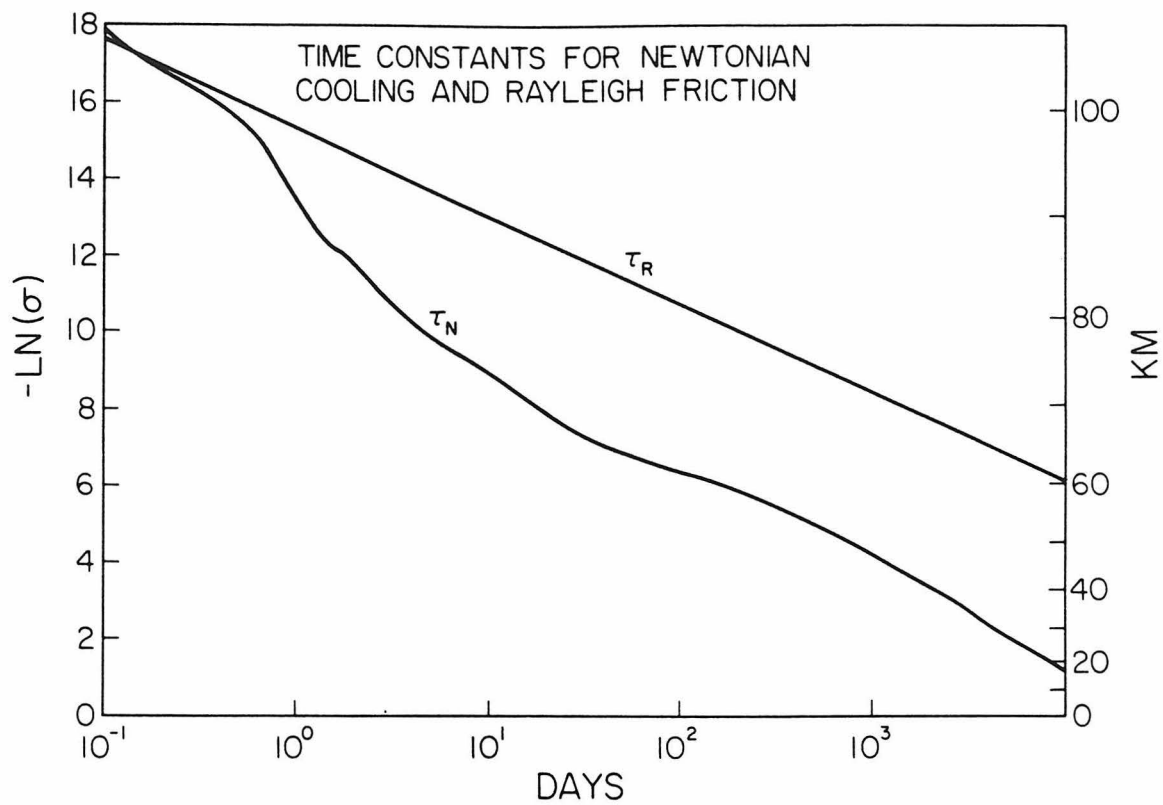


Figure 3.13 The profiles of the Newtonian cooling and Rayleigh friction time constants which will be used in all model calculations unless otherwise noted.

the solution at these levels is dominated by a propagating wave.

Also shown in Figure 3.13 is the nominal profile of τ_R , the Rayleigh friction time constant. Since the profile of τ_R has not been well constrained by models or observations, we have simply chosen $\tau_R \propto \sigma$. The sensitivity of the results to the constant of proportionality will be evaluated using the gravity wave model in section 4.5. Damping of momentum perturbations may not be very well approximated by Rayleigh friction, but including a higher order parameterization such as a diffusion term would unacceptably increase the complexity of the calculation.

3.5 Tidal Forcing

The forcing for our model is derived from the daily variation in heating due to absorption of solar radiation. Most of the absorption takes place in the upper cloud region between 60 and 70 km. Data on this absorption was obtained by the Pioneer Venus Large (or Sounder) Probe Solar Flux Radiometer (LSFR) (Tomasko et al., 1980a). The LSFR measured the net flux in the spectral region 0.4-1.8 from 65 km to the surface at a solar zenith angle of 65.7° . A model was constructed by Tomasko et al. (1980a) to estimate the globally averaged bolometric net flux from the data as shown in Figure 3.14. The results were extrapolated to the top of the atmosphere by the dashed curve. The heating rate at each level is proportional to the vertical derivative of the net flux. We assume that all the absorbed radiative energy goes directly into thermal energy.

Above the levels at which the LSFR operated, theoretical results predict large heating rates due to absorption of near infrared radiation by CO_2 (Figure 3.15) (Dickinson, 1972). Since the heating rate peaks at $400^\circ/\text{day}$, this absorption provides a significant tidal forcing. Although the heating rates are large, the amount of energy absorbed is quite small due to the low density at these altitudes.

The forcing as a function of time is resolved into a net heating and a variable component which has a zero daily mean. There is also a net cooling due to infrared radiation to space. The infrared cooling is assumed to have negligible daily variation. The globally averaged net solar heating and infrared cooling should balance unless there is a

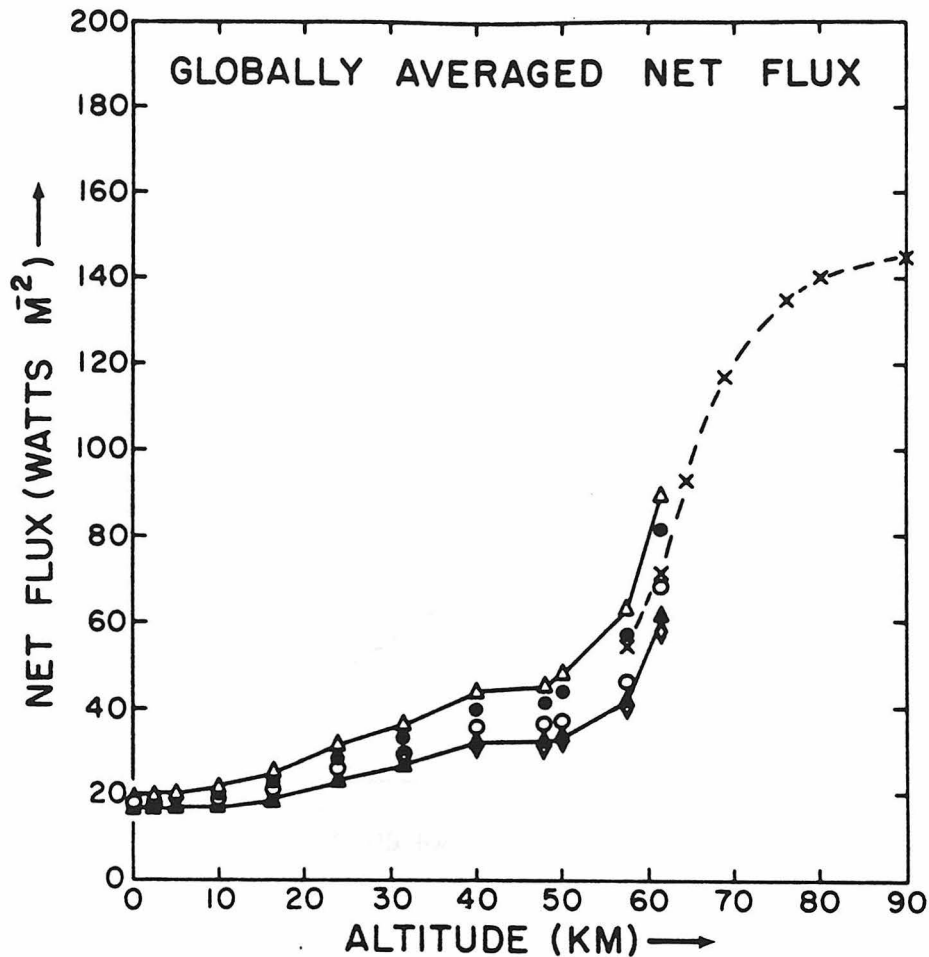


Figure 3.14 The lower curve is the bolometric, globally averaged, net solar flux according to the nominal model of Tomasko et al. (1980a). The solid triangles are based on measurements in the LSFR 0.4-1.0 μm spectral channel, while the diamonds are based on the 0.4-1.0 μm and 1.0-1.8 μm channels combined. The upper curve and the open triangles are the largest possible offset of the nominal model due to calibration errors. The solid and open circles represent intermediate calibration errors. The net flux above 65 km is modeled by Tomasko et al. (1980a) as the dashed curve and crosses. This figure is from Tomasko et al. (1980a).

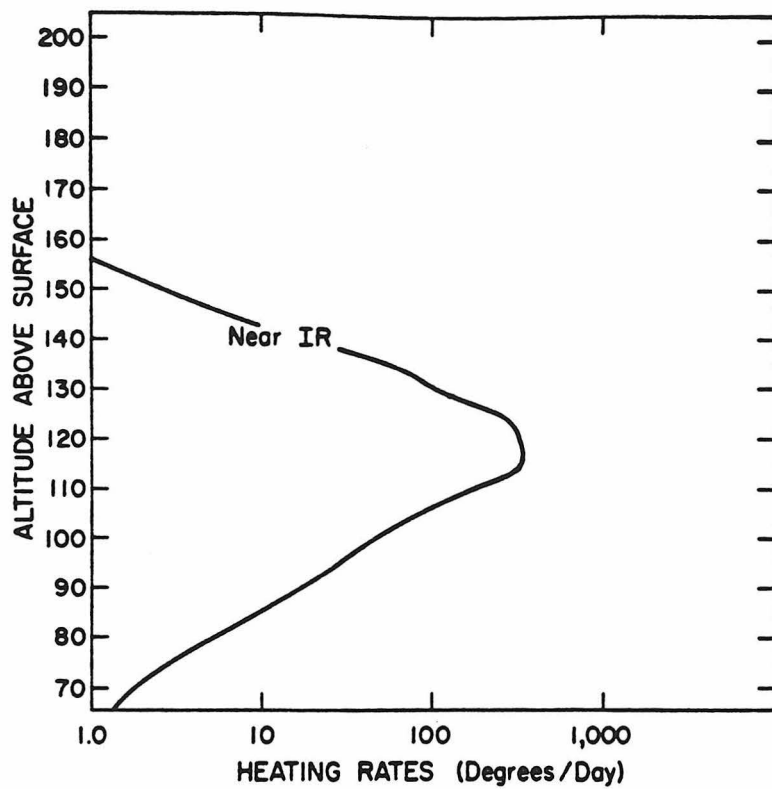


Figure 3.15 The theoretical heating rate due to absorption of solar near infrared radiation by CO_2 . This figure is from Dickinson (1972).

significant heat source in the interior of Venus or a secular warming or cooling of the atmosphere. The globally averaged thermal flux from the planet, based on OIR data, is $153 \pm 13 \text{ W/m}^2$, while the amount of sunlight absorbed is $132 \pm 13 \text{ W/m}^2$, based on a Bond albedo of $0.80 \pm .02$, also measured by the OIR (Tomasko et al., 1980b). The measurements agree within the error bars. In the model the globally averaged incoming solar flux, which determines the amplitude of the daily variation, is based on these measurements. 122 W/m^2 is absorbed in the clouds and 5.5 W/m^2 is absorbed higher in the atmosphere by CO_2 in the near infrared. 17 W/m^2 is absorbed at the ground (Tomasko et al., 1980a).

The forcing in the model is provided by the term Q' in the heat equation (2.20); its units are $\text{degrees} \cdot \text{sec}^{-1}$. The flux in W/m^2 is related to Q' as follows:

$$Q' = \frac{10^{-2}}{\rho c_p} \frac{\partial F'}{\partial z} = \frac{-g}{c_p p_s} 10^3 \frac{\partial F'}{\partial \sigma}$$

where F' is in W/m^2 , z is in km, and the other terms are in cgs units. F' is the total flux minus the zonal mean flux. The total flux is a function of the solar zenith angle, θ_s , and is approximated in this work by

$$F(\sigma, \theta_s) = \begin{cases} \bar{F}(\sigma) C_n \cos^n \theta_s & , \quad \theta_s \leq \pi/2 \\ 0 & , \quad \theta_s > \pi/2 \end{cases}$$

where $\bar{F}(\sigma)$ is the global mean flux and C_n is a normalization factor. $C_n = 2(n + 1)$. Substituting $\cos \theta_s = \cos \theta \cos \phi$, where θ and ϕ are latitude and longitude, and determining the Fourier components of the ϕ dependence gives

$$F(\sigma, \theta_s) = \bar{F}(\sigma) C_n \cos^n \theta \sum_{m=-\infty}^{\infty} C_m e^{im\phi}$$

F' is given by the same expression minus the $m = 0$ term. The sum of the $|m| = 1$ terms gives the diurnal component of the flux, the $|m| = 2$ terms give the semidiurnal component, etc.

$$C_m = \frac{1}{2\pi} \int_{-\pi/2}^{\pi/2} \cos^n \phi e^{im\phi} d\phi$$

An n of 1.6 gives the best fit to the values of Tomasko et al. (1980a) for relation between the globally averaged flux and the flux at the sounder site from the ground up to 65 km. This value for n is not based on data, but on a model of the scattering properties of the atmosphere. This is unavoidable since only one probe has measured the net flux as a function of height. At the ground, where the net flux is approximately equal to the downward flux if the surface albedo is low, n may be estimated by comparing the Pioneer Venus and Venera probe data as is done by Tomasko et al. (1980b). This gives $n = 1.7$, nearly in

agreement with the model. High in the atmosphere n should decrease until the flux becomes independent of solar zenith angle. However, since the level at which $n = 0$ is not well constrained, in our model $n = 1.6$ at all levels.

The vertical dependence of the absorption in the clouds measured by the LSFR was fit to an analytic expression for use in the model. The formula chosen was

$$\frac{\partial \bar{F}}{\partial \sigma} = \frac{C}{(1 + \sigma/\sigma_0)^r}$$

C , σ_0 , and r are free parameters. The corresponding heating rate is nearly constant high in the atmosphere, decreases rapidly below the clouds, and is nearly zero in the lower atmosphere. Since the data are in terms of \bar{F} (Figure 3.14), the above expression was integrated to yield

$$\Delta \bar{F} = \bar{F}(0) - \bar{F}(\sigma) = \frac{C\sigma_0}{-r+1} [1 - (1 + \sigma/\sigma_0)^{-r+1}]$$

The parameters C , σ_0 , and r were determined by a brute force nonlinear least squares fit to $\Delta \bar{F}$. The LSFR values for \bar{F} and $\Delta \bar{F}$ are given in Table 3.2 along with the best fit analytic $\Delta \bar{F}$. For the best case $C = -.902145 \times 10^5$, $\sigma_0 = .122096 \times 10^{-2}$, and $r = 1.9$.

A net flux of 17 W/m^2 at $z = 0$ is absorbed by the ground (Tomakso, et al., 1980a). This absorption will heat the surface which will, in turn, heat the atmosphere in contact with it. The heat will then be distributed over the lower atmosphere by convection, radiation,

TABLE 3.2

SOLAR FLUX, \bar{F} , and $\Delta\bar{F} = \bar{F}(95) - \bar{F}(z)$ in W/m^2

Altitude, km	\bar{F} from LSFR*	$\Delta\bar{F}$ from LSFR	$\Delta\bar{F}$ from model
0	17	125	122
5	17	125	122
10	17	125	122
15	17	125	122
20	18	124	121
25	23	119	121
30	26	116	120
35	29	113	119
40	32	110	117
45	33	109	113
50	33	109	107
55	38	104	97
60	59	83	77
65	100	42	51
70	118	24	25
75	128	14	11
80	136	6	4
85	140	2	1
90	142	0	0
95	142	0	0

*LSFR data are from Figure 17 of Tomasko et al. (1980). (Figure 3.14 of this thesis)

and/or conduction. This heat will also contribute to the tidal forcing. Unfortunately, not enough is known about the state of the lower atmosphere to constrain its distribution very well. We have studied its effect in various cases in the gravity wave program. If the stability near the ground is low, as in our nominal basic state, the propagation of the tidal disturbance into the upper layers is weak. Also, if the heating is confined to the lowest level in the model, the tidal response falls off rapidly with height independent of the stability. Thus, the heating at the ground has been omitted under the assumption that it would not affect the solution at the clouds and above. However, this heating is important locally so our solution is incomplete in the lowest layers.

Another important component in the tidal forcing is due to absorption of solar near-infrared radiation by CO_2 . According to Dickinson (1972) the heating rate due to this absorption has the vertical dependence shown in Figure 3.15. It reaches a peak of about 400K/day at 120 km and appears to fall off exponentially above and below that. However, assuming that the fall off is exponential over the entire atmosphere leads to a total absorption of 3600 W/m^2 ! Since the actual absorption must be much less than this, a better representation for the vertical dependence is

$$\frac{\partial \bar{F}}{\partial \sigma} = C_e^{-\{|\mathcal{Z} - \mathcal{Z}_0|/d\}^n}$$

where \mathcal{Z} is in $-\ln \sigma$ units; \mathcal{Z}_0 is $-\ln \sigma$ at 120 km. If $C = -3.54 \times 10^6 \text{ W/m}^2$, then the heating rate is 400 K/day at 120 km. Values

of 3.1 for d and 1.5 for n were chosen to give a good fit to the curve in Figure 3.15 below 120 km and to give a total absorption of about $5W/m^2$.

CHAPTER 4

RESULTS OF THE VENUS TIDAL CALCULATIONS

4.1 Introduction

The most important results of our model for Venus atmospheric thermal tides are an explanation of the unusual aspects of the Pioneer Venus orbiter infrared radiometer (OIR) tidal data and an estimate of the effects of the tides on the mean state of the atmosphere.

The ability of the model to reproduce the OIR tidal amplitudes and phases, which is discussed in Section 4.2, increases our confidence in the validity of the model input parameters described in the previous chapter and in the validity of the model itself. Most of the input parameters for the basic state, forcing, and damping were based on temporally and spatially limited data or theoretical models. Since the tides are a global scale phenomenon, the success of the model gives support to the assumptions that the model inputs are not significantly affected by transient or local perturbations and that the models also adequately represent globally averaged conditions. Since studies other than ours rely on these assumptions, independent work which supports their validity is important.

The output of the model can be used to understand some aspects of the OIR tidal data which could not be easily explained by classical tidal theory. This is interesting and important because the model calculations reveal the true nature of Venus thermal tides, which was not at all evident in the OIR data. The puzzling OIR results, which are described in Section 4.2, arose because of the low vertical resolution of the experiment. Its resolution is low due to the 10 km width of the

weighting functions. Our model calculations have much higher vertical resolution, which when degraded to the OIR level, reproduce the OIR results. At the end of Section 4.2 our results are checked for consistency with data from other Pioneer Venus experiments.

In Section 4.3 we discuss the sensitivity of the OIR weighting functions to changes in the cloud properties. The weighting functions of the two lowest OIR channels are affected by the height distribution of cloud particles. The cloud properties are not well constrained by observations. A good fit of our model results to the OIR data is obtained with a cloud in the mid range of those allowed by the observations. However, the fit is not unique since other combinations of cloud properties also give good results.

The agreement of the model solution and the OIR data is meaningful only if the convergence and spatial resolution of the model are adequate. In Section 4.4 an evaluation of these model properties is presented. Several areas of weakness exist, but in general the model is numerically sound.

The important question of the model's sensitivity to changes in the input parameters is discussed in Section 4.5. The sensitivity study was done primarily using the gravity wave model. It is shown that the results of the gravity wave model and the full model are analogous for the same input parameters. The general properties of the tidal fields are unaffected by large changes in the input parameters, but the details of the solutions are often quite sensitive.

The ultimate goal of this research was to ascertain whether the tides make a significant contribution to maintaining the basic state of

the atmosphere. Since our model is linear, to first order the tides have no mean affect. However, second order transports of energy and momentum can be calculated from the tidal perturbations. These results are presented in Section 4.6. The tidal transports compete for dominance with those due to eddies other than the tides and the mean meridional circulation. The net effect of all these together must be to maintain the high zonal winds against friction and to keep the latitudinal temperature gradient small. The other eddies, of course, have been omitted in this study. However, we have solved for the net effect of the tides and the mean meridional circulation. The mean meridional circulation is forced mainly by the latitudinal gradient in the mean solar heating, but is modified by the presence of the tides. Our calculations show that the magnitude of the zonal angular momentum flux due to the tides is several times larger than that due to dissipation. The dissipative term was based on several estimates of the eddy viscosity. Even though the magnitude of the tidal terms is certainly large enough for them to have an effect on the mean zonal wind, the profile of the tidal accelerations with height is not such that it transports momentum into the core of the jet as required. The same is true of the accelerations due to the mean circulation, although these calculations are very uncertain. Thus, it seems likely that other eddies play an important role in maintaining the rapid rotation of the atmosphere, although the tides and the mean circulation cannot be neglected.

4.2 Comparison of Model Tides with Observations

A determination of the solar fixed component of the variable brightness temperature has been obtained from the Pioneer Venus OIR data by Taylor et al. (1980) and Elson (1982). In this section, after a brief discussion of the OIR instrument data analysis, a comparison of this determination with the model results for the solar thermal tides is presented. The vertical dependence of the OIR tidal amplitudes and phases is explained in light of the model results. Finally, our model results are compared with other relevant data sets.

4.2.1 The OIR Data:

The OIR measures the brightness temperature in five infrared spectral channels. The spectral passbands of these channels are in parts of the spectrum with different amounts of absorption due to CO_2 so that each channel samples a different altitude range. The tidal signal in the OIR data is determined by Fourier analyzing the brightness temperatures with respect to solar-fixed longitude. The results are the diurnal and semidiurnal amplitudes and phases as a function of latitude with some information about the vertical dependence. These results were obtained by Taylor et al. (1980) for a preliminary data set and by Elson (1982) for the final, much larger, data set.

The channels for which tidal data are available are channels 2-5 and the 'high sieve' component of channel 1. The weighting functions for these channels, which represent the sensitivity of the detectors as a function of altitude, are shown in Fig. 4.1. Channels 2-4 are located within the 667 cm^{-1} ($15 \mu\text{m}$) band of CO_2 and are about 10 cm^{-1} wide. They are sensitive to the altitude range 70-90 km with weighting

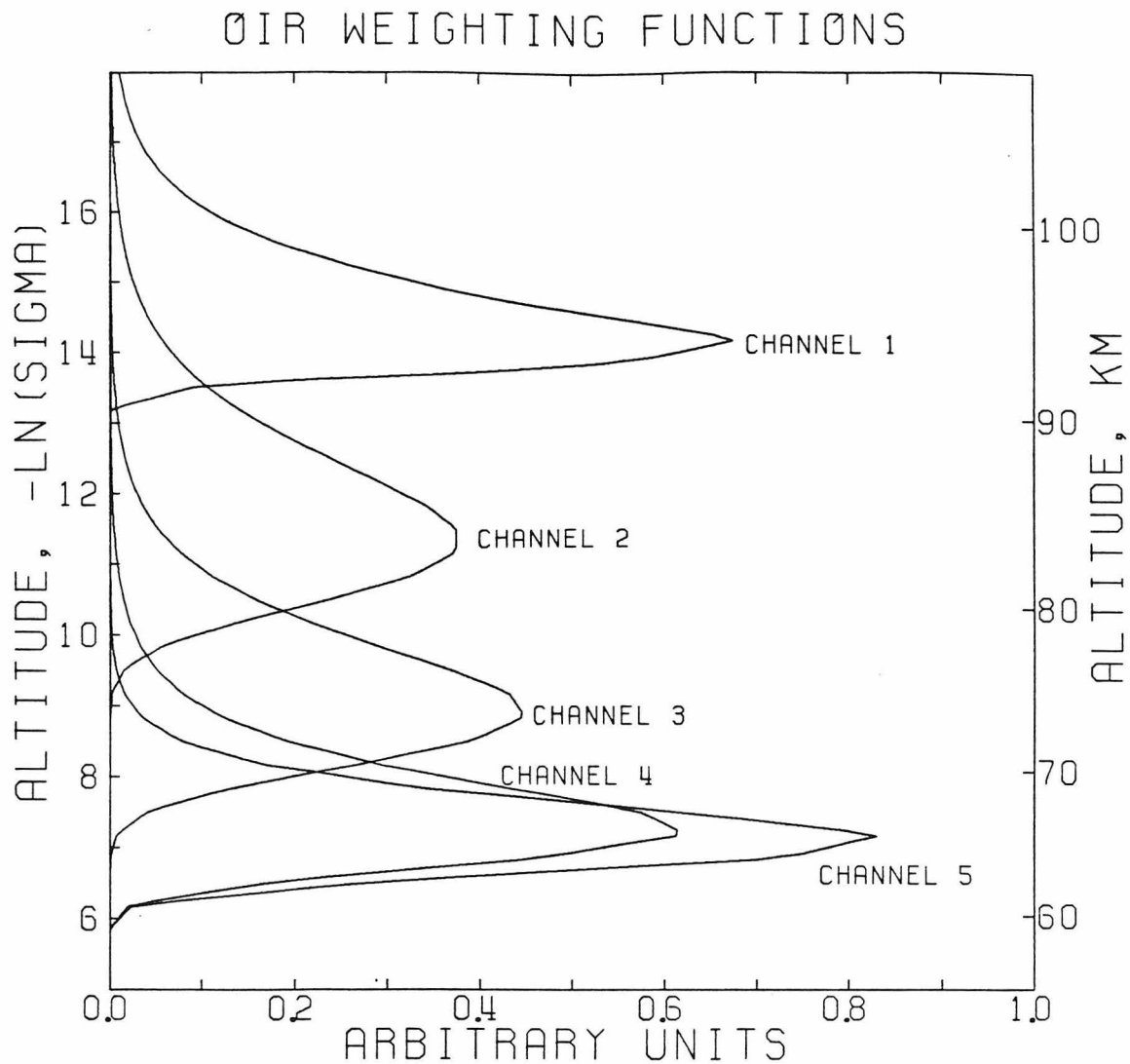


Figure 4.1 Weighting functions used to obtain model brightness temperatures in the OIR channels. A table of weighting function values was provided by L. Elson (personal communication, 1982).

function widths such that each channel measures the mean temperature in a 10 km layer. The weighting function of the lowest channel in this group, channel 4, is somewhat affected by cloud opacity. In channels 2 and 3 only CO₂ opacity is important. Channel 5 is located in a window of low CO₂ absorption at 11.5 μm and is sensitive to temperatures near the cloud tops. The channel 5 weighting function depends on the height of optical depth unity of the cloud particles and on the scale height of the cloud particles. The weighting function for the 'high sieve' component of channel 1 (which will be referred to simply as channel 1) peaks at about 100 km.

Elson (1982) Fourier analyzed the brightness temperatures from channels 2-5 into diurnal and semidiurnal amplitudes and phases vs. latitude. These recent results are more reliable than those in Taylor et al. (1980) because the final data set included more observations and had improved geometry. The data were averaged over 1° latitude bins, but were Fourier analyzed without binning in longitude. Limb darkening effects were removed by an empirical polynomial technique. The results for channel 1 in Taylor et al. (1980) were obtained by averaging the data in 500 km square bins before Fourier analysis of the channel 1 brightness temperatures. Limb darkening effects were not removed. Therefore the results for channel 1 must be considered more uncertain.

The OIR tidal results for channels 2-5 (Elson, 1982) are shown in Figs. 4.2-4.9. These figures contain plots of brightness temperature amplitude and phase versus latitude for both the diurnal and semidiurnal tide. Curves from the nominal tidal model of this thesis are shown also. In Tables 4.1-4.4 observed and model values for amplitude and

phase of the brightness temperature variation are given at two latitudes for a quantitative comparison. In the tables and plots phase is given in terms of the time of maximum temperature. These times are local solar times on Venus. An 'hour' is 1/24 of the distance around the planet. Since the rotation rate varies with height, the time interval of an 'hour' of local time will also vary with height. Semidiurnal maxima occur twice a day so the phases are conveniently given in the tables in terms of an ordinary 12-hour clock. Diurnal phases are given in terms of a 24-hour clock.

4.2.2 Model Brightness Temperatures:

The model brightness temperatures were obtained by first calculating infrared radiances at the appropriate frequency for each channel from the model temperature, $T^*(\sigma) + T_1(\sigma, \lambda) + T'(\sigma, \lambda, \phi)$. $T'(\sigma, \lambda, \phi)$ consists of the diurnal and semidiurnal tidal temperature perturbation. For each channel the radiance at a given latitude and longitude was convolved with the weighting function, and the result was converted to a brightness temperature. Then, at each latitude the brightness temperature as a function of ϕ was Fourier analyzed to give the diurnal and semidiurnal amplitude and phase. It is necessary to perform this Fourier analysis because the radiance is a nonlinear function of the temperature. The weighting functions used are shown in Fig. 4.1 (Taylor et al., 1980; Elson, written communication, 1982). The weighting functions for channels 4 and 5 were calculated for a cloud that reaches optical depth unity at 100 mb (about 65 km) with a cloud scale height of 0.4 times the gas scale height.

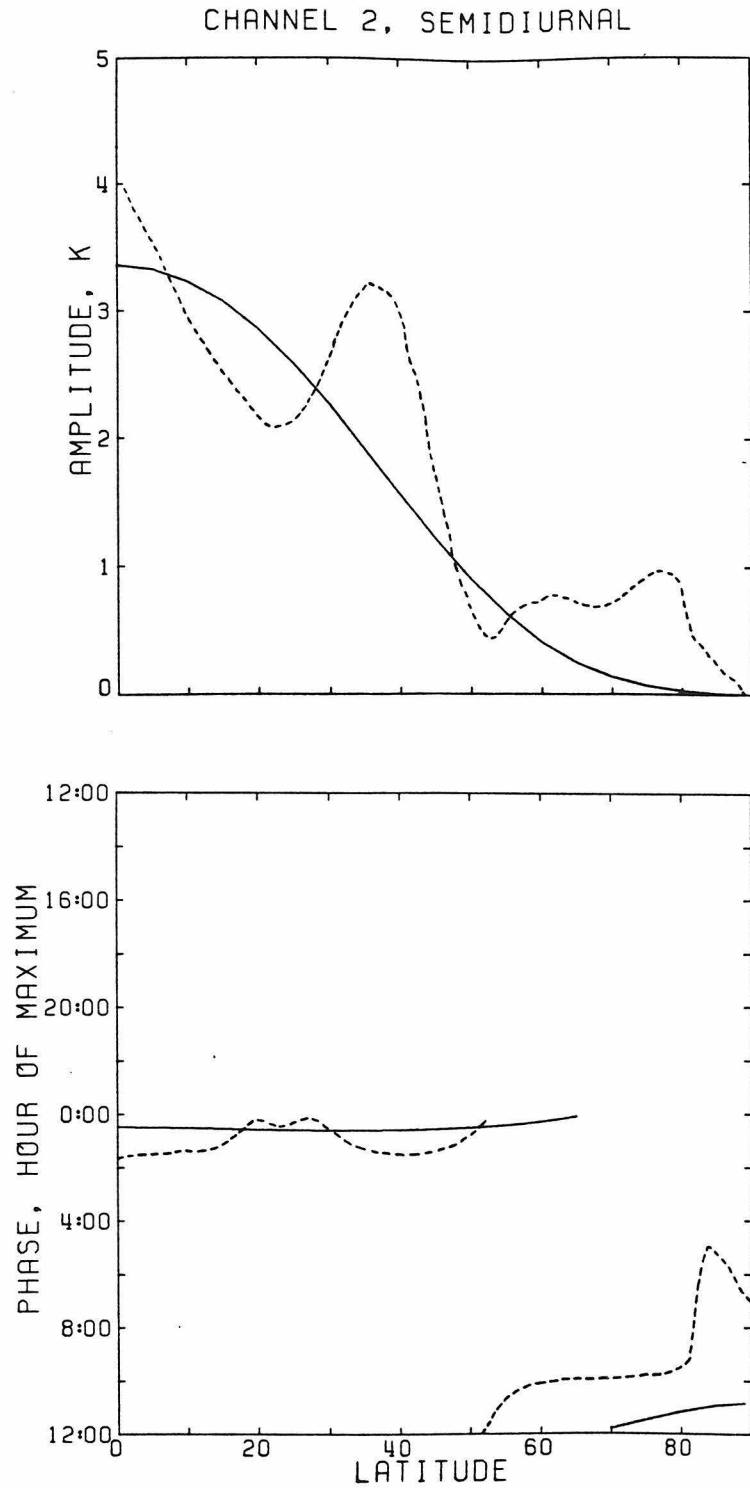


Figure 4.2 Semidiurnal amplitude and phase in OIR Channel 2 from the LPE model (solid curve) and the OIR brightness temperatures (dashed curve). Fourier analysis of the OIR data was done by Elson (1982).

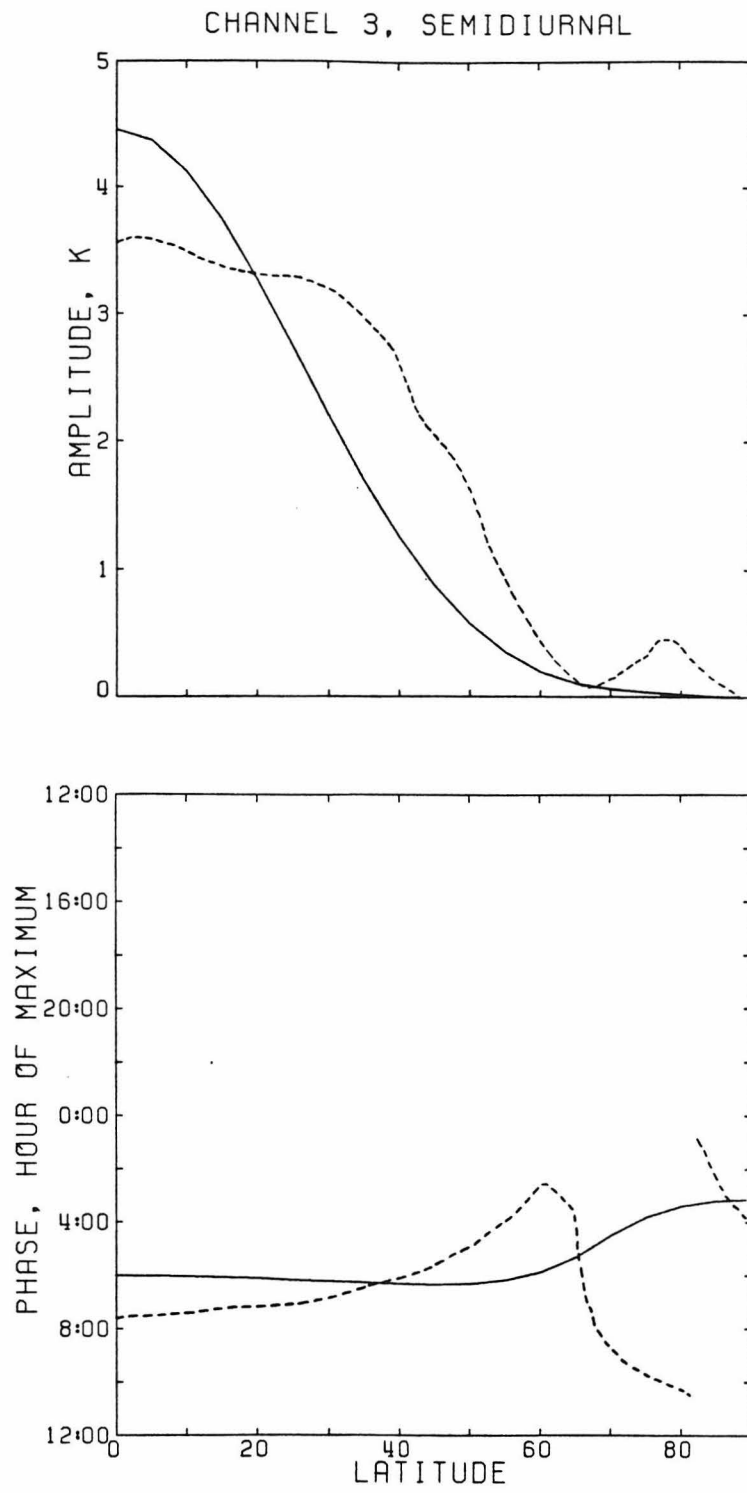


Figure 4.3 Same as Fig. 4.2 for OIR Channel 3.

CHANNEL 4, SEMIDIURNAL

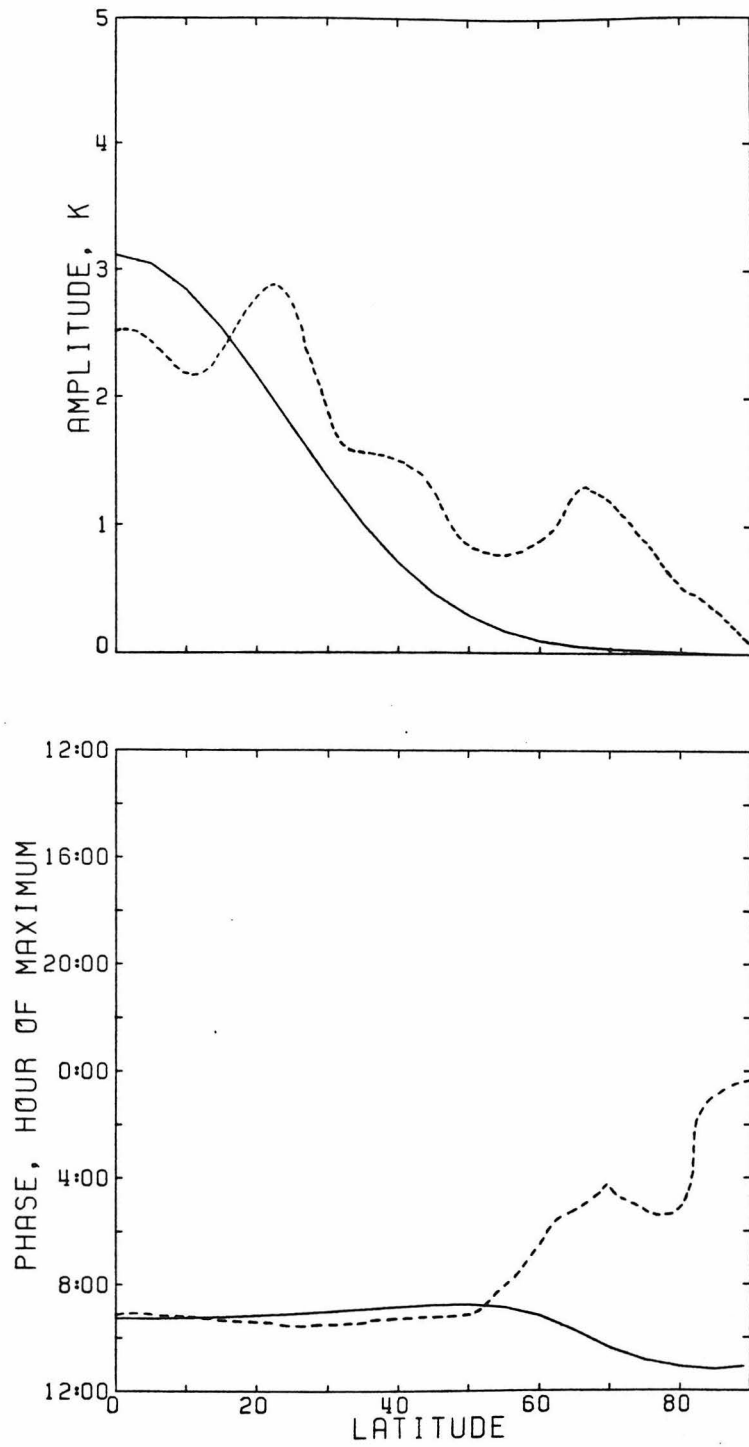


Figure 4.4 Same as Fig. 4.2 for OIR Channel 4.

CHANNEL 5, SEMIDIURNAL

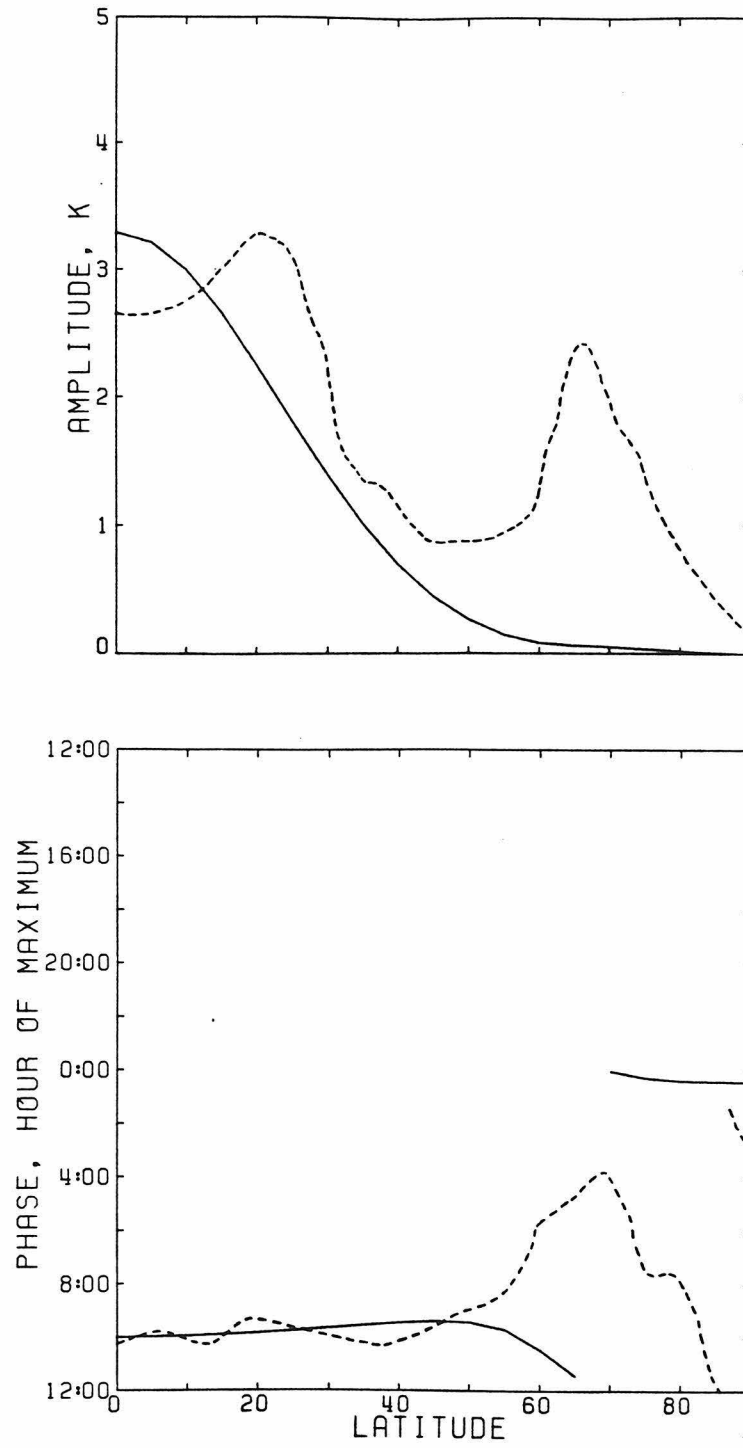


Figure 4.5 Same as Fig. 4.2 for OIR channel 5.

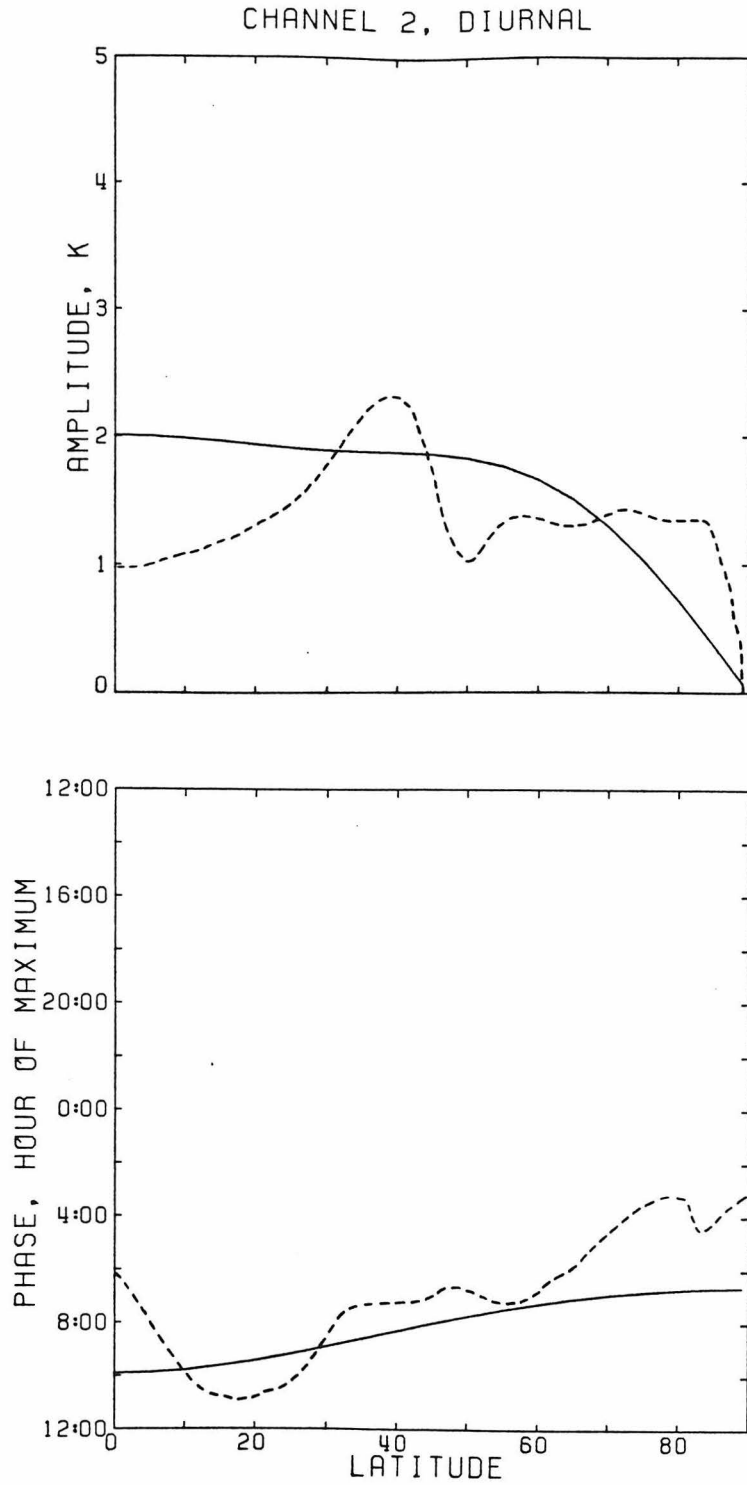


Figure 4.6 Diurnal amplitude and phase in OIR Channel 2 from the LPE model (solid curve) and the OIR brightness temperatures (dashed curve). Fourier analysis of the OIR data was done by Elson (1982).

CHANNEL 3, DIURNAL

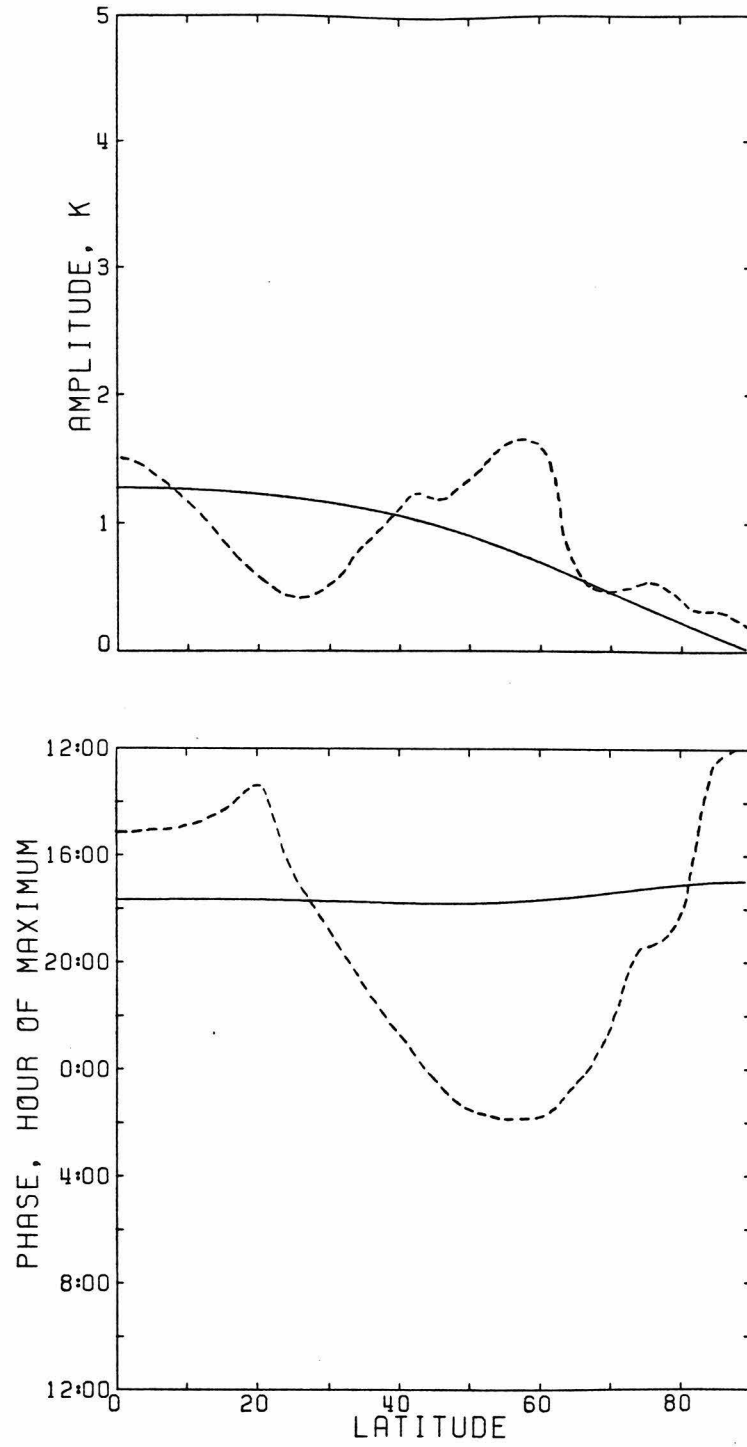


Figure 4.7 Same as Fig. 4.6 for OIR Channel 3.

CHANNEL 4, DIURNAL

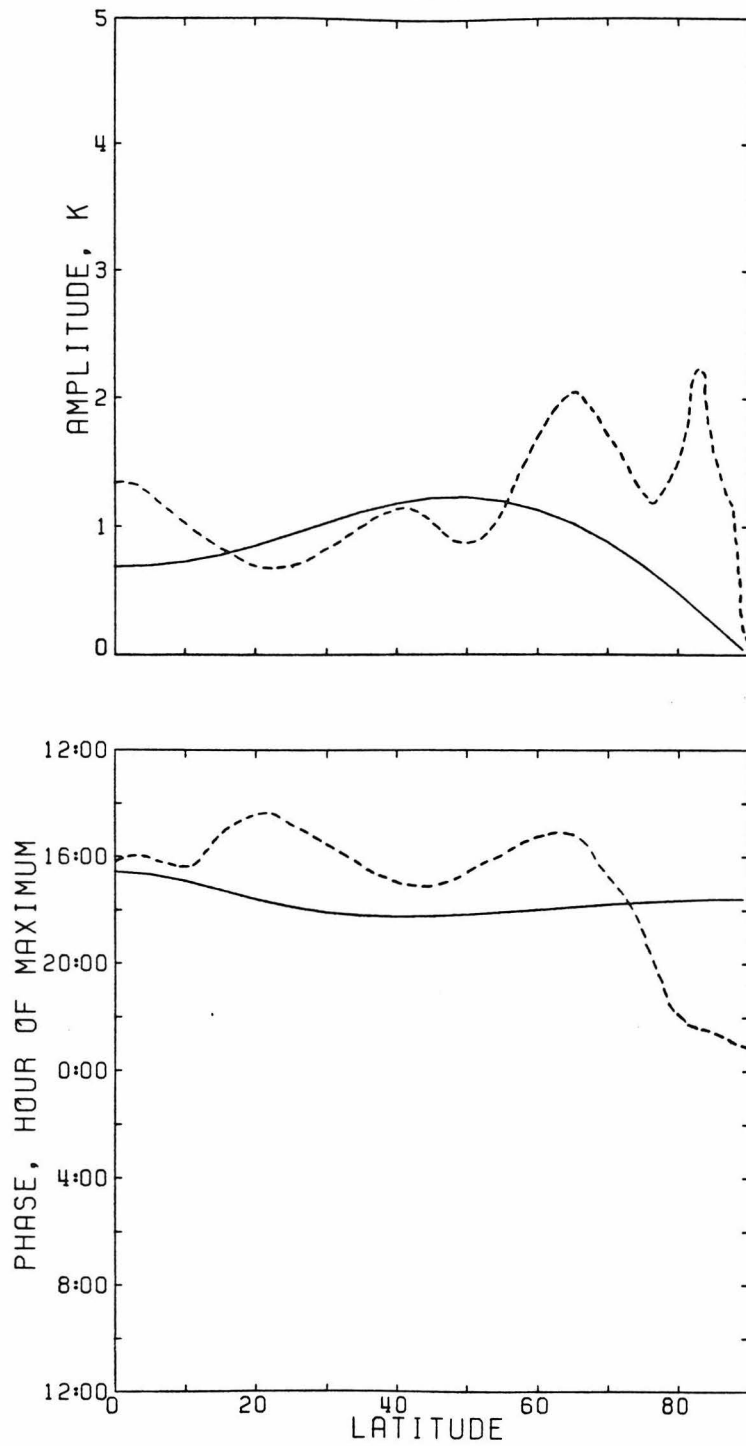


Figure 4.8 Same as Fig. 4.6 for OIR Channel 4.

CHANNEL 5, DIURNAL

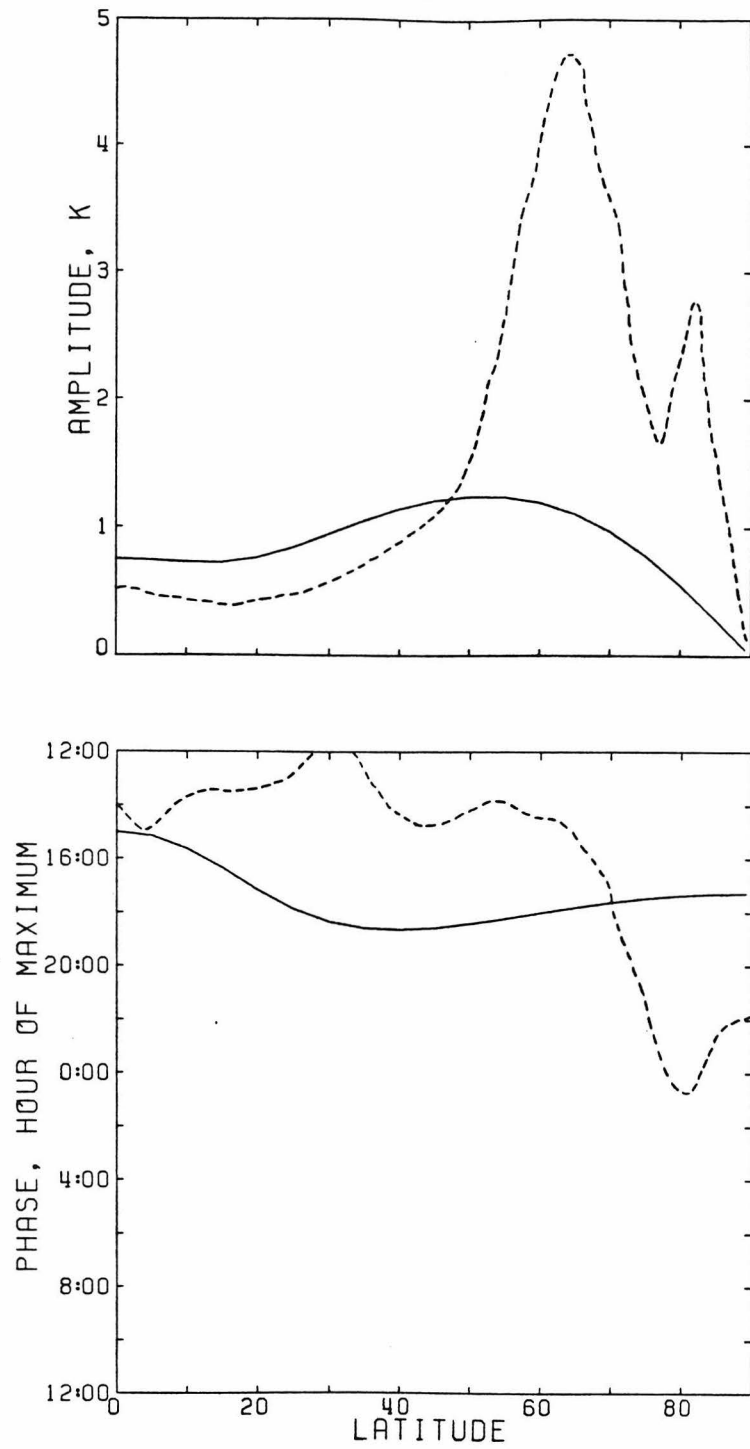


Figure 4.9 Same as Fig. 4.6 for OIR Channel 5.

TABLE 4.1

SEMIDIURNAL TIDE AT THE EQUATOR

CHANNEL	HEIGHT	AMPLITUDE, DEG		PHASE, HOUR OF MAX	
		OIR	MODEL	OIR	MODEL
1	100 km	6.0	4.9	12:00	11:58
2	90 km	4.0	3.5	1:40	12:27
3	80 km	3.7	4.4	7:40	5:54
4	70 km	2.5	3.1	9:00	9:16
5	cloud tops	2.6	3.3	10:00	10:00

TABLE 4.2

SEMIDIURNAL TIDE AT 40°

CHANNEL	HEIGHT	AMPLITUDE, DEG		PHASE, HOUR OF MAX	
		OIR	MODEL	OIR	MODEL
1	100 km	3.7	3.0	1:00	11:57
2	90 km	2.9	1.5	1:40	12:29
3	80 km	2.6	1.2	6:15	6:11
4	70 km	1.5	.7	9:15	8:49
5	cloud tops	1.2	.7	10:00	9:26

TABLE 4.3

DIURNAL TIDE AT THE EQUATOR

CHANNEL	HEIGHT	<u>AMPLITUDE, DEG</u>		<u>PHASE, HOUR OF MAX</u>	
		OIR	MODEL	OIR	MODEL
1	100 km	10.0	17.4	10:00	11:59
2	90 km	1.0	2.0	6:00	9:48
3	80 km	1.5	1.3	15:00	17:36
4	70 km	1.3	0.7	16:00	16:34
5	cloud tops	0.5	0.7	14:00	15:00

TABLE 4.4

DIURNAL TIDE AT 40⁰

CHANNEL	HEIGHT	<u>AMPLITUDE, DEG</u>		<u>PHASE, HOUR OF MAX</u>	
		OIR	MODEL	OIR	MODEL
1	100 km	8.0	12.8	10:00	11:59
2	90 km	2.3	1.9	7:15	8:16
3	80 km	1.1	1.0	22:45	17:44
4	70 km	1.2	1.2	17:00	18:14
5	cloud tops	0.9	1.1	14:15	18:39

From Figs. 4.2-4.9 it may be noted that the agreement between the model and the data is best between the equator and about 50° latitude. Poleward of 50° there is a tendency for there to be more structure in the data than in the model. Since the nominal model was run with only the three lowest order terms in the Legendre expansion, this is not too surprising. There is probably also latitudinal dependence in the mean zonal wind and temperature profiles that was not included in the model. Even with these restrictions, however, in many cases the model curves show a general trend which is consistent with the data at higher latitudes. See, for example, the diurnal amplitude in channels 4 and 5 (Figs. 4.8 and 4.9) and the semidiurnal phase in channel 2 (Fig. 4.2). It is probable that fine tuning model parameters and inclusion of additional latitudinal structure in the basic state and tidal fields would result in closer agreement between the model and the data. However, the expense of the computing time required for such a study is prohibitive, and the data does not warrant it. First, parameters of the basic state and solar forcing are somewhat uncertain. Second, although it is difficult to determine error bars for the data, near the equator the amplitudes are probably accurate to within one or two degrees, and the phase is good to an hour or two (Elson, personal communication, 1982). The accuracy is better in the polar regions because of better OIR coverage. Thirdly, the OIR weighting functions are uncertain, especially in channels 4 and 5, so the brightness temperatures derived from the model are equally uncertain.

Perhaps the best argument for not striving to achieve the best possible agreement with the data is the fact that the actual tidal

profiles are not as sensitive to the input parameters as the brightness temperature amplitudes and phases derived from them. As shown in Section 4.5, changes in the basic state and solar forcing which do not alter the tidal solution significantly may have a relatively large effect on the brightness temperature amplitude and phase. Therefore, the conclusions we draw about the significance of tides in the Venus atmosphere are not likely to be affected by the changes in the input parameters which would be required to match the data exactly.

The tidal temperatures calculated by the model are shown in Figs. 4.10-4.13. Diurnal and semidiurnal amplitudes and phases are plotted at the equator and 40° . These tidal temperatures are from the same case used to calculate the model brightness temperature amplitudes and phases shown in Figs. 4.2-4.9 and Tables 4.1-4.4. The points on the figures give the values at each level of the vertical grid, thus giving a rough idea of the adequacy of the vertical resolution. The grid points are equally spaced in $-\ln \sigma$. A summary of the numerical parameters in the nominal model is given in Table 4.5. The basic state was described in Chapter 3.

4.2.3 Semidiurnal Temperature Variations:

The amplitude and phase of the semidiurnal tidal temperature perturbations revealed in Figs. 4.10 and 4.11 could not be determined from the information in Tables 4.1 and 4.2 alone. In fact, the nature of the brightness temperature perturbations in the 5 OIR channels led to some very puzzling interpretations. Since the phase does not change much in the lowest 3 channels, it was thought that the tide did not propagate in this region (Taylor et al, 1980). There are four

TABLE 4.5

	DIURNAL	SEMIDIURNAL
NUMBER OF VERTICAL POINTS	218	110
TOP OF RESOLVED REGION (IN $-1n\sigma$)	18	18
NUMBER OF TERMS IN LEGENDRE EXPANSION	3	3
NUMBER OF POINTS IN GAUSSIAN LATITUDE GRID	7	7
TIME STEP	14400sec.	7200 sec.
NUMBER OF TIME STEPS	1200	1600

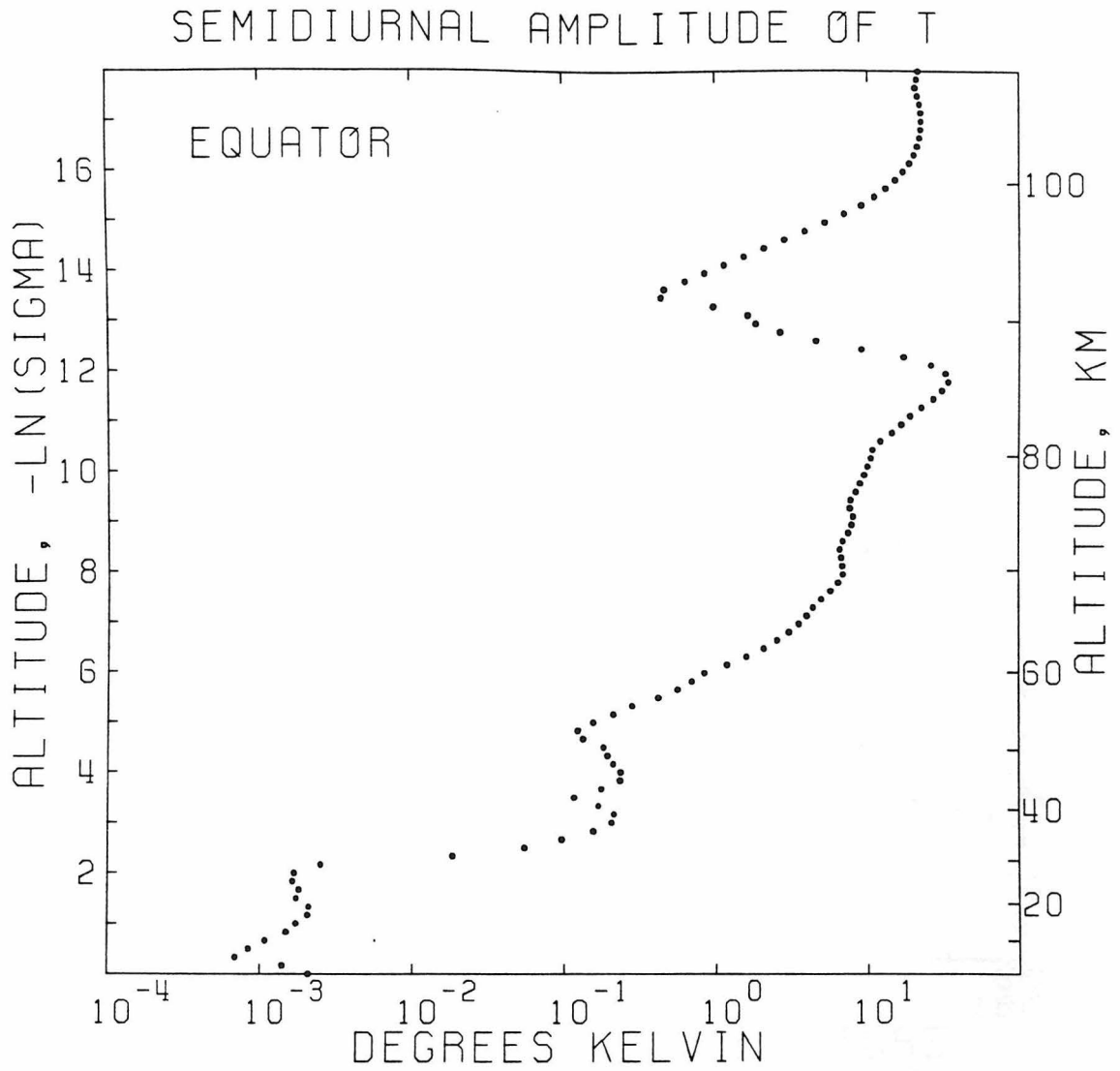


Figure 4.10a Semidiurnal amplitude at the equator of the tidal perturbation in the temperature as predicted by the LPE model.

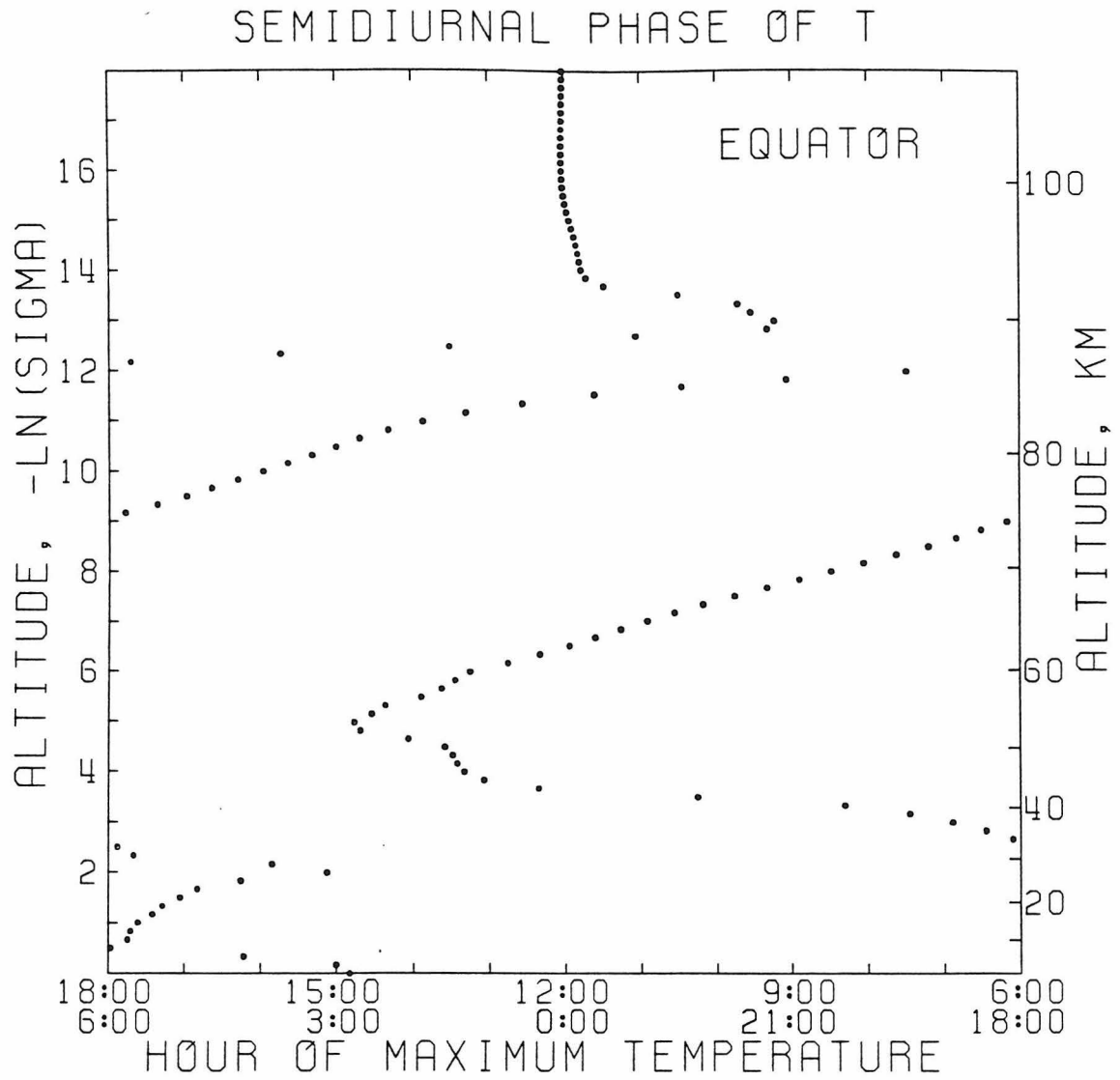


Figure 4.10b Semidiurnal phase at the equator of the tidal perturbation in the temperature as predicted by the LPE model.

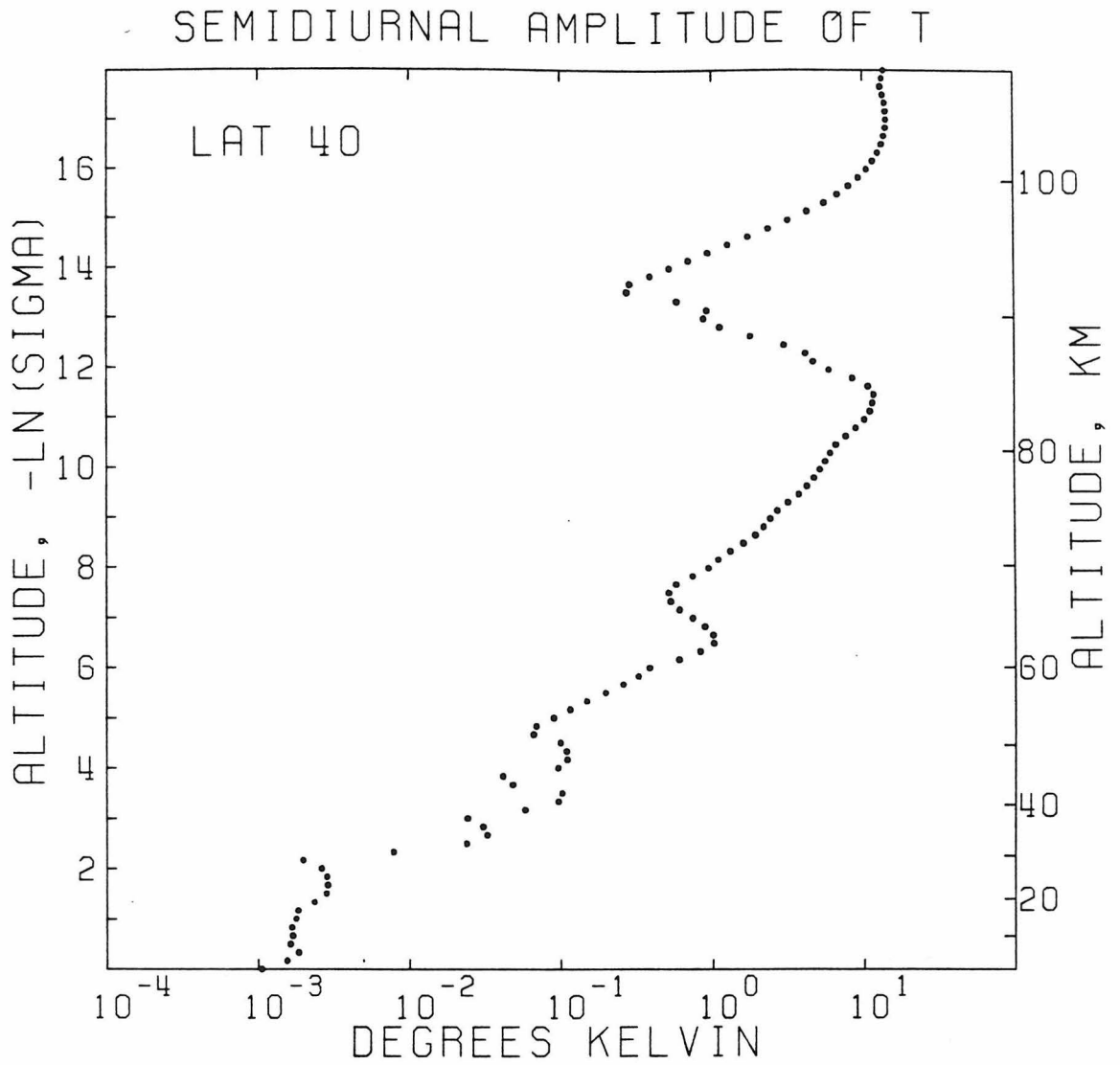


Figure 4.11a Semidiurnal amplitude at 40° of the tidal perturbation in the temperature as predicted by the LPE model.

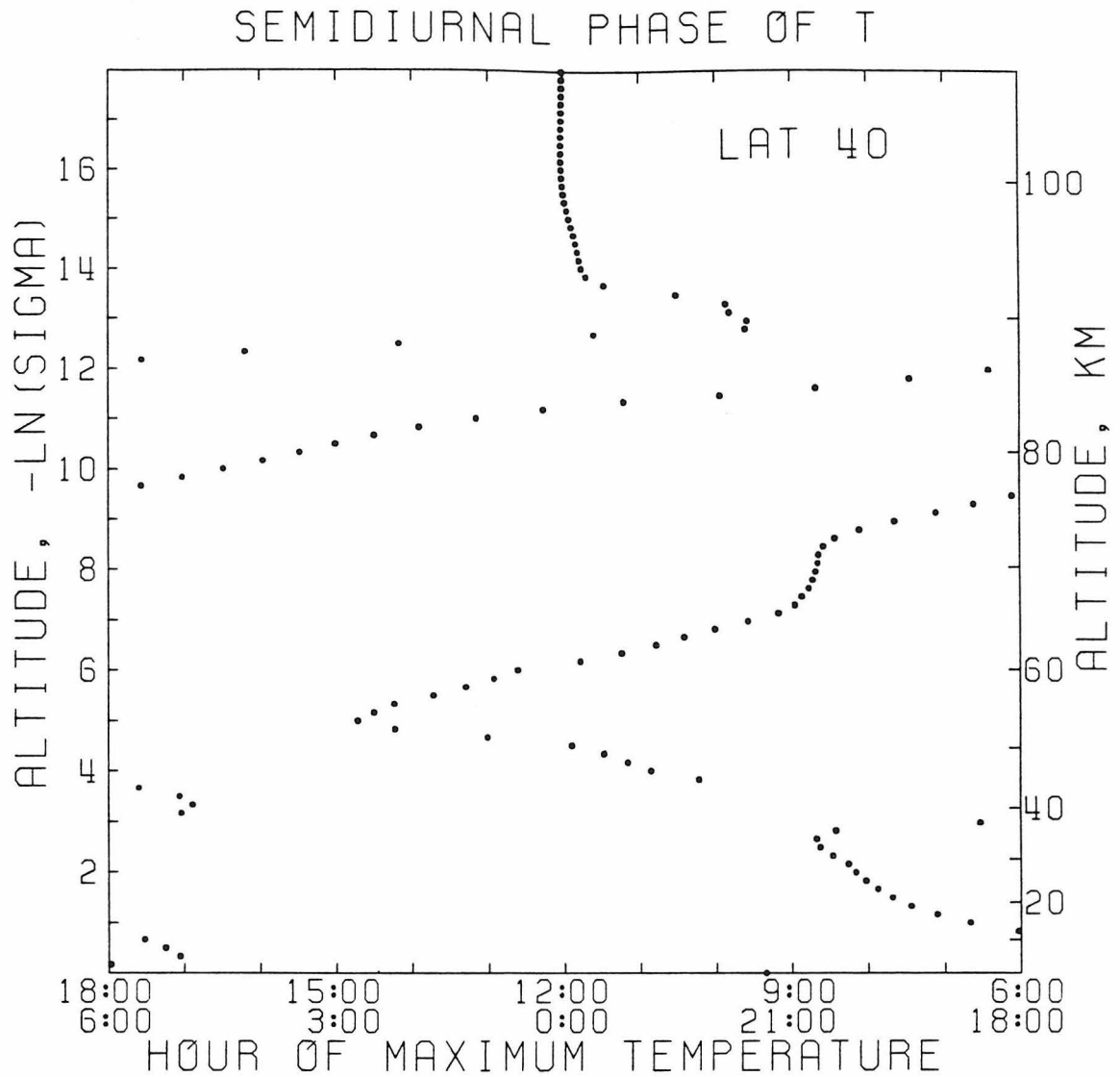


Figure 4.11b Semidiurnal phase at 40° of the tidal perturbation in the temperature as predicted by the LPE mode.

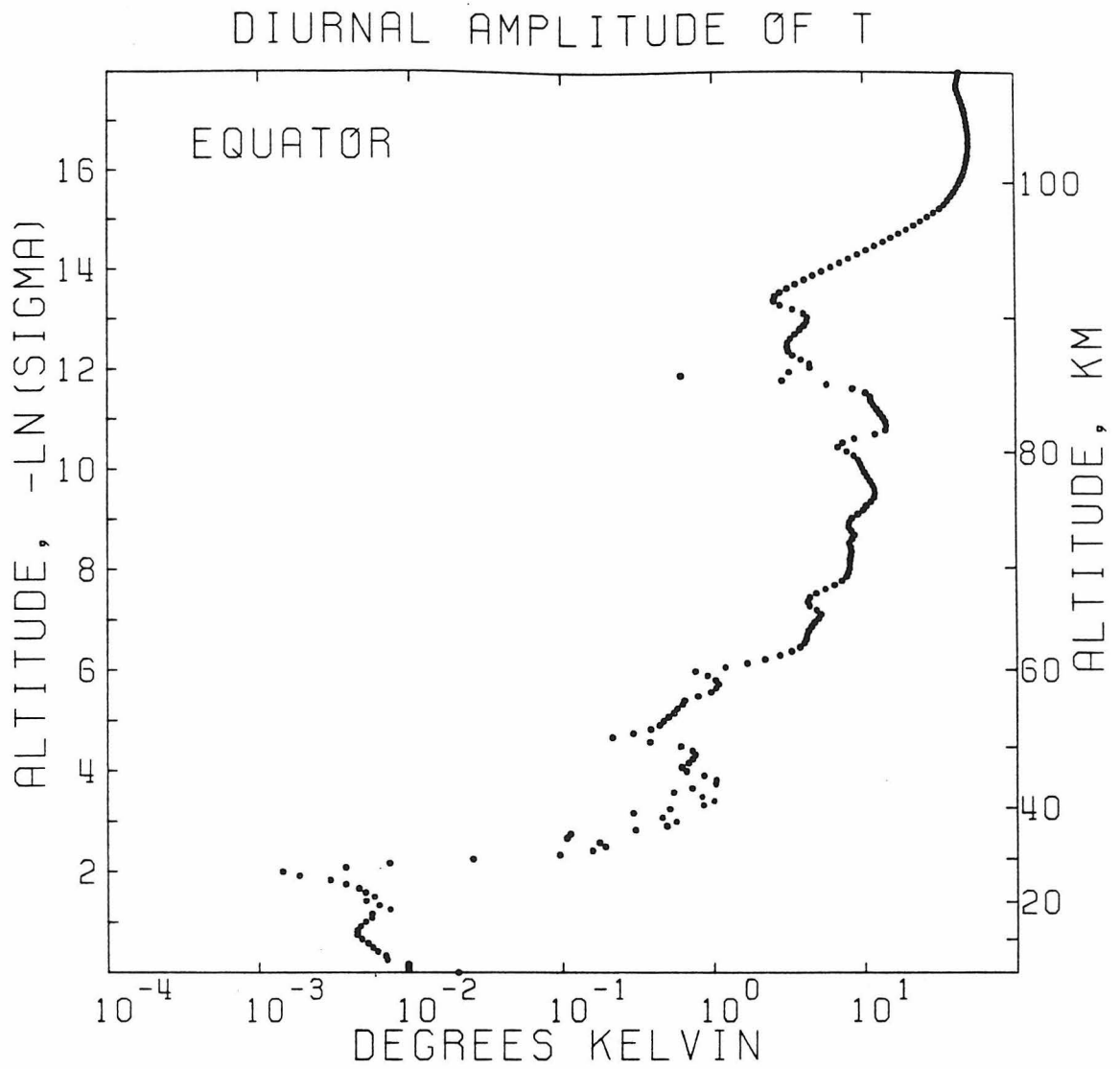


Figure 4.12a Diurnal amplitude at the equator of the tidal perturbation in the temperature as predicted by the LPE model.

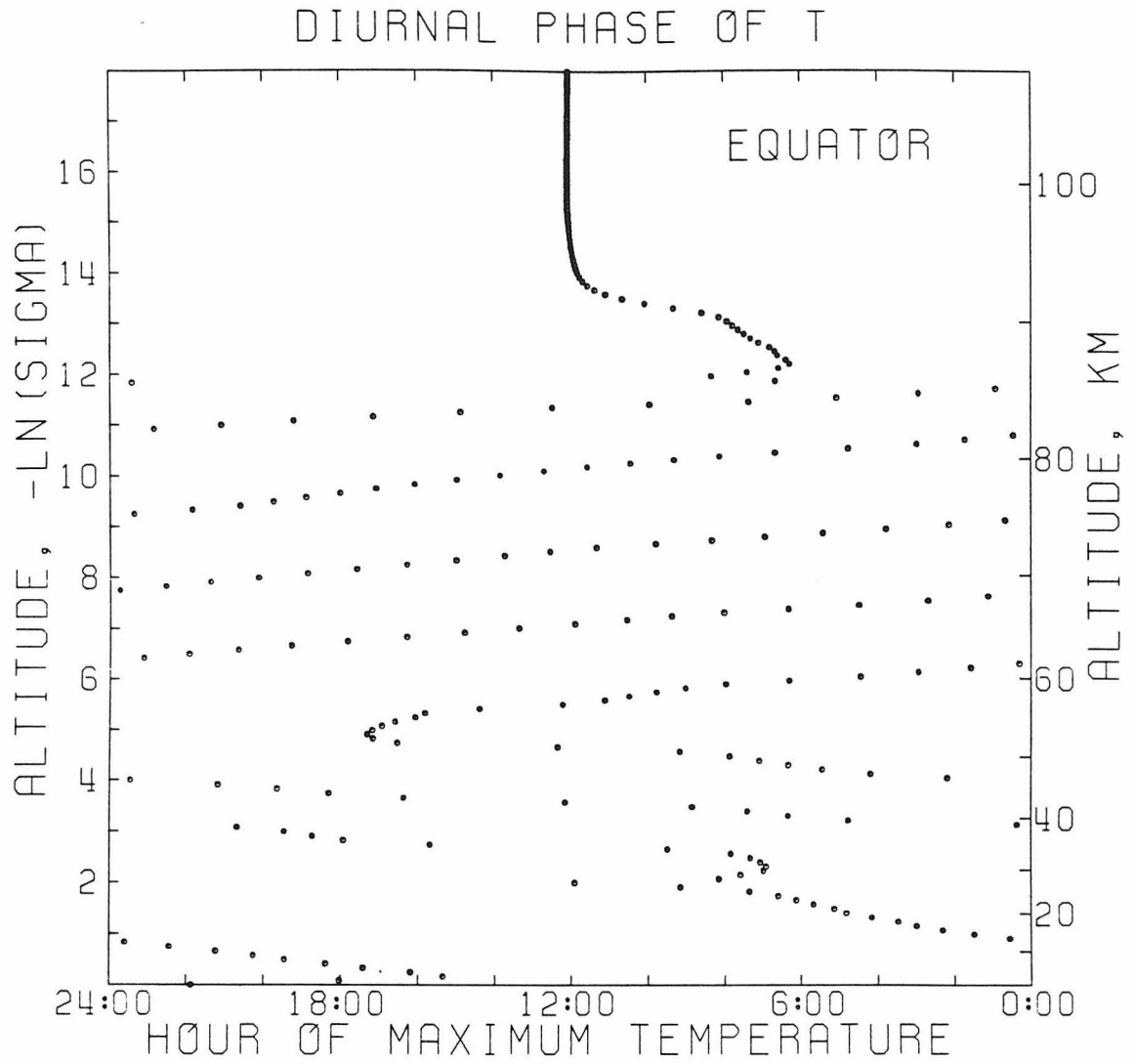


Figure 4.12b Diurnal phase at the equator of the tidal perturbation in the temperature as predicted by the LPE model.

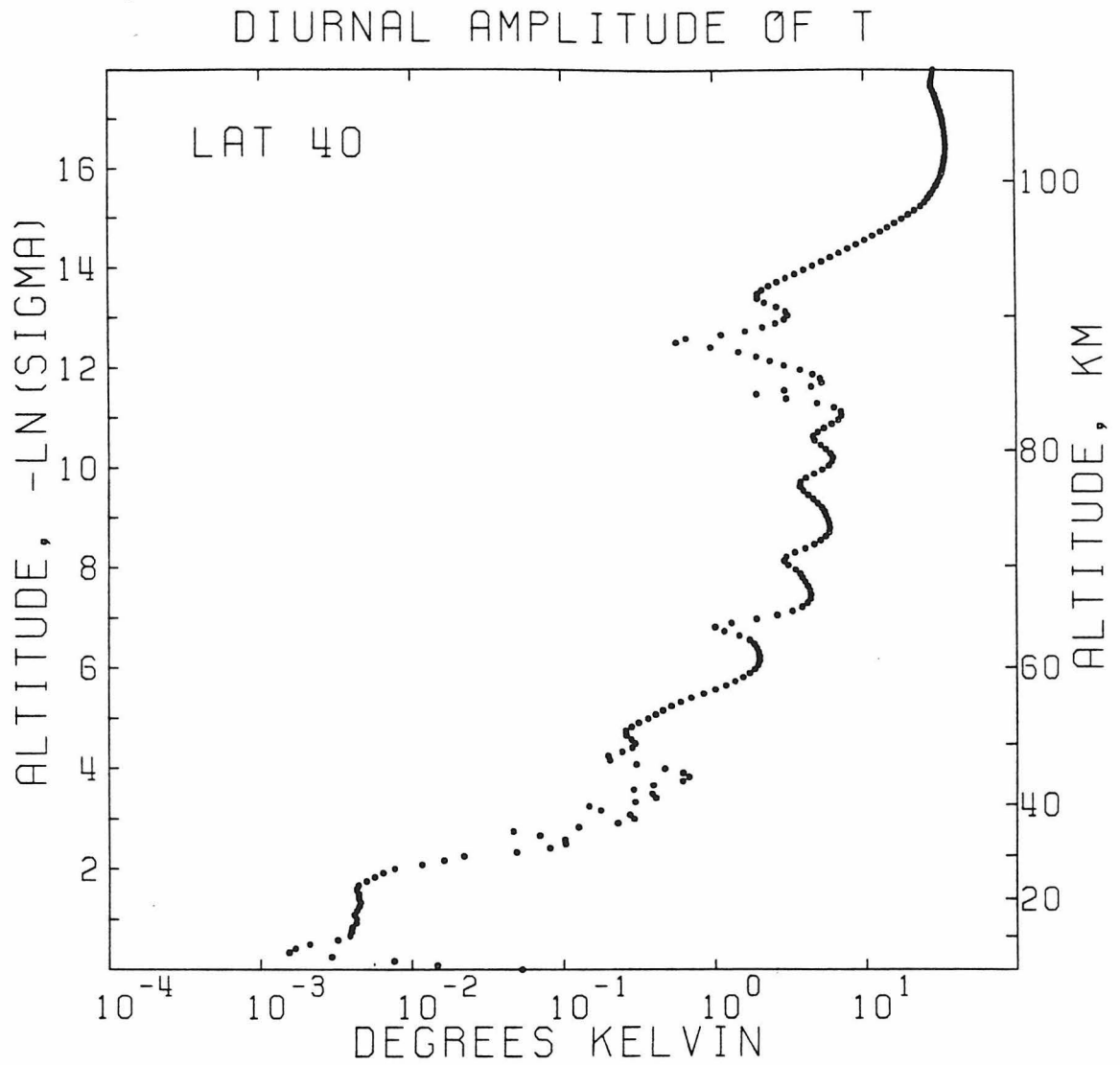


Figure 4.13a Diurnal amplitude at 40° of the tidal perturbation in the temperature as predicted by the LPE model.

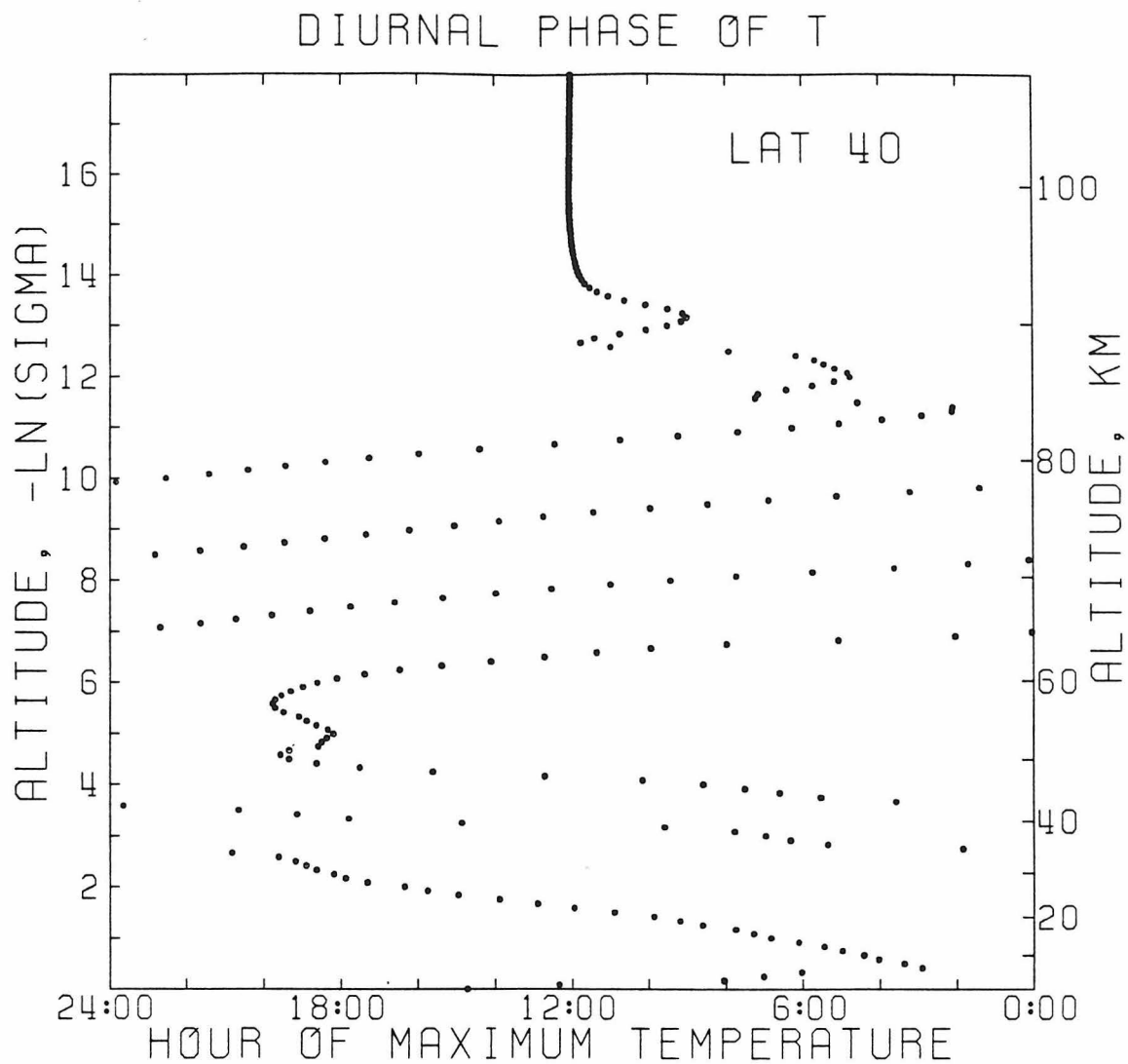


Figure 4.13b Diurnal phase at 40° of the tidal perturbation in the temperature as predicted by the LPE model.

situations which lead to a non-propagating solution: the trapping of the response due to the frequency being less than twice the vertical component of the rotation vector, trapping due to the frequency being greater than the Brunt-Vaisala frequency, the suppression of propagation by damping, or the presence of a standing wave. We discuss these possibilities below.

As discussed in the section on terrestrial thermal tides in Chapter 2, the condition that the frequency be more than $2\Omega_R \sin\lambda$ for propagation to be possible is an extrapolation from a theory derived for a rotating plane (Eckart, 1960). The semidiurnal tide meets this frequency requirement at all latitudes and therefore should not be trapped, but if it were trapped, the maximum temperature would occur at 3:00 AM and 3:00 PM, following the peak heating, instead of 7:40 to 10:00 AM and PM as seen in the data. In the atmosphere at the cloud tops and above, the static stability is quite high, so there is no doubt that the tidal frequency is less than the Brunt-Vaisala frequency.

If radiative damping were the dominant restoring force, then in terms of Newtonian cooling, $T'/\tau_N = Q$, so the phase of the temperature perturbation would track forcing at all levels. Thus, for the semidiurnal tide the maximum temperature would occur at noon and midnight, which disagrees with the data. It is unlikely that radiative damping is the dominant force anyway, since if the models for the radiative time constant reviewed in Chapter 3 are correct, then τ_N varies from 5 to 40 earth days between 80 and 65 km. Since the atmosphere rotates with a period of about 4 days in this region, radiative damping may not be negligible, but it is probably not the most important effect. If

viscous damping is the dominant force, the situation is more complicated, but in terms of Rayleigh friction, if τ_R decreases with height, as in the model, the phase of T' will once again track the forcing.

In the case of a standing wave, the phase could have the correct value. However, to create a standing wave in this region, the major source of forcing must be located above 80 km. From the measurements made by the solar flux radiometer, it is clear that most of the radiation is absorbed in the clouds. The near-infrared absorption by CO_2 , which peaks at 120 km, should set up a standing wave between this level and the ground, but its presence is masked by the response to the much larger forcing below.

The resolution of these difficulties can be seen in Figs. 4.10 and 4.11. Above 55 km there is an upward propagating wave. In the region sampled by channels 3-5 the wavelength is quite long, about 30 km, so that the phase does not change much from one channel to the next. In the clouds around 55 km there is a thin layer where the wave does not propagate due to low static stability. In this layer the terms involving γ^* in the thermodynamic equation are negligible, so the zonal advection and the forcing nearly balance:

$$im\Omega T' \approx Q$$

The phase of T' lags the phase of Q by $\pi/2$ so the semidiurnal maxima of temperature are at 3:00 AM and 3:00 PM. The combination of the phase being fixed at 3:00 at 55 km and the long wavelength above

that level leads to the post-dawn and post-sunset maxima seen in the three lowest OIR channels. Between 80 and 90 km the wavelength decreases due to increasing stability and decreasing zonal wind. (The dependence of the wavelength on these parameters can be qualitatively determined from the dispersion relation for gravity waves. See equation (2.43).) This decrease causes a large phase shift to occur between channels 2 and 3. The channel 2 weighting function actually gives most weight to the points near 85 km, resulting in a phase near 12:00.

Above 90 km the model response is damped which causes the phase to be near 12:00 as discussed above. In the OIR data the channel 1 semidiurnal phase varies from 12:00 to 1:00 between 0° and 40° . Obviously, if the wave continued to propagate above 90 km, the phase in channel 1 could still come out to be near 12:00, but the damped model is preferred because the predicted amplitude is close to the OIR amplitude. In an undamped upward propagating gravity-type wave, the amplitude increases proportional to $\sigma^{-1/2}$, which would lead to too large an amplitude in channel 1. Also, the wave cannot propagate upward indefinitely since energy cannot be transported to infinity dynamically. At some point the energy must be converted to heat and radiated to space. We have modeled this process by the damping terms. It was originally intended that the 'sponge layer' should become effective at a level far above those of interest. However, the theoretical values of the radiative Newtonian time constant, τ_N , are short compared to $1/2\pi$ times the tidal periods at altitudes above 90 km. Moreover, our model results agree with the amplitude and phase of the OIR data when these τ_N

values are used. Thus, we conclude that the tides are heavily damped above 90 km.

4.2.4 Diurnal Temperature Variations - Amplitude:

The diurnal tide, like the semidiurnal, could not be understood from the OIR measurements alone. The major mystery for the diurnal tide is the observed amplitudes in channels 2-5 which are smaller than the observed semidiurnal amplitudes from the equator to 50°. This phenomenon is reproduced by the model brightness temperatures. See Figs. 4.2-4.9 and Tables 4.1-4.4. The relatively low diurnal brightness temperature amplitude is mysterious because there are two factors which tend to make the diurnal temperature amplitude larger. First, recall from Chapter 3 that the amplitude of the forcing for a given longitudinal wavenumber, m , is proportional to $\int_{n/2}^{n/2} \cos^n \phi e^{im\phi} d\phi$. For $n = 1.6$, $C_1/C_2 = 1.864$. Second, for thermally forced gravity-type waves the amplitude of T' is inversely proportional to the frequency. The diurnal frequency, Ω , is half the semidiurnal frequency, 2Ω . Thus, the diurnal amplitude would exceed the semidiurnal by a factor of ~ 3.7 if the frequency and the forcing amplitude were the only contributing factors.

From the model temperature amplitudes shown in Figs. 4.12 and 4.13 it is clear that the diurnal amplitude of the model temperature perturbation is larger than the amplitude of the model brightness temperature perturbation. Also, the model diurnal and semidiurnal temperature amplitudes are not in the above ratio over most of the altitude range covered by the OIR. In fact at the equator they are nearly equal from 60 to 80 km. Thus, the problem of the diurnal brightness temperature amplitudes has been broken down into two separate

questions: 1. Why are the diurnal amplitudes of the model brightness temperatures less than those of the model temperatures from which they were calculated? 2. Why isn't the ratio of the model temperature amplitudes equal to ~3.7?

The answer to the first question is straightforward. As shown in Figs. 4.12 and 4.13, the diurnal tide is characterized by an upward propagating wave between 60 and 90 km. The semidiurnal tide also propagates in this region, but with a much longer wavelength. The wavelength of the diurnal tide is about 7 km. Since the width of the OIR weighting functions is between 5 and 10 km, the convolution of the model temperatures and the weighting functions performed to calculate the model brightness temperatures in the OIR channels results in a significant amount of cancellation. A simple example of this effect is obtained by considering a cosine wave with constant amplitude and a normalized Gaussian weighting function. The resulting 'brightness temperature' is proportional to

$$(2a/\sqrt{\pi}) \int_0^{\infty} e^{-a^2 z^2} \cos bz \, dz = e^{-b^2/4a^2}$$

which decreases monotonically as b increases or a decreases. The actual case is not as simple because it involves the radiance instead of the temperature itself and empirically determined weighting functions, but the principle is the same. At the equator where the diurnal and semidiurnal amplitudes of the model temperature perturbations are nearly the same, the diurnal amplitude of the model brightness temperature is less because the diurnal tide has a shorter wavelength.

As latitude increases, the diurnal brightness temperature amplitude increases relative to the semidiurnal until finally they cross as can be seen in Figs. 4.2-4.9. The crossover occurs at a lower latitude in the model than in the data, another probable consequence of our simple latitude dependence. Even at mid-latitudes, however, the diurnal brightness temperature amplitude in channels 3-5 is only about 1 K while our model predicts a temperature oscillation between 60 and 80 km with an amplitude of about 10 K. Note that if the ~1 K diurnal amplitude in the OIR brightness temperature is real and if the model wavelength of ~7 km is correct, then the actual diurnal temperature oscillation on Venus must have an amplitude of about 10 K at equatorial and mid-latitudes.

The answer to the second question is not so unambiguous. It seems likely that the diurnal response is somewhat suppressed for the same reason the terrestrial diurnal tide is weak. Since the forcing is spread out over more than a diurnal wavelength, destructive interference takes place between waves excited at different levels. The semidiurnal wavelength is longer, so the atmosphere tends to respond more coherently to the forcing at this frequency. On the earth the wavelength of the main semidiurnal mode is much longer, about 200 km, so this effect is very strong. On Venus the semidiurnal wavelength in the region of the forcing is about 30 km, four times the diurnal wavelength, which might be enough to equalize the response at the two frequencies.

The above discussion may put the question of the relative amplitudes to rest, but it raises the question of the relative vertical

wavelengths. Why is the wavelength of the semidiurnal tide about four times the wavelength of the diurnal tide? The dispersion relation for two dimensional gravity waves derived in Chapter 2 (equation 2.43) predicts that the vertical wavelength for the diurnal and semidiurnal tides should be the same. For a gravity wave the vertical wavelength depends only on the static stability and the phase speed and not on the frequency. Since the gravity wave theory is inadequate, the difference in wavelength must come about because of the meridional structure of the tides. This dependence is illustrated by the separable tidal equations where the eigenvalue for each meridional eigenfunction or Hough mode determines the vertical wavelength. These eigenvalues have been calculated for the earth, but knowing what they are does not insure understanding why they differ. A simple derivation will help. Consider an atmosphere on a horizontal x-y plane with a constant velocity in the x direction. Let the atmosphere be isothermal. Then the linearized divergence and heat equations (2.19 and 2.20) reduce to

$$Rv^2 T' = (iku^* + iv) \sigma \frac{\partial^2 W}{\partial \sigma^2}$$

$$\gamma^* W' = (iku^* + iv) T'$$

At this point in the gravity wave case we assumed that the solution had no y dependence. Now let $W' \propto e^{ily}$, where l is constant, so that $\nabla^2 W' = -(k^2 + l^2) W'$. The solution for the vertical structure is then $W'(\sigma) = W_{\pm} \sigma^{1/2} e^{\pm i\omega \ln \sigma}$ where the dispersion relation for W is $R(\sigma \gamma^*) (k^2 + l^2) = (u^* k + v)^2 (\omega^2 + \frac{1}{4})$. $\sigma \gamma^*$ is a constant. This dispersion relation is the same as the one for gravity waves except for the factor

1². Let $\nu = 0$, $u^* = a\Omega$, and $k = 2\pi m/a$ to obtain a 'tidal' equivalent gravity wave as before. Then

$$\frac{\omega_1}{\omega_2} = \frac{\sqrt{1 + (n_1)^2} - 1/4}{\sqrt{1 + (n_2)^2/4} - 1/4}$$

where $n_m = 1_m a/2\pi$. If $n_1 \gtrsim n_2/2$, then $\omega_1 > \omega_2$ which implies that the diurnal wavelength will be shorter. This simple case cannot be expected to accurately predict the ratio of the diurnal to the semidiurnal wavelength, but since both are dominated by the low Legendre modes ($n_1 \approx n_2$), qualitatively one expects the diurnal wavelength to be shorter. Since only the three lowest modes were included in the model, it might be suspected that this result is an artifact of the low horizontal resolution. It will be shown in the next section that the resolution is adequate.

4.2.5 Diurnal Temperature Variations - Phase:

The diurnal phases do not require a lengthy discussion like the diurnal amplitudes. Overall, the agreement between the model and the OIR is quite good for the diurnal phases (see Tables 4.3 and 4.4). When comparing discrepancies in the diurnal phase to those in the semidiurnal, remember to take $\Delta t/p$ where Δt is the difference between the model and the OIR and p is the period. A one hour discrepancy in the diurnal phase is the same as a half hour discrepancy in the semidiurnal. The diurnal agreement is remarkable because all the fine adjustments of the basic state and weighting functions were made to optimize the fit to the semidiurnal amplitudes and phases. No special effort was made to fit the diurnal results. Thus, the good agreement

between the model and the OIR for the diurnal amplitudes and phases may be considered an independent check of the validity of the model, unless the agreement is fortuitous.

The agreement in the diurnal phase is surprising because the diurnal wavelength is so short. Since the phase is varying so rapidly with height, the phase of the brightness temperature is expected to be very sensitive to any changes in the patterns seen in Figs. 4.12 and 4.13. Small changes in the basic state could affect the variation of phase with height enough to cause a significant change in the phase of the brightness temperature. The phase of the brightness temperature would also be sensitive to a variation in the cloud properties which would alter the weighting functions of channels 4 and 5.

Evidence that the diurnal phase is difficult to determine accurately is given by Diner et al. (1982). This paper reviews all the ground-based observations of solar-locked components in the infrared emission and compares them to the OIR results. The ground-based observations are in the 11 μm region so they can be compared to the OIR's channel 5. They cover solar longitudes not observed by the OIR in the equatorial region, specifically in the pre-dawn and afternoon quadrants. The semidiurnal amplitude and phase and the diurnal amplitude determined from the entire data set agree well with those based on the OIR channel 5 data alone. However, the diurnal maximum determined from the entire data set is at about 4:00 AM local time, whereas the OIR diurnal maximum in channel 5 is at 2:15 PM. Diner et al. (1982) interpret this discrepancy as being due to inadequate

longitudinal coverage by the OIR. This is certainly possible and, indeed, is the most probable explanation. However, it is also possible that the discrepancy is caused by the different spectral passbands of the ground-based and spacecraft observations. The different spectral passbands will cause the weighting functions to differ. Because of the short diurnal wavelength caution should be exercised in comparing results from instruments with different weighting functions.

4.2.6 Channel 1 Results:

The results for channel 1 were not included in the above discussion because they do not fit the pattern seen in the other channels. In channel 1 the diurnal amplitude is larger than the semi-diurnal at equatorial to mid-latitudes (Taylor et al., 1980). According to our model this occurs because the response is damped in the region of the channel 1 weighting function. Since the phase is constant near noon in both the diurnal and semidiurnal components, there are no interference effects, and the model temperature amplitude is observed in the model brightness temperature. The 10:00 diurnal phase seen in the OIR (Tables 4.3 and 4.4) is a minor problem. As mentioned earlier in Section 4.2.1, the channel 1 results are not as reliable as the other channels, so an error of two hours is possible. The discrepancy between the model and OIR diurnal amplitude could also be explained by the poor quality of the channel 1 results. Varying the amount of damping will change the diurnal amplitude, but not independent of the semidiurnal amplitude.

4.2.7 Other Pioneer Venus Observations:

Of the instruments on Pioneer Venus, only the OIR obtained a data set of large enough spatial and temporal extent to detect tidal oscillations in the Venus atmosphere. However, we can at least check to see if our tidal results are consistent with other more limited data sets. For example, see Figs. 4.14-4.16. These figures show the model temperature profiles, including T^* , T_1 , and T' , at the probe sites. The perturbation temperature, T' , includes both the diurnal and semidiurnal components. The oscillations between 60 and 90 km are the manifestation of the solar tide. The short vertical wavelength indicates that the diurnal tide is most prominent. These profiles may be compared to those obtained by Seiff et al. (1980) from the atmospheric structure experiment on the Pioneer Venus probes. The probe data show some waviness in the region 60-90 km, but for the day and north probes the tidal oscillation, if present, is obscured by noise. The predicted oscillation at the sounder probe site is large enough to have been detected, but the observed sounder probe profile is the smoothest of all the probes. The tidal signal may have been lost due to low resolution. The data in this region was obtained from the probe decelerations and has a vertical resolution of about 3 km. Seiff et al. (1980) also note that only waves with vertical wavelengths greater than 7.5 km are to be considered real. Smaller scale oscillations are due to measurement noise. Thus, the diurnal tide is on the borderline of detectability by this experiment, and most of its amplitude may have been smoothed out.

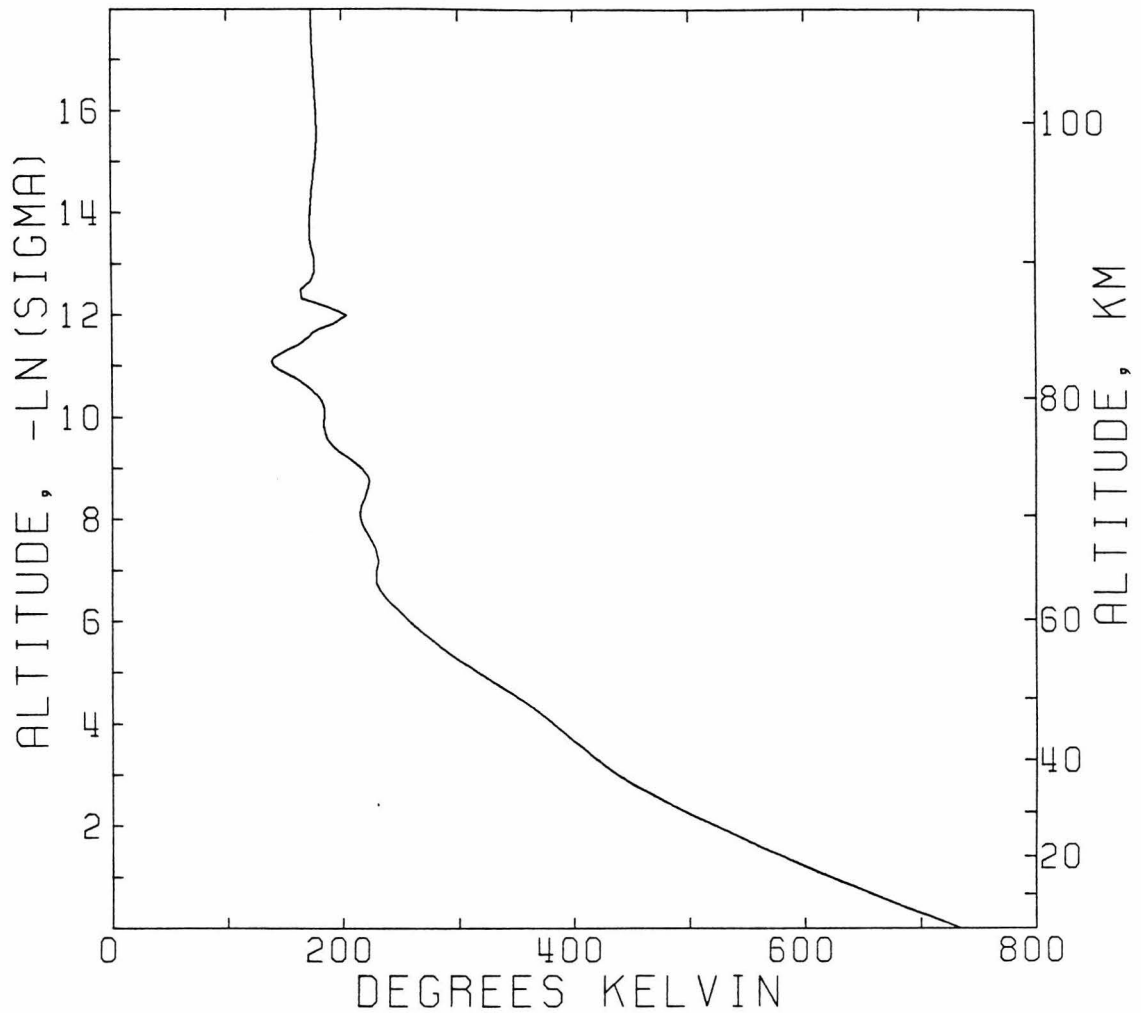
MODEL TEMPERATURE PROFILE
AT THE SOUNDER PROBE SITE

Figure 4.14 The model temperature profile at the sounder probe site including the basic state and the tidal perturbation.

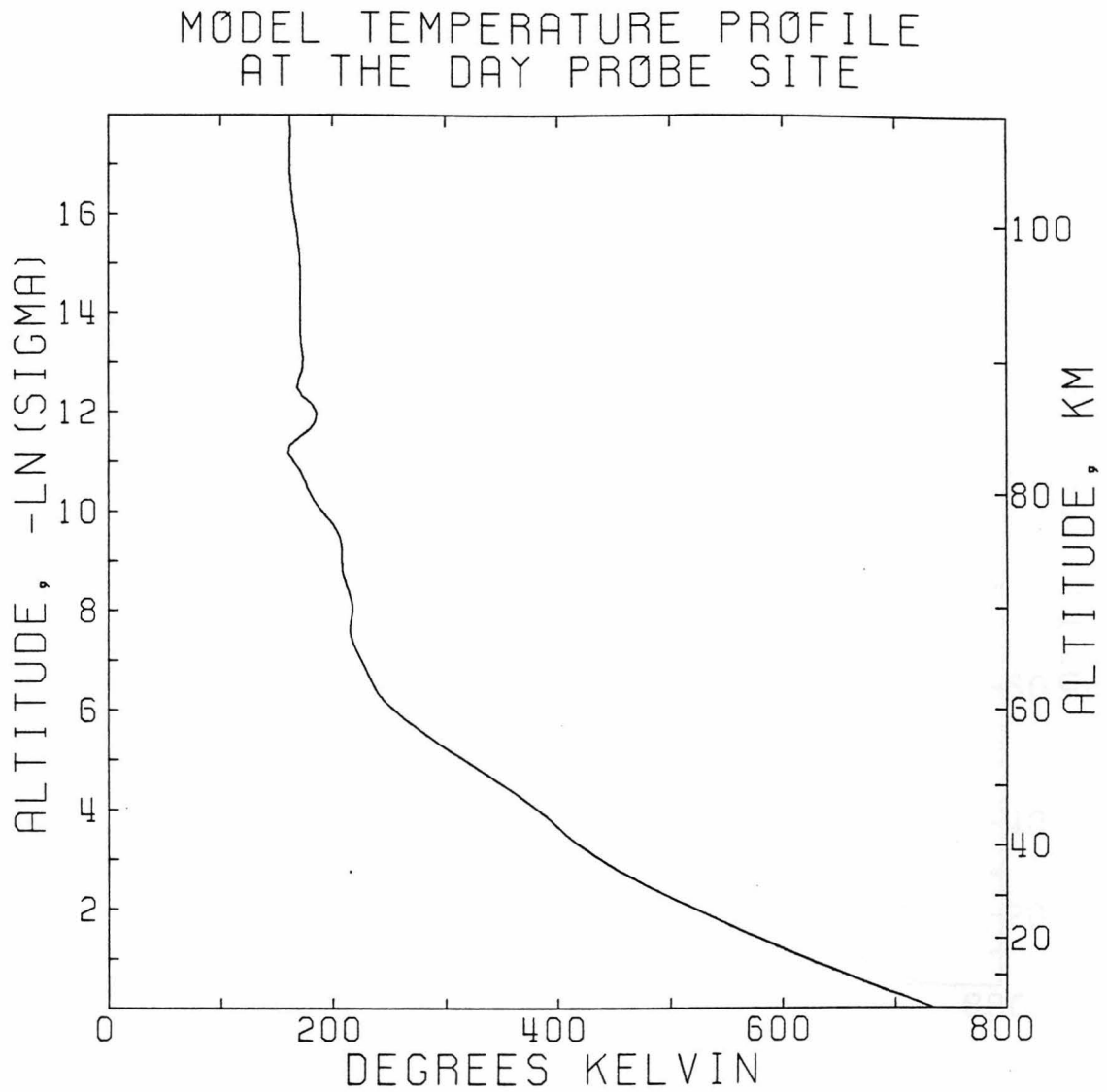


Figure 4.15 The model temperature profile at the day probe site including the basic state and the tidal perturbation.

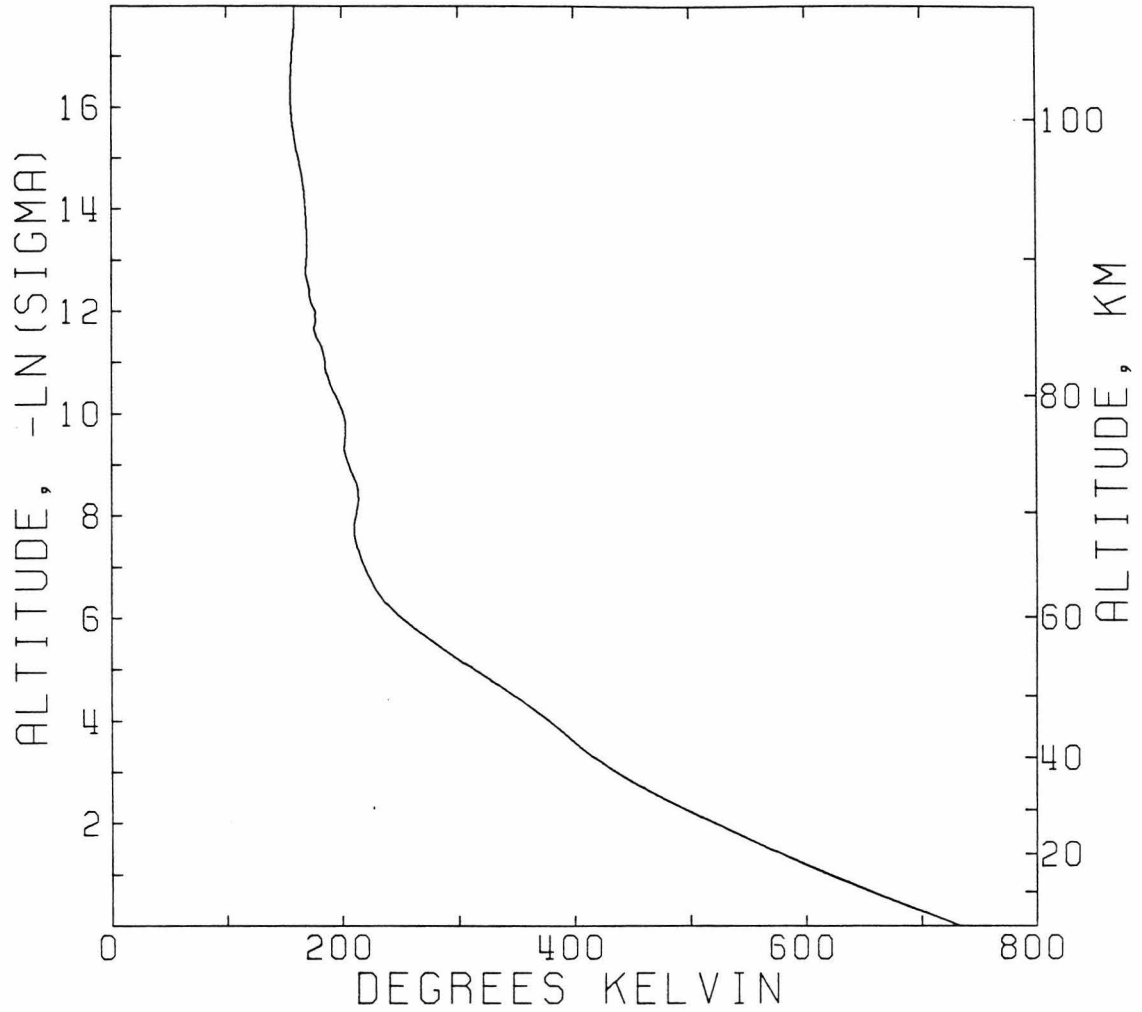
MODEL TEMPERATURE PROFILE
AT THE NORTH PROBE SITE

Figure 4.16 The model temperature profile at the north probe site including the basic state and the tidal perturbation.

In the observed day and north probe profiles there is an oscillation with an amplitude of about 100 K above 110 km. According to our model, this oscillation cannot be due to thermal tides because the tides are damped in this region. This large oscillation may be some other type of eddy disturbance or may be a feature of the mean state.

The temperature profiles of the Venus stratosphere obtained by radio occultations have a vertical resolution of about 1 km determined by the Fresnel size (Woo et al., 1980). Kliore and Patel (1980, 1982) have published numerous profiles ranging from equatorial to polar latitudes. The altitude range covered by these profiles is 50 to 80 km. Most of the profiles show wavelike structure between 60 to 80 km. The most prominent wavelength seems to be around 5 km, somewhat shorter than the 7 km predicted for the diurnal tide. The observed amplitude is comparable to the model amplitude in Figs. 4.14-4.16 at mid and high latitudes but is smaller at low latitudes. In fact, the observed amplitudes increase at higher latitudes, a trend which is the reverse of that seen in the model. Whether or not these oscillations in the radio occultation profiles are solar locked disturbances cannot be determined from the small number of profiles available. However, the model predicts that a more sizeable oscillation should be seen at low latitudes.

Finally, we may compare our tidal meridional velocities to those measured by the Pioneer Venus DLBI experiment (Counselman et al., 1980). The measured meridional velocities are much smaller than the zonal velocities above the lowest 5 km of the atmosphere. The meridional velocity is due to a combination of eddy motions, including tides, and a

mean circulation, presumably of the Hadley cell type (Schubert et al., 1980). Since it cannot be determined if the measured velocities are due to the tides, all that can be done is to make sure that tidal velocities are less than or equal to the measured velocities over most of the atmosphere. A comparison of the tidal model and probe profiles of the meridional velocity is given in Fig. 4.17. From this figure it can be seen that the amplitude of the tidal model velocities, which includes the diurnal and semidiurnal contributions, is not inconsistent with the measured velocities. In fact, the tides may be responsible for some of the structure seen in the data above 40 km. The wavelengths are nearly the same, but the variation of phase with height often does not agree.

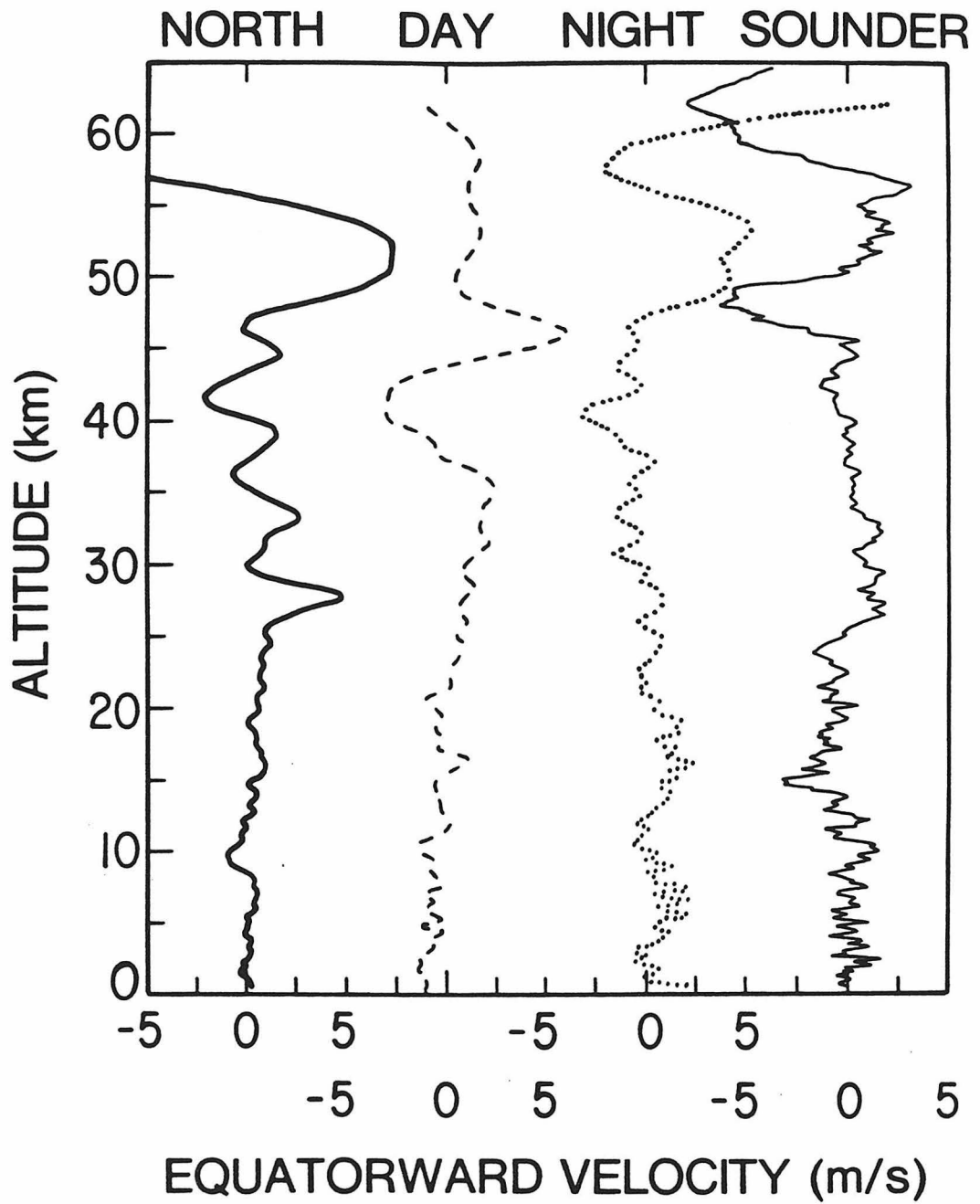


Figure 4.17a The meridional component of the wind at the Pioneer Venus probe sites from the DLBI experiment (Counselman et al., 1980). This figure is from Schubert et al. (1980).

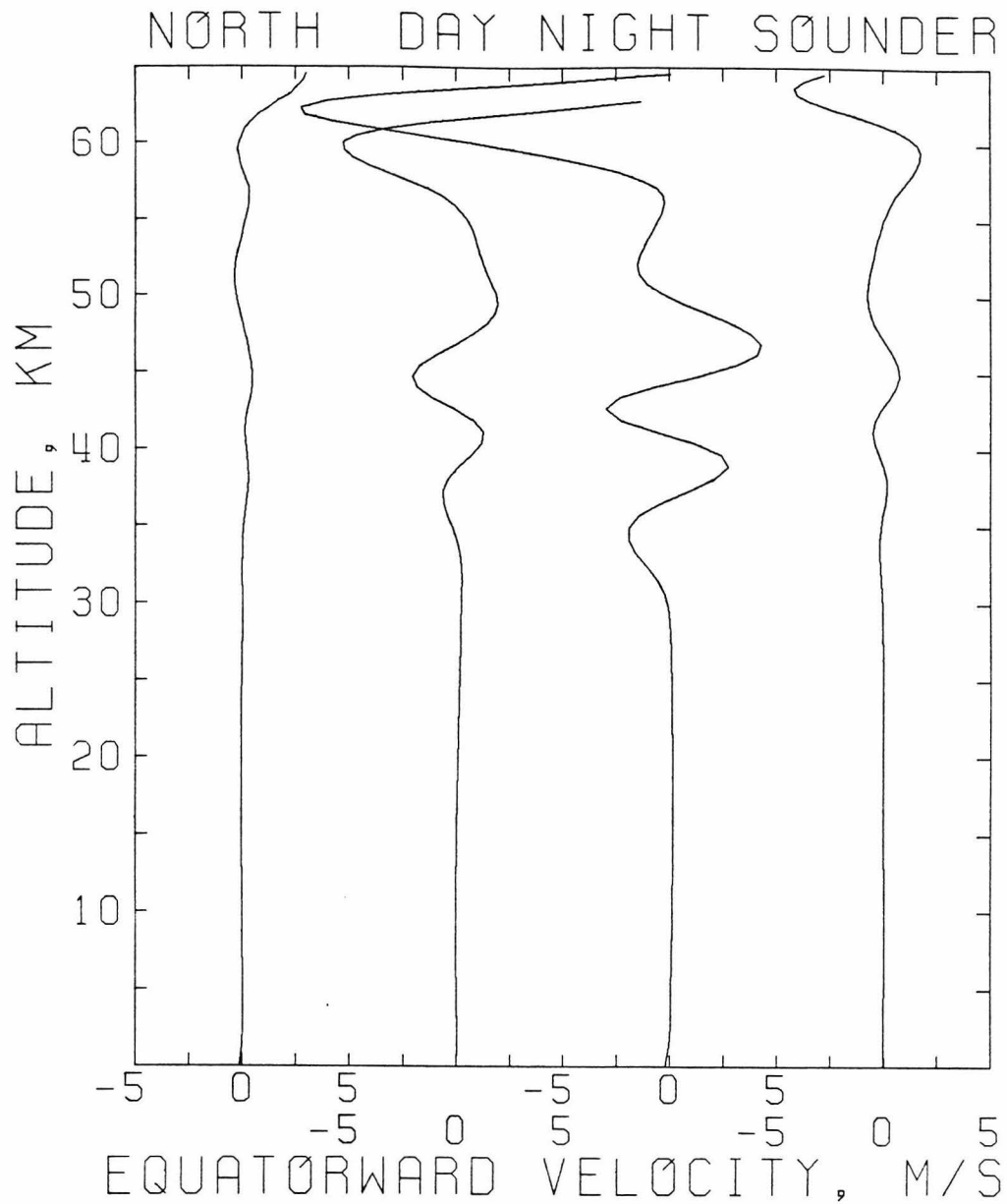


Figure 4.17b The model tidal perturbation in the meridional wind at each of the Pioneer Venus probe sites. The scale of the axes is the same as in Fig. 4.17a.

4.3 Weighting Functions and Cloud Parameters

It is easy to imagine that changing various input parameters would have some effect on the model output. However, it is also possible to change the model brightness temperatures for channels 4 and 5 by changing the weighting functions independent of any model parameters. These channels are affected by the presence of clouds whose structure can be characterized by H_c , the ratio of the cloud scale height to the gas scale height, and p_c , the pressure at which optical depth unity is reached. p_c is uncertain by at least a hundred millibars (Elson, personal communication, 1982), and H_c is somewhere between 0.1 and 1.0 (Diner et al., 1982). Our nominal case is $H_c = 0.4$ and $p_c = 100$ mb.

In a sense, uncertainties in the OIR weighting functions are a problem for the OIR experiment team. However, since these uncertainties affect the fit between our tidal model and the OIR data, we discuss them at some length below.

The effects of varying H_c and p_c are shown in Tables 4.6 and 4.7 for the semidiurnal tide at the equator and 40° . As expected, channel 5 is more sensitive to changes in the cloud parameters than channel 4 since it is a 'window' channel designed to measure cloud top temperature. If H_c is kept constant and p_c is increased, the weighting functions will peak lower in the atmosphere. From Figs. 4.10 and 4.11 one can predict that the effects of lowering the weighting functions will be to decrease the amplitude and shift the phase towards noon. The first four entries in Tables 4.6 and 4.7 show these effects. The phase

TABLE 4.6

SENSITIVITY TO CLOUD PARAMETERS: SEMIDIURNAL TIDE AT THE EQUATOR

H_c	p_c (mbar)	<u>CHANNEL 4</u>		<u>CHANNEL 5</u>	
		Amplitude	Phase	Amplitude	Phase
0.4	50	4.3	8:26	4.9	8:29
0.4	100	3.1	9:16	3.3	10:00
0.4	200	2.5	9:29	1.8	11:12
0.4	300	2.3	9:35	1.0	11:11
0.85	100	2.9	8:34	2.6	8:43
0.85	200	2.6	9:06	1.6	9:53
0.15	50	4.4	8:55	5.2	9:15
0.15	100	2.8	9:35	3.0	10:55

TABLE 4.7

SENSITIVITY TO CLOUD PARAMETERS: SEMIDIURNAL TIDE AT 40°

H_c	p_c (mbar)	<u>CHANNEL 4</u>		<u>CHANNEL 5</u>	
		Amplitude	Phase	Amplitude	Phase
0.4	50	0.9	8:15	0.9	8:26
0.4	100	0.7	8:49	0.7	9:26
0.4	200	0.6	9:08	0.6	10:39
0.4	300	0.6	9:15	0.4	11:23
0.85	100	0.7	8:17	0.7	8:27
0.85	200	0.7	8:47	0.5	9:40
0.15	50	0.7	8:23	0.7	8:47
0.15	100	0.7	9:01	0.8	9:59

in channel 5 at the equator was the determining factor in choosing $p_c = 100$ mb from this sequence. The effects of increasing H_c are shown in the next two entries. Increasing H_c while p_c is constant broadens the weighting function and raises its peak altitude. Broadening the weighting function causes more cancellation to occur since the convolution includes a larger fraction of a wavelength. However, raising the weighting function gives more weight to levels with larger amplitudes. These two effects nearly balance so increasing H_c to 0.85 does not change the amplitude very much. The maxima occur earlier, as expected, when the weighting function is raised. The agreement with the OIR data for $p_c = 200$ mb and $H_c = 0.85$ is as good as in the nominal case. Thus, there is no unique best fit case. $H_c = 0.4$ was chosen for the nominal case because it is an intermediate value. Two cases of clouds with sharp upper boundaries are included in Table 4.6 and 4.7 for comparison.

The weighting functions used to calculate the results in Tables 4.1-4.4, 4.6 and 4.7 assumed a viewing angle of the instrument from the nadir of 35° . The OIR data used in the determination of the tides covered the range 0° to 69.5° (Taylor et al., 1980); 35° was chosen as a representative value. The effect of changing the viewing angle to 0° is shown in Table 4.8. The effect is essentially negligible.

In calculating model brightness temperatures it has been assumed that the weighting functions and, thus, H_c and p_c are constant in space and time. If this were true, the OIR channels 4 and 5 would be sensitive only to temperature differences on constant pressure surfaces. Actually, p_c is thought to increase towards the pole and to be

TABLE 4.8 - SENSITIVITY TO VIEWING ANGLE

CHANNEL	Viewing Angle = 35°		Viewing Angle = 0°	
	Amplitude	Phase	Amplitude	Phase
<u>SEMIDIURNAL TIDE AT THE EQUATOR</u>				
2	3.5	12:27	3.5	12:43
3	4.4	5:54	4.3	6:03
4	3.1	9:16	3.0	9:24
5	3.3	10:00	3.1	10:09
<u>SEMIDIURNAL TIDE AT 40°</u>				
2	1.5	12:29	1.6	12:46
3	1.2	6:11	1.2	6:20
4	0.7	8:49	0.7	8:57
5	0.7	9:26	0.7	9:36
<u>DIURNAL TIDE AT THE EQUATOR</u>				
2	2.0	9:48	1.8	9:56
3	1.3	17:36	1.3	17:37
4	0.7	16:34	0.7	16:37
5	0.7	15:00	0.8	15:35
<u>DIURNAL TIDE AT 40°</u>				
2	1.9	8:16	1.8	8:10
3	1.0	17:44	1.0	17:46
4	1.2	18:14	1.1	18:13
5	1.1	18:39	1.0	18:33

particularly high in the collar region (Elson, 1982; Diner et al., 1982). However, since the basic state in the polar region is not adequately represented in the model, it is at least consistent to neglect the latitude dependence of the weighting functions.

It is also probable that H_c and p_c vary randomly due to atmospheric disturbances with different time and space scales than the tides. These fluctuations will shift the weighting functions for channels 4 and 5 up and down, causing a spread in brightness temperature at constant solar longitude. These disturbances will also probably have temperature perturbations on constant pressure surfaces associated with them. The effect on the tidal results should be small if enough observations are made at each solar-fixed longitude to statistically determine the mean brightness temperature. If there are longitude regions which were poorly observed, or if there are disturbances with time scales comparable to the observing period of the OIR (2.5 months), then some error may be present in the results due to aliasing. The error in the observed tidal amplitudes is estimated to be less than a degree in the polar regions, but increases to a few degrees near the equator due to uneven coverage by the OIR (Elson, personal communication, 1982). However, the relative diurnal and semidiurnal amplitudes observed near the equator are reliable. It is more difficult to determine the error bars on the observed tidal phase. Errors in the range of an hour or so are likely near the equator.

A more serious problem can occur if variations in H_c and p_c are correlated with the tidal perturbations. There are several cases to consider. If the cloud particles move with the gas velocity, and the

upper boundary of the cloud is very sharp ($H_c \ll 1$), then the tidal vertical velocity will cause the cloud and, thus, the weighting functions for channels 4 and 5 to shift up and down (Diner et al., 1982). The semidiurnal amplitude of the vertical velocity, w , near the cloud tops at the equator is about 1.8 cm/sec. If Δz_c is the shift in the height of the cloud, then

$$\Omega \frac{\partial(\Delta z_c)}{\partial \phi} = 1.8 \text{ cm/sec} \cdot \cos(2\phi + \phi_w)$$

where ϕ_w is the phase of w and Ω is the mean rotation rate of the atmosphere. From the above expression

$$\Delta z_c = (1.8 \text{ cm/sec}/2\Omega) \cdot (\sin 2\phi + \phi_w) = 0.5 \text{ km} \cdot \sin(2\phi + \phi_w)$$

The basic state temperature lapse rate at this level is such that in 0.5 km, the temperature changes by 1.7 K. In this case a change of roughly this magnitude would be observed in the channel 5 brightness temperature. Thus, there could be a semidiurnal brightness temperature perturbation in channel 5 due to vertical motion of the cloud with an amplitude about half of that shown in Table 4.1. The value in Table 4.1 was calculated from the model temperature oscillation at constant pressure. The amplitude of the perturbation due to vertical motion would be less in channel 4 since the weighting function for this channel is not entirely determined by cloud opacity.

The sharp cloud case described above is the worst case in the sense that it results in the largest amplitude due to vertical motions. Consider the case where $H_c = 1$, i.e., the cloud particles are uniformly

mixed in the gas. Then, an oscillating vertical velocity will have no effect on the weighting functions because the distribution of the cloud particles with respect to pressure remains unchanged. In this case the random fluctuations discussed above would also have no effect on the weighting functions.

It is also possible, if the cloud boundary is sharp, that the pressure at the boundary remains constant in spite of vertical motions (Diner et al., 1982). The cloud particles would not be entrained in the gas flow. This could occur if the particles evaporated almost immediately upon being raised above a certain level. However, rapid evaporation is unlikely because particle lifetimes at the cloud tops are on the order of months (Toon et al., 1979; Knollenburg et al., 1980). It is also unlikely that settling causes any relative motion of the particles with respect to the gas since the Stokes fall velocity of 1 μm cloud particles at the cloud tops is less than .1 cm/sec (Young, 1975), negligible when compared to the 1.8 cm/sec calculated above. Since the atmosphere at the cloud tops is stably stratified, it is also unlikely that small scale turbulent mixing determines the cloud top level.

From the above discussion it is clear that the assumption that the vertical motions associated with the tides do not affect the measured brightness temperatures in channels 4 and 5 is consistent only with diffuse models for the cloud top. Comparisons of our model results with the OIR do not contribute much to constraining the value of H_c . Our results are certainly consistent with $H_c > 0.4$, and H_c could be as great as 0.85.

The diurnal results in channels 4 and 5 are expected to show a

dependence on the cloud parameters similar to the semidiurnal. The diurnal phase may be more sensitive to changes in the weighting functions because of its more rapid change with height. This effect can be seen in Tables 4.9 and 4.10. These tables give the diurnal amplitude and phase in channels 4 and 5 for the same values of H_c and p_c discussed previously for the semidiurnal tide. At the equator, changes in p_c result in at least twice as big a change $\Delta t/p$ in the diurnal phase as in the semidiurnal. This is not true at 40° , but at 40° the semidiurnal phase does not vary smoothly with height in the region of the channel 4 and 5 weighting functions.

TABLE 4.9

SENSITIVITY TO CLOUD PARAMETERS: DIURNAL TIDE AT THE EQUATOR

H_c	p_c (mbar)	<u>CHANNEL 4</u>		<u>CHANNEL 5</u>	
		Amplitude	Phase	Amplitude	Phase
0.4	50	1.0	19:47	1.3	20:10
0.4	100	0.7	16:34	0.7	15:00
0.4	200	0.8	17:35	0.7	20:09
0.4	300	0.8	17:52	0.2	22:08
0.85	100	0.8	17:40	0.8	17:45
0.85	200	0.8	17:40	0.6	18:29
0.15	50	1.2	23:53	2.2	0:27
0.15	100	1.0	15:46	1.9	15:00

TABLE 4.10

SENSITIVITY TO CLOUD PARAMETERS: DIURNAL TIDE AT 40°

H_c	p_c (mbar)	<u>CHANNEL 4</u>		<u>CHANNEL 5</u>	
		Amplitude	Phase	Amplitude	Phase
0.4	50	1.3	17:18	1.2	16:49
0.4	100	1.2	18:14	1.1	18:39
0.4	200	1.1	17:52	1.0	17:03
0.4	300	1.0	17:47	1.1	17:48
0.85	100	1.1	17:54	1.1	17:52
0.85	200	1.1	17:53	1.0	17:43
0.15	50	1.9	16:51	2.2	16:12
0.15	100	1.0	18:41	0.6	20:57

4.4 Convergence and Spatial Resolution

In this section the model's reliability is considered from a numerical point of view. Although the agreement of the model with the OIR data is good evidence for the validity of the model, the convergence and the spatial resolution should be evaluated by changing model parameters such as the number of time steps, the number of vertical points, and the number of Legendre modes. The large amount of computer time required to run the model prevented us from obtaining more than a few cases, but these cases demonstrate the adequacy of the convergence and the spatial resolution.

The amount of computer time required was not the only obstacle which prevented us from running the model out to many thousands of time steps. Unfortunately, there is an instability present in the lower atmosphere. However, the growth rate is slow enough that the model is nearly converged before the instability becomes important. The behavior of the instability for different values of the model parameters indicates that it is probably of physical origin. It seems to be generated in the low static stability region near the ground. It is possible that it is related to shear instability. At the equator Ri , the Richardson number, is less than one in the lowest two scale heights and is less than 0.25 in a narrow layer near the top of the second scale height. At these heights the static stability decreases with increasing latitude, so Ri will decrease towards the pole. $Ri < 0.25$ is often sufficient for instability. Determining the exact nature of this instability is a top priority in further work with this model as applied to Venus.

The convergence can be evaluated by comparing the solution at the final time step to the solution at an earlier time step. This is done in Fig. 4.18 for the semidiurnal temperature perturbation. The circles are the solution at 1600 Δt , and the pluses are the solution at 800 Δt . The time step was two hours. The solution at 1600 Δt was used in all previous discussions of the semidiurnal tide. Fig. 4.18 shows that the convergence is excellent at 1600 Δt from the equator to mid-latitudes. The main exception to this occurs near the ground, especially in the phase at the equator. The problems near the ground are due to the instability mentioned above. The convergence is not quite as good at 80° latitude, but as mentioned previously, our model is not expected to be accurate there for other reasons.

The discussion of the model results in this chapter have concentrated heavily on the temperature perturbations since the OIR data exist for comparison. Other meteorological variables, e.g. wind velocities, also show tidal perturbations. The semidiurnal amplitude and phase of u' and v' at 1600 Δt and 800 Δt at three latitudes are shown in Figs. 4.19 and 4.20. The convergence in these and the rest of the variables is as good as that in the temperature.

The convergence in the diurnal temperature perturbations is shown in Fig. 4.21 at 0° , 40° , and 80° . The circles are at 1200 Δt and the pluses are at 600 Δt . The time step was four hours. The solution at 1200 Δt has been used throughout this chapter. The convergence of the diurnal solution is not as good as that of the semidiurnal solution, but it is acceptable. At 70 km at the equator the amplitude increased from 6.63 k to 7.86 k, a change of 17%, between 600 and 1200 Δt . The

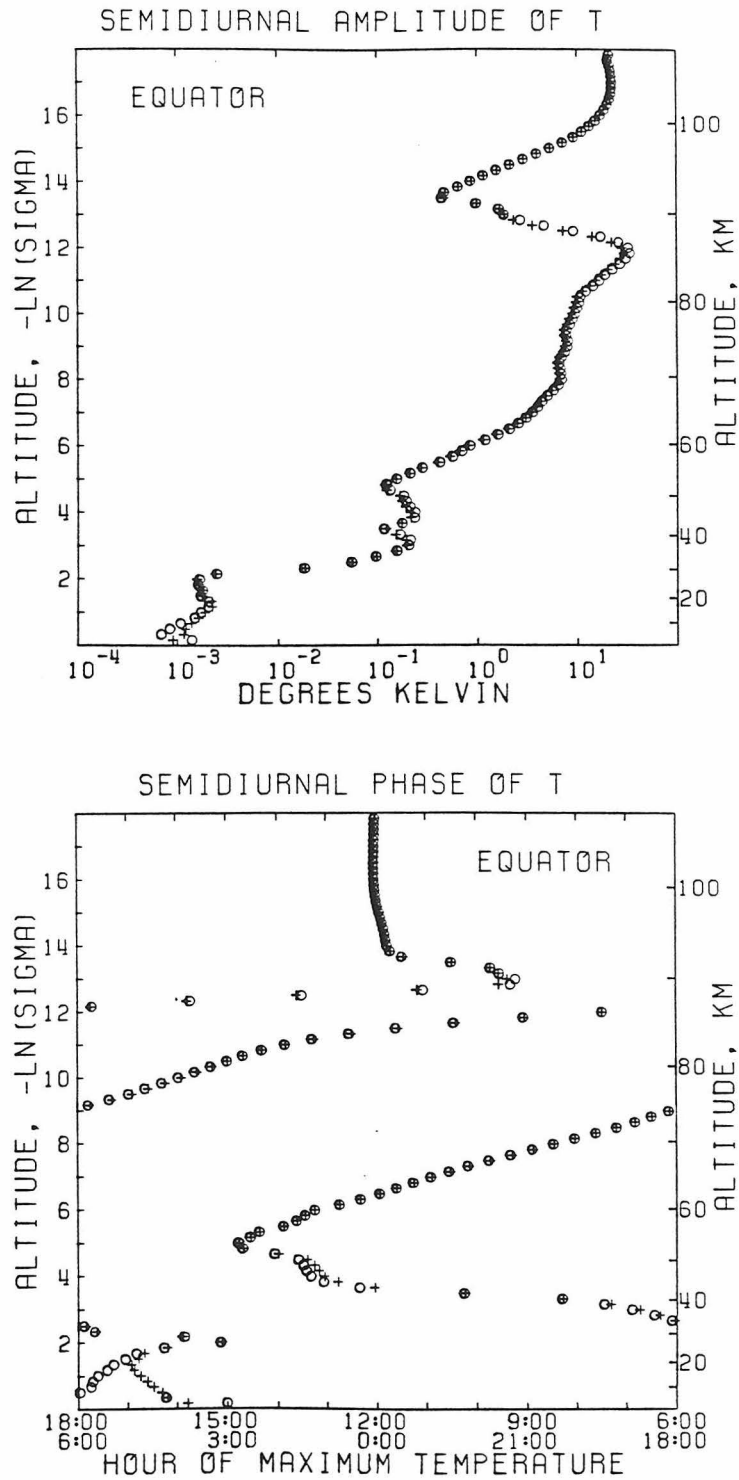


Figure 4.18a A comparison of the solutions for the semidiurnal temperature perturbation at the equator at 800 At (pluses) and 1600 At (circles).

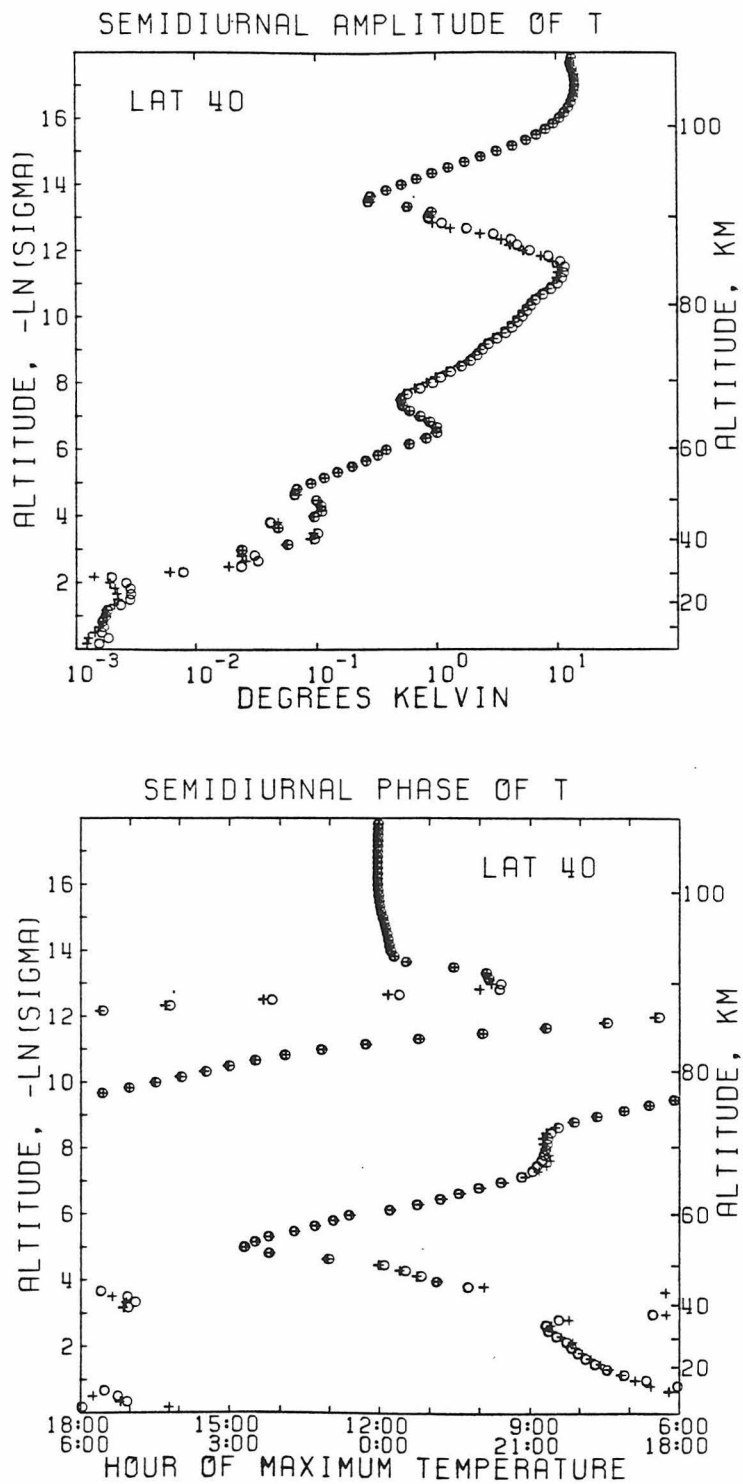


Figure 4.18b Same as Fig. 4.18a at 40°.

186
CONVERGENCE STUDY

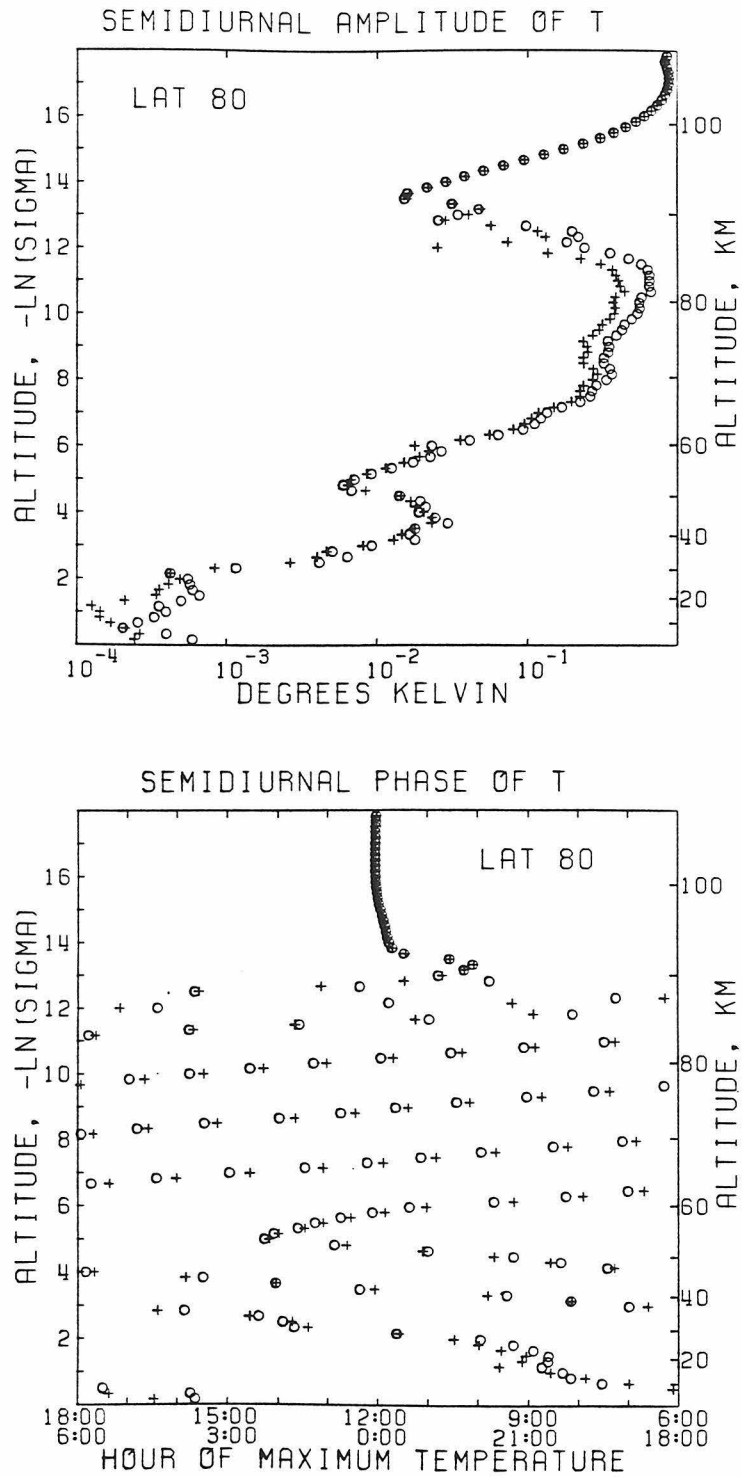


Figure 4.18c Same as Fig. 4.18a at 80°.

CONVERGENCE STUDY

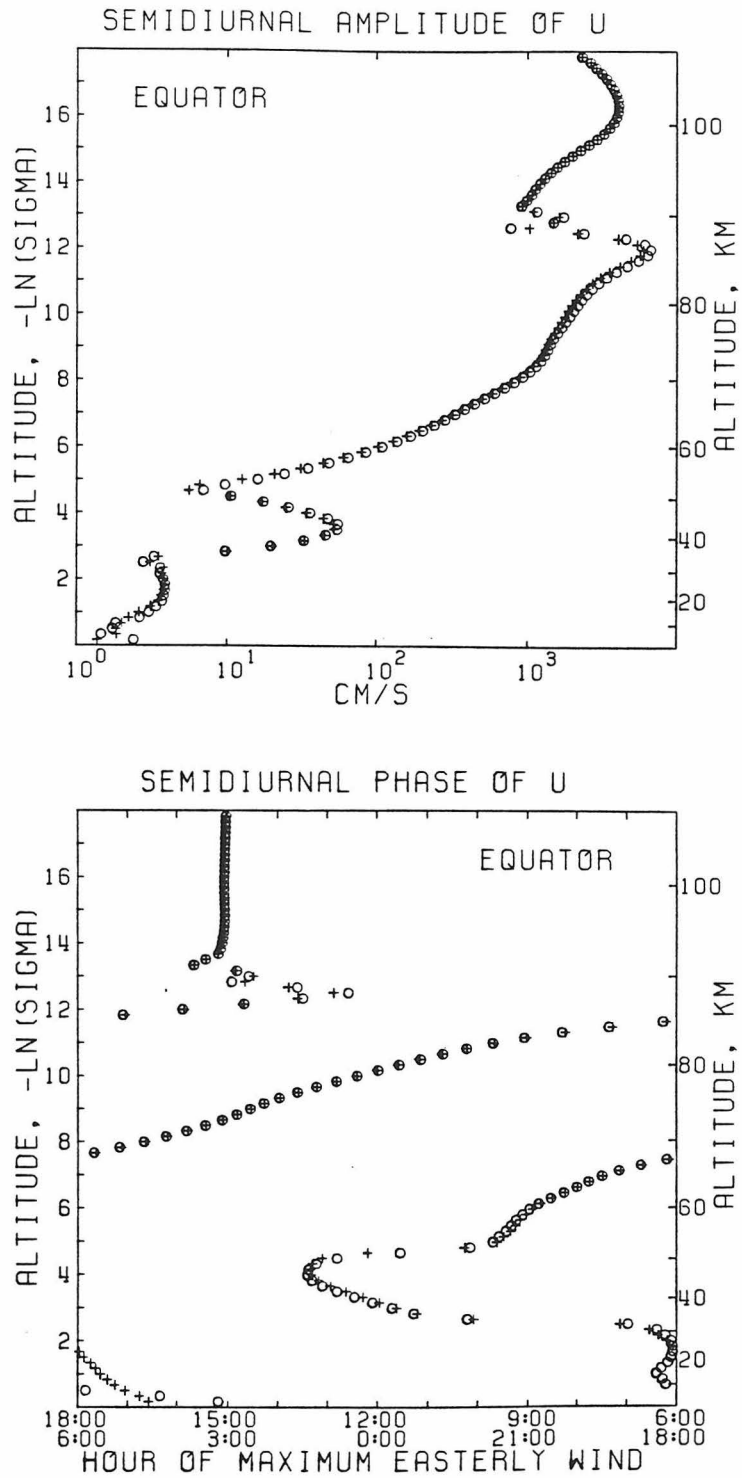


Figure 4.19a A comparison of the solutions for the semidiurnal zonal wind perturbation at the equator at 800 Δt (pluses) and 1600 Δt (circles).

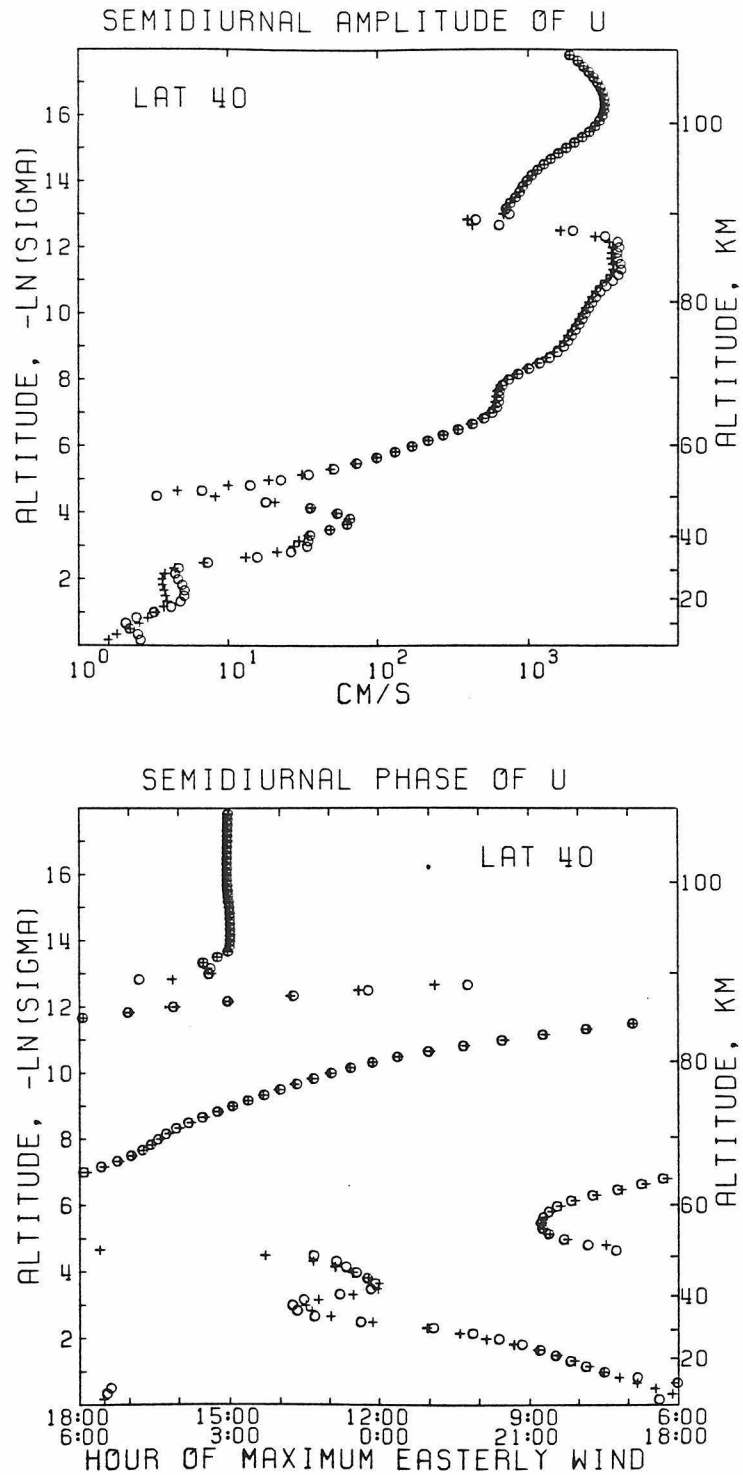


Figure 4.19b Same as Fig. 4.19a at 40°.

CONVERGENCE STUDY

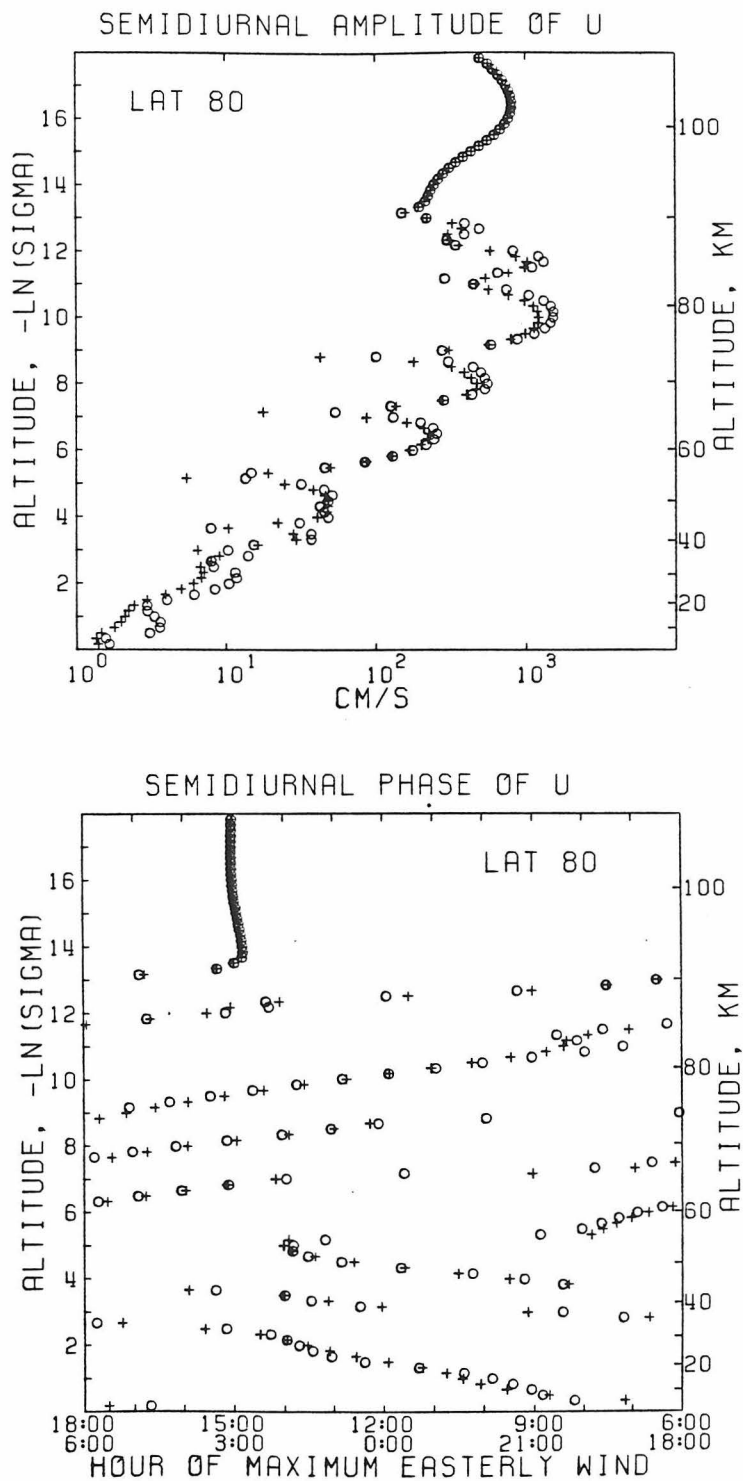


Figure 4.19c Same as Fig. 4.19a at 80°.

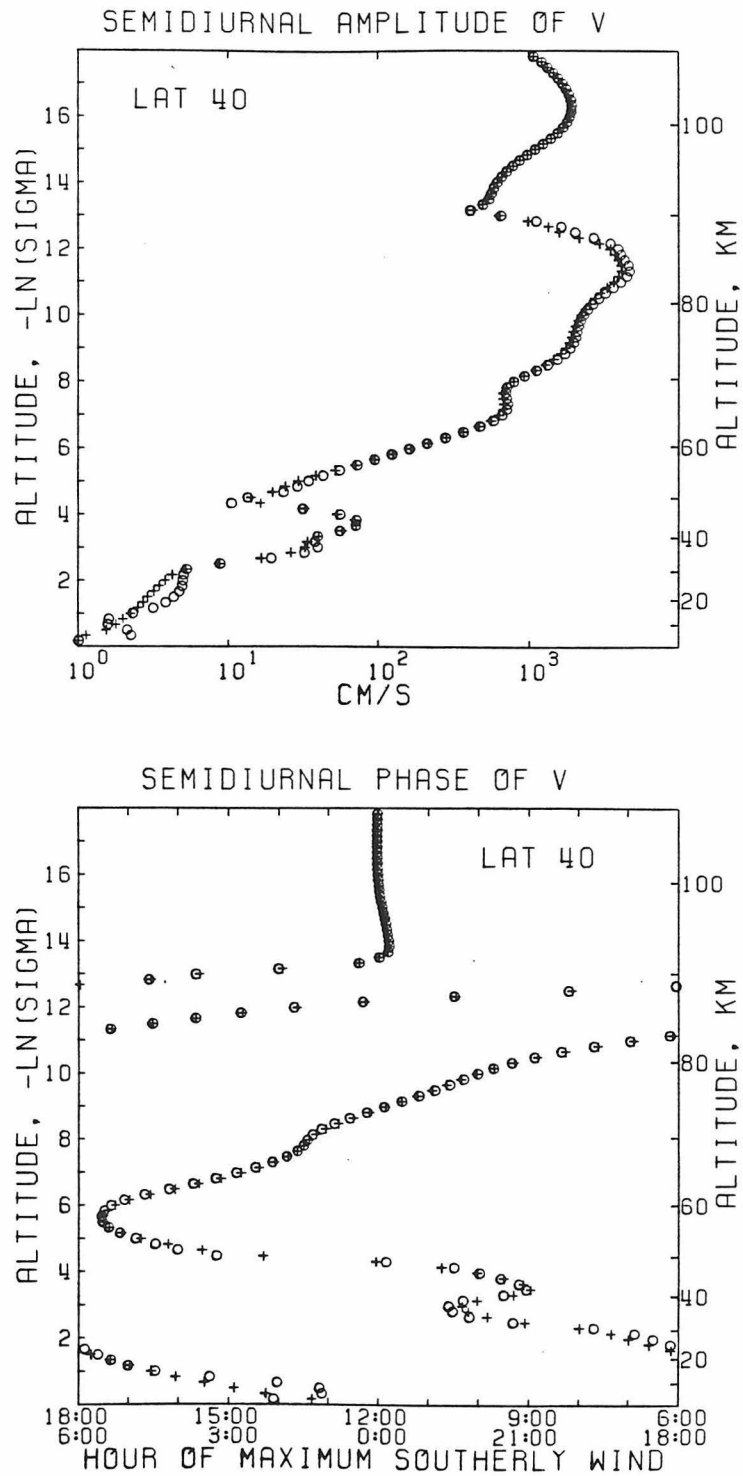


Figure 4.20a A comparison of the solutions for the semidiurnal meridional wind perturbation at 40° at 800 At (pluses) and 1600 At (circles).

CONVERGENCE STUDY

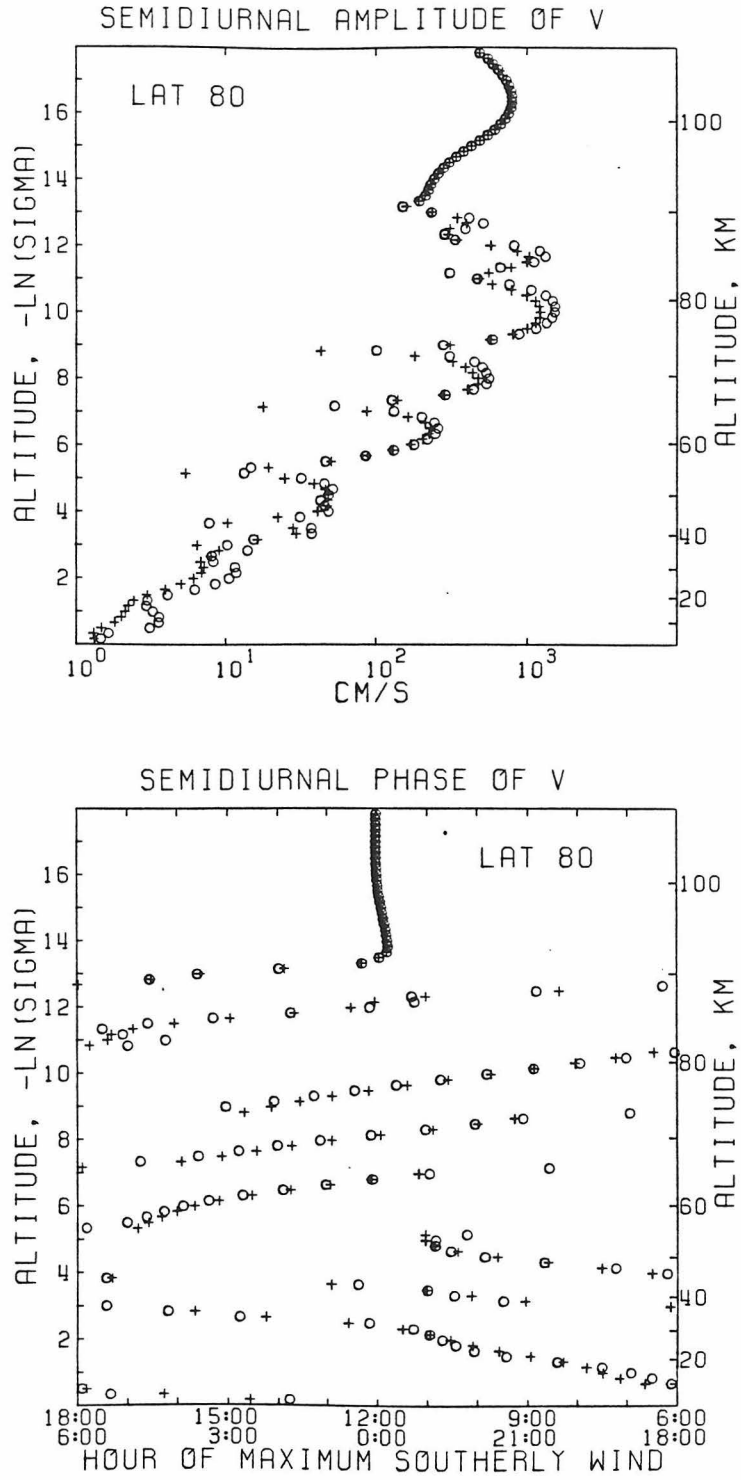


Figure 4.20b Same as Fig. 4.20a at 80°.

CONVERGENCE STUDY

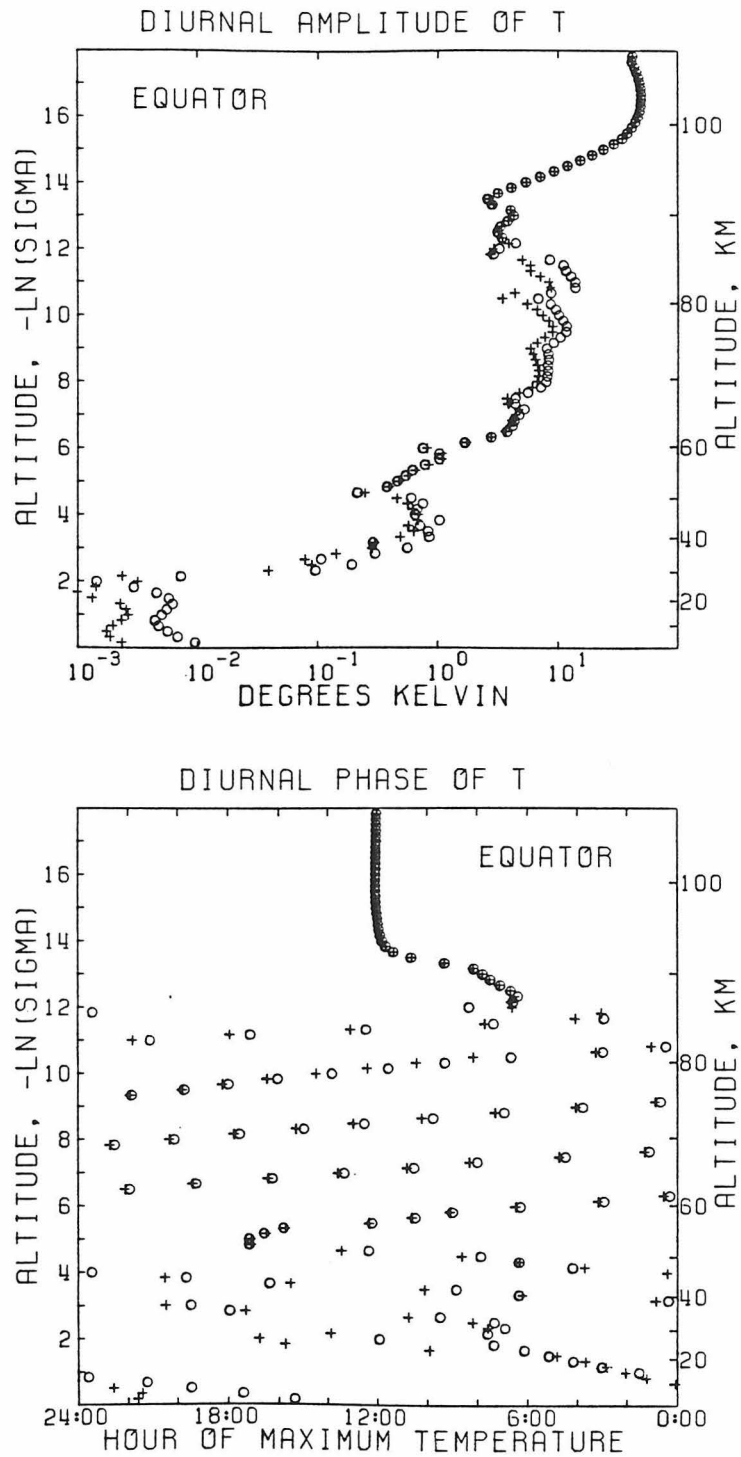


Figure 4.21a A comparison of the solutions for the diurnal temperature perturbation at the equator at 600 Δt (pluses) and 1200 Δt (circles).

CONVERGENCE STUDY

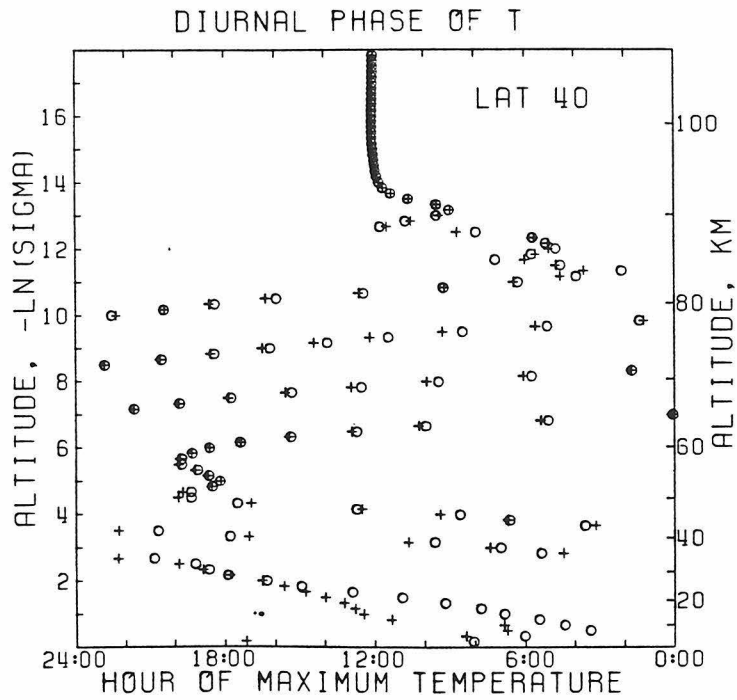
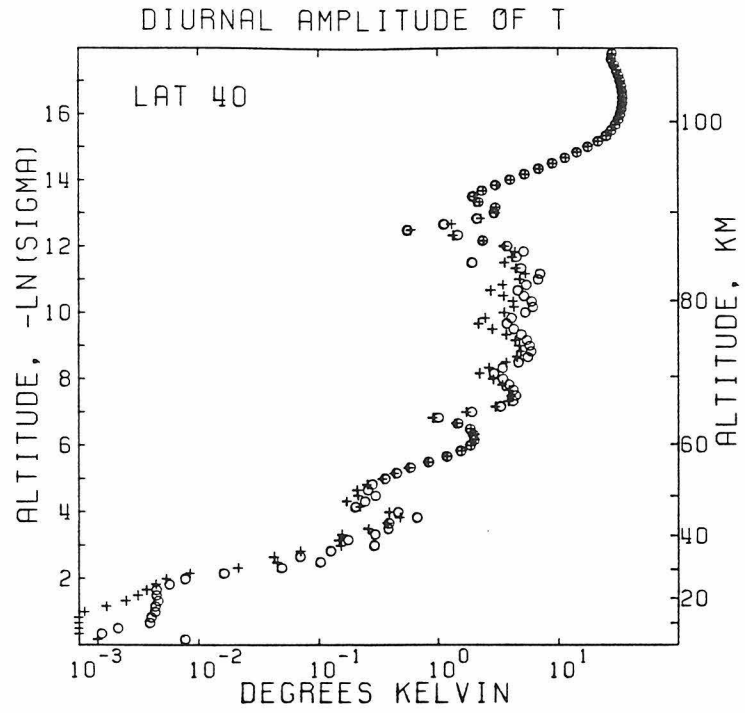


Figure 4.21b Same as Fig. 4.21a at 40°.

CONVERGENCE STUDY

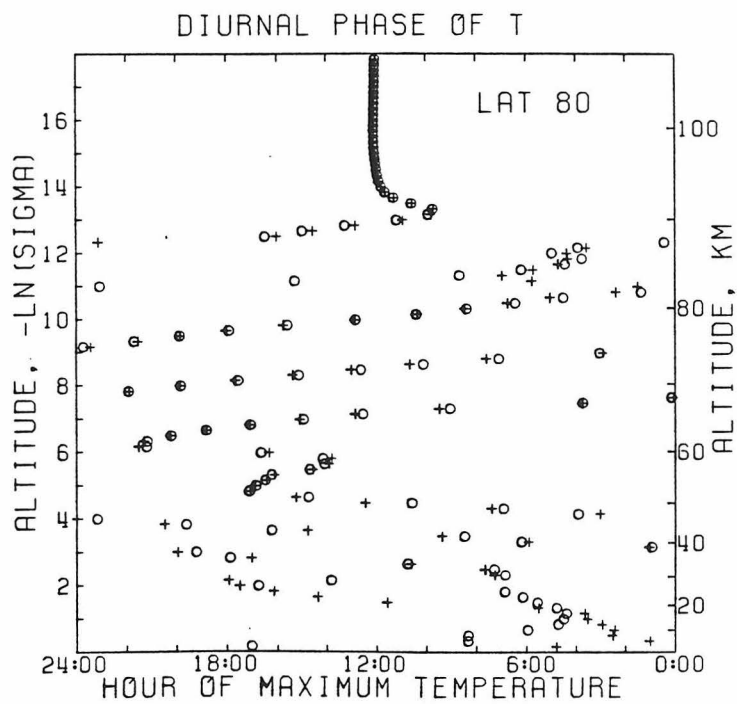
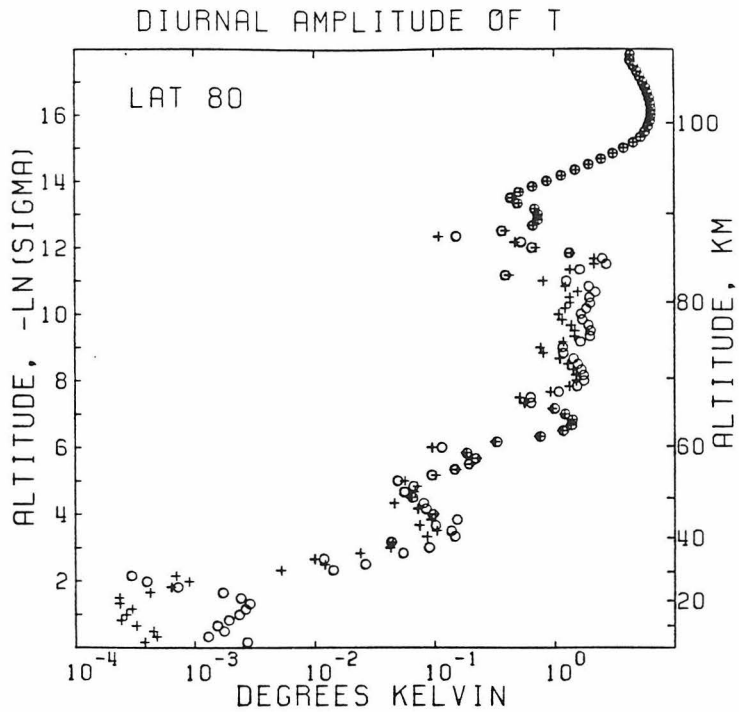


Figure 4.21c Same as Fig. 4.21a at 80°.

phase at 70 km at the equator at 600 Δt was 20:19, while at 1200 Δt it was 20:08, a change of less than 1% of the period. If the solution between 600 Δt and 1200 Δt is tracking the quadratic increase in the forcing, with little or no contribution from the free modes, then the solution at $t \rightarrow \infty$ can be estimated. The numerical solution is $T' = T'_0 + T'_1/t$ (see Section 2.2), and the final solution is T'_0 . Assuming this time dependence between 600 Δt and 1200 Δt , T'_0 and T'_1 can be calculated. The amplitude at $t \rightarrow \infty$ at 70 km at the equator is 9.11 K, a further change of 15%. The phase is 19:58, a change of about 0.5% of the period. This estimate of the change between 1200 Δt and infinity is actually an upper limit because the free modes may still be important between 600 Δt and 1200 Δt . If this were the case then part of the change between 600 Δt and 1200 Δt would decay as $1/t^2$. Because of the faster decay rate of the transient terms, the solution at 1200 Δt would be closer to the converged solution than our estimate indicates. However—to be on the safe side—the diurnal amplitudes are assumed to be good only to 15%. If the same estimate of the final solution is made for the semidiurnal tide, then at 70 km at the equator the estimated error in the amplitude at 1600 Δt is 5%, and at 80° it is 18%. The phase errors are less than 2% of the period.

Two quantitative estimates of the convergence of the solution are given in Table 4.11. Both are based on calculations of the total perturbation energy of the system. The first convergence parameter is based on the time rate of change of the energy. Since the forcing increases quadratically with time, convergence is achieved when all terms in the solution that increase less rapidly have become negligible.

TABLE 4.11

CONVERGENCE PARAMETERS

Senidiurnal Tide

Δt	800	1600	3200
C_1	.052	.027	.4
C_2	-.0006	-.0097	-.1018

Diurnal Tide

Δt	400	800	1200
C_1	.124	.094	.085
C_2	-.0124	-.0030	-.0279

If there are terms which increase faster than quadratically, i.e., an instability is present, then the solution will never completely converge. If the solution is converged, the energy should be increasing as t^4 since it depends on the square of perturbation quantities. If ε is the total energy, then $\partial\varepsilon/\partial t = 4\varepsilon/t$ for the converged solution. The first convergence parameter is defined as

$$C_1 = (\Delta\varepsilon/\Delta t - 4\bar{\varepsilon}/t) / \sqrt{\frac{1}{2} [(\Delta\varepsilon/\Delta t)^2 + (4\bar{\varepsilon}/t)^2]}$$

where $\Delta\varepsilon/\Delta t = \frac{\varepsilon(t) - \varepsilon(t - \Delta t)}{\Delta t}$ and $\bar{\varepsilon} = \frac{\varepsilon(t) + \varepsilon(t - \Delta t)}{2}$. The energy was calculated by the procedure described in Section 2.5. C_1 is the fractional change in the energy which is due to the free modes. C_1 should decrease as t increases, and the free modes and linear terms become less important. If the stable and unstable free modes are negligible, C_1 should decrease by a factor of two between $t/2$ and t . This occurs between $800 \Delta t$ and $1600 \Delta t$ for the semidiurnal tide. However, by $3200 \Delta t$ the instability has become dominant, and C_1 increases to 0.4. For the diurnal tide, C_1 decreases slowly from 0 to $1200 \Delta t$, indicating either that the free modes are still important or that the instability is affecting the convergence.

The second convergence parameter is based on a calculation of the energy balance. The procedure for calculating the discretized energy balance was discussed in Section 2.5. If all the terms are discretized correctly in space and time, then the energy balance equation should be exactly satisfied. C_2 is proportional to the sum of all the terms in the energy balance equation discretized correctly in

space but not in time. All the terms, whether implicit or explicit, were evaluated explicitly at the same time step except for the rate of change of the energy, $\Delta\varepsilon/\Delta t$, which is defined above. If the solution is converging, i.e. if it is approaching a steady state, then the imbalance caused by the incorrect time discretization should decrease with time. It turns out that C_2 is very sensitive to the presence of the instability.

Both C_1 and C_2 measure the convergence of the system as a whole by inspecting the behavior of the total energy. Even though C_1 and C_2 may be affected by the presence of the instability, the convergence over most of the atmosphere may still be very good. This could occur if the instability was confined to a small region, as seems to be the case. Of course, if the integration was extended for many more time steps, the instability would come to dominate the whole system.

The effects of increasing the vertical resolution for the semidiurnal tide are shown in Fig. 4.22 and Table 4.12. In Fig. 4.22 the circles represent the standard semidiurnal solution which was obtained using 110 points in the vertical grid. The model calculation which generated the pluses was run out to $1600 \Delta t$ and had the same input parameters as the standard case except that the number of vertical points was 218. Only every other point in the high resolution case is plotted in Fig. 4.22 for clarity. Increasing the vertical resolution had little effect on the solution, so the original resolution was adequate. A similar test was not done for the diurnal tide. Since the diurnal tide has a shorter wavelength than the semidiurnal, it may be more affected by changing the vertical resolution. The standard diurnal

VERTICAL RESOLUTION STUDY

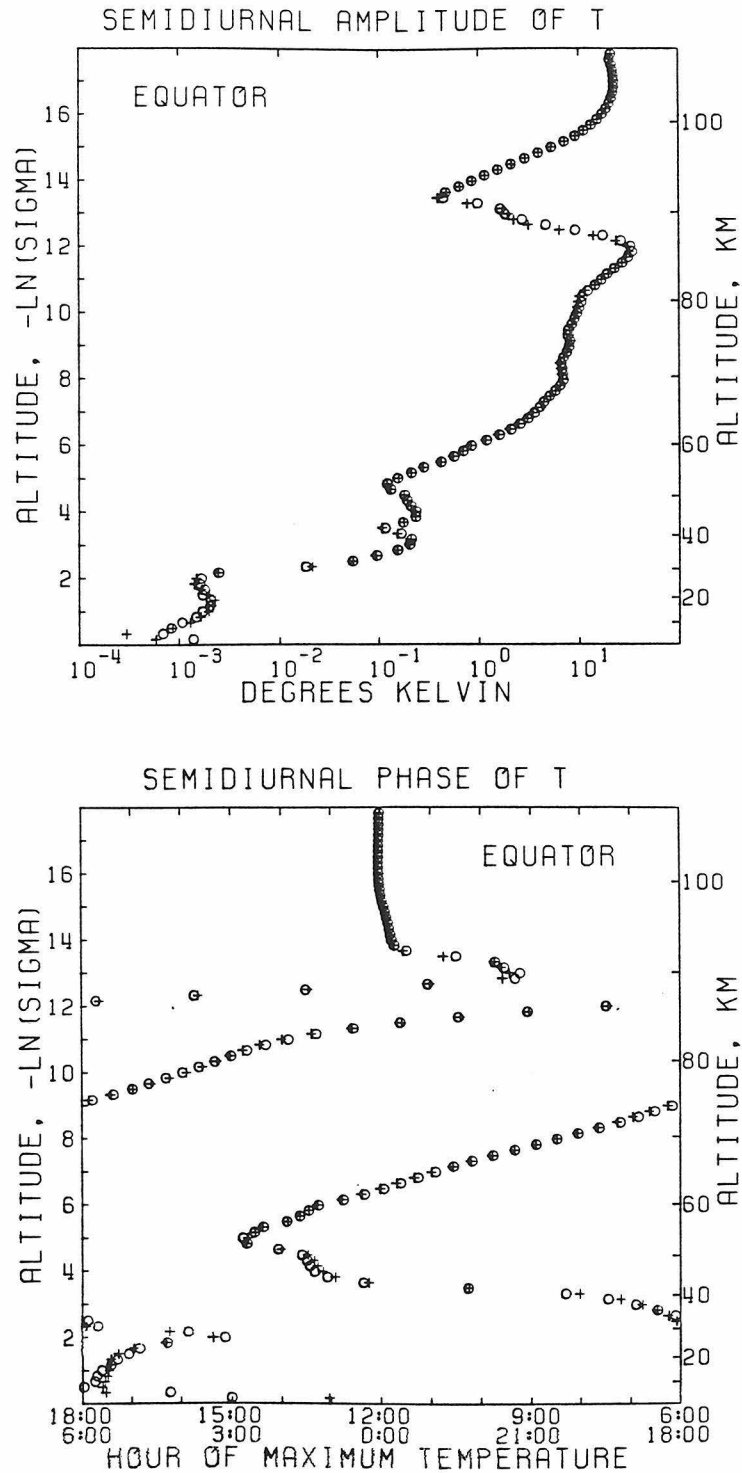
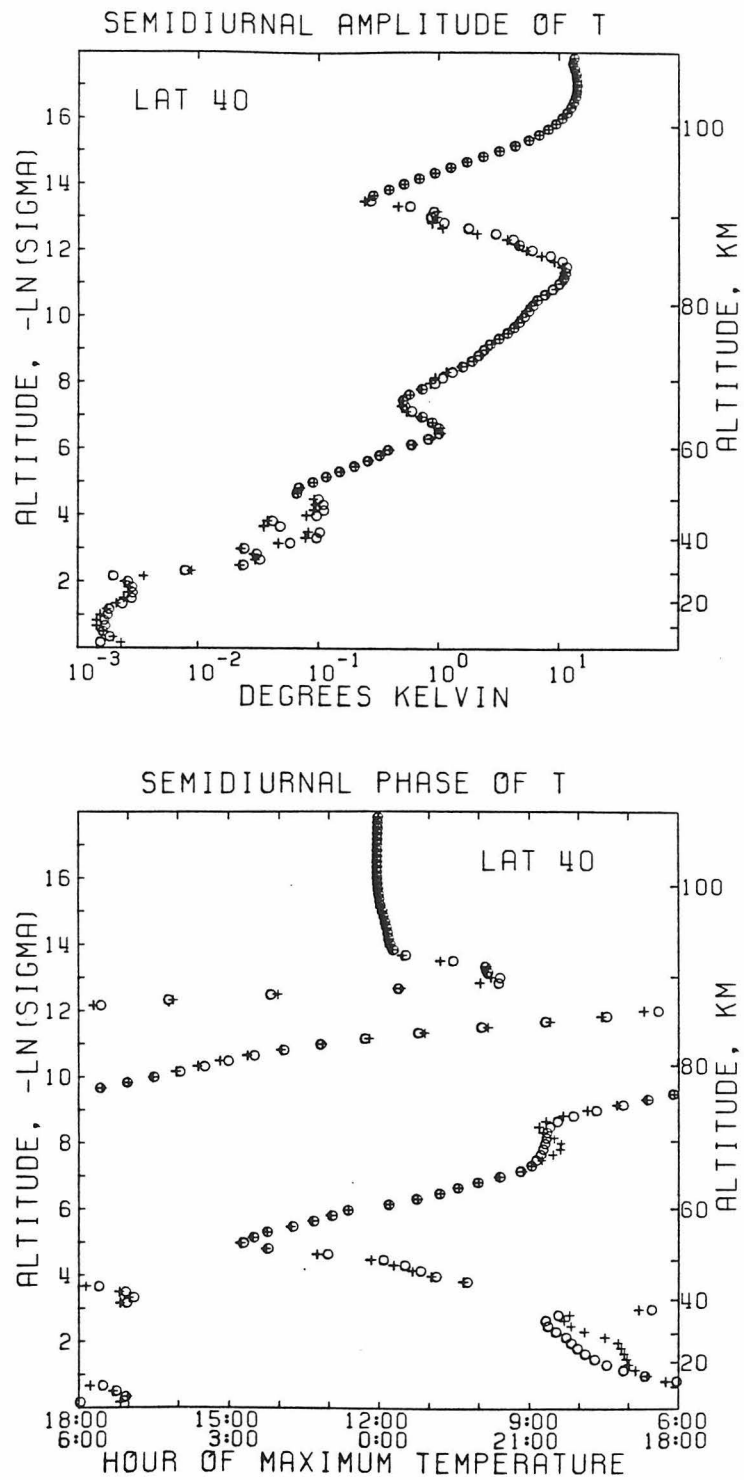


Figure 4.22a A comparison of the solutions for the semidiurnal temperature perturbation at the equator using 110 vertical points (circles) and 218 vertical points (pluses). Only every other point in the high resolution case is plotted.

VERTICAL RESOLUTION STUDY

Figure 4.22b Same Fig. 4.22a at 40° .

VERTICAL RESOLUTION STUDY

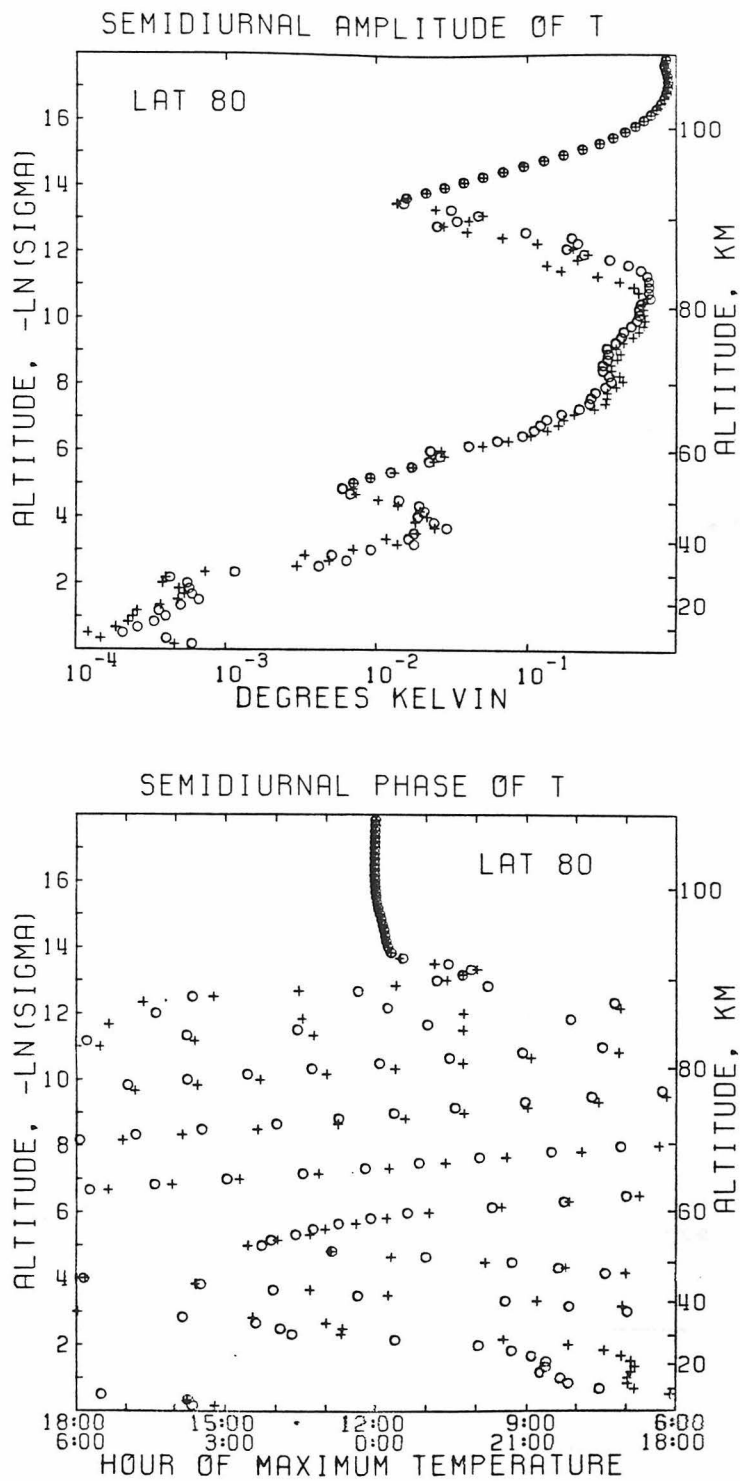


Figure 4.22c Same as Fig. 4.22a at 80°.

TABLE 4.12

SEMIDIURNAL TIDE

Standard Case: NVPTS = 110, NMODE = 3, Δt = 7200 sec

Δt	800	1600
C_1	.052	.027
C_2	-.00061	-.0097

Higher Vertical Resolution: NVPTS = 218, NMODE = 3, Δt = 7200 sec

Δt	800	1600
C_1	.055	.037
C_2	-.00036	-.0085

Higher Horizontal Resolution: NVPTS = 110, NMODE = 5, Δt = 7200 sec

Δt	800	1600
C_1	.051	.030
C_2	-.0012	-.0102

Smaller Time Step: NVPTS = 110, NMODE = 3, Δt = 3600 sec

Δt	1600	3200
C_1	.052	.027
C_2	-.00044	-.0093

case has about 20 points per wavelength. For this resolution the error in the wavelength or phase should be about 3%. The error in the amplitude should be much smaller. These estimates are based on a simple model of a discretized sine wave. The effect of increasing the resolution on the convergence is shown in Table 4.12. C_2 is proportional to the vertical spacing, so it should decrease if the spacing is decreased. C_1 should remain unchanged. These expectations are met approximately at 800 Δt , but at 1600 Δt the values of C_1 and C_2 indicate that the instability is growing faster for the higher resolution case. This behavior does not rule out either a numerical or physical instability.

A similar study to investigate the effects of increasing the horizontal resolution was performed. The results are shown in Fig. 4.23 and Table 4.12 for the semidiurnal tide and in Fig. 4.24 and Table 4.13 for the diurnal tide. Only every other point is plotted in Fig. 4.24. To increase the horizontal resolution the number of even Legendre modes was increased from 3 to 5, and the number of points in the Gaussian $\sin \lambda$ grid was increased from 7 to 12. From Fig. 4.23, it can be seen that increasing the horizontal resolution has little effect on the semidiurnal tide. The same is true of the diurnal tide from the equator to mid-latitudes (Fig. 4.24a and b). At high latitudes, as shown in Fig. 4.24c, the higher resolution diurnal case has a more extensive region of nearly constant phase from 50 km to 75 km. As discussed in the previous section and in Chapter 2, the diurnal tide may be trapped at high latitudes in a rapidly rotating atmosphere. If this is the case the solution has a fundamentally different character at high and low

HORIZONTAL RESOLUTION STUDY

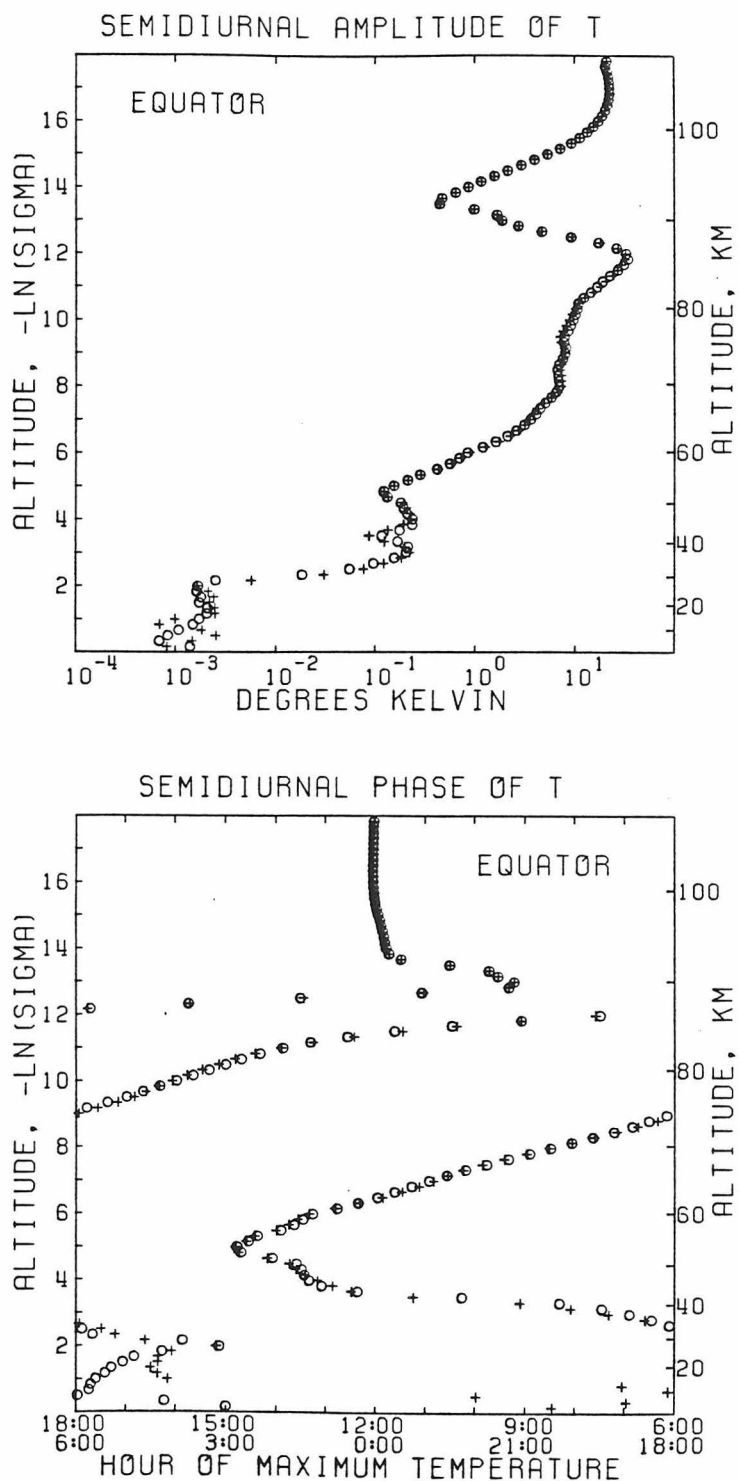


Figure 4.23a The standard solution for the semidiurnal temperature perturbation at the equator (circles) and a solution obtained with higher resolution in latitude (pluses). The number of Legendre modes was increased from 3 to 5.

205
HORIZONTAL RESOLUTION STUDY

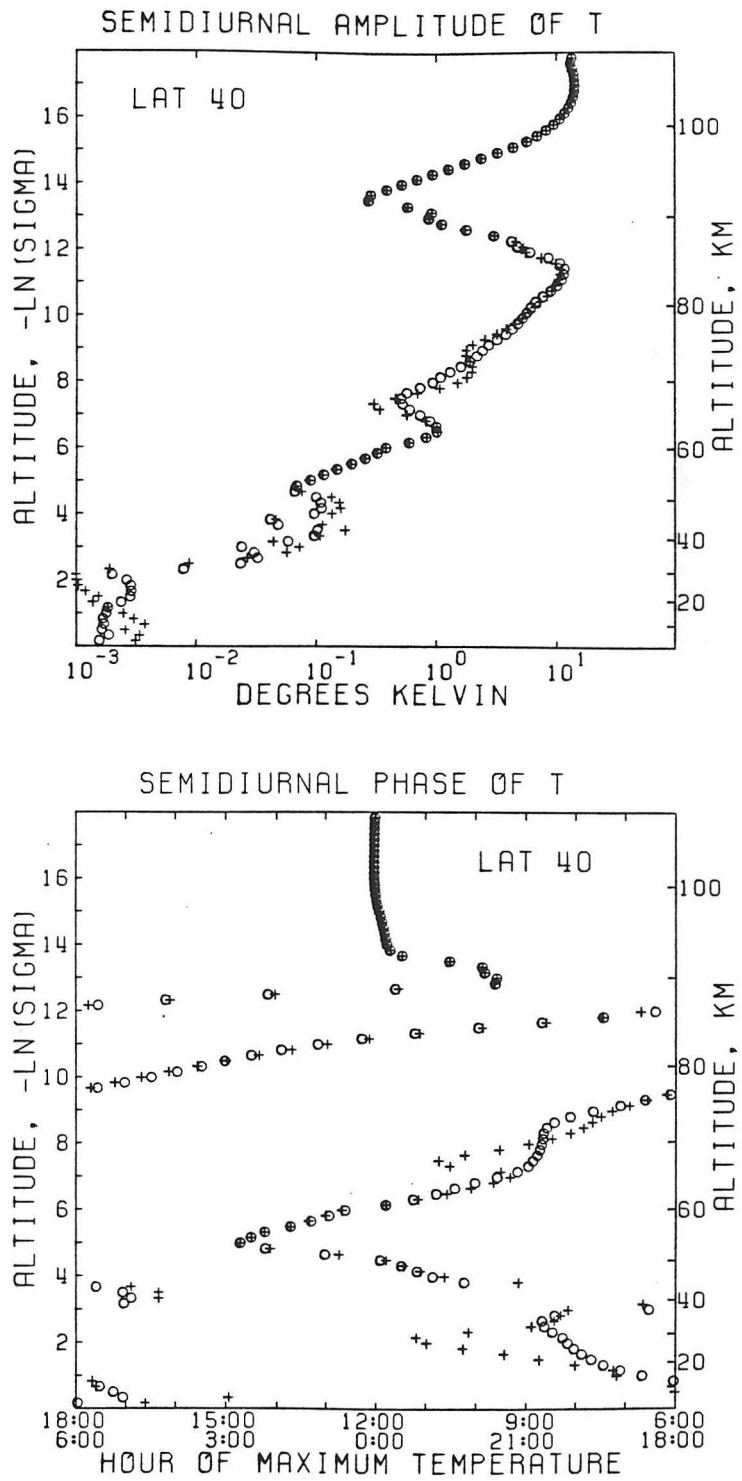


Figure 4.23b Same as Fig. 4.23a at 40°.

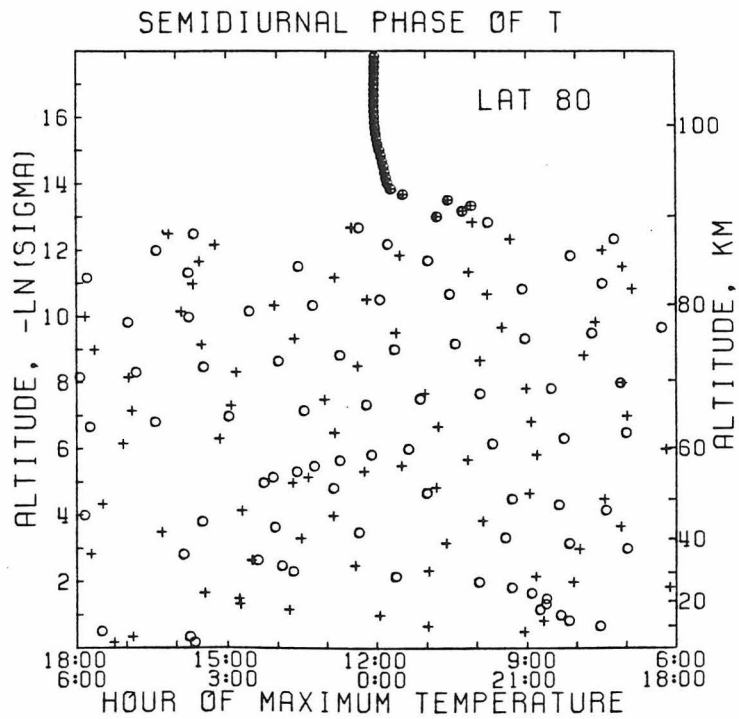
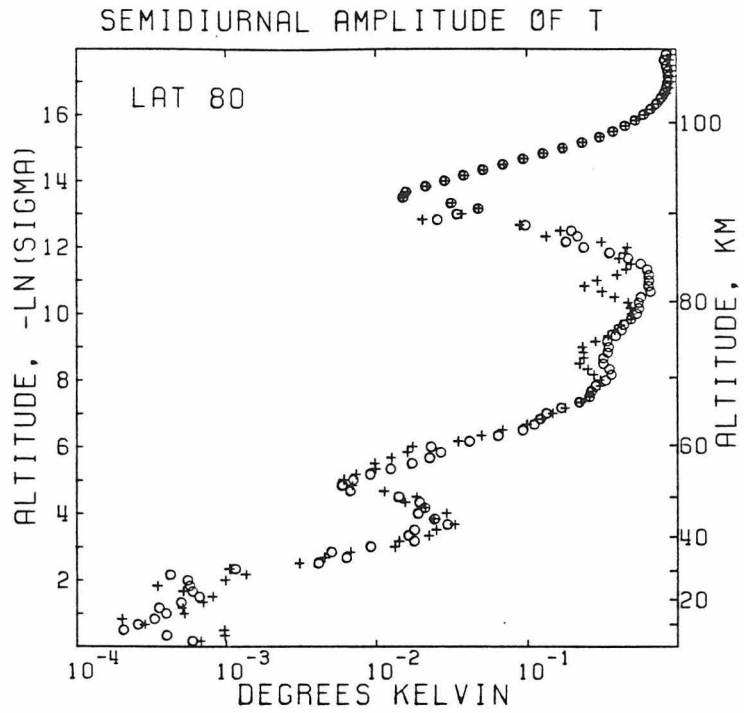


Figure 4.23c Same as Fig. 4.23a at 80°.

HORIZONTAL RESOLUTION STUDY

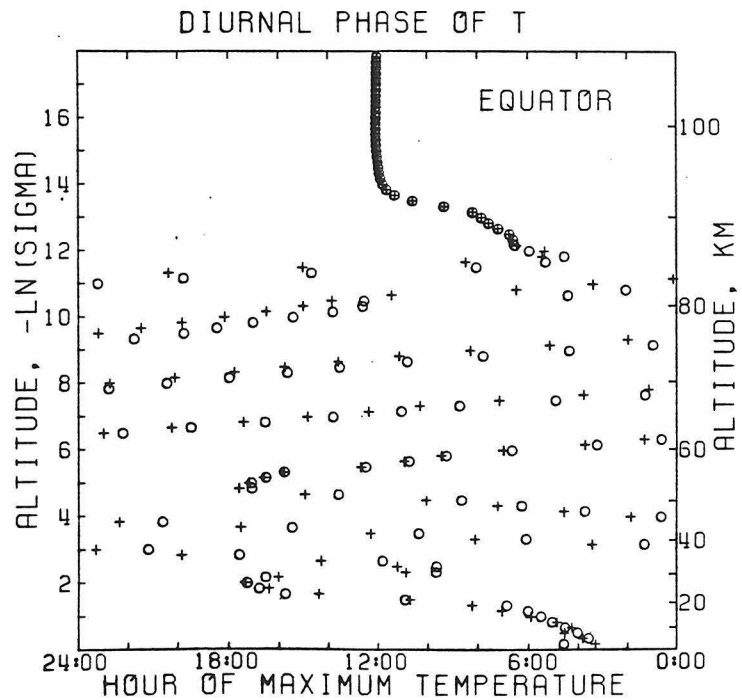
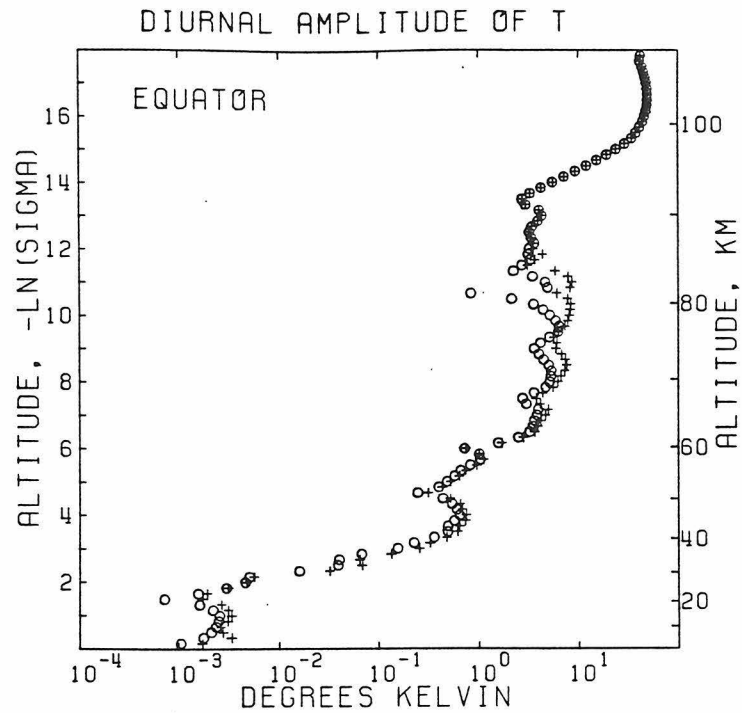


Figure 4.24a The standard solution for the diurnal temperature perturbation at the equator (circles) and a solution obtained with higher resolution in latitude (pluses). The number of Legendre modes was increased from 3 to 5. Only every other vertical point is plotted.

HORIZONTAL RESOLUTION STUDY

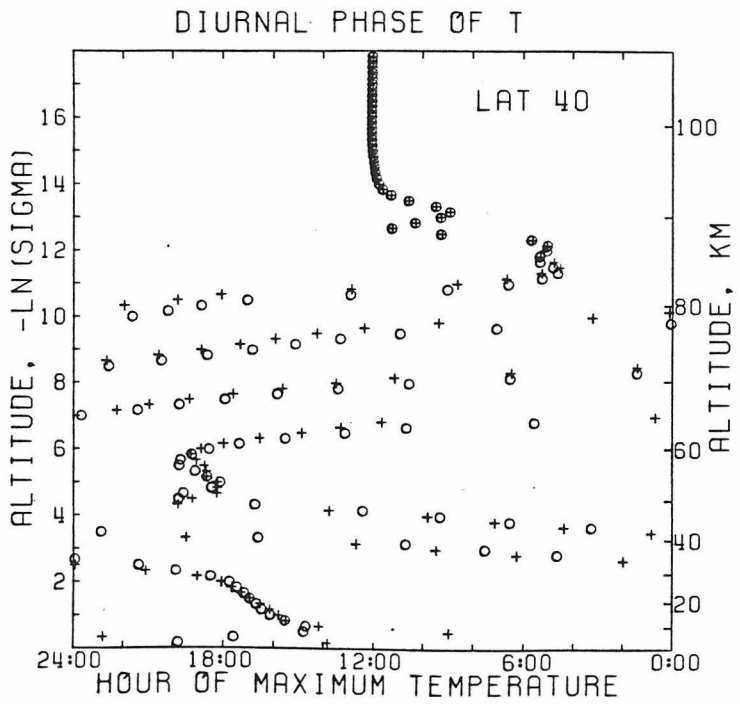
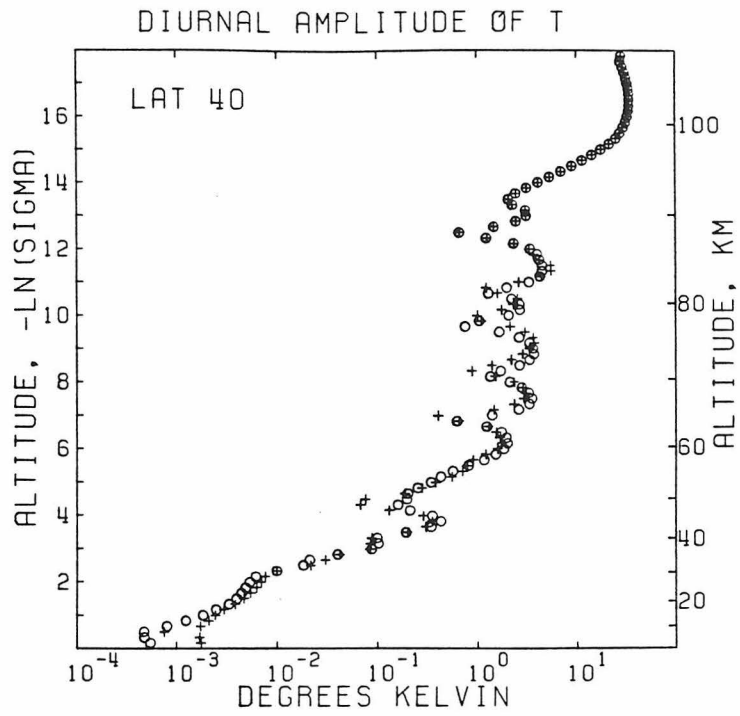


Figure 4.24b Same as Fig. 4.24a at 40°.

HORIZONTAL RESOLUTION STUDY

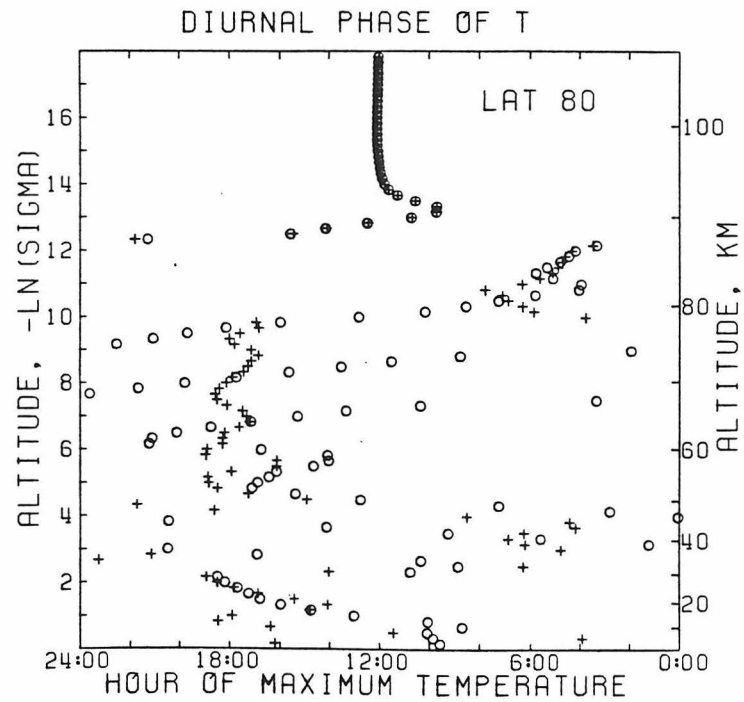
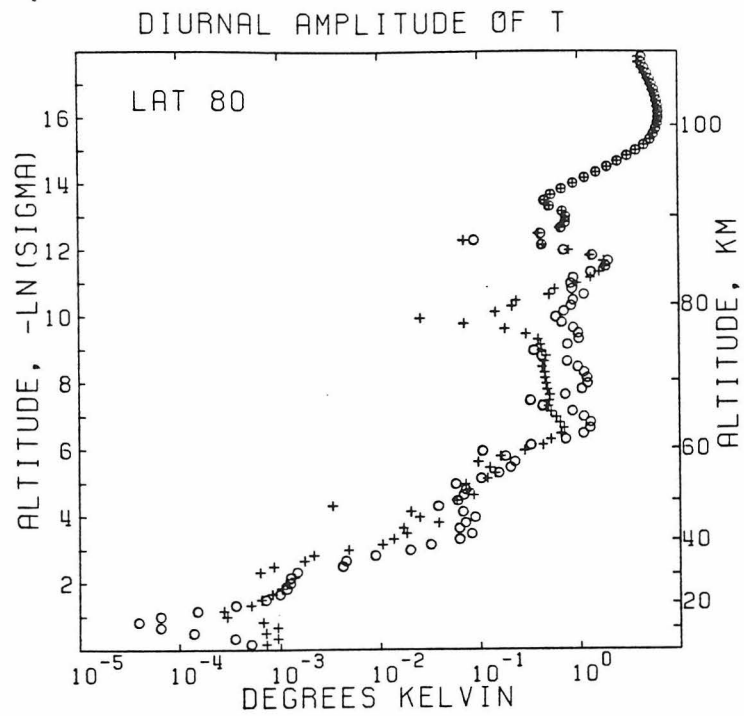


Figure 4.24c Same as Fig. 4.24a at 80°.

TABLE 4.13

DIURNAL TIDE

Standard Case: NVPTS = 218, NMODE = 3, Δt = 14,400 sec

Δt	400	800
C_1	.124	.094
C_2	-.0124	-.0030

Higher Horizontal Resolution: NVPTS = 218, NMODE = 5, Δt = 14,400 sec

Δt	400	800
C_1	.104	.306
C_2	-.0267	-.0801

latitudes, and higher horizontal resolution is required to resolve this difference. The higher Legendre modes have relatively more amplitude at high latitudes, so including more modes results in a more accurate solution there. It is unclear how much further the solution at high latitudes would be altered by adding even more modes, but at any rate, the resolution of the standard case is inadequate for the diurnal tide at high latitudes. Since there are several other reasons why the solution at high latitudes cannot be trusted, this is not a serious drawback.

The convergence parameters shown in Tables 4.12 and 4.13 indicate that increasing the horizontal resolution causes an increase in the growth rate of the instability, just as increasing the vertical resolution did. The effect the spatial resolution has on the growth rate may indicate that the instability is numerical, since for certain instabilities the growth rate is proportional to $\Delta t/\Delta x$ where Δx is the effective resolution of the spatial grid. The instability may also be physical and be characterized by a short spatial length scale which is better resolved in the higher resolution cases. In the standard case the instability would have been suppressed by the low resolution.

If the instability is numerical then decreasing the time step should have the effect of slowing down the growth rate. This is not the case as shown in Table 4.12 for the semidiurnal tide. Although there is some early improvement, after $.1152 \times 10^8$ sec (1600 Δt in the standard case and 3200 Δt with the shorter time step) there is no appreciable difference. Thus, it seems likely that the instability is physical and has a short spatial length scale. It would be interesting to determine

the exact nature of this instability. Hopefully, this will be the subject of future work with this model. With respect to the present study of tides, we are fortunate that the solution is adequately converged, as shown in Figs. 4.18-4.21, before the instability becomes important over most of the atmosphere.

4.5 Sensitivity to Basic State and Forcing Parameters

The purpose of this section is to assess the effect on the solution of changing various parameters in the basic state and forcing functions. Most of the cases to be presented were obtained using the gravity wave model which is much cheaper to run than the full LPE model. Another advantage of the gravity wave model is that it can be run until convergence is achieved at all levels without becoming unstable. The gravity wave model is described in detail in section 2.4. First we compare the gravity wave model solution to that of the full model at the equator for the standard basic state and forcing described in Chapter 3. The agreement of the two models establishes that the gravity wave model is a valid approximation to the tidal problem at low latitudes. We also have two cases in which the LPE model was run with a slightly modified basic state; these cases will be compared to analogous gravity wave runs. A series of gravity wave runs will then be presented in which the changes in the basic state range from minor alterations to major revisions which completely alter the nature of the solution. It is by no means an exhaustive study since the number of combinations of parameters is infinite. We concentrate on cases in the neighborhood of our standard basic state to show that the solution is not overly sensitive to slight modifications. In some of these cases the amplitude and phase changed enough to seriously affect the agreement with the OIR data, but the general structure of the solution is unaffected. We will also present a few cases in which large, and usually unrealistic, changes are made in the basic state. These cases illustrate part of the possible range of solutions. All the discussion in this section will

deal with the temperature perturbations. The other variables exhibit a similar degree of dependence on the input parameters.

In Figs. 4.25 and 4.26 we compare the results of the gravity wave model to those of the LPE model at the equator for the standard basic state for the semidiurnal and diurnal tides. As shown in section 2.4, the gravity wave model should give a better approximation to the tidal structure at the equator than at other latitudes. Both models were run with the same vertical resolution. We were able to use a time step twice that of the LPE model in the gravity wave model. The additional spatial dimension in the LPE model apparently introduces higher frequency free modes which would be unstable unless a short time step is used. The gravity wave model was run for 800 time steps except where otherwise noted. The time step was 4 hours for the semidiurnal tide and 8 hours for the diurnal tide.

The semidiurnal amplitudes and phases from the two models in Fig. 4.25 are in good qualitative agreement. The major discrepancies are in the amplitude below 30 km and between 90 and 100 km and in the phase below 50 km. The best agreement seems to be where the mean zonal wind is greatest. The approximation which was made to separate the tidal problem in height and latitude in the gravity wave model involves a modification of the horizontal wavelength which depends on the mean zonal wind. It is possible that this modification results in a more inaccurate solution when u^* is small.

The agreement in the diurnal amplitudes and phases in Fig. 4.26 is quite poor. Thus, the gravity wave model does not result in as good an approximation for the diurnal as for the semidiurnal tide. This may

GRAVITY WAVE MODEL
SEMIDIURNAL AMPLITUDE AND PHASE OF T

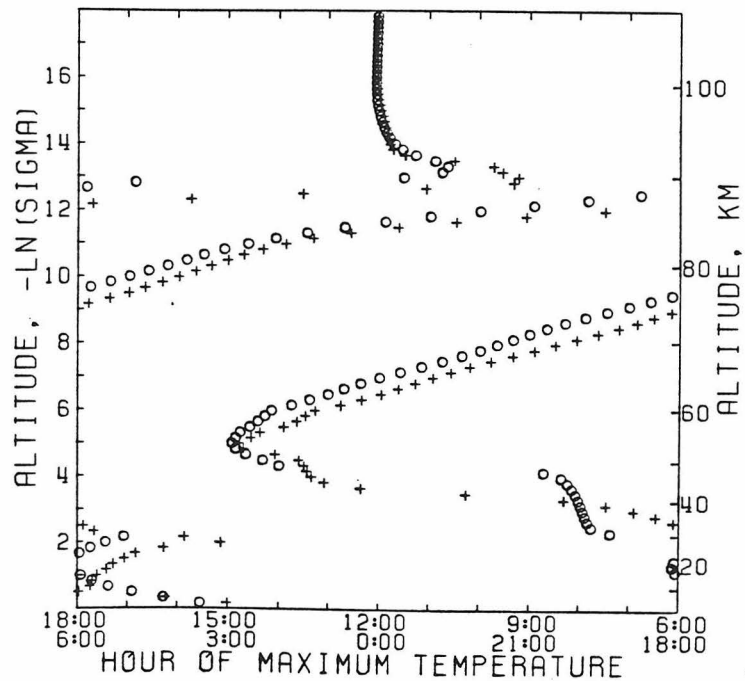
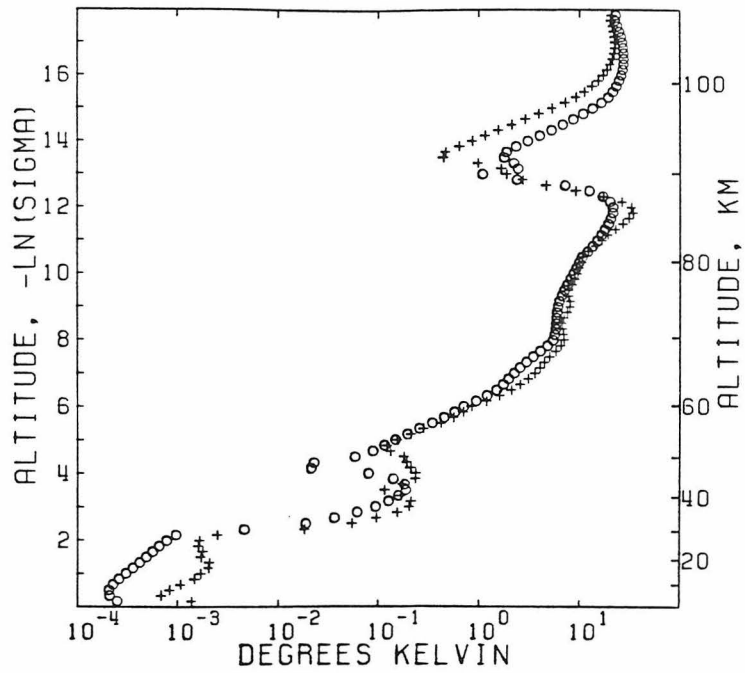


Figure 4.25 The equatorial semidiurnal temperature perturbation predicted by the gravity wave model (circles) and the LPE model (pluses) using the standard basic state and forcing described in Chapter 3.

GRAVITY WAVE MODEL
DIURNAL AMPLITUDE AND PHASE OF T

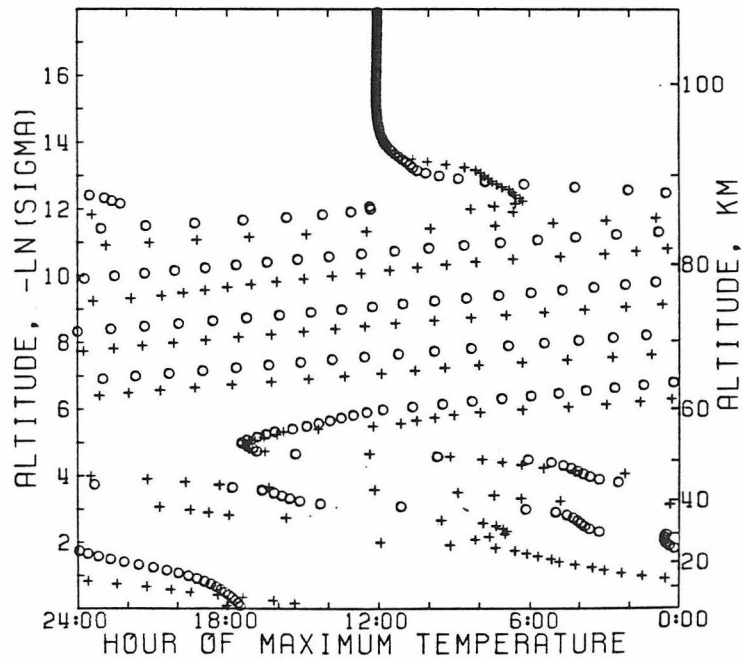
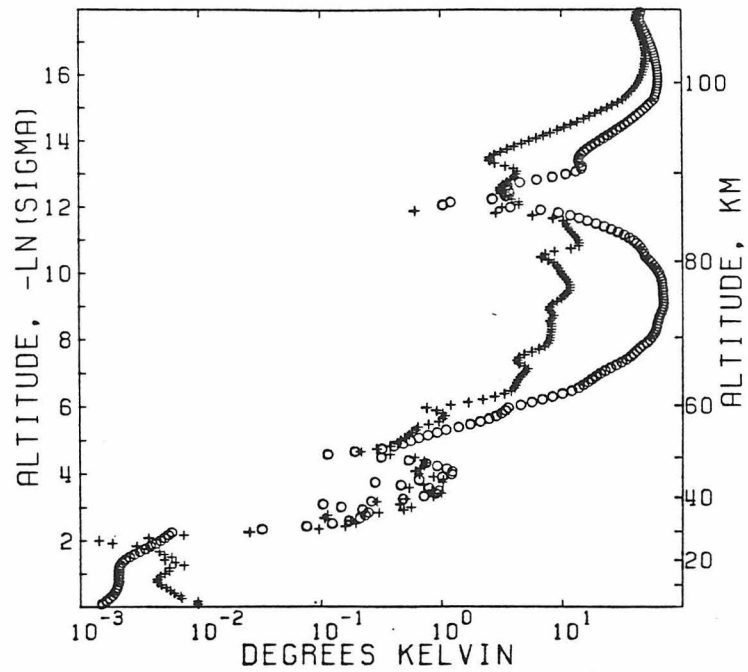


Figure 4.26 The equatorial diurnal temperature perturbation predicted by the gravity wave model (circles) and the LPE model (pluses) using the standard basic state and forcing described in Chapter 3.

TABLE 4.14 - GRAVITY WAVE AND LPE MODEL COMPARISON

CHANNEL	Amplitude, Deg.		Phase, Hour of Max.	
	Gravity Wave	LPE at 0°	Gravity Wave	LPE at 0°
<u>SEMIDIURNAL TIDE</u>				
1	9.9	4.9	11:57	11:58
2	4.1	3.5	12:57	12:27
3	3.2	4.4	6:58	5:54
4	2.3	3.1	10:09	9:16
5	2.3	3.3	10:54	10:00
<u>DIURNAL TIDE</u>				
1	35.4	17.4	11:57	11:59
2	4.5	2.0	12:38	9:48
3	0.9	1.3	16:20	17:36
4	1.6	0.7	16:43	16:34
5	3.1	0.7	18:11	15:00

be due to the greater degree of latitudinal and vertical structure in the diurnal tide which could make the separability approximation less valid. In the rest of this section we will deal only with the semidiurnal tide. However, the general properties of the diurnal solutions in Fig. 4.26 are similar. The vertical wavelengths are nearly the same, and the most significant difference in the amplitudes is due to the more pronounced maximum in the gravity wave between 65 and 86 km.

A quantitative comparison of the gravity wave and LPE model results is given in Table 4.14. This table gives the brightness temperature amplitudes and phases in the OIR channels for the cases plotted in Figs. 4.25 and 4.26. Even for the semidiurnal tide the gravity wave model gives only fair agreement with the LPE model. Thus, the LPE model was needed to match the OIR data even at the equator. If the gravity wave model had been used, the best fit to the data would have been obtained for a basic state significantly different from our standard basic state.

In Fig. 4.27 we show the results of running both the LPE and gravity wave models with a slightly different profile of Γ^* . In the standard case (Fig. 3.6) there is a peak in Γ^* at 70 km where $\Gamma^* = 11$ K/km. In the present case the peak value is 10.5 K/km at 75 km, and the peak is slightly broadened. Also, Γ^* at 60 km is increased to 2 K/km from 1 K/km. The LPE model in this case was run for only 800 time steps so the convergence is not quite as good as the standard case. The solutions in Fig. 4.25 and 4.27 are very similar, and the agreement between the two models is also about the same. The major change in both models is in the vertical wavelength between 60 and 70 km. The

semidiurnal brightness temperature amplitudes and phases at the equator in the OIR channels for the modified Γ^* profile are given in Table 4.15 for the LPE model. A comparison of this table with the standard case and the OIR data given in Table 4.1 shows that this modification of Γ^* does not result in large changes.

The same is not true of the next case given in Fig. 4.28 and Table 4.15. In this case the standard Γ^* profile was used but the maximum equatorial wind was reduced to 100 m/s from 125 m/s. The LPE model was run for 800 time steps. Again, the general vertical structure is unchanged, but the amplitudes and phases in the OIR channels are significantly different. The values in the OIR channels are affected because the vertical wavelength from about 65 to 90 km is shorter than in the standard case. The dispersion relation for gravity waves derived in section 2.4 predicts a shorter wavelength when u^* is decreased. Because of the averaging effect of the weighting functions, the shorter wavelength causes the amplitudes in the OIR channels to decrease. Also, the phase as a function of height is affected by the change in wavelength, and this shows up after convolution with the weighting functions in Table 4.15. As mentioned in Chapter 3, the maximum zonal wind reached above the clouds has not been directly measured. The poor agreement with the OIR data, particularly the phases, in this case illustrates why a maximum u^* of 125 m/s was chosen for the standard case. It may be possible to get better agreement with a smaller value of u^* using a different Γ^* profile. However, it would be difficult because Γ^* may not be changed arbitrarily. The temperature profile derived from the stability must be realistic.

GRAVITY WAVE MODEL
SEMIDIURNAL AMPLITUDE AND PHASE OF T

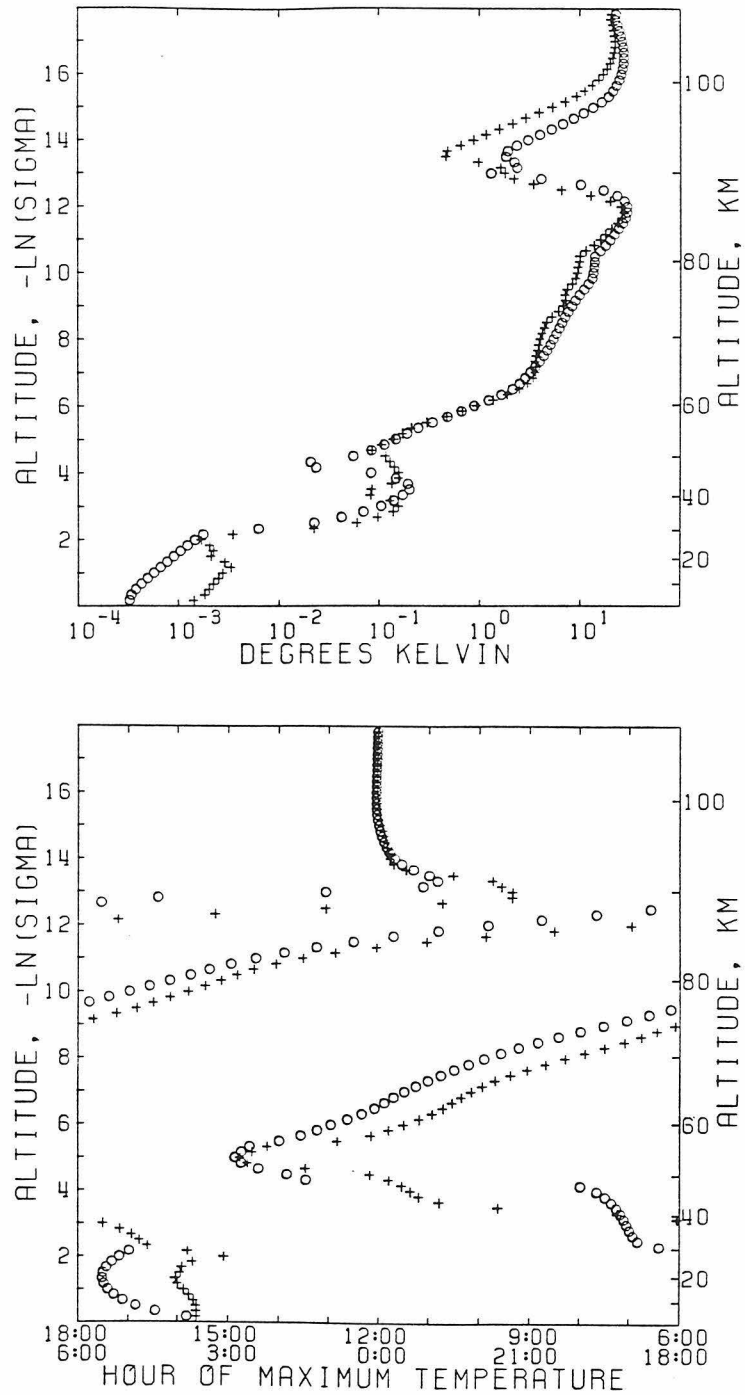


Figure 4.27 The equatorial semidiurnal temperature perturbation predicted by the gravity wave model (circles) and the LPE model (pluses) with the modified Γ^* profile described in the test. Except for Γ^* the standard input parameters for the basic state and forcing were used.

GRAVITY WAVE MODEL
SEMIDIURNAL AMPLITUDE AND PHASE OF T

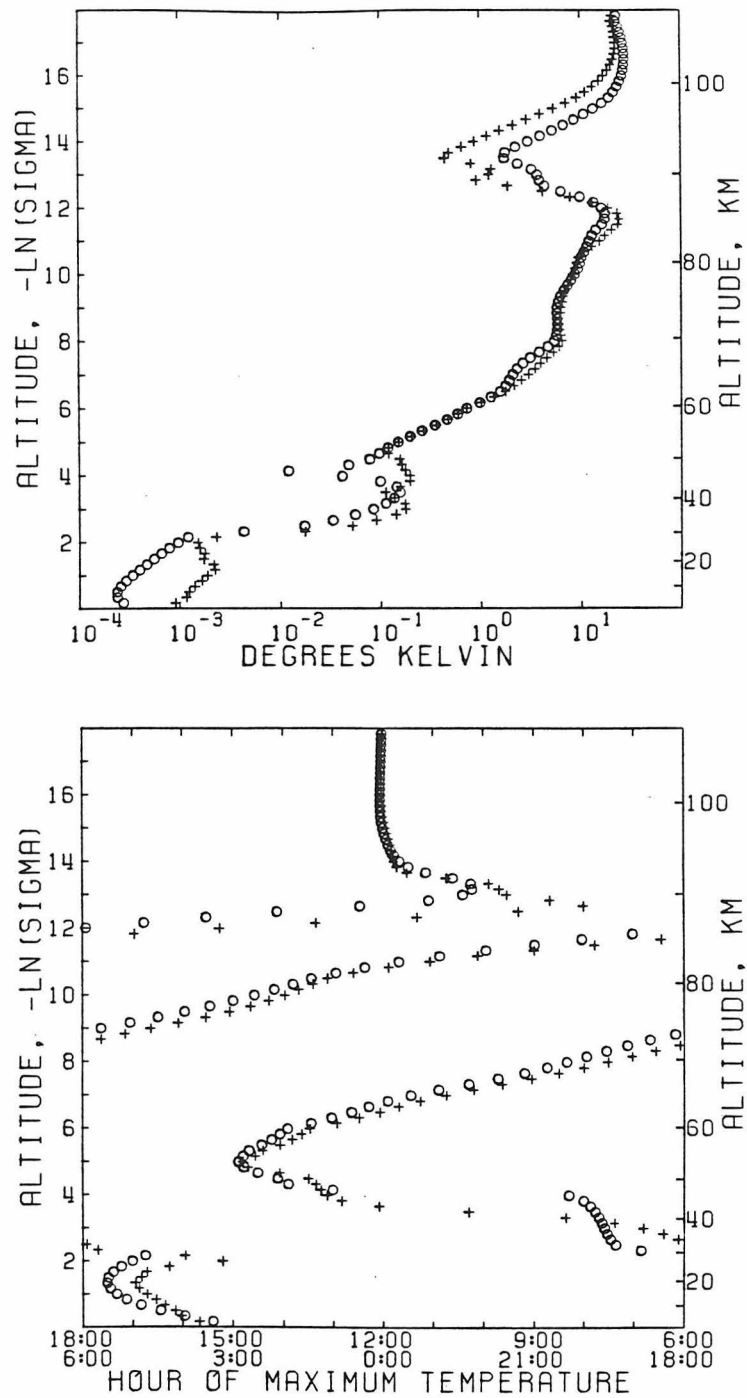


Figure 4.28 The equatorial semidiurnal temperature perturbation predicted by the gravity wave model (circles) and the LPE model (pluses) with a maximum mean zonal wind of 100 m/s. Except for u^* the standard input parameters for the basic state and forcing were used.

TABLE 4.15

SENSITIVITY OF LPE MODEL TO BASIC STATE PARAMETERS

SEMIDIURNAL TIDE AT THE EQUATOR

	CHANNEL	AMPLITUDE, DEG	PHASE, HOUR OF MAX.
Standard Basic State*	1	4.8	11:58
	2	3.5	12:29
	3	3.8	5:53
	4	2.7	9:13
	5	2.9	9:56
Modified Γ^* Profile (Described in Text)	1	4.9	11:58
	2	3.0	12:16
	3	3.6	5:24
	4	2.7	9:08
	5	3.1	9:41
Maximum u^* = 100 m/s	1	4.9	11:58
	2	1.7	10:36
	3	2.9	4:24
	4	2.2	8:35
	5	2.4	9:26

* 800 time steps

It is interesting that in the case of maximum $u^* = 100$ m/s the agreement between the gravity wave model and the LPE model is better than in the standard case, as can be seen by comparing Figs. 4.25 and 4.28. This may be because a smaller maximum value of u^* results in less shear. If there were no shear, the tidal problem would be separable and the gravity wave model would give the exact solution. Thus, a basic state with less shear may result in a better approximation by the gravity wave model.

In Figs. 4.29 and 4.30 we further explore the sensitivity of the solution to the basic state zonal wind profile using the gravity wave model. In Fig. 4.29 we compare the standard case to a case in which the zonal wind has constant shear with respect to $\ln\sigma$ below 70 km. This change to a smoother profile has very little effect on the solution except on the phase below about 30 km. The phases in the OIR channels are nearly unchanged from the standard gravity wave case, while the amplitudes in channels 2-5 decrease by an average of 0.6 K. Thus, the solution seems to be less sensitive to the details of the u^* profile below 70 km than to the value of the peak zonal wind at 70 km.

In Fig. 4.30 we present a case in which the zonal wind remains at 125 m/s above 70 km. With $u^* = 125$ m/s up to the top level in the model, the wavelength above 70 km is increased, significantly affecting the amplitude and phase in OIR channels 1-3. The solution is not completely damped at high altitudes because the sponge layer is less effective when τ is a larger fraction of the local diurnal period. It may be possible by adjusting the damping and the static stability to reach agreement with the OIR data for a basic state with some degree of

GRAVITY WAVE MODEL
SEMIDIURNAL AMPLITUDE AND PHASE OF T

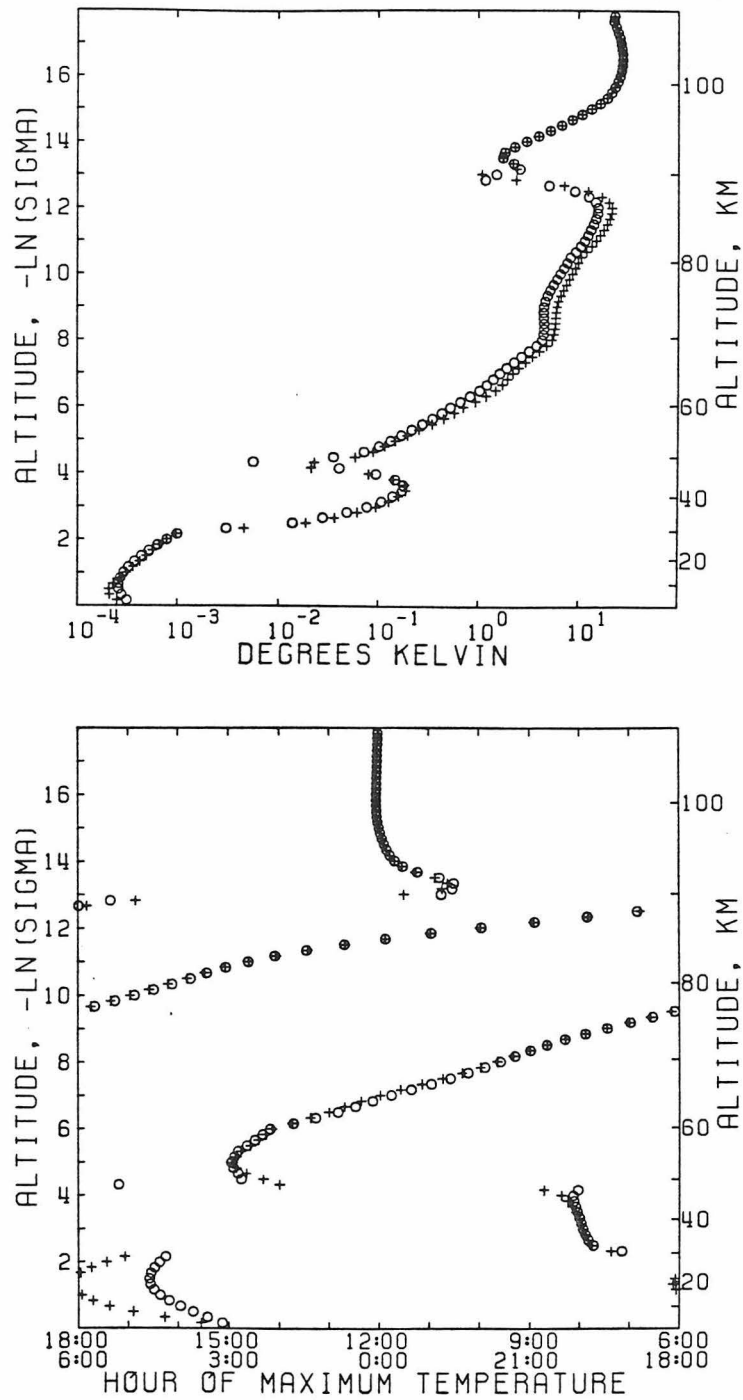


Figure 4.29 A comparison of the gravity wave model solutions for the semidiurnal temperature perturbation using the standard u^* profile (pluses) and a profile with constant shear with respect to $\ln \sigma$ below 70 km (circles). Except for u^* the standard basic state and forcing were used in both cases.

GRAVITY WAVE MODEL
SEMIDIURNAL AMPLITUDE AND PHASE OF T

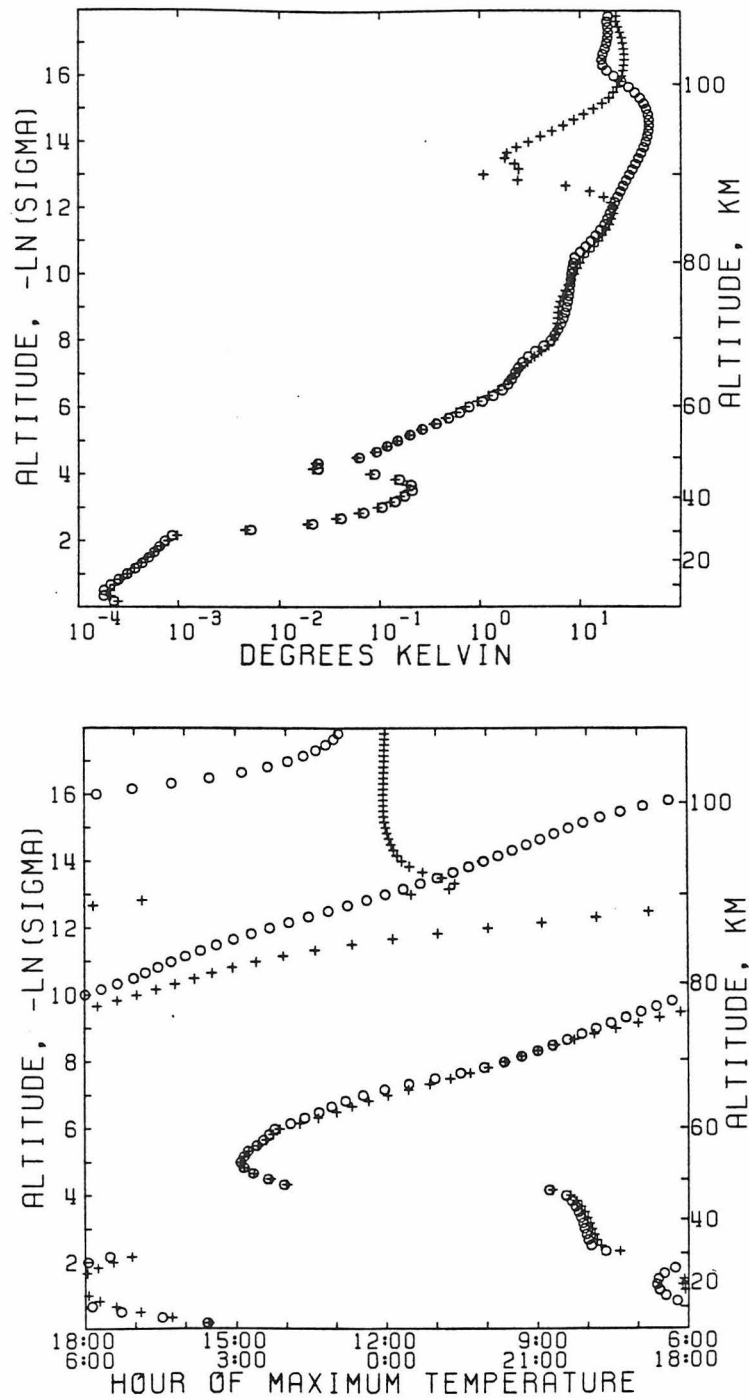


Figure 4.30 A comparison of the gravity wave model solutions for the semidiurnal temperature perturbation using the standard u^* profile (pluses) and a profile with $u^* = 125$ m/s above 70 km (circles). Except for u^* the standard basic state and forcing were used in both cases.

super-rotation above 90 km. It is possible that this situation exists on Venus because no direct wind velocity measurements have been made in the upper atmosphere. However, it is unlikely because the OIR measurements show that the mean temperature of the pole is warmer than the equator on constant pressure surfaces above 70 km, and when cyclostrophic balance is assumed, this temperature gradient tends to produce a decrease of the zonal wind with height (Taylor et al., 1980).

In Chapter 3 it was mentioned that just before the Pioneer Venus probes failed they observed increasing static stability as they descended (Seiff et al., 1980). In Fig. 4.31 we examine the effects of higher stability in the lower atmosphere by comparing a case with $\Gamma^* = 0.5$ K/km below 30 km with the standard case which has $\Gamma^* = 0.05$ K/km. The case with $\Gamma^* = 0.5$ K/km was run for 1600 time steps because the higher stability slows down the convergence. Below 30 km the amplitude is greatly increased, and the phase is seriously affected. Thus, the tidal perturbations near the ground cannot be determined accurately until the static stability there is known. Fortunately, the solution above 30 km is not sensitive to this change in Γ^* .

Another parameter whose effect on the solution ought to be determined is τ_R , the time constant for Rayleigh friction. We have used τ_R to model small scale momentum dissipation, but its value was chosen somewhat arbitrarily. The standard profile for τ_R is shown in Fig. 3.13. We may decrease τ_R by a factor of 2 with only minor effects on the solution as shown in Fig. 4.32. A change of the same magnitude in the opposite direction occurs if τ_R is increased by a factor of 2. Only the amplitude in channel 1 is significantly affected. Thus, the

GRAVITY WAVE MODEL
SEMIDIURNAL AMPLITUDE AND PHASE OF T

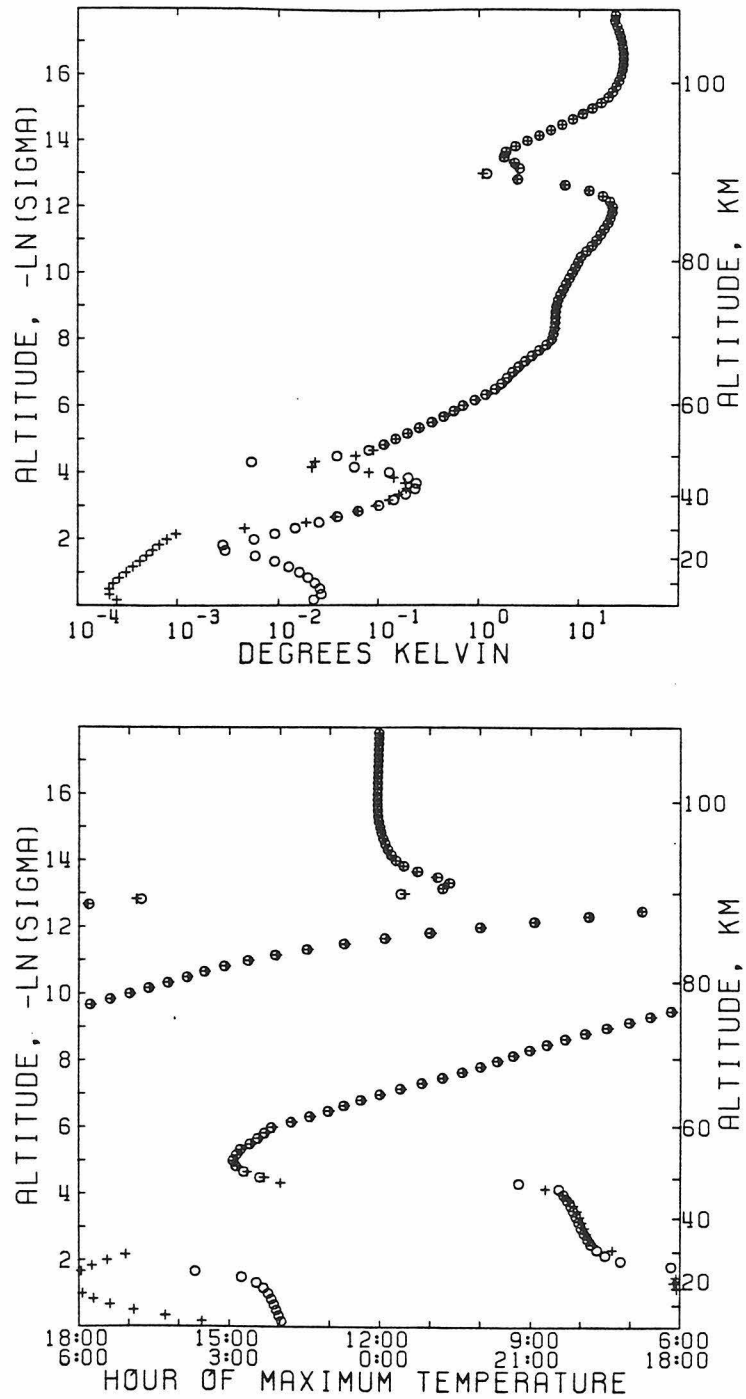


Figure 4.31 A comparison of the gravity wave model solutions for the semidiurnal temperature perturbation using the standard Γ^* profile (pluses) and a profile with $\Gamma^* = 0.5$ K/km below 30 km (circles). Except for Γ^* , T^* , and c_p the standard basic state and forcing were used in both cases.

GRAVITY WAVE MODEL
SEMIDIURNAL AMPLITUDE AND PHASE OF T

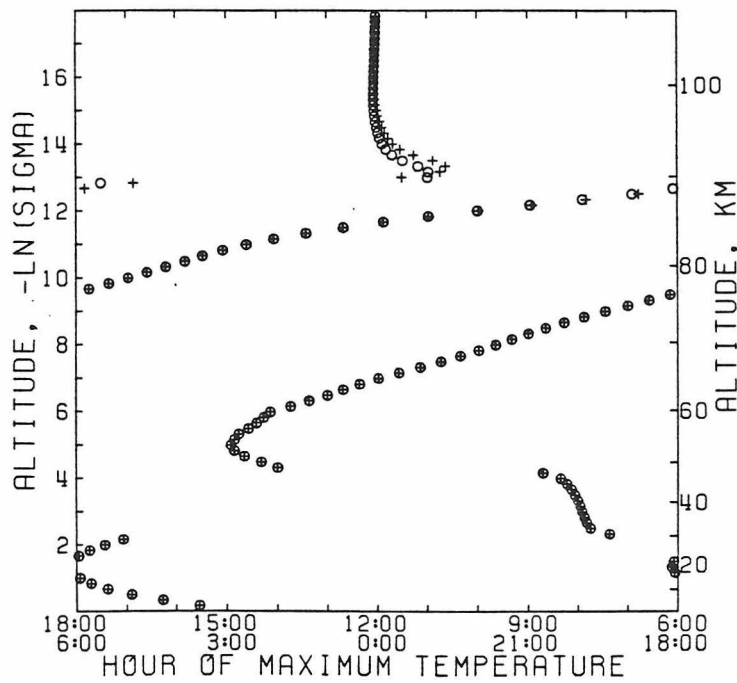
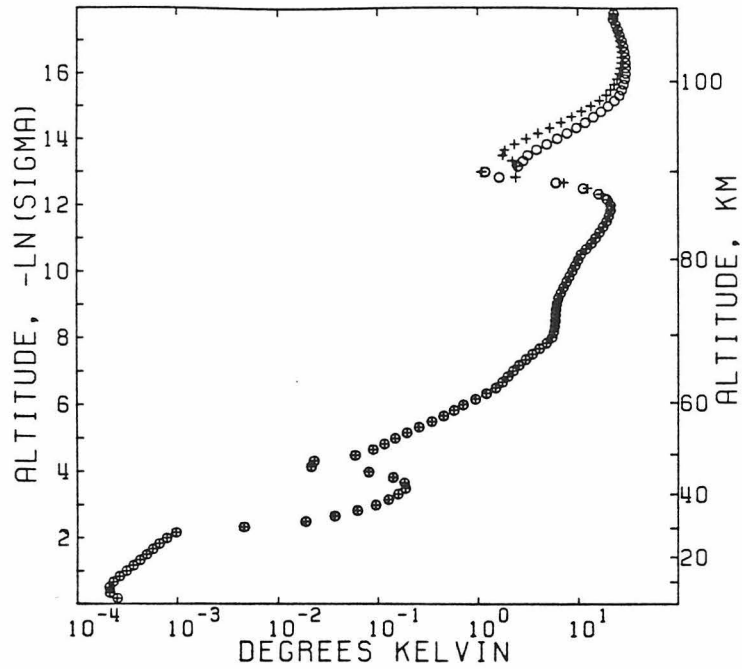


Figure 4.32 A comparison of the gravity wave model solutions for the semidiurnal temperature perturbation using the standard τ_R profile (pluses) and a profile with τ_R decreased by a factor of 2 (circles). Except for τ_R the standard basic state and forcing were used in both cases.

GRAVITY WAVE MODEL
SEMIDIURNAL AMPLITUDE AND PHASE OF T

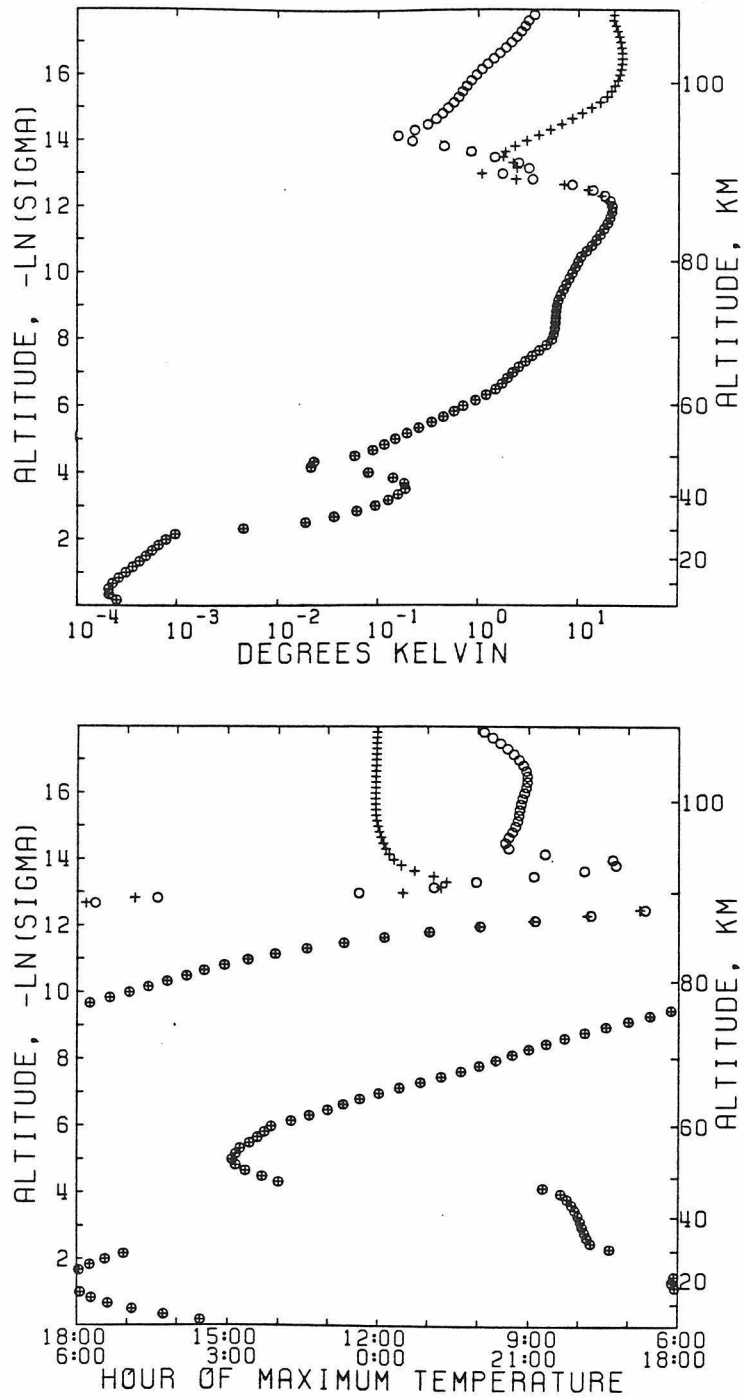


Figure 4.33

A comparison of the gravity wave model solutions for the semidiurnal temperature perturbation using the standard τ_R profile (pluses) and a profile with τ_R increased by a factor of $10^{4.0}$ (circles). Except for τ_R the standard basic state and forcing were used in both cases.

solution is not extremely sensitive to the value of τ_R . Even if the damping by Rayleigh friction is negligible, the solution below about 90 km is unaffected as shown in Fig. 4.33. Thus, the sponge layer seems to work with Newtonian cooling alone. However, to match the amplitude and phase in channels 1 and 2 some amount of Rayleigh friction is needed.

On a global average a solar flux of about 17 W/m^2 reaches the ground. This flux was neglected in our standard model. The solar radiation will heat the ground which will in turn heat the atmosphere above it. The distribution of this heating with height depends on the properties of the thermal boundary layer which are not well known. The heat is transported upward from the ground by some combination of radiation, convection, and conduction. If we use the diffusion model of Dobrovolskis (1978) to approximate this heat transport and assume that the thermal skin depth equals the atmospheric scale height the results are as shown in Fig. 4.34. This case has no heating in the clouds. The forcing in this case is proportional to σ . We also show in Fig. 4.35 the results when the heating is presented by a δ -function at the ground. The two cases are very similar above 30 km, about 2 scale heights. Below that the amplitude and phase are affected by the details of the heating function. Thus, the solution near the ground cannot be accurately determined, not only because of the uncertainty in the static stability, but because of the unknown vertical distribution of heating. Note that the amplitude due to the heating near the ground is negligible compared to that due to heating aloft above about 20 km as illustrated in Fig. 4.36.

GRAVITY WAVE MODEL
SEMIDIURNAL AMPLITUDE AND PHASE OF T

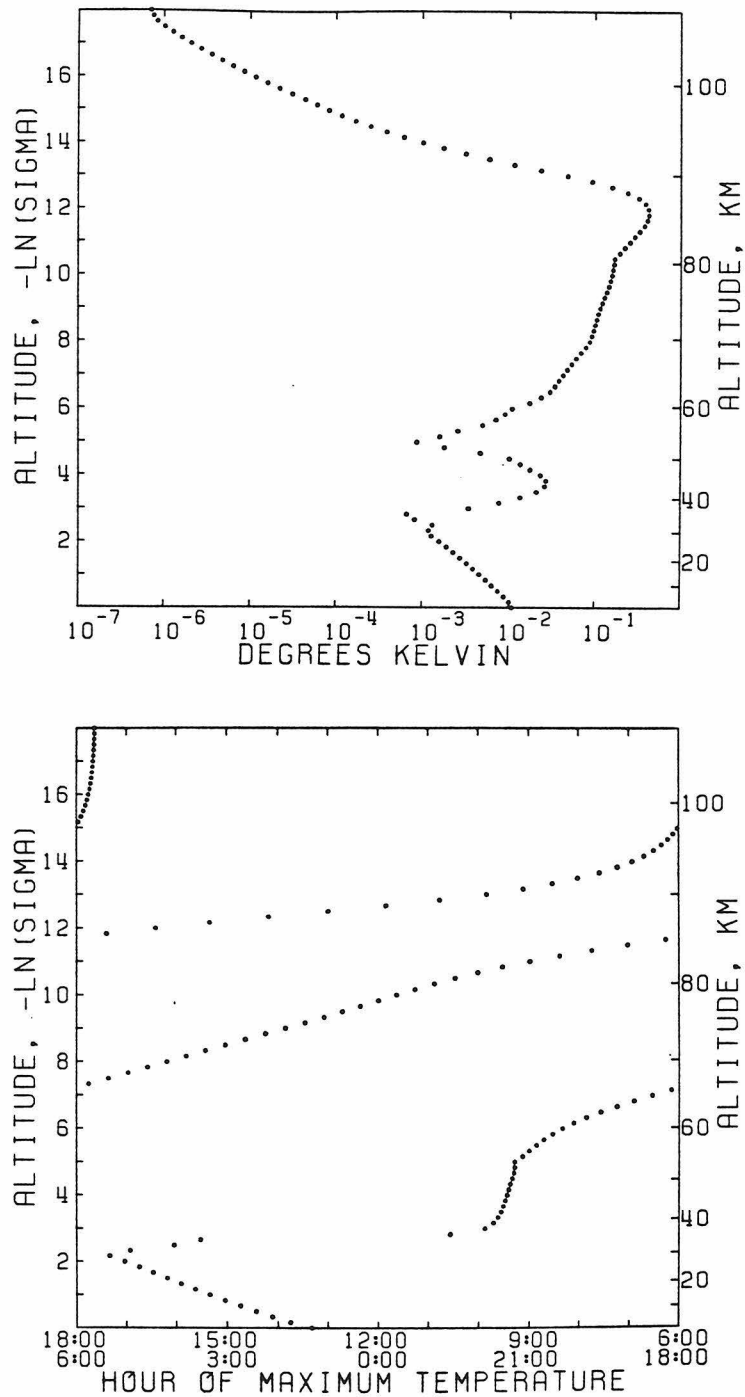


Figure 4.34 The gravity wave model solution for the semidiurnal temperature perturbation using the standard basic state and a diffusion model of heating near the ground (Dobrovolskis, 1978). The thermal skin depth equals the atmospheric scale height. The globally averaged solar flux at the ground is 17 W/m^2 .

GRAVITY WAVE MODEL
SEMIDIURNAL AMPLITUDE AND PHASE OF T

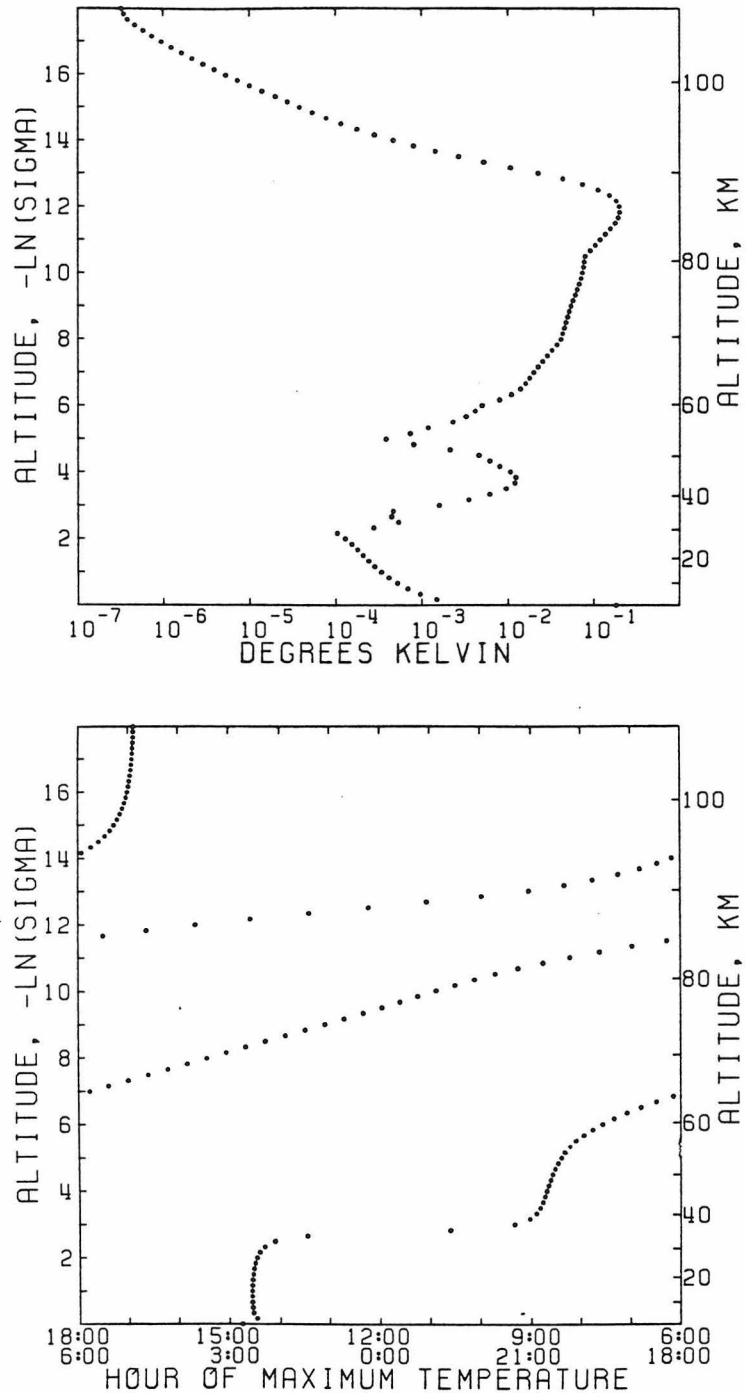


Figure 4.35 The gravity wave model solution for the semidiurnal temperature perturbation using the standard basic state and heating at the ground in the form of a δ -function. The globally averaged solar flux at the ground is 17 W/m^2 .

GRAVITY WAVE MODEL
SEMIDIURNAL AMPLITUDE AND PHASE OF T

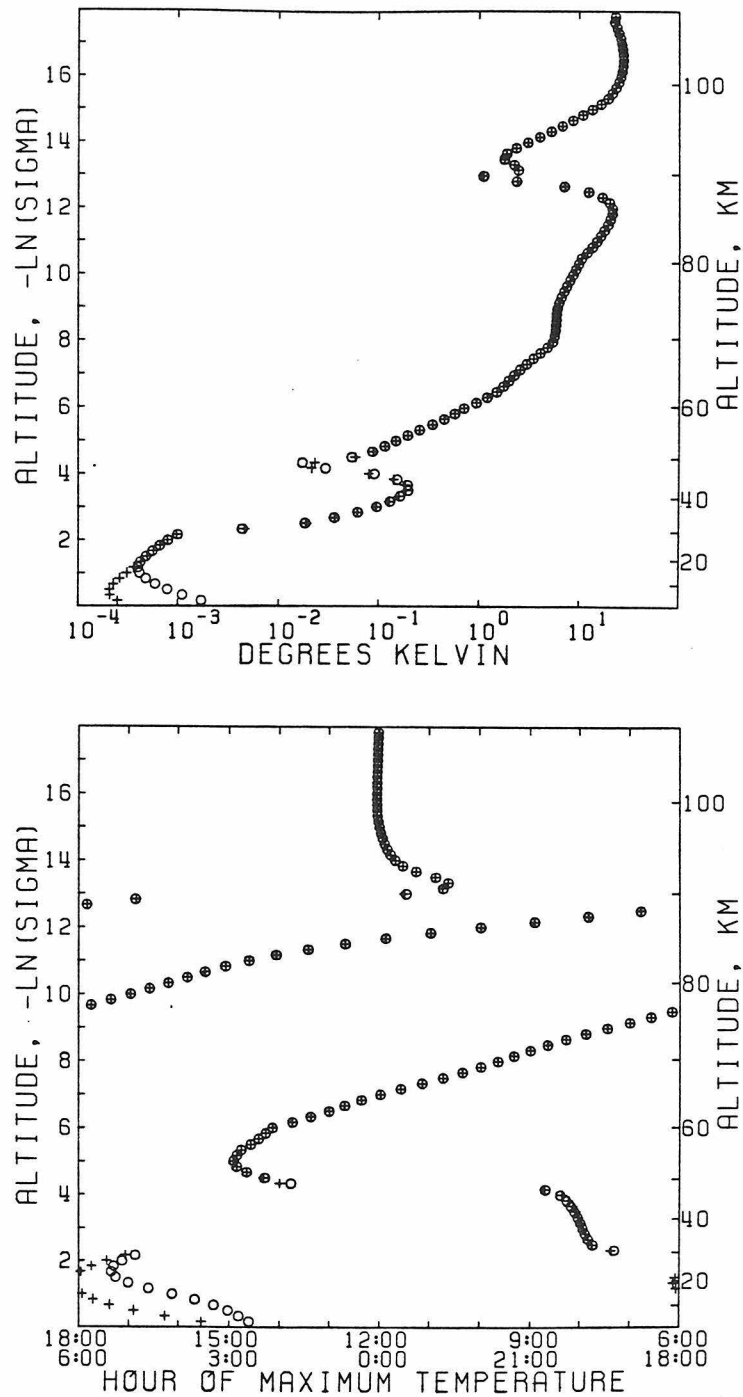


Figure 4.36

A comparison of the gravity wave model solutions for the semidiurnal temperature perturbation with the standard forcing (pluses) and the standard forcing plus δ -function heating at the ground (circles). The globally averaged solar flux at the ground is 17 W/m^2 . The standard basic state was used in both cases.

Dobrovolskis (1978) used a gravity wave model similar to ours to calculate Venus thermal tides. The results were used to estimate the torque which the sun exerts on the atmosphere due to the tidal redistribution of mass. This torque may be transmitted to the solid planet by friction and play an important role in maintaining the planet's rotation. The torque is proportional to the imaginary part of the semidiurnal component of the surface pressure oscillation. Dobrovolskis (1978) found that the torque was not overly sensitive to the form of the heating distribution near the ground and the torque due to heating in the clouds was negligible. Our results support the second conclusion but not the first. We compare the imaginary part of the semidiurnal surface pressure oscillation from both models for 3 heating functions in Table 4.16. We take the results from Dobrovolskis' basic state D since it is most similar to our standard basic state. Important differences in input parameters are noted in the table. The results for the δ function heating are actually consistent when allowance is made for the different values of the heating, surface temperature, and specific heat used in each model. However, discrepancy in the results for the diffusion model is greater than can be explained by these factors or the difference in D/H . D/H is the ratio of the thermal skin depth to the scale height. For $D/H = 10$ Dobrovolskis obtained an imaginary part of the semidiurnal surface pressure oscillation of 0.8 mbar, so we expect the results for $D/H = 1.0$ and $D/H = 1.4$ to differ by considerably less than a factor of 2. The discrepancy is probably due to differences in the basic state. Near the ground Dobrovolskis' atmosphere is adiabatic while ours has a small positive static

TABLE 4.16

COMPARISONS WITH DOBROVOLSKIS (1978)

Heating Distribution	Imaginary Part of the Semidiurnal Component of the Surface Pressure Oscillation (mbar)		Global Average Heating (W/m^2)	
	This Study	Dobrovolskis (1978)	This Study	Dobrovolskis (1978)
δ -Function at the Ground	1.6	2.2	17	25
Diffusion Model	0.3	1.2	17	25
Constant Heating Rate in the Upper Atmosphere (Step Function)**	0.03	-0.004	125	125

*This Study: $D/H = 1.0$; Dobrovolskis (1978): $D/H = 1.4$

**Step at $-\ln \sigma = 7$ (This Study); $-\ln \sigma = 7.5$ (Dobrovolskis (1978))

stability. We also have more shear in the zonal wind near the ground than Dobrovolskis. For the step function representing heating in the clouds the agreement is also not good, but in both models the amplitude is small compared to that generated by heating at or near the ground. Our LPE model results also show a small torque generated by heating in the clouds. Dobrovolskis found that the torque generated by heating in the upper atmosphere was sensitive to the basic state zonal wind and static stability profiles. Perhaps the reason he found a lesser degree of sensitivity for the heating near the ground was that the basic states he tested were nearly identical below 10 km.

We conclude this section with some examples of more extreme departures from the standard case. The basic state parameters and the forcing in the standard case have complicated vertical structures which make the amplitude and phase of the solution difficult to analyze in detail. By simplifying the various input profiles we can get some idea of the effect of their vertical structure on the solution. The simplest case of all is an upward propagating gravity wave forced from below in an isothermal, infinite atmosphere with constant u^* . As discussed in Section 2.4, the phase propagation would be downward with constant wavelength, and the amplitude of T' would be proportional to $\sigma^{-1/2}$.

The effect of the vertical structure of the basic state on an upward propagating gravity wave can be seen in Fig. 4.35, the case of δ -function heating at the ground. In the amplitude the change in slope at 30 km, the maximum at 44 km, and the minimum at 54 km are analogous to the behavior of the Γ^* profile at the same altitudes. The standard case shows similar behavior in the amplitude except that the minimum is

slightly lower. Thus, we conclude that the structure in the amplitude below about 60 km is at least partially controlled by the variation in Γ^* . The decrease in amplitude above 87 km is due to the sponge layer. Such a decrease is not seen in the standard case because the forcing extends into the damped region. The phase in Fig. 4.35 generally shows the characteristics of an upward propagating wave. The phase propagation is downward as can be seen from, for example, the temperature maximum which occurs at 80 km at 9:00 but at 75 km at 12:00. Below 60 km the regions of nearly constant phase are indicative of a standing wave, probably caused by reflections due to the sudden increase in Γ^* and/or u^* which occur at this level. Such a standing wave may also be present in the standard case, where most of the forcing is above 60 km, but the residual forcing in the lower atmosphere seems to dominate at some levels near the ground causing phase variations with height. In the sponge layer for the δ -function heating at the ground the phase of T' is no longer required to be 12:00, since there is no forcing in this region. In the standard case the phase of T' tracked the forcing in the damped region.

The effect of the residual heating in the lower atmosphere is shown in Fig. 4.37. This figure compares a step function distribution of the heating rate to the standard case. The heating in the standard case is modeled by two analytic functions. In the first, which represents the solar absorption measured by the LSFR, the heating rate approaches zero in the lower atmosphere and a constant in the upper atmosphere. The second, which represents heating due to absorption of solar near IR, reaches its maximum heating rate at the top of the model.

GRAVITY WAVE MODEL
SEMIDIURNAL AMPLITUDE AND PHASE OF T

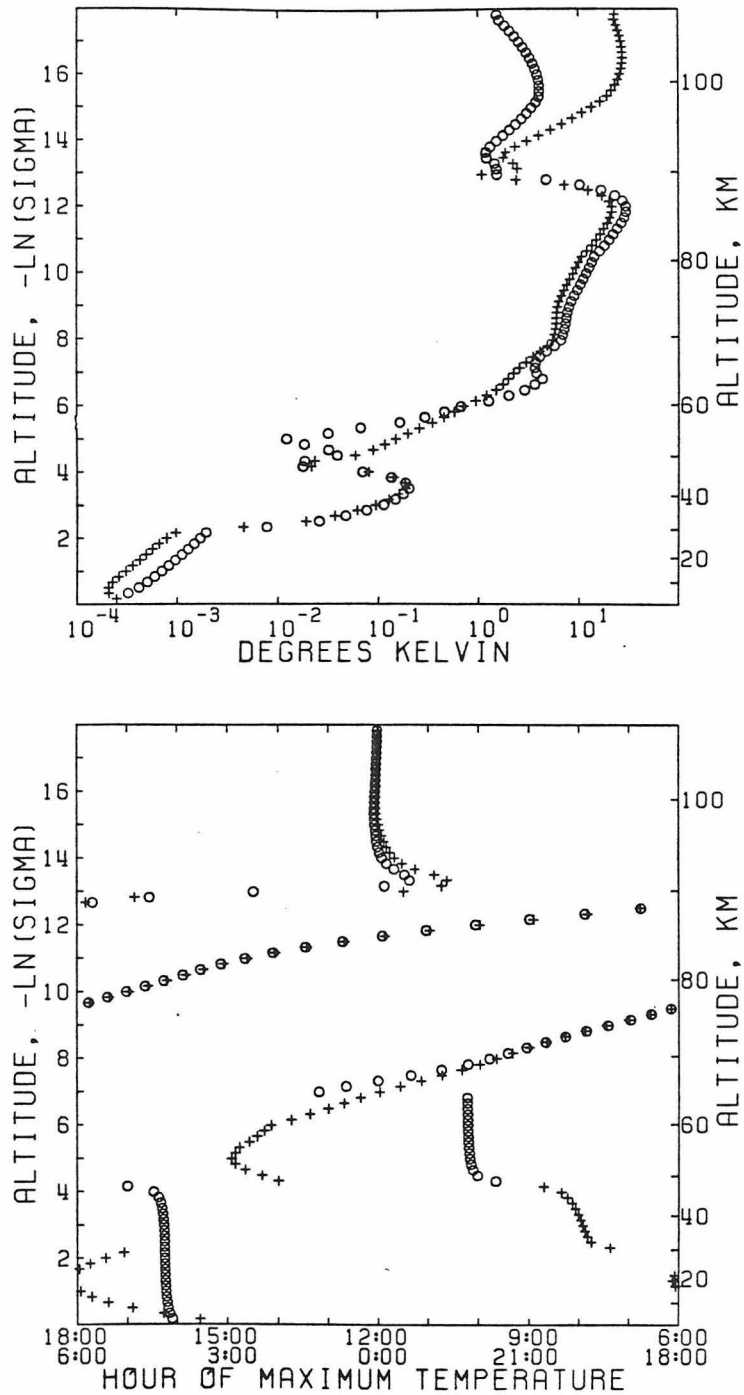


Figure 4.37 A comparison of the gravity wave model solutions for the semidiurnal temperature perturbation with the standard forcing (pluses) and a step function heating distribution (circles). The step function has constant heating rate above $-\ln\sigma = 7$ with 125 W/m^2 absorbed on a global average. The standard basic state was used.

In the step function case the total energy absorbed is approximately the same as in the standard case, but the heating rate is constant above $-1n\sigma = 7$ and zero below that level. In this case a standing wave is clearly set up below the step at $-1n\sigma = 7$. Neither this case nor the standard case accurately model the solar absorption in the lower atmosphere measured by the LSFR, which is somewhat variable with height (Tomasko et al., 1980a). Also, these measurements may not represent global average conditions. Therefore, uncertainty in the heating distribution is yet another reason why the phase in the lower atmosphere is not well determined; the amplitude is not much affected. Above the step the phase agrees very well with the standard case. In the OIR channels the phases are not significantly different from the standard case. In channels 2-5 the amplitude is increased by an average of 0.8 K, while in channel 1 the amplitude is less by 7.5 K. The lower amplitude in the sponge layer in the case of the step function is due to the constant heating rate. In the standard case the heating rate increases with height because of the near IR absorption.

In Fig. 4.38 we compare the standard case to a case where u^* is constant with height. The value of u^* is 100 m/s. In the lower atmosphere the amplitude is nearly the same as the standard case which is consistent with the idea that the profile of Γ^* is controlling the amplitude structure. However, once again the phase in the lower atmosphere is significantly affected. In the upper atmosphere the results are similar to the case shown in Fig. 4.30 in which $u^* = 125$ m/s above 70 km. The minimum in amplitude at about 90 km in the standard case seems to be correlated with the drop in u^* to zero at this altitude

GRAVITY WAVE MODEL
SEMIDIURNAL AMPLITUDE AND PHASE OF T

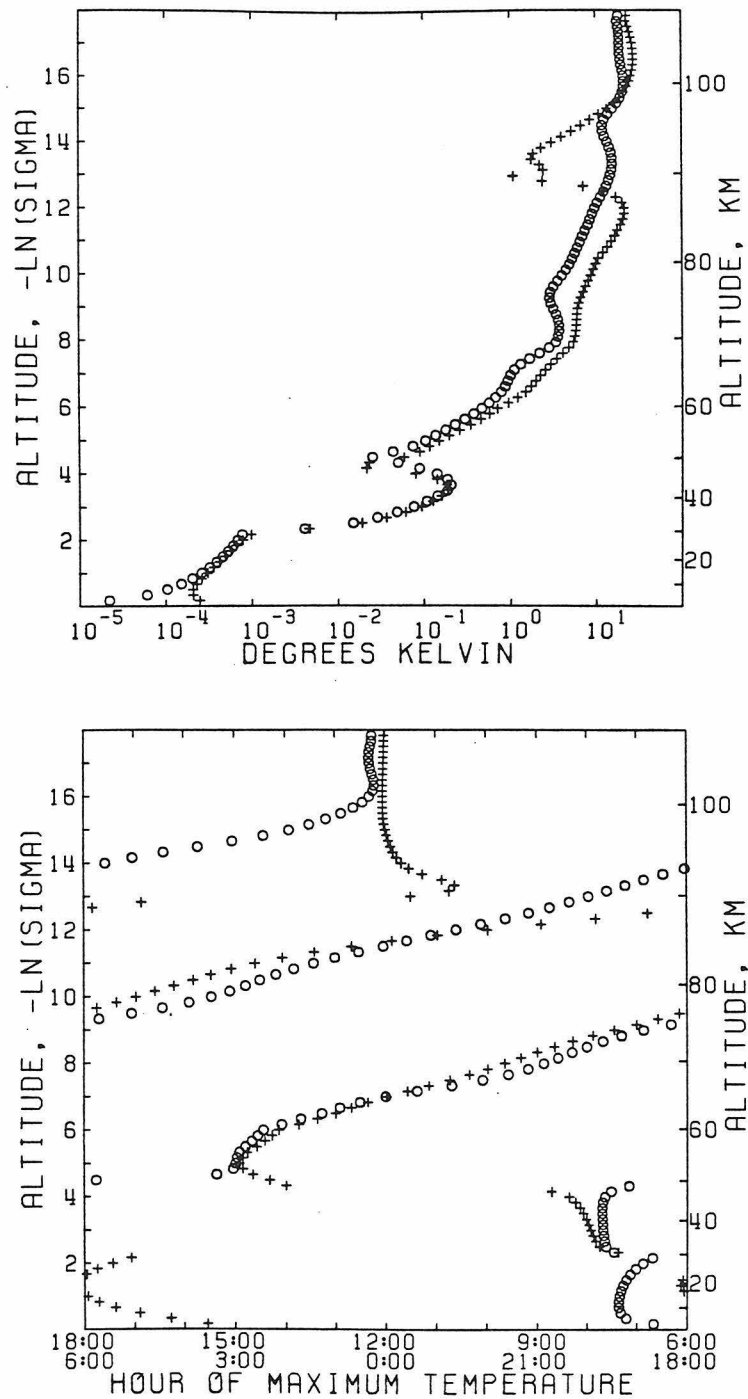


Figure 4.38 A comparison of the gravity wave model solutions for the semidiurnal temperature perturbation with standard u^* profile (pluses) and u^* constant with height at 100 m/s (circles). Except for u^* the standard base state and forcing were used in both cases.

since it disappears when u^* remains large.

Finally, we discuss two cases with different Γ^* profiles. The first, compared to the standard case in Fig. 4.39, was modified so that $\Gamma^* = 1$ K/km below 60 km. As expected, this change has a large effect on the amplitude, as well as the phase, below 60 km. However, the amplitude structure has not been reduced to a smooth increase as $\sigma^{-1/2}$. The amplitude minima occur at altitudes at which a large phase change occurs. This is consistent with a standing wave dominating the lower atmosphere. An amplitude minimum signifies a node in the standing wave at which a phase change of 180° occurs. In the standard case the altitude of the nodes is correlated with changes in Γ^* . Above 60 km the solution is only slightly affected by the change in Γ^* . In the OIR channels 2-5 the amplitudes are increased by about 0.5 K. There are no other important changes. In Fig. 4.40 we show the results for an isothermal atmosphere with $T^* = 300$ K. This case was very slow to converge in the lower atmosphere. It was run for 3200 time steps. Although this solution is very different from the standard case, some features are present in both. In Fig. 4.40 there is a standing wave below 60 km and an upward propagating wave above that level.

In summary, the solution near the ground is not well determined because of the uncertainty in Γ^* and in the vertical distribution of heating at low levels. In the lower atmosphere the phase of the solution is sensitive to any changes in the basic state or forcing. The amplitude seems to be affected significantly only by changes in Γ^* . Below about 55 km the solution has the characteristics of a standing wave except that in some cases at some levels the heating in the lower

GRAVITY WAVE MODEL
SEMIDIURNAL AMPLITUDE AND PHASE OF T

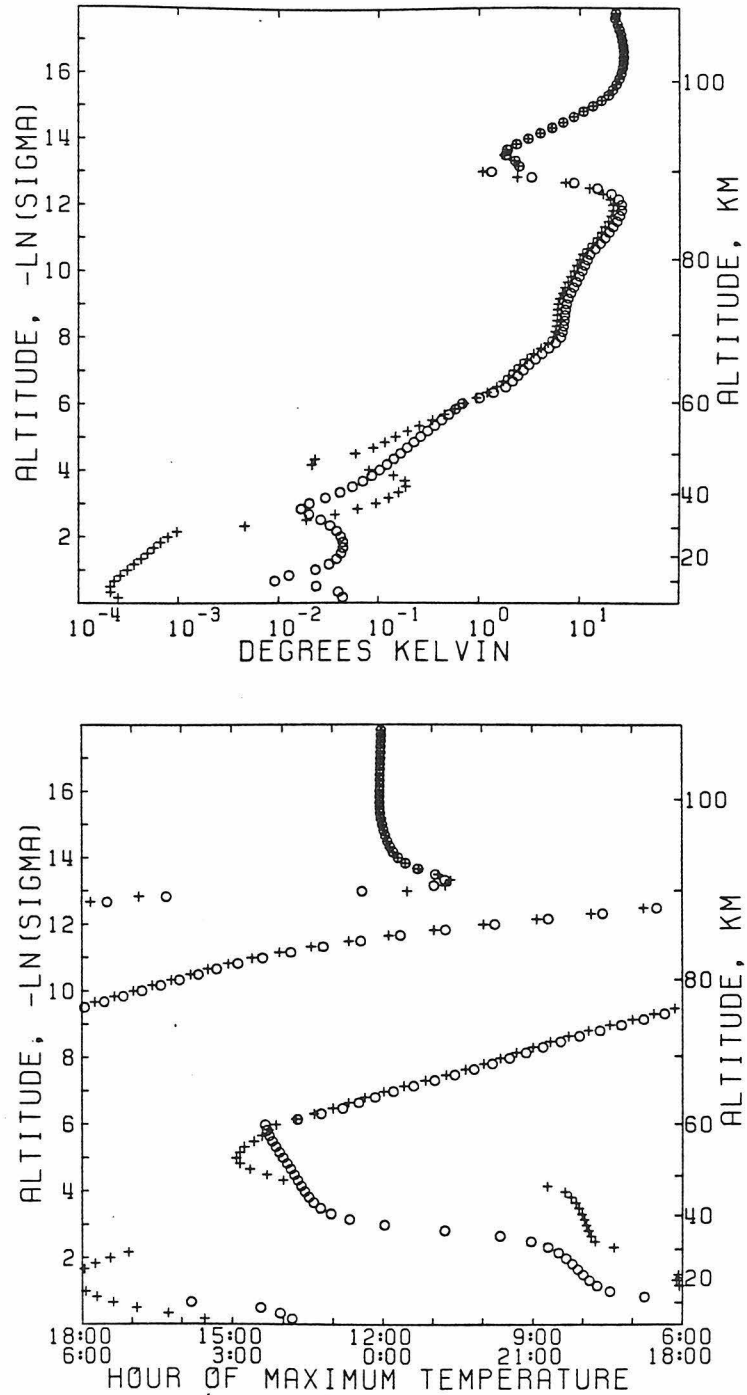


Figure 4.39

A comparison of the gravity wave model solutions for the semidiurnal temperature perturbation with the standard Γ^* profile (pluses) and a profile with $\Gamma^* = 1.0$ K/km. Except for Γ^* , T^* , and c_p the standard basic state and forcing were used in both cases.

GRAVITY WAVE MODEL
SEMIDIURNAL AMPLITUDE AND PHASE OF T

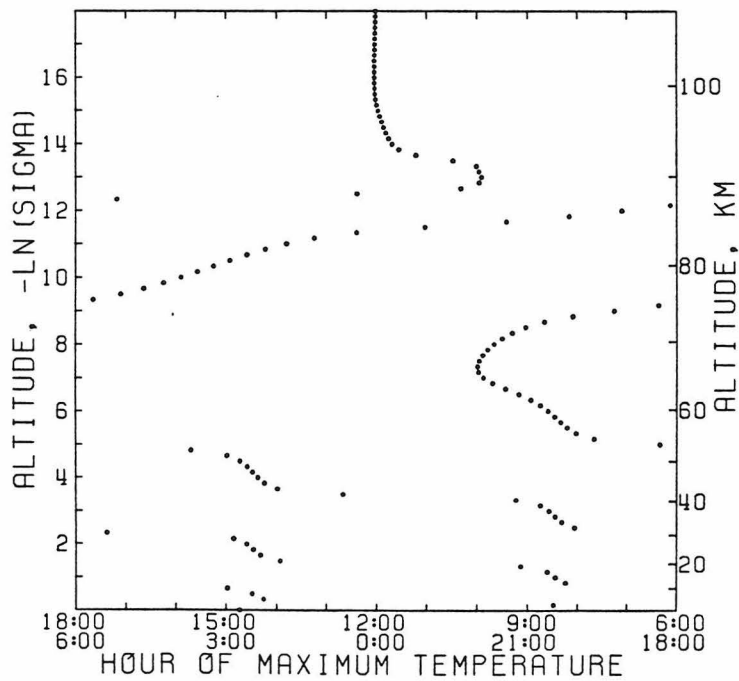
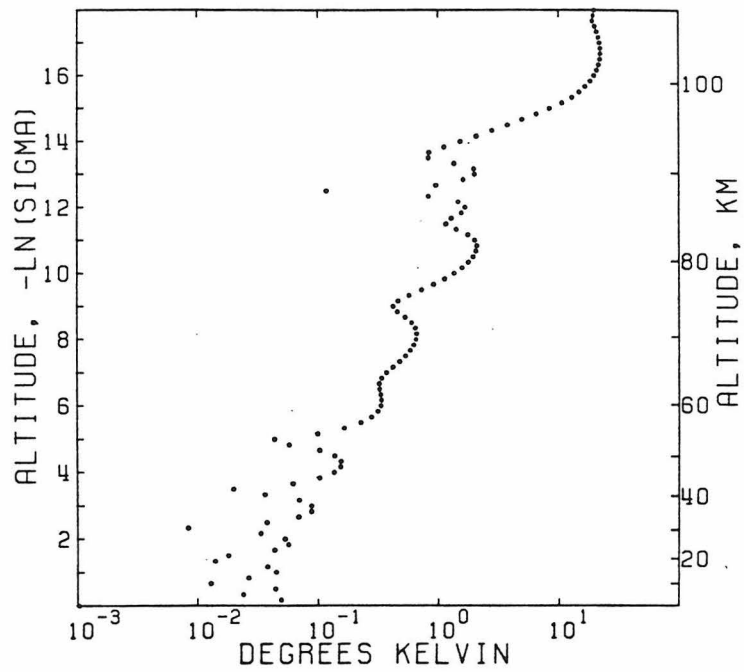


Figure 4.40 A comparison of the gravity wave model solutions for the semidiurnal temperature perturbation with the standard T^* profile (pluses) and T^* constant with height at 300K. Except for Γ^* , T^* , and c_p the standard basic state and forcing were used in both cases.

atmosphere causes the phase to change with height. In the upper atmosphere we found that the solution, and thus, the results in the OIR channels were not very sensitive to the details of the heating function, the value of τ_R , or changes in the basic state below 60 km. However, a small change in the mean zonal wind profile above 60 km has an effect on the amplitude and phase in the OIR channels because of the effect it has on the vertical wavelength. The results are less sensitive to small changes in Γ^* , but larger variations in the Γ^* profile have a major effect. The standard basic state and forcing were chosen because they are consistent with observations and give results in good agreement with the OIR data. From the above cases it is clear that the details of the choice were not crucial except perhaps for the mean zonal wind profile above 60 km.

4.6 Second Order Calculations

This section deals with the effect of the tides on the basic state of the atmosphere. To first order, terms the tidal perturbations have no effect because their zonal average is zero. (The zonal average is the same as the average over time in a rotating frame.) But the zonal average of second order terms involving the product of two perturbation quantities is not necessarily zero. In this section we derive equations relating the second order tidal terms to each other and other second order terms by expanding the primitive equations introduced in Chapter 2 to second order. Since we have previously assumed that the zeroth order and first order terms balance, it follows that the second order terms must also balance if the third order terms can be considered negligible.

The second order equations involve such quantities as the previously neglected \bar{v} and $\bar{\sigma}$, the mean meridional and vertical velocities, the time rate of change of the basic state, the frictional drag on the basic state momentum, and the mean differential heating between the equator and the pole. It is somewhat arbitrary to designate all these quantities as second order. We don't know beforehand that their magnitude will be small compared to lower order terms. This is an unfortunate consequence of linearization. It would be ideal to solve the complete non-linear primitive equations. However, the capability to solve for phenomena like the tides, which require a model with high vertical resolution, does not presently exist in non-linear global general circulation models. Our second order calculations are an attempt to estimate the non-linear effects of the tides. These

calculations are somewhat arbitrary, but they are the limit to which a linearized model may be carried with any degree of validity.

In this section we first derive the second order equations and discuss the significance of various terms. Then we evaluate the importance of the tides by comparing the effects of tidal transports of energy and angular momentum with the radiative imbalance between the equator and pole and the frictional drag on the mean zonal wind. These later quantities can be estimated from data or models. It would not be unreasonable to stop at this point and present these comparisons as our final conclusions. However, the mean meridional circulation involving \bar{v} and $\bar{\sigma}$ may also be important in transporting energy and momentum. After discussing how the second order equations are solved for \bar{v} and $\bar{\sigma}$, we present our final results.

The second order equations we will use are those of conservation of energy and angular momentum and the continuity equation. Due to the form of the continuity equation it is possible to express the mean meridional circulation in terms of a stream function. The energy equation may be used to solve for this stream function if the basic state quantities and tidal transports are known. Then, as a check, all the terms in the momentum equation may be evaluated. If the momentum equation does not balance, the remaining quantity may be viewed as an acceleration or deceleration of the basic state zonal wind. If the equation is very far from balancing, then our procedure is probably invalid. This could happen if other eddies are as important or more important than the tides or if our basic state is very inaccurate.

We begin the derivation of the energy conservation equation with the equation for the rate of change of total potential energy per unit mass in sigma coordinates:

$$\frac{\partial}{\partial t} c_p T + \vec{\nabla} \cdot \vec{\nabla} c_p T + \dot{\sigma} \frac{\partial}{\partial \sigma} c_p T = RT \left(\frac{\partial q}{\partial t} + \vec{\nabla} \cdot \vec{\nabla} q \right) + \frac{RT \dot{\sigma}}{\sigma} + Q$$

where Q is the total energy input to the system, and the continuity equation:

$$\frac{\partial}{\partial t} p_s + \vec{\nabla} \cdot p_s \vec{\nabla} + p_s \frac{\partial \dot{\sigma}}{\partial \sigma} = 0$$

These are the full non-linear equations. We combine these equations by multiplying the first by p_s and the second by $c_p T$ and dividing by g :

(4.1)

$$\frac{\partial}{\partial t} \left(\frac{p_s c_p T}{g} \right) + \vec{\nabla} \cdot \frac{p_s \vec{\nabla}}{g} c_p T + \frac{\partial}{\partial \sigma} \frac{p_s \dot{\sigma} c_p T}{g} = \frac{RT}{g} \left(\frac{\partial p_s}{\partial t} + \vec{\nabla} \cdot \vec{\nabla} p_s \right) + \frac{RT}{\sigma} \frac{p_s \dot{\sigma}}{g} + \frac{p_s Q}{g}$$

This equation is an expression for the time rate of change of total potential energy per unit horizontal area. The total potential energy

in the column is just $\int_0^1 \frac{p_s c_p T}{g} d\sigma$.

We also need an equation for the time rate of change of kinetic energy which is obtained by dotting $\vec{\nabla}$ into the two-dimensional momentum equation:

$$\frac{\partial \varepsilon}{\partial t} + \vec{\nabla} \cdot \vec{\nabla} \varepsilon + \dot{\sigma} \frac{\partial \varepsilon}{\partial \sigma} = - \vec{\nabla} \cdot \vec{\nabla} \phi + \sigma (\vec{\nabla} \cdot \vec{\nabla} q) \frac{\partial \phi}{\partial \sigma} + \vec{\nabla} \cdot \vec{f}$$

where $\varepsilon = \frac{1}{2} |\vec{V}|^2$, the kinetic energy per unit mass, and \vec{f} is the frictional dissipation. We multiply this equation by p_s , combine with the continuity equation, and divide by g to obtain

$$\frac{\partial p_s \varepsilon}{\partial t g} + \vec{\nabla} \cdot \frac{p_s \vec{V} \varepsilon}{g} + \frac{\partial p_s \dot{\sigma} \varepsilon}{\partial \sigma g} = - \frac{p_s}{g} \vec{V} \cdot \vec{\nabla} \Phi + \sigma \frac{\vec{V} \cdot \vec{\nabla} p_s}{g} \frac{\partial \Phi}{\partial \sigma} + \frac{p_s}{g} \vec{V} \cdot \vec{f} \quad (4.2)$$

The continuity equation is used to rewrite $-\frac{p_s}{g} \vec{V} \cdot \vec{\nabla} \Phi$:

$$\begin{aligned} - \frac{p_s}{g} \vec{V} \cdot \vec{\nabla} \Phi &= - \vec{\nabla} \cdot \frac{p_s \vec{V} \Phi}{g} + \frac{\Phi}{g} \vec{\nabla} \cdot p_s \vec{V} \\ &= - \vec{\nabla} \cdot \frac{p_s \vec{V} \Phi}{g} - \frac{\Phi}{g} \left(\frac{\partial p_s}{\partial t} + \frac{\partial (p_s \dot{\sigma})}{\partial \sigma} \right) \end{aligned}$$

If we add (4.1) and (4.2) using the above expression and the hydrostatic equation, $\sigma \frac{\partial \Phi}{\partial \sigma} = -RT$, we have

$$\begin{aligned} \frac{\partial p_s}{\partial t g} (\varepsilon + c_p T) + \vec{\nabla} \cdot \frac{p_s \vec{V}}{g} (\varepsilon + \Phi + c_p T) + \frac{\partial}{\partial \sigma} \left(\frac{p_s \dot{\sigma}}{g} (\varepsilon + \Phi + c_p T) + \frac{\sigma \Phi}{g} \frac{\partial p_s}{\partial t} \right) \\ = \frac{p_s \vec{V} \cdot \vec{f}}{g} + \frac{p_s Q}{g} \quad (4.3) \end{aligned}$$

Now we take a zonal average which is denoted by an overbar. For example, $\bar{u} = \frac{1}{2\pi} \int_0^{2\pi} u d\phi$. Neglecting terms higher than second order we obtain

$$\begin{aligned}
& \frac{\partial}{\partial t} \left(\frac{\overline{p_s}}{g} (\varepsilon + c_p T) \right) + \nabla_\lambda \cdot \left(\frac{\overline{p_s v}}{g} (\varepsilon + \Phi + c_p T) + \frac{\overline{p_s}}{g} v' (\varepsilon' + \Phi' + c_p T') \right) \\
& + \frac{\partial}{\partial \sigma} \left(\frac{\overline{p_s \dot{\sigma}}}{g} (\varepsilon + \Phi + c_p T) + \frac{\overline{p_s}}{g} \dot{\sigma}' (\varepsilon' + \Phi' + c_p T') + \frac{\sigma \overline{\Phi} \partial \overline{p_s}}{g \partial t} + \frac{\sigma \overline{\Phi}' \partial p_s'}{g \partial t} \right) \\
& = \frac{\overline{p_s \vec{V} \cdot \vec{f}}}{g} + \frac{\overline{p_s Q}}{g}
\end{aligned} \tag{4.4}$$

Note that this equation for the conservation of energy is not the same as that derived in Section 2.5. In Section 2.5 we obtained an equation for the rate of change of perturbation energy, i.e., the sum of equations (2.45) and (2.46). Equation (4.4) is the rate of change of the total energy of the system, including the basic state as well as perturbation energies.

In (4.4) $\nabla_\lambda \cdot [] = \frac{1}{a \cos \lambda} \frac{\partial}{\partial \lambda} []$. $\overline{\varepsilon + c_p T}$ is the basic state energy per unit mass, a zeroth order quantity. Actually, $\bar{\varepsilon} = \frac{1}{2} (\bar{u}^2 + \bar{v}^2)$ but the \bar{v}^2 term is neglected because it is fourth order. Also, we have $\overline{p_s v} = \bar{p}_s \bar{v} + \overline{p_s' v'}$ and, likewise, $\overline{p_s \dot{\sigma}} = \bar{p}_s \bar{\dot{\sigma}} + \overline{p_s' \dot{\sigma}'}$. These are second order quantities. \bar{p}_s is the basic state surface pressure. The term $\nabla_\lambda \cdot \frac{\overline{p_s}}{g} v' (\varepsilon' + \Phi' + c_p T')$ is the rate of change of energy due to meridional tidal transport. We are assuming that tides are the only eddies contributing to these terms. The term $\nabla_\lambda \cdot \frac{\overline{p_s' v'}}{g} (\varepsilon + \Phi + c_p T)$ is also a tidal transport term. The rate of change due to meridional transport of energy by the mean circulation is given by $\nabla_\lambda \cdot \frac{\overline{p_s v}}{g} (\varepsilon + \Phi + c_p T)$. A similar breakdown for the vertical transport can be made from the terms involving $\dot{\sigma}$. Of the terms on the right-hand

side, $\frac{\overline{p_s Q}}{g}$ is the rate of zonally averaged thermal energy input to the system. This includes the net solar heating, the net infrared cooling, and the thermal energy generated by dissipation. The term $\frac{p_s \vec{V} \cdot \vec{f}}{g}$ is also a dissipation term.

In order to solve (4.4) for \bar{v} and $\bar{\sigma}$, we must assume that the time derivatives of the basic state variables are zero to second order. Thus, $\frac{\partial}{\partial \sigma} \left(\frac{\sigma \bar{\phi}}{g} \frac{\partial \bar{p}_s}{\partial t} \right) = 0$. Also, $\frac{\partial}{\partial t} \left(\frac{\bar{p}_s}{g} (\bar{\epsilon} + c_p \bar{T}) + \frac{p'_s}{g} (\epsilon' + c_p T') \right) = 0$ because of the above assumption and because the tidal fields are steady in time. The steadiness of the tidal fields also leads to $\frac{\partial}{\partial \sigma} \left(\frac{\sigma \phi'}{g} \frac{\partial p'_s}{\partial t} \right) = 0$. Assuming that the basic state is steady in time to second order essentially means that the tidal transports and the forcing terms on the right-hand side are balanced by a mean meridional circulation instead of affecting the basic state energy. This assumption would be wrong if the meridional circulation derived was inconsistent with existing data.

An interesting comparison is made in Fig. 4.41. Here we show the mean zonal radiation budget compared to the latitudinal transport of thermal energy (heat) by the tides. The mean zonal radiation budget is equal to $\int_0^1 \frac{p_s Q}{g} d\sigma = - \int_0^1 \frac{\partial (F_\downarrow - F_\uparrow)}{\partial \sigma} d\sigma = (F_\downarrow - F_\uparrow)|_{\sigma=0}$ where F_\downarrow is the downward solar flux at any level, and F_\uparrow is the upward planetary infrared flux at any level. We assume $(F_\downarrow - F_\uparrow)|_{\sigma=1} = 0$. In Fig. 4.41, \bar{F}_\downarrow and \bar{F}_\uparrow for 10° latitude bins were taken from Table 1 of Tomasko et al. (1980b). Both are based on OIR measurements. \bar{F}_\downarrow was calculated using the broad band solar channel on the OIR, while \bar{F}_\uparrow was calculated from the brightness temperature in the $11.5 \mu\text{m}$ cloud-top channel. To obtain the total infrared flux, Venus was assumed to radiate like a

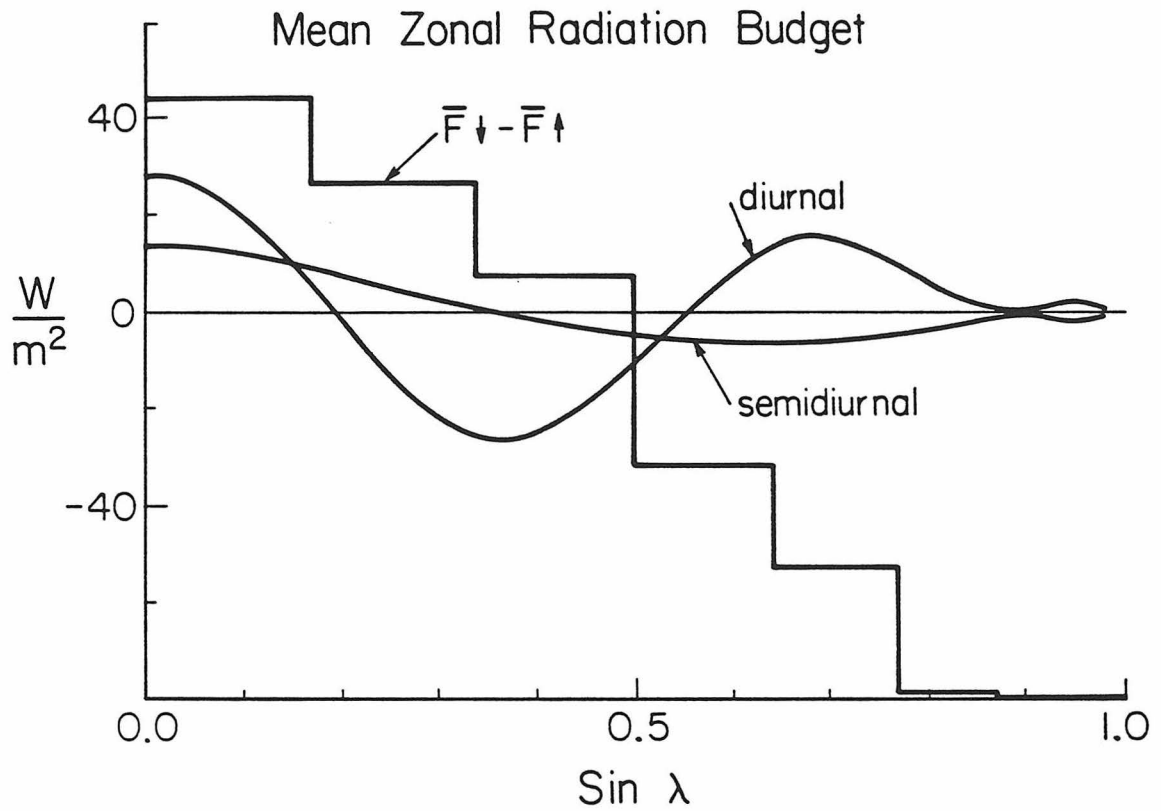


Figure 4.41 The mean zonal radiation budget, $\bar{F}_\downarrow - \bar{F}_\uparrow$, compared with the heat flux due to latitudinal transport by the diurnal and semidiurnal tides. The mean zonal radiation budget is the difference between the zonally averaged incoming solar radiation and outgoing planetary infrared radiation. $\bar{F}_\downarrow - \bar{F}_\uparrow$ is based on data in Tomasko et al. (1980b).

black-body at this temperature. Tomasko et al. (1980b) claim this flux is accurate to 5-10%.

At low latitudes more energy is absorbed than emitted; $\bar{F}_\downarrow > \bar{F}_\uparrow$. This excess energy must be transported by dynamical processes to higher latitudes where $\bar{F}_\uparrow > \bar{F}_\downarrow$. At each latitude the rate of change of energy due to latitudinal transport of heat by the tides is given by $-\int_0^1 \nabla_\lambda \cdot \frac{\bar{p}_s c_p v' T'}{g} d\sigma$. The latitudinal transport of kinetic energy by the tides has not been included here. The diurnal and semidiurnal contributions to this integral are shown in Fig. 4.41. A positive value in Fig. 4.41 means that heat is being deposited while a negative value means that heat is being carried away. Thus, the diurnal tide removes heat from 12° to 33° and deposits it at higher and lower latitudes. The semidiurnal tide carries heat from high latitudes towards the equator. Obviously, this tidal transport is not the answer to balancing the gradient in Venus' global radiation budget. However, these tidal transports, particularly the diurnal, are not negligible compared to $\overline{F_\downarrow - F_\uparrow}$. This led us to believe that the tidal terms should not be neglected in (4.4).

The derivation of the equation of conservation of angular momentum is very similar to that of (4.4). We begin with the zonal momentum equation:

$$\frac{\partial u}{\partial t} + \vec{V} \cdot \vec{\nabla} u + \dot{\sigma} \frac{\partial u}{\partial \sigma} - \frac{uv \tan \lambda}{a} = - \frac{1}{a \cos \lambda} \frac{\partial \Phi}{\partial \phi} + \frac{\sigma}{a \cos \lambda} \frac{\partial q}{\partial \phi} \frac{\partial \Phi}{\partial \sigma} + f \quad .$$

Multiplying by p_s/g and combining with the continuity equation multiplied by u/g we obtain

$$\frac{\partial}{\partial t} \frac{p_s u}{g} + \vec{\nabla} \cdot \frac{u p_s \vec{V}}{g} + \frac{\partial p_s u \dot{\sigma}}{\partial \sigma} - \frac{p_s u v \tan \lambda}{a g} = \frac{-p_s}{g} \frac{1}{a \cos \lambda} \frac{\partial \Phi}{\partial \phi}$$

$$+ \frac{\sigma}{g} \frac{1}{a \cos \lambda} \frac{\partial p_s}{\partial \phi} \frac{\partial \Phi}{\partial \sigma} + \frac{p_s f}{g} .$$

We use

$$\nabla_{\lambda} \cdot \frac{u p_s v}{g} - p_s \frac{u v \tan \lambda}{a g} = \frac{1}{a \cos^2 \lambda} \frac{\partial}{\partial \lambda} \left(\frac{u p_s v \cos^2 \lambda}{g} \right) .$$

Multiplying by $a \cos \lambda$, taking the zonal average, and neglecting terms higher than second order yields

$$\frac{\partial}{\partial t} \frac{\overline{p_s L}}{g} + \nabla_{\lambda} \cdot \frac{\overline{p_s v} \overline{L}}{g} + \frac{\overline{p_s v' L'}}{g} + \frac{\partial}{\partial \sigma} \frac{\overline{p_s \dot{\sigma} L}}{g} + \frac{\overline{p_s \dot{\sigma}' L'}}{g} + \sigma \frac{\overline{p_s' \partial \Phi'}}{g \partial \phi}$$

$$= \frac{\overline{p_s f}}{g} a \cos \lambda \quad (4.5)$$

where $L = u a \cos \lambda$, the angular momentum per unit mass. $\overline{p_s L}/g$ is the mean zonal angular momentum per unit horizontal area. In the mks system $\frac{\partial}{\partial t} \frac{\overline{p_s L}}{g}$ has the units Joules/m². As in the energy equation, the ∇_{λ} terms are latitudinal transport terms and the $\frac{\partial}{\partial \sigma}$ terms are vertical transport terms. $\frac{\overline{p_s f}}{g} a \cos \lambda$ is a dissipation term.

At second order the dissipation may be expressed in terms of a stress which tends to decrease the shear in the basic state zonal wind. If $\bar{\tau}(\sigma)$ is the stress, then

$$\frac{\overline{p_s f}}{g} a \cos \lambda = - \frac{\delta \overline{\tau}}{\partial \sigma} a \cos \lambda$$

The stress is proportional to the shear in the basic state zonal wind.

Thus,

$$\overline{\tau}(\sigma) = \rho K \frac{\partial \overline{u}}{\partial z} = - \frac{\rho^2 K g}{p_s} \frac{\partial \overline{u}}{\partial \sigma}$$

where K is the eddy viscosity in units of cm^2/sec . K is a convenient measure of the amount of mixing in the atmosphere. By using this formulation of the dissipation we have included in a crude way the effects of small scale eddies. To include them accurately we would, of course, have to calculate their structure as we did for the tides. A profile of $K(\sigma)$ may be constructed using values from various sources. We may then calculate $-\frac{\partial \overline{\tau}}{\partial \sigma} a \cos \lambda$ and compare it with the rate of change of angular momentum due to tidal transports.

$K(z)$ has been determined by von Zahn et al. (1980) from composition data obtained by the Pioneer Venus bus neutral mass spectrometer near the homopause. At high altitudes K can be derived from the variation of the mixing ratios with height of gases with different molecular weights. Von Zahn et al. (1980) extrapolate their results lower in the atmosphere by assuming that K is proportional to $n^{-1/2}$ where n is the number density of molecules. At the top of our model, at 111 km, this extrapolation gives $K = 1.9 \times 10^6 \text{ cm}^2/\text{sec}$. From 90 to 70 km we use the value $1.5 \times 10^5 \text{ cm}^2/\text{sec}$ determined from the photochemical model of Yung and DeMore (1982). In this model, K does not decrease between 90 and 70 km. Higher values of K are needed in this region for the rapid transport of O_2 to the lower atmosphere.

Finally, at about 60 and 45 km, K has been estimated by Pioneer Venus radio scintillation data. The radio scintillations are caused by variations in the refractive index which in turn are caused by temperature variations. They can only be observed in stable regions of the atmosphere where a vertical displacement of an air parcel will result in a horizontal temperature contrast. Presumably these displacements are indicative of turbulence. At 60 km $K = 4 \times 10^4$ cm²/sec according to Woo and Ishimaru (1981). Woo and Armstrong (1982) found that $K = 2 \times 10^3$ cm²/sec at 45 km. We extrapolate from 45 km to the surface assuming K proportional to $n^{-1/2}$. This gives $K(0) = 4 \times 10^2$ cm²/sec.

Using these values for K and the basic state zonal wind we calculate $\frac{-(\partial\bar{\tau}/\partial\sigma) \text{acos}\lambda}{\bar{p}_s v' L' \frac{\partial}{\partial\sigma}} + \frac{\text{compare it to the tidal transport terms,}}{\bar{p}_s \dot{\sigma}' L' \frac{\partial\Phi'}{\partial\phi}}$ in Fig. 4.42. The quantities in Fig. 4.42 have been multiplied by σ . Since the vertical axis is $-\ln\sigma$, the area under each curve is equal to the rate of change in angular momentum per unit area. The dissipation term acts to decrease the shear in the mean zonal wind. Thus, as expected, the dissipation tends to decelerate the wind in the core of the jet, from 62 to 75 km, and accelerate it above and below this region. The oscillation in the lower atmosphere is due to the alternating regions of high and low shear, which the dissipation tends to smooth out. It would have been very gratifying if the tidal transports had been the mirror image of the dissipation curve. Then the tides would replace the momentum in the jet which the dissipation removes. In so far as the term $-(\partial\bar{\tau}/\partial\sigma) \text{acos}\lambda$ correctly represents the small scale dissipative processes, the problem of the maintenance of the large zonal wind on Venus would have been

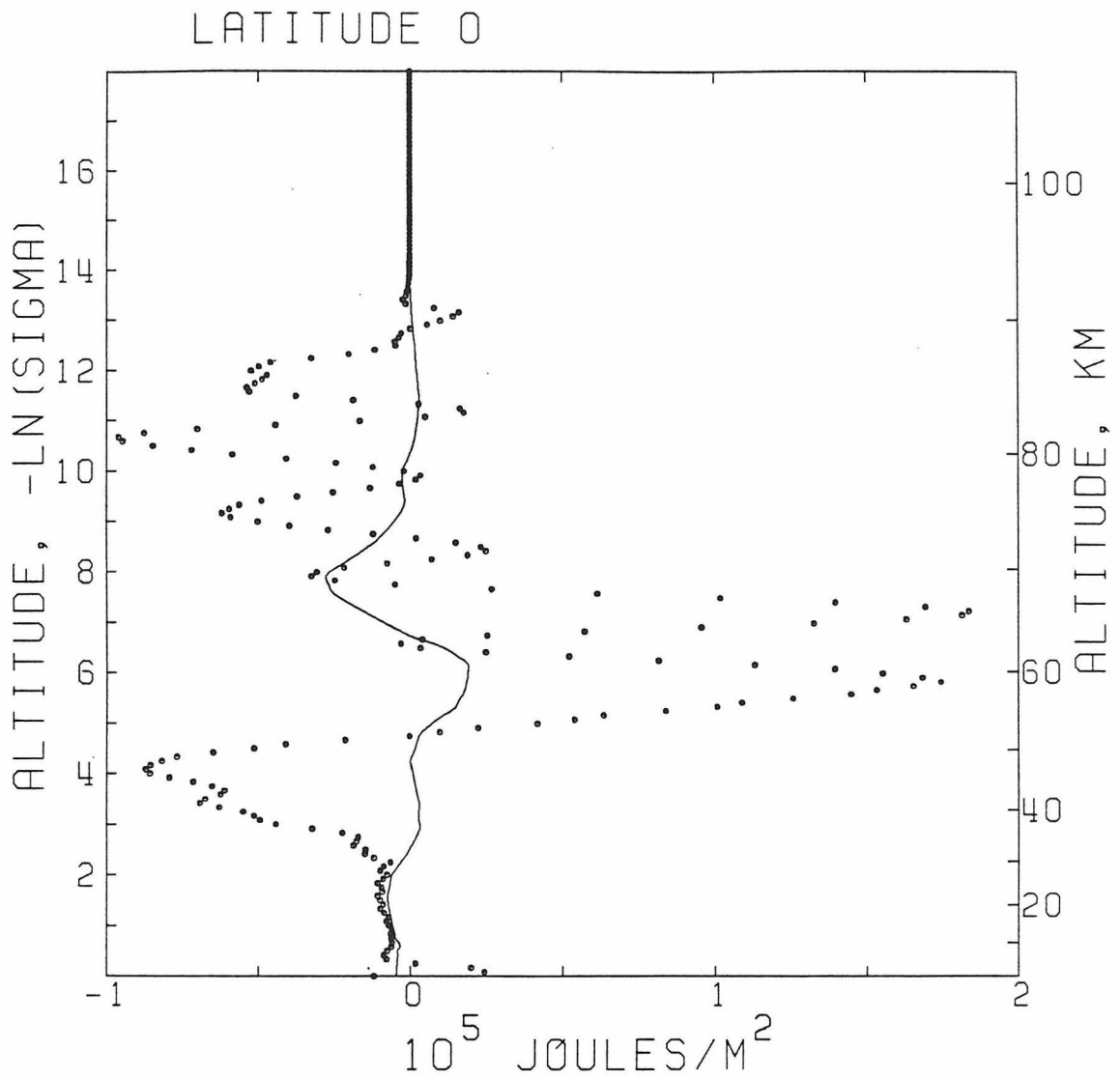


Figure 4.42 The rate of change of angular momentum at the equator, scaled by σ due to dissipation (solid curve) and tidal transports (data points). The dissipation is based upon eddy viscosities discussed in the text. The angular momentum flux due to dissipation is proportional to $\omega^2 \lambda$. At higher latitudes it is still small compared to the flux due to tidal transports which do not decrease as rapidly with latitude.

solved! A constant source of angular momentum would not be needed in this case, so the super-rotation could have been generated in an initial spin up of the atmosphere (Schubert, 1982).

Although the tides do not balance the dissipation, we are left with an interesting situation. The rate of change of angular momentum due to tidal transports is an order of magnitude larger than the dissipative torque over most of the atmosphere. This is true at higher latitudes as well as the equator. If the mean zonal wind is to remain steady in time, the balance in the angular momentum equation must be made up of transports not correctly modeled by our dissipation term. These transports could be due to other types of eddies or the mean meridional circulation. We will attempt to determine the contribution of the mean circulation.

We solve for the mean meridional circulation using the continuity and the energy conservation equations. The zonally averaged second order continuity equation is

$$\frac{1}{a \cos \lambda} \frac{\partial}{\partial \lambda} (\cos \lambda \overline{p_s v}) + \frac{\partial}{\partial \sigma} \overline{p_s \dot{\sigma}} = 0 \quad (4.6)$$

where we have assumed that $\partial \overline{p_s} / \partial t = 0$. The zonal average of $\frac{1}{a \cos \lambda} \frac{\partial}{\partial \phi} p_s u$ is zero. To satisfy (4.6) we define

$$\overline{p_s v} \cos \lambda = \frac{\partial \psi}{\partial \sigma} \quad ; \quad \overline{p_s \dot{\sigma}} = - \frac{1}{a \cos \lambda} \frac{\partial \psi}{\partial \lambda}$$

where ψ is the stream function. Since $\overline{p_s v} = \overline{p_s \bar{v}} + \overline{p_s' v'}$, once we have solved for ψ we must subtract the second term if we want \bar{v} . The same

holds true for $\overline{p_s \sigma}$. Now we rewrite (4.4) in terms of ψ :

$$\nabla_{\lambda} \cdot \left(\frac{\partial \psi}{\partial \sigma} \overline{\varepsilon}_{\text{total}} \right) - \frac{\partial}{\partial \sigma} \left(\frac{1}{a \cos \lambda} \frac{\partial \psi}{\partial \lambda} \overline{\varepsilon}_{\text{total}} \right) + D' - \frac{\overline{p_s Q}}{g} - \frac{\overline{p_s \vec{V} \cdot \vec{f}}}{g} = 0 \quad (4.7)$$

where

$$D' = \nabla_{\lambda} \cdot \left(\frac{\overline{p_s}}{g} \overline{v' (\varepsilon' + \Phi' + c_p T')} \right) + \frac{\partial}{\partial \sigma} \left(\frac{\overline{p_s}}{g} \overline{\dot{\sigma}' (\varepsilon' + \Phi' + c_p T')} \right)$$

and $\overline{\varepsilon}_{\text{total}} = (\varepsilon + \Phi + c_p T)/g$. D' and $\overline{\varepsilon}_{\text{total}}$ may both be evaluated, the first from the tidal fields and the second from the basic state.

The term $\frac{\overline{p_s Q}}{g}$ may be broken up into terms due to absorption of solar radiation, the emission of infrared radiation, and the generation of thermal energy by dissipation. In terms of $\overline{\tau}(\sigma)$, the dissipative generation is $-\overline{\tau} \partial \overline{u} / \partial \sigma$. Thus,

$$\begin{aligned} \frac{\overline{p_s Q}}{g} + \frac{\overline{p_s \vec{V} \cdot \vec{f}}}{g} &= \frac{\overline{p_s Q_{\text{sun}}}}{g} + \frac{\overline{p_s Q_{\text{IR}}}}{g} - \overline{\tau} \frac{\partial \overline{u}}{\partial \sigma} - \overline{u} \frac{\partial \overline{\tau}}{\partial \sigma} \\ &= \frac{\overline{p_s Q_{\text{sun}}}}{g} + \frac{\overline{p_s Q_{\text{IR}}}}{g} - \frac{\partial}{\partial \sigma} (\overline{\tau} \overline{u}). \end{aligned}$$

$\frac{\overline{p_s Q_{\text{sun}}}}{g}$ can be evaluated using the same model of net solar flux as a function of height and latitude that was used for the tidal forcing. This model is based on measurements of the net solar flux by the LSFR on Pioneer Venus (Tomasko et al, 1980a). Here we use the zonal mean instead of the longitudinally oscillating components. Actually, $\overline{p_s Q_{\text{sun}}}$

$= \overline{p_s Q_{\text{sun}}} + \overline{p'_s Q'_{\text{sun}}}$ where Q'_{sun} is the tidal forcing. However, $\overline{Q_{\text{sun}}}$ and $|Q'_{\text{sun}}|$ are of the same order of magnitude while $|p'_s| \approx 4 \times 10^{-5} \overline{p_s}$, so that $\overline{p'_s Q'_{\text{sun}}}$ can be neglected. This value of $|p'_s|$ is that which would be forced by 17 W/m^2 of heating at the ground. This is the largest possible value of $|p'_s|$ since heating at the ground is much more efficient at driving surface pressure oscillations than heating aloft as shown in Section 4.3. Unfortunately, $\overline{p_s Q_{\text{IR}}}$ is not well constrained by observations as a function of height or latitude. We evaluate it subject to the boundary conditions on σ and an assumption about its latitude dependence.

$$\text{Let } D = D' - \frac{\overline{p_s Q_{\text{sun}}}}{g} + \frac{\partial}{\partial \sigma} (\overline{\tau u}) \text{ and } \frac{\overline{p_s Q_{\text{IR}}}}{g} = \frac{\partial \overline{F_{\uparrow}}}{\partial \sigma}. \text{ Then (4.7) may}$$

be rewritten as

$$\frac{\partial \overline{\varepsilon}}{\partial x} \frac{\partial \psi}{\partial \sigma} - \frac{\partial \overline{\varepsilon}}{\partial \sigma} \frac{\partial \psi}{\partial x} + D - \frac{\partial \overline{F_{\uparrow}}}{\partial \sigma} = 0 \quad (4.8)$$

where the 'total' subscript has been dropped and $x = a \sin \lambda$. To solve this equation we transform from (x, σ) to (x, ε) coordinates. Then,

$$\left(\frac{\partial \psi}{\partial x} \right)_{\sigma} = \left(\frac{\partial \psi}{\partial x} \right)_{\varepsilon} + \left(\frac{\partial \psi}{\partial \varepsilon} \right)_{x} \left(\frac{\partial \varepsilon}{\partial x} \right)_{\sigma}$$

and,

$$\left(\frac{\partial \psi}{\partial \sigma} \right)_{x} = \left(\frac{\partial \psi}{\partial \varepsilon} \right)_{x} \left(\frac{\partial \varepsilon}{\partial \sigma} \right)_{x},$$

so

$$\left(\frac{\partial \overline{\varepsilon}}{\partial x} \right)_{\sigma} \left(\frac{\partial \psi}{\partial \sigma} \right)_{x} - \left(\frac{\partial \overline{\varepsilon}}{\partial \sigma} \right)_{x} \left(\frac{\partial \psi}{\partial x} \right)_{\sigma} = - \left(\frac{\partial \psi}{\partial x} \right)_{\varepsilon} \left(\frac{\partial \overline{\varepsilon}}{\partial \sigma} \right)_{x}$$

and

and

$$\left(\frac{\partial \psi}{\partial x}\right)_{\bar{\varepsilon}} \left(\frac{\partial \bar{\varepsilon}}{\partial \sigma}\right)_x - D + \left(\frac{\partial \bar{F}_{\uparrow}}{\partial \bar{\varepsilon}}\right)_x \left(\frac{\partial \bar{\varepsilon}}{\partial \sigma}\right)_x = 0 \quad (4.9)$$

Since the atmosphere is statically stable everywhere, $\bar{\varepsilon}$ is a monotonically decreasing function of σ . Therefore, $\partial \bar{\varepsilon} / \partial \sigma$ is never zero, and we may divide through by this derivative. Then

$$\int_{\bar{\varepsilon}} \frac{\partial \psi}{\partial x} dx = \int_{\bar{\varepsilon}} D \frac{\partial \sigma}{\partial \bar{\varepsilon}} dx - \int_{\bar{\varepsilon}} \frac{\partial \bar{F}_{\uparrow}}{\partial \bar{\varepsilon}} dx \quad (4.10)$$

where the integrals are over a constant $\bar{\varepsilon}$ surface. A surface of constant $\bar{\varepsilon}$ may intersect the ground, or it may extend from the equator to the pole. The lowest value of $\bar{\varepsilon}$ is found at the ground at the pole. We require $\bar{v} = 0$ at the equator and the pole, and $\bar{\sigma} = 0$ at the ground. The corresponding conditions on ψ are $\psi = 0$ at $x = 0$ and 1 , and $\psi = 0$ at $\sigma = 1$. Thus, if we integrate (4.10) over the whole length in x of an $\bar{\varepsilon}$ surface, we obtain

$$\int_{x_1}^{x_2} \frac{\partial \bar{F}_{\uparrow}}{\partial \bar{\varepsilon}} dx = \int_{x_1}^{x_2} D \frac{\partial \sigma}{\partial \bar{\varepsilon}} dx \quad (4.11)$$

where the $\bar{\varepsilon}$ surface extends from x_1 to x_2 .

In order to calculate \bar{F}_{\uparrow} from (4.11) we assume that \bar{F}_{\uparrow} is constant on constant $\bar{\varepsilon}$ surfaces. This is roughly equivalent to assuming that the infrared flux is independent of latitude. At the top of the atmosphere this assumption is valid, since according to the OIR measurements the total mean zonal infrared flux from Venus is nearly

independent of latitude (Tomasko et al., 1980b), and near the top of the atmosphere the $\bar{\varepsilon}$ and σ surfaces nearly coincide. Lower in the atmosphere $(\partial\bar{\varepsilon}/\partial x)_\sigma < 0$. Since $(\partial\bar{F}_\uparrow/\partial\bar{\varepsilon})_x > 0$, our assumption that $\bar{F}_\uparrow(\bar{\varepsilon})$ is a constant implies $(\partial\bar{F}_\uparrow/\partial x)_\sigma = (\partial\bar{F}_\uparrow/\partial\bar{\varepsilon})_x (\partial\bar{\varepsilon}/\partial x)_\sigma < 0$. Thus, the net upward IR flux is greater near the than the pole on constant σ surfaces, as would be expected since the equator is warmer near the surface. The $\bar{\varepsilon}$ surfaces level out in the upper atmosphere because in the region where the zonal wind falls to zero, the pole is warmer than the equator on constant σ surfaces.

With the above assumption,

$$\frac{\partial\bar{F}_\uparrow}{\partial\bar{\varepsilon}} = \frac{1}{x_2 - x_1} \int_{x_1}^{x_2} D(x, \bar{\varepsilon}) \frac{\partial\sigma}{\partial\bar{\varepsilon}} dx$$

where $\partial\bar{F}_\uparrow/\partial\bar{\varepsilon}$ is a constant.

Finally, $\psi(x, \bar{\varepsilon})$ may be found by integrating (4.10) from x_1 to x and substituting the above expression for $\frac{\partial\bar{F}_\uparrow}{\partial\bar{\varepsilon}}$:

$$\psi(x, \bar{\varepsilon}) = \int_{x_1}^x D(x, \bar{\varepsilon}) \frac{\partial\sigma}{\partial\bar{\varepsilon}} dx - \frac{x - x_1}{x_2 - x_1} \int_{x_1}^{x_2} D(x, \bar{\varepsilon}) \frac{\partial\sigma}{\partial\bar{\varepsilon}} dx \quad (4.12)$$

We solve this equation by numerical integration. In evaluating D we neglect the term $\partial(\bar{\tau} \bar{u})/\partial\sigma$. Or if we use the eddy viscosity profile described earlier to determine $\bar{\tau}$, $\partial(\bar{\tau} \bar{u})/\partial\sigma$ is negligible.

After solving (4.12) we substitute the resulting stream function into the angular momentum conservation equation (4.5). In terms of ψ this is

$$\frac{\partial \overline{p_s L}}{\partial t} = - \frac{1}{g} \frac{\partial \overline{L}}{\partial x} \frac{\partial \psi}{\partial \sigma} + \frac{1}{g} \frac{\partial \overline{L}}{\partial \sigma} \frac{\partial \psi}{\partial x} - A' - \frac{\partial \overline{\tau}}{\partial \sigma} a \cos \lambda \quad (4.13)$$

where $A' = \nabla_{\lambda} \cdot \left(\frac{\overline{p_s v' L'}}{g} + \frac{\partial}{\partial \sigma} \left(\frac{\overline{p_s \sigma' L'}}{g} + \frac{\overline{\sigma p_s' \partial \Phi'}}{g \partial \sigma} \right) \right)$. \overline{L} is known from the basic state and A' is known from the tidal calculations. If all relevant processes had been included correctly the left-hand side of (4.13) would be zero. This is not the case as shown in Figs. 4.43-4.45. As in Fig. 4.42, in Figs. 4.43-4.45 the left-hand side of (4.13) has been multiplied by σ and plotted against $-\ln \sigma$. The term $\partial \overline{\tau} / \partial \sigma (a \cos \lambda)$ was not $\partial \sigma$ included in Figs. 4.43-4.45, but as shown in Fig. 4.42, it less than 0.5×10^5 Joules/m² at all levels at the equator. It will also be negligible at other latitudes since it decreases as $\cos^2 \lambda$.

Although the angular momentum equation does not balance, some insight can be gained from the results of these calculations. First we compare Fig. 4.43 to Fig. 4.46. In Fig. 4.46 we plot the rate of change of angular momentum at the equator due to the tides including the transport by the mean meridional circulation forced by the tides. To calculate this mean circulation we evaluate D in equation (4.12) with $\overline{p_s Q_{\text{sun}}}/g = 0$. Since (4.12) is linear in D, the difference between Fig. 4.43 and Fig. 4.46 is due to the mean meridional circulation forced by the latitudinal gradient in the solar heating. Thus, the oscillations above 55 km in Fig. 4.43 are due to the tides, while the larger peaks below that level are due primarily to transports driven by the solar heating.

In Figs. 4.44 and 4.45 the rate of change of angular momentum due to the imbalance in equation (4.13) is shown at latitudes 24° and

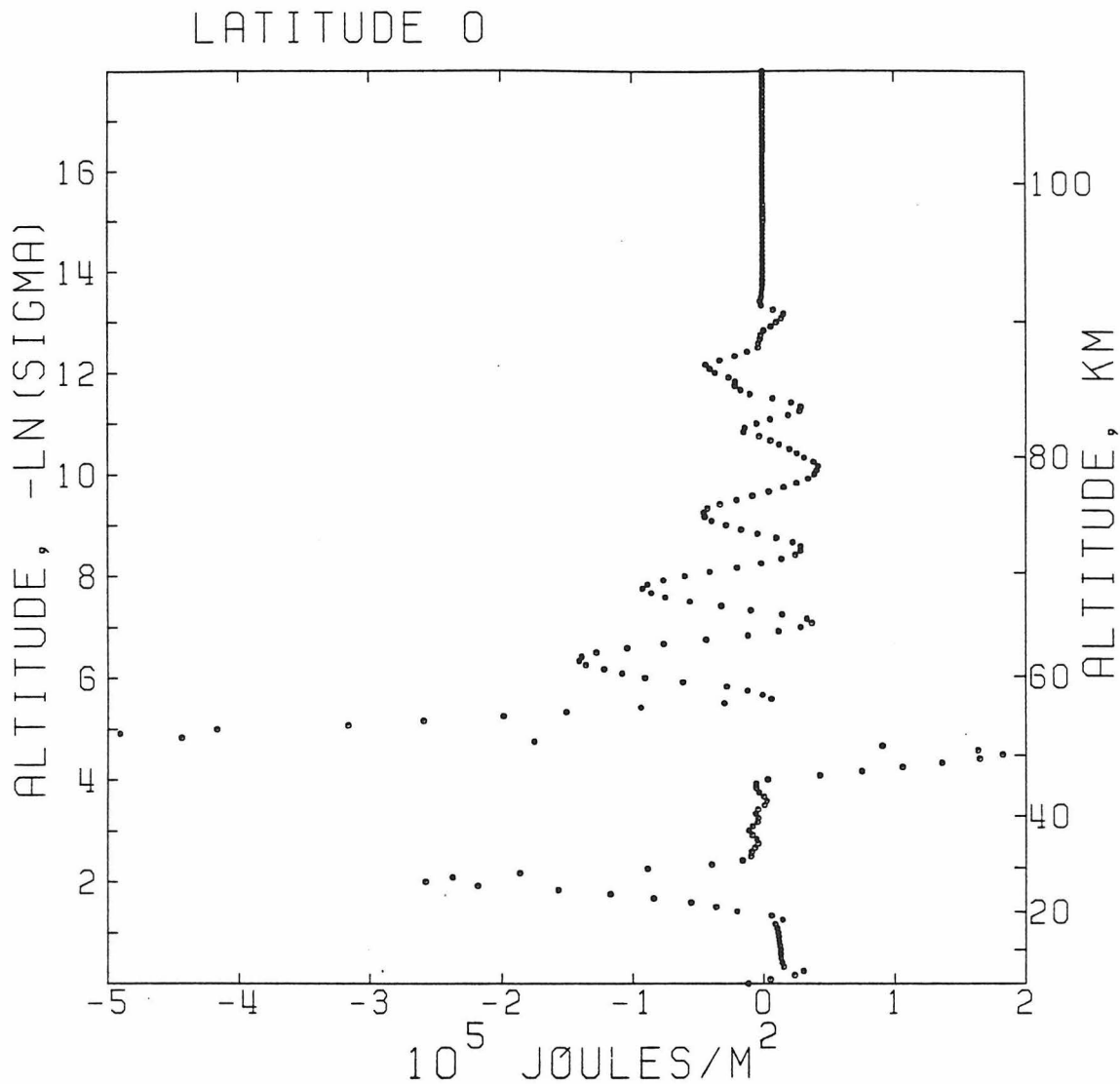


Figure 4.43 The equatorial rate of change of zonal retrograde angular momentum per unit area, scaled by σ , due to transport by the tides and the mean meridional circulation. The area under the curve is equal to the total angular momentum flux in a column of unit area at the equator. The rate of change of angular momentum is proportional to the acceleration of the mean zonal wind. The decelerations at 20 and 55 km are due to transport by direct Hadley cells, while the acceleration at 50 km is due to an indirect cell. The oscillations above 60 km are due to the tides.

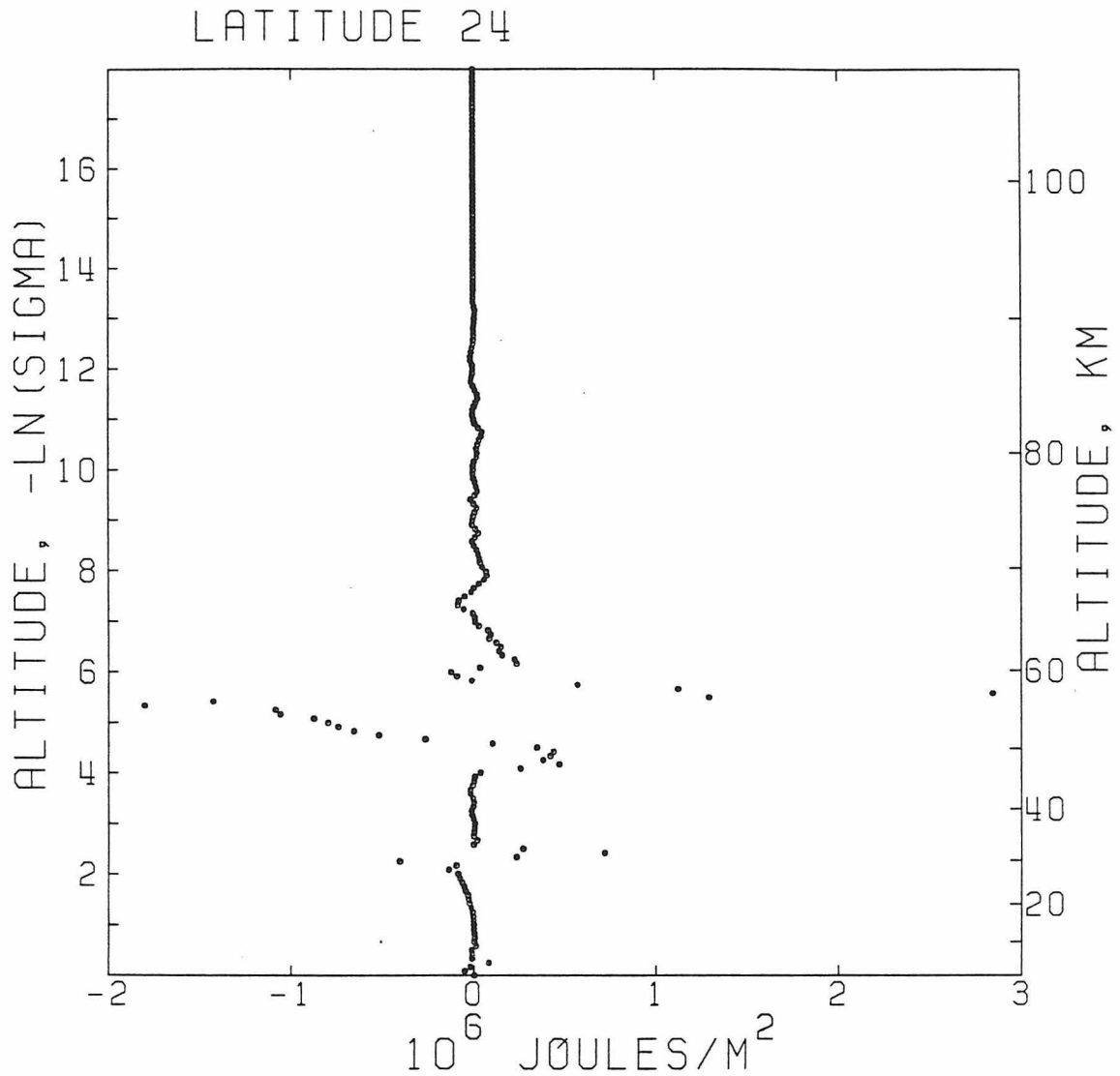


Figure 4.44 Same as Fig. 4.43 at 24° . At this latitude the peaks of angular momentum flux due to the mean meridional circulation are much larger and confined to a narrower altitude region. The direct Hadley cells now cause an acceleration of the mean zonal wind, while the indirect cell causes a deceleration.

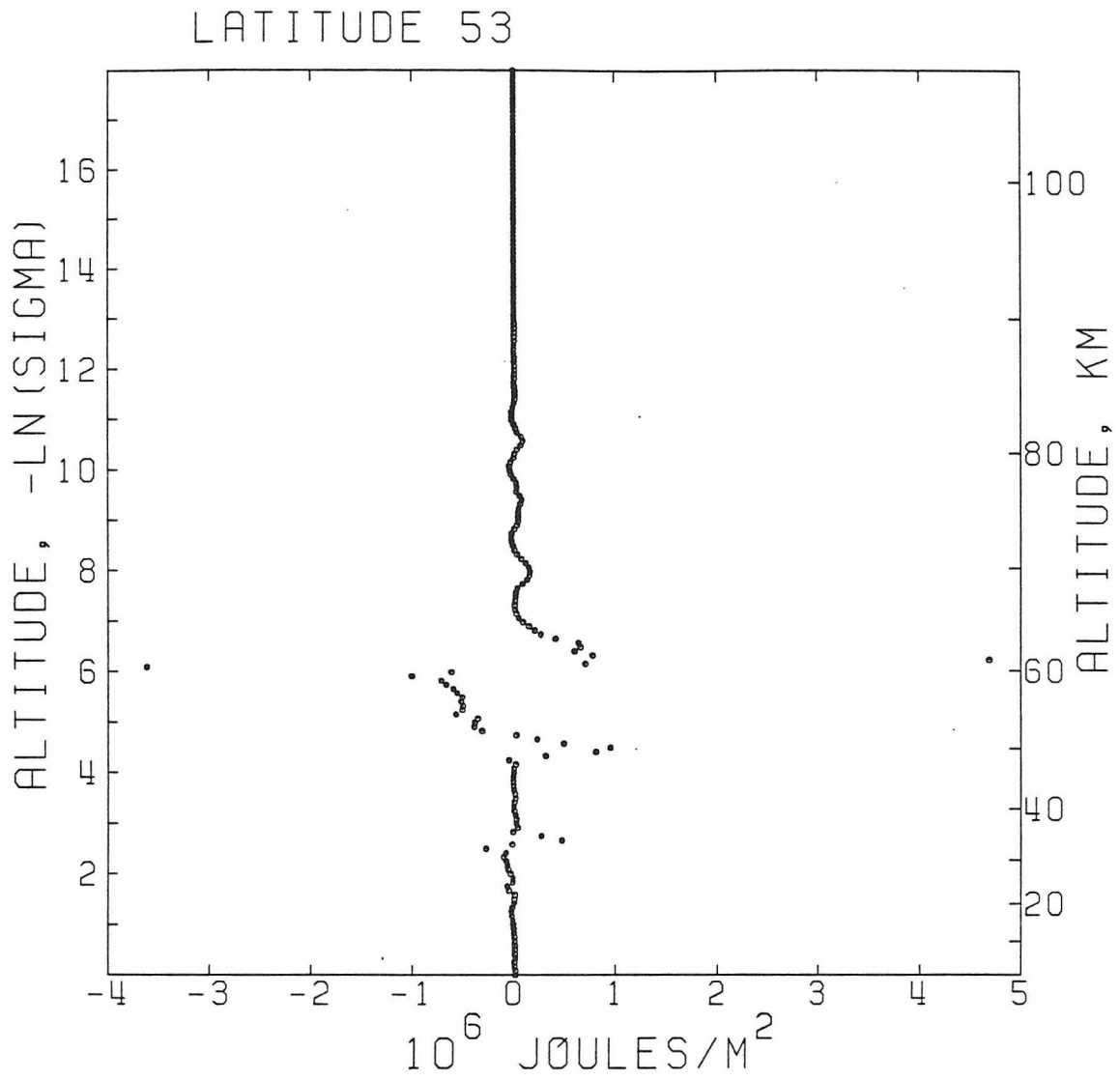


Figure 4.45 Same as Fig. 4.44 at 53° .

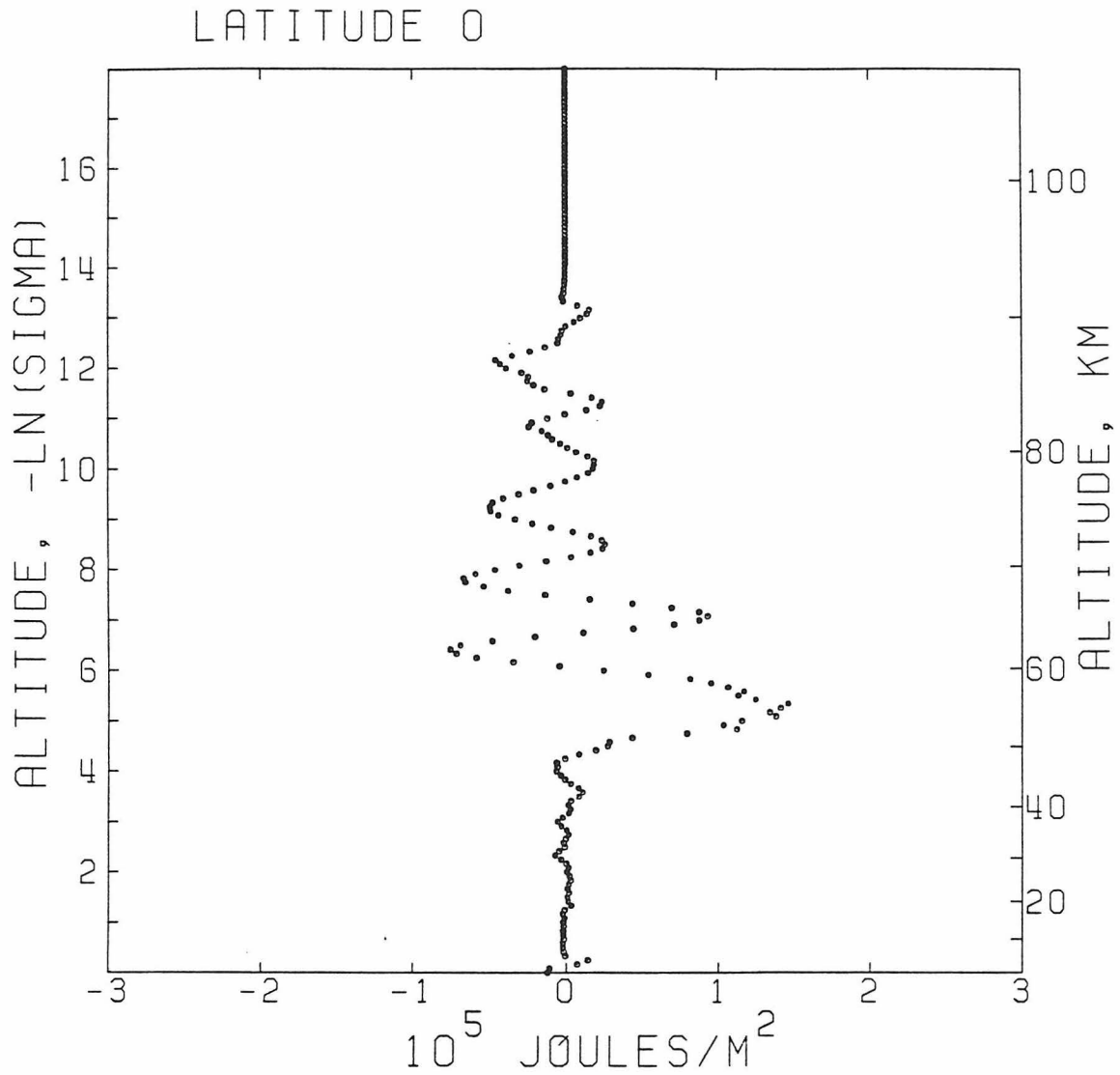


Figure 4.46 The equatorial rate of change of zonal retrograde angular momentum per unit area, scale by σ , due to transport by the tides and the mean meridional circulation driven by the tides. This mean circulation is that which is required to balance the tidal energy flux at each latitude and altitude. The area under the curve is equal to the total angular momentum flux in a column of unit area at the equator.

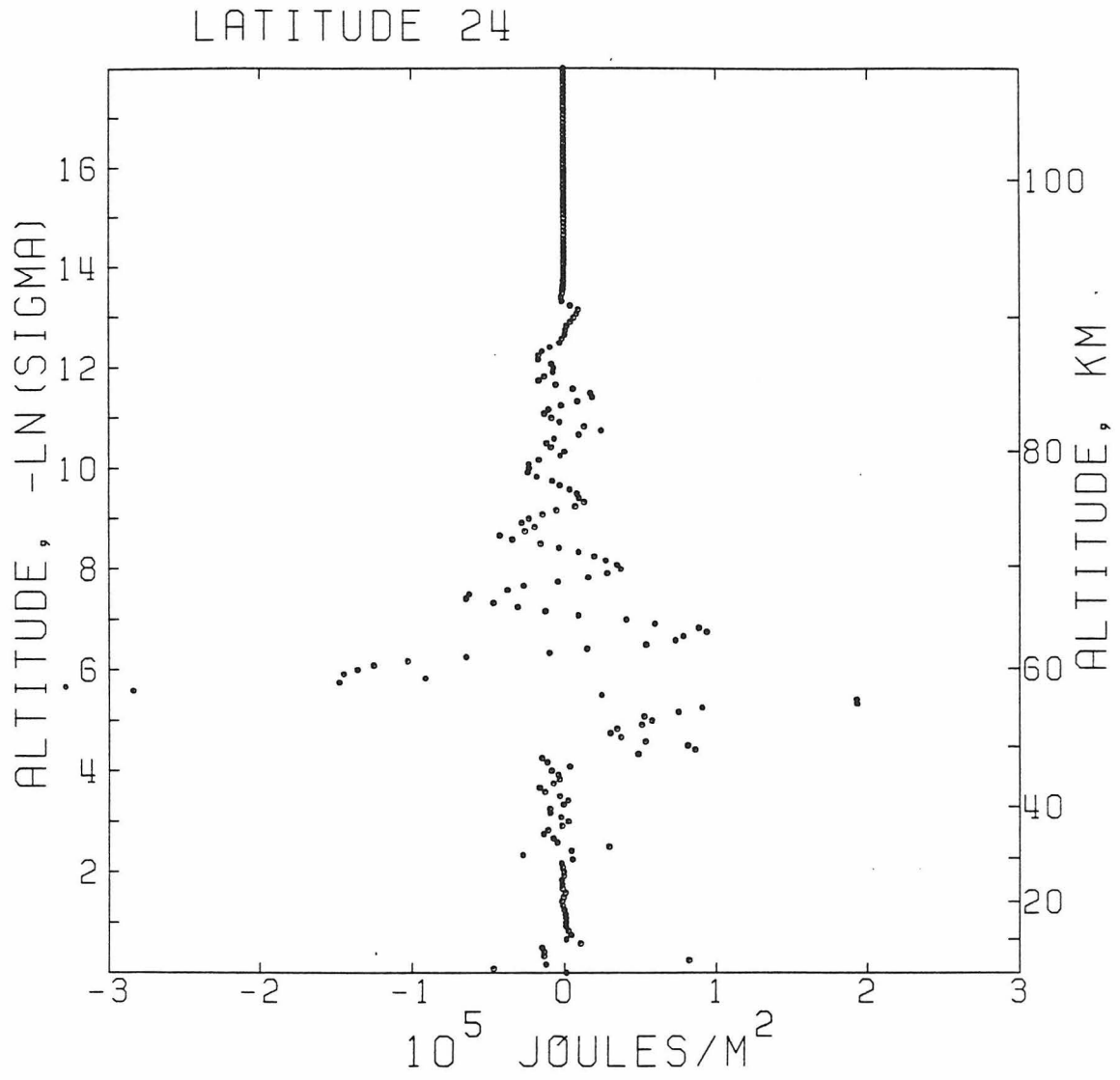


Figure 4.47 Same as Fig. 4.46 at 24°.

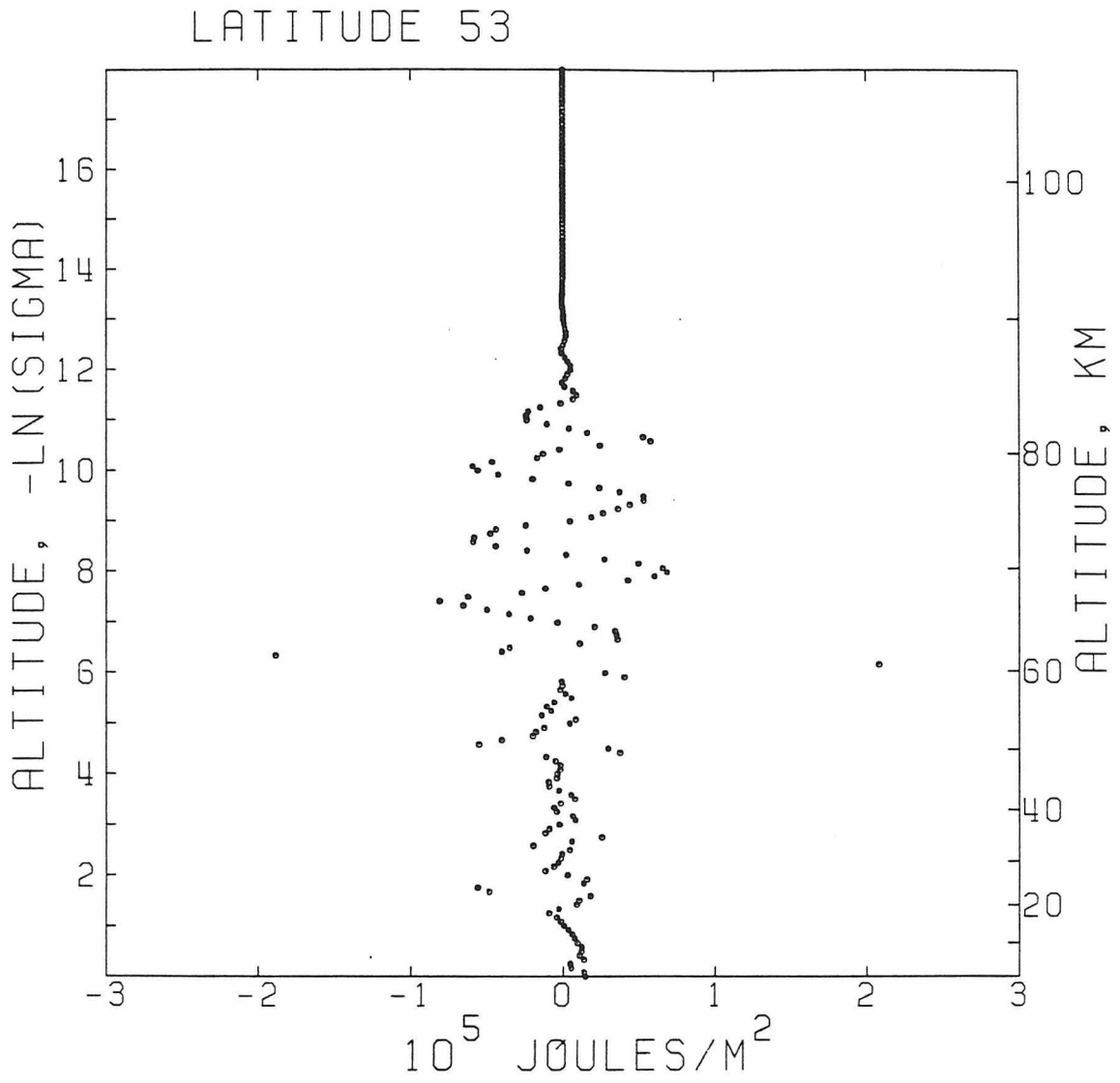


Figure 4.48 Same as Fig. 4.46 at 53°.

53°. At these latitudes the effects of the transports due to the solar-driven mean circulation are confined to a narrower altitude region and are much larger. The rate of change of angular momentum due to tidal transports is qualitatively the same at higher latitudes as at the equator as shown in Figs. 4.47 and 4.48.

The stream function associated with the solar-driven circulation indicates that this circulation is made up of a series of direct and indirect Hadley cells stacked on top of each other. This type of layered structure in the meridional circulation has been suggested by many previous investigations (Kálnay de Rivas, 1973, 1975; Schubert et al., 1980; Rossow, 1982; Schubert, 1982). In our calculation we find a weak indirect cell below 20 km, a direct cell from 20 km to 45 km, an indirect cell from 45 to 55 km and a direct cell above that. The presence of the indirect cell near the ground is probably due to the omission of heating at the ground. This heating could drive a direct cell which would be in agreement with the investigations cited above.

The mean meridional wind associated with the stream function derived when tidal and solar contributions are included in D is shown at latitudes 12°, 24°, and 53° in Figs. 4.49-4.51. The only significant velocities are associated with the cloud level Hadley cell. The shears are unrealistically high at 53° and would be destroyed by shear instabilities. The magnitude of \bar{v} is also higher than observed. Perhaps in the real atmosphere the cell does not narrow and intensify at higher latitudes as in the model or perhaps the Hadley cell does not extend so far poleward.

The strongest flow and the largest transports of angular

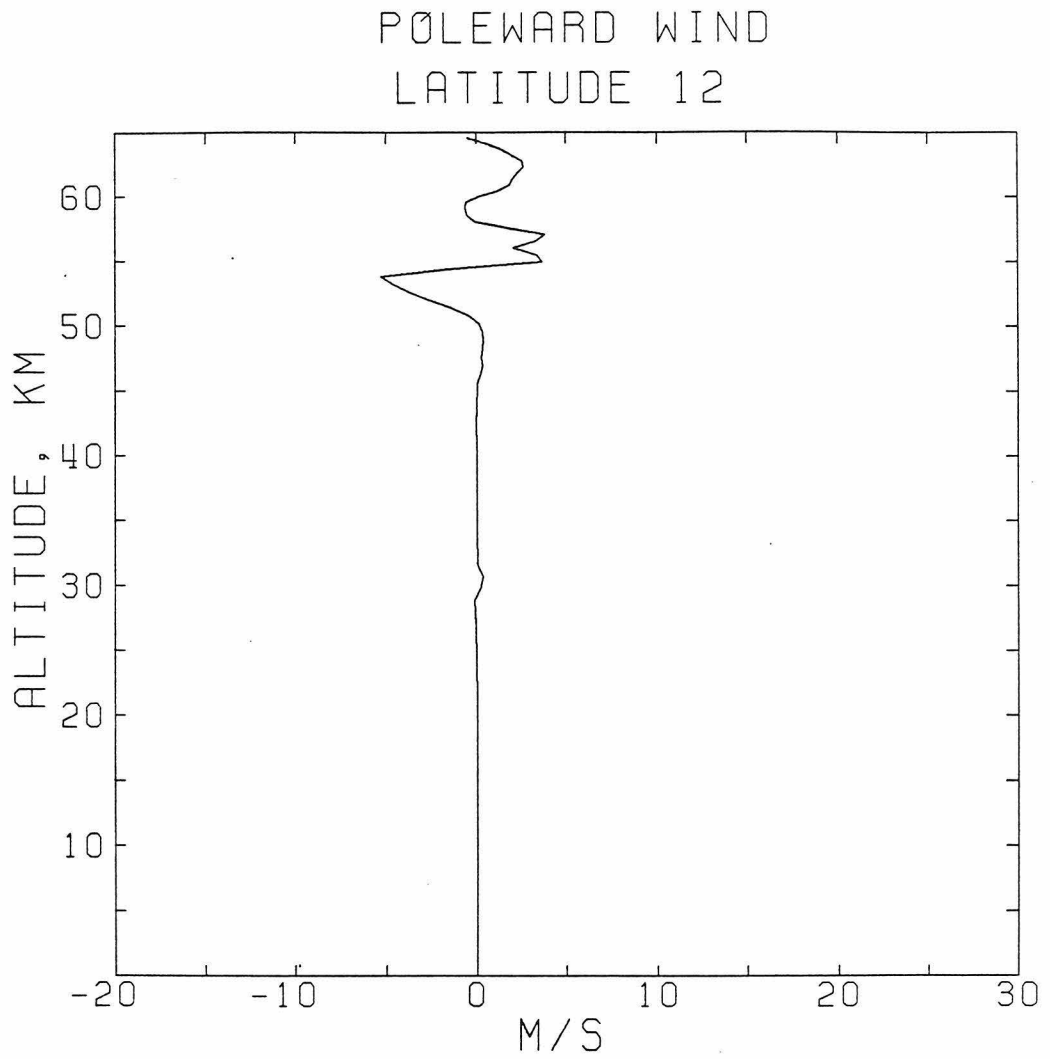


Figure 4.49 The mean meridional wind at 12° including the solar driven and tidal driven circulations.

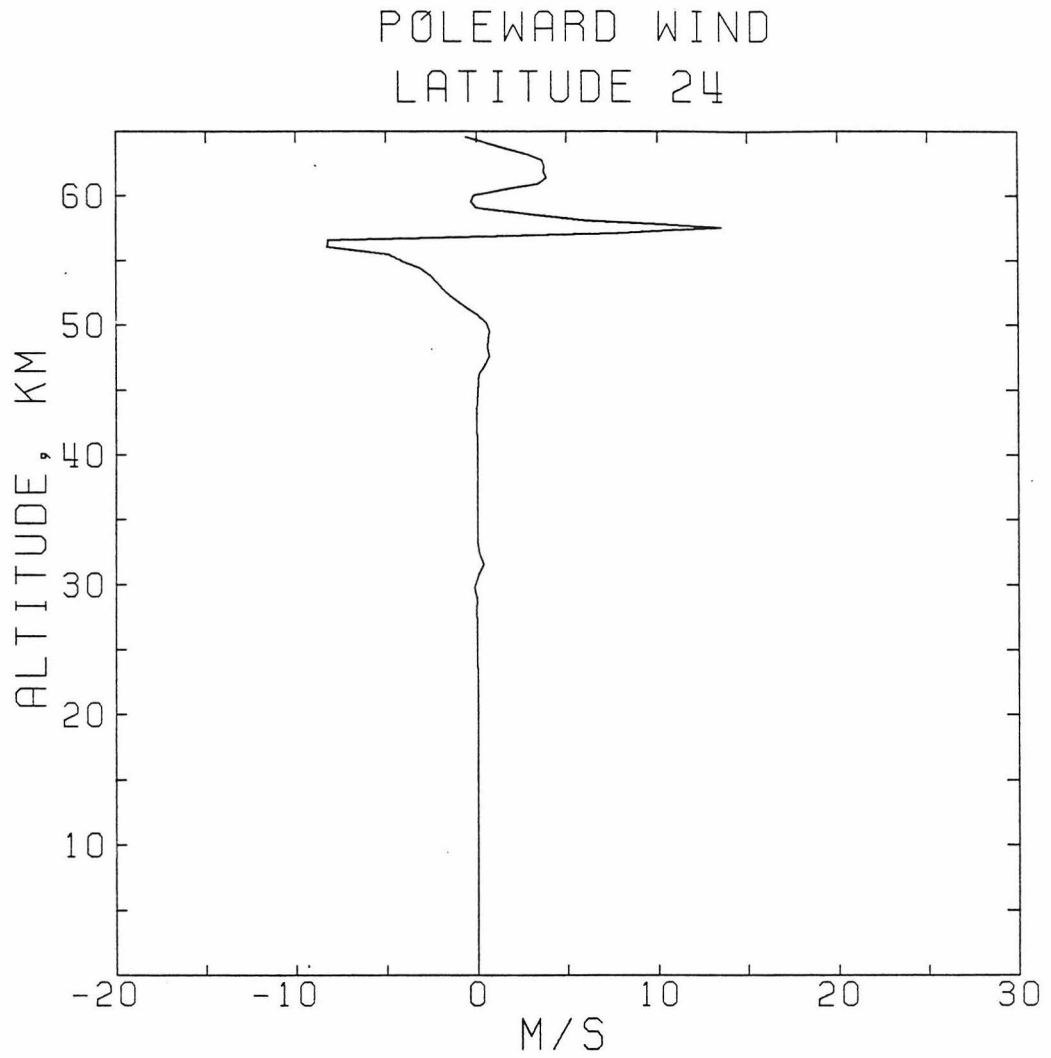


Figure 4.50 The mean meridional wind at 24° including the solar driven and tidal driven circulations.

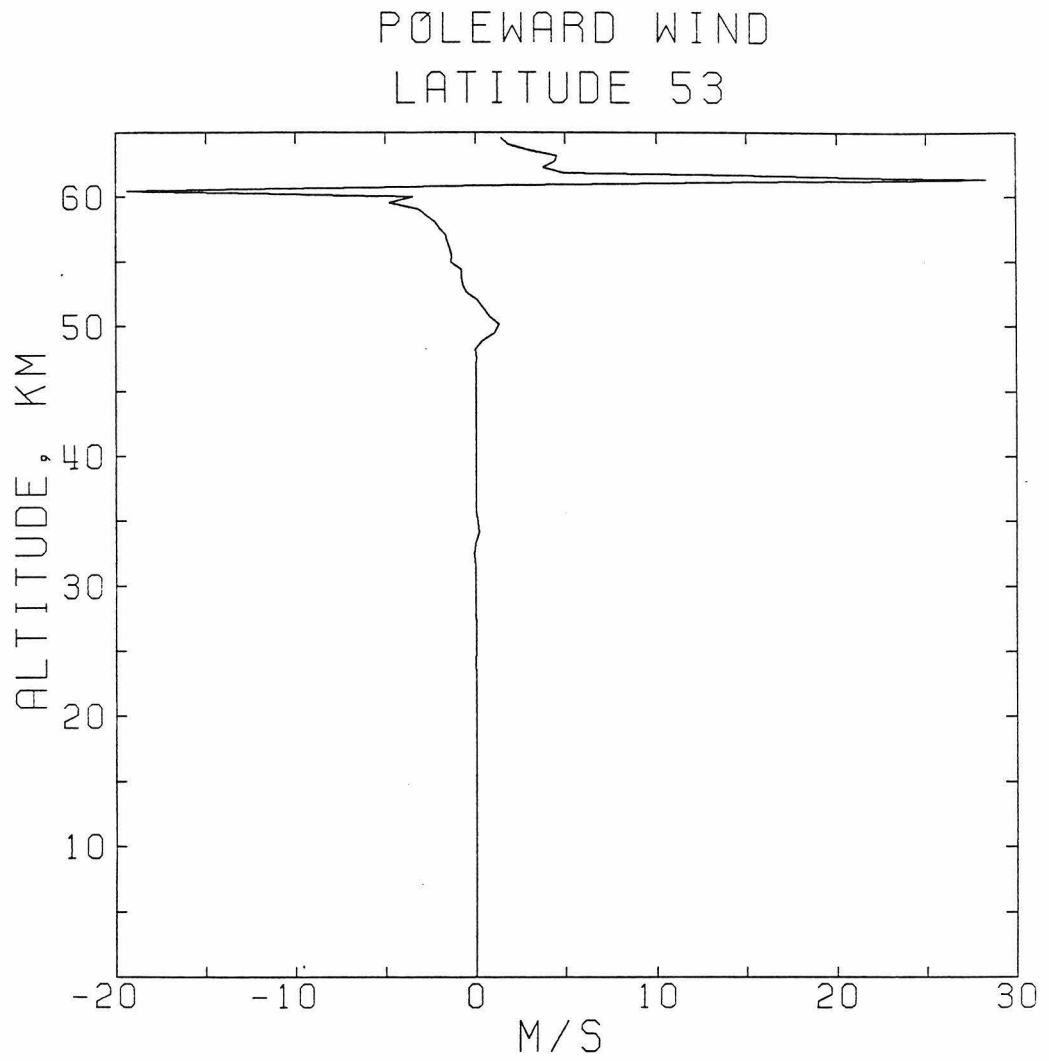


Figure 4.51 The mean meridional wind at 53° including the solar driven and tidal driven circulations.

momentum occur in the low stability regions of the atmosphere. The mean meridional circulation tends to be confined to these regions because of the dependence of ψ on $\partial\sigma/\partial\bar{\epsilon}$ [see equation (4.12)]. $\bar{\epsilon}$ is nearly a constant at each latitude in regions close to being adiabatic, so $\partial\sigma/\partial\bar{\epsilon}$ becomes very large. At high latitudes the flow intensifies and is channeled into a narrow layer where the stability is very close to zero. The confinement of the flow may be partially offset by a redistribution of the heat deposited in the nearly adiabatic layer. Convection may transport some of this heat upward into the adjacent stable layers. In equation (4.12) the heating is included in $D(x, \bar{\epsilon})$. Decreasing $D(x, \bar{\epsilon})$ in the nearly adiabatic layer and increasing it in the layer above would smooth out the integrand in (4.12) and tend to cause the flow to spread out over a thicker layer.

A theory for the maintenance of the high zonal wind based on angular momentum transport by Hadley cell was first proposed by Gierasch (1975). The net effect of a direct Hadley cell is to carry angular momentum upward since the rising motions near the equator carry more angular momentum than the sinking motions at higher latitudes. This upward transport could balance downward transport of angular momentum by small scale diffusive processes. The solid planet is a sink for the downward transport. The return branch of a ground level Hadley cell may pick up angular momentum through friction with the solid planet completing the cycle. For a Hadley cell which does not reach the ground, some other process must be postulated to transport angular momentum over the intervening atmosphere. Indirect cells, if present, will tend to transport angular momentum downward.

The latitudinally averaged rate of change of angular momentum due to vertical transport by the solar-driven circulation of our model is shown in Fig. 4.52. The area under this curve is zero since the total angular momentum is conserved. Angular momentum is transported upward in the lower direct Hadley cell as shown by the deceleration at about 20 km and the acceleration at 30 km. According to Gierasch's theory, the angular momentum deficit at 20 km would have to be balanced by another process transporting angular momentum upward while the excess angular momentum at 30 km would be diffused downward by small scale eddies. If this cell reached the ground, we could assume that the lost angular momentum was regained through friction from the solid planet. Although this cell extends upward to 45 km, no significant amount of transport occurs in the stable layer. From 52 to 58 km the direct and indirect cells combine in removing angular momentum. Approximately equal amounts of angular momentum are transported upward and downward from this region as shown by the comparable size of the peaks at 50 and 62 km. For Gierasch's theory to work in this case, some other process not included here must balance the downward transport and supply angular momentum to the direct cell. Angular momentum must also be transported upward to 70 km for consistency with our basic state in which the peak zonal wind is reached at this level.

The contribution of the tidal transport to the latitudinally averaged rate of change of angular momentum is shown in Fig. 4.53. This includes transport due to the mean meridional circulation forced by the tides. The magnitude in Fig. 4.53 is generally smaller than that due to the solar-driven circulation, and the alternating layers of acceleration

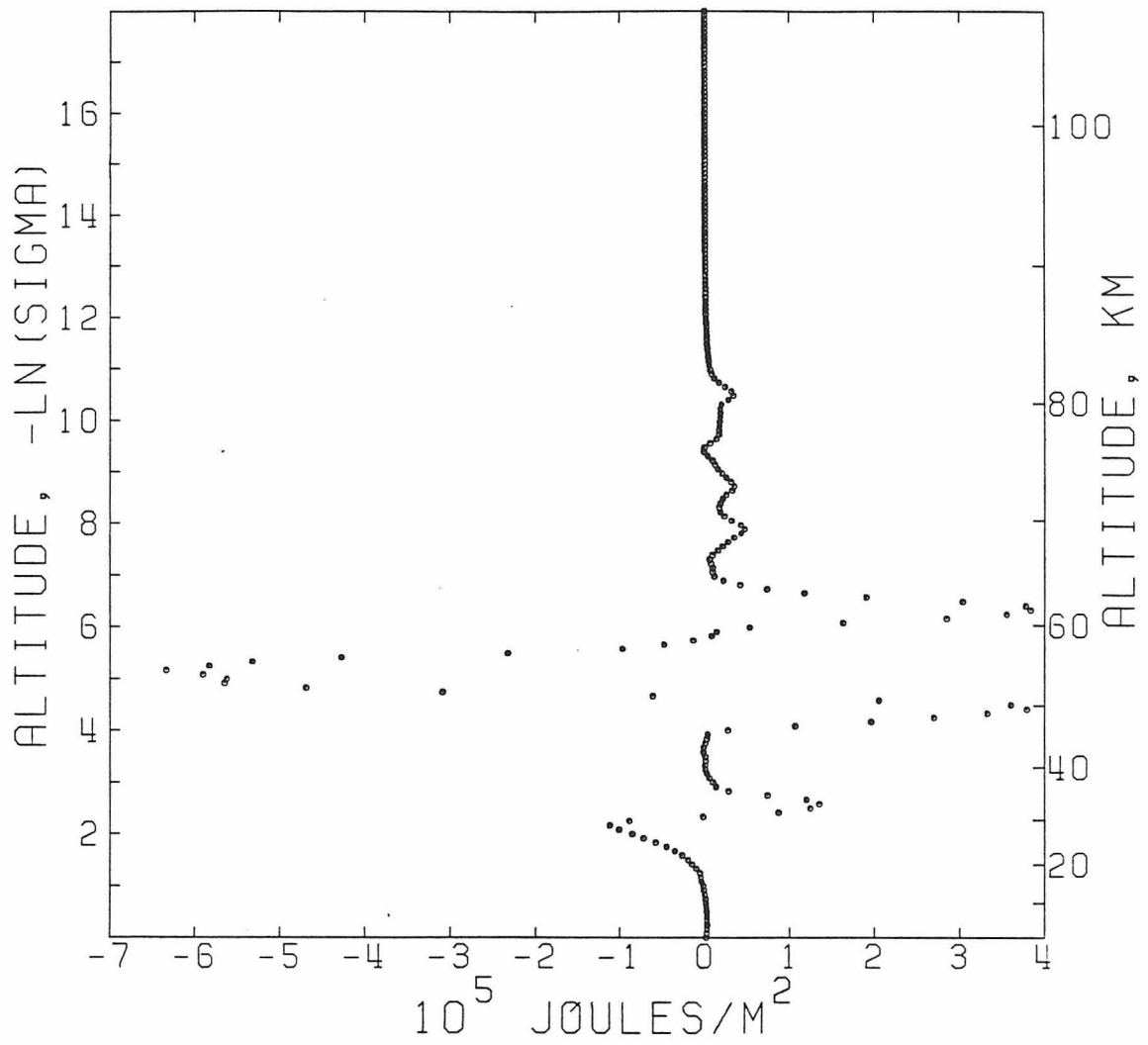


Figure 4.52 The latitudinally averaged rate of change of zonal retrograde angular momentum per unit area, scaled by σ , due to vertical transport by the solar driven mean meridional circulation.

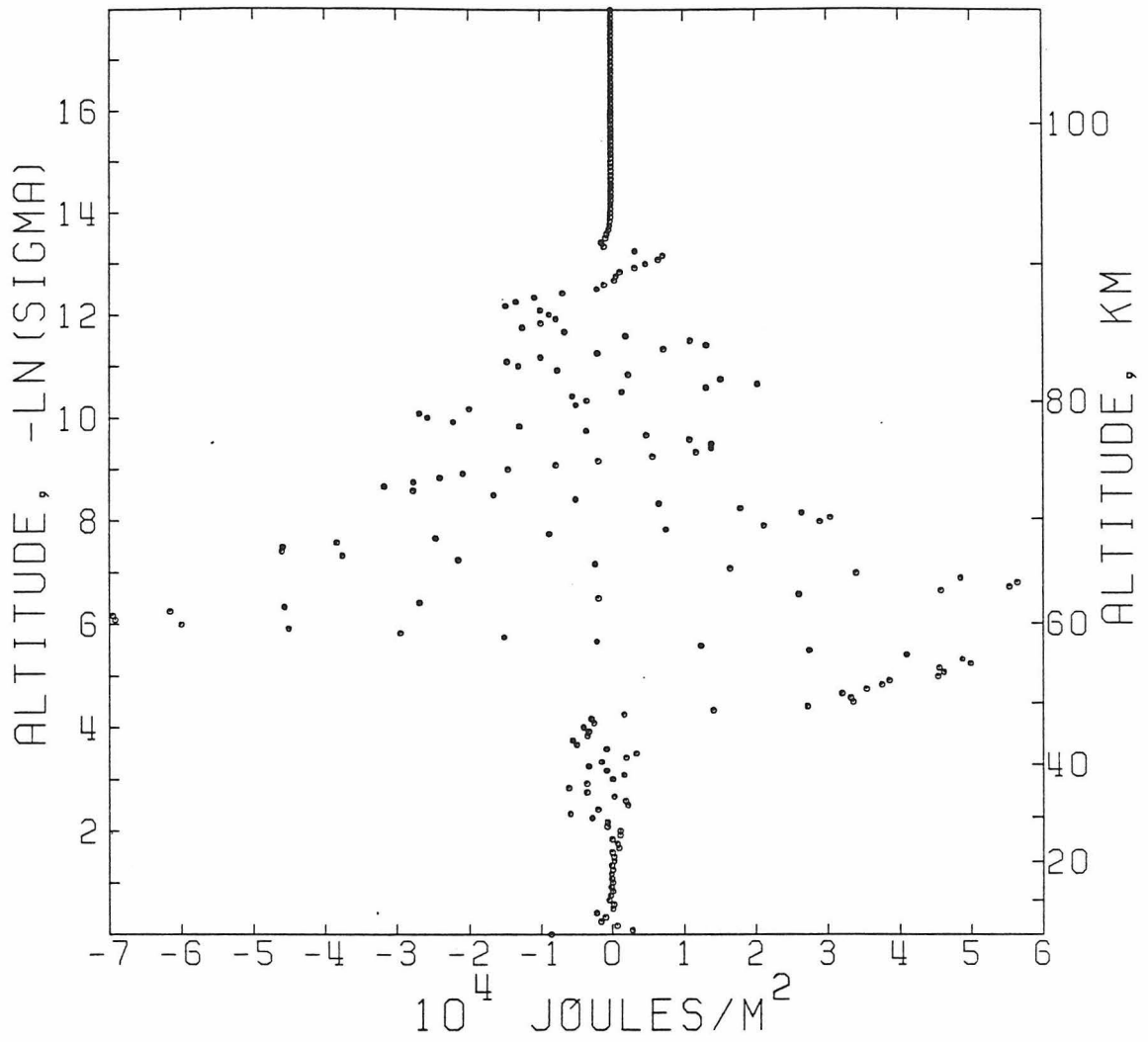


Figure 4.53 The latitudinally averaged rate of change of zonal retrograde angular momentum per unit area, scaled by σ , due to vertical transport by the tides and tidal driven mean meridional circulation.

and deceleration do not indicate a general upward transport. Thus, the tides are probably not the missing link required to supply angular momentum to the upper atmosphere. The effect of the alternating regions of acceleration and deceleration would be to create alternating regions of positive and negative shear in the zonal wind superimposed on the basic state profile. The tendency to create these shears is opposed by small scale diffusive processes. Shear instabilities would set in if the shears became large enough.

One problem with the Hadley cell theory is the necessity of supplying the equatorial region with angular momentum to replace that transported away. In the upper branch of each direct cell the flow is away from the equator. This flow is down the gradient of angular momentum so it tends to decelerate the equatorial zonal wind as shown in Fig. 4.43. Although the upward transport of angular momentum in the Hadley cell may be able to balance the downward transport due to small scale eddies, it is impossible for the mean meridional circulation to accelerate the equatorial wind (Hide, 1969; Held and Hou, 1980). Gierasch (1975) proposed that strong horizontal mixing could keep the winds at higher latitudes from accelerating at the expense of the equator. However, if the mixing process transports heat as well as momentum, it tends to eliminate the need for a mean meridional circulation (Kálnay de Rivas, 1975).

If the atmosphere were barotropic at the levels at which the horizontal mixing occurred, then it would be possible to transport momentum but very little heat (Rossow and Williams, 1979). The mixing could be triggered by barotropic instability. There is some

observational support for this possibility. The mid-latitude jet in the zonal wind present at the time of the Mariner 10 fly-by meets the criterion necessary for barotropic instability (Travis, 1978; Elson, 1978). Similar jets have been observed during the Pioneer Venus extended mission (Rossow and Kinsellar, 1982). These jets could be formed by the poleward transport of angular momentum by the Hadley cell. When they become unstable, they might give up their excess angular momentum to barotropic eddies. The transport by the eddies could return the atmosphere to a state of solid body rotation. Whether or not the atmosphere actually behaves barotropically is unknown. An estimate by Schubert (1982) indicates that baroclinic effects are probably important for large scale eddies in the low stability region in the clouds. Also, all observations of cloud level motions to date show poleward transport of angular momentum by the eddies (Limaye and Suomi, 1981; Limaye et al., 1982). Barotropic eddies might also be the mechanism transporting angular momentum equatorward in the lower direct Hadley cell, but there are no observations available to determine if this is the case.

The contribution of the tides to the equatorward transport of angular momentum can be determined from our calculations. The rate of change of angular momentum at the equator due to latitudinal transport by the tides and the mean meridional circulation forced by the tides is obtained by integrating the quantity plotted in Fig. 4.46 over $-\ln\sigma$. The integral is positive so the tides do tend to accelerate the equatorial zonal wind. In fact, from 0° to 17° latitude the tides supply angular momentum to the zonal wind at an average rate of $6.3 \times$

10^4 J/m^2 . This rate must be compared to the rate of loss of angular momentum from the equatorial region due to the solar-driven circulation which is $-3.2 \times 10^5 \text{ J/m}^2$ from 0° to 15° latitude. Thus, the tidal transport supplies about $1/5$ the angular momentum lost due to Hadley cell transport. Outside the equatorial region from 17° to 53° the tides remove angular momentum at an average rate of $3.9 \times 10^4 \text{ J/m}^2$ and deposit it from 53° to 90° at an average rate of $0.6 \times 10^4 \text{ J/m}^2$. The pattern is similar to that of the latitudinal heat transport by the diurnal tide shown in Fig. 4.41. Since the tides transport heat up the temperature gradient to the equator from mid-latitudes, they will not have the effect of eliminating the need for the solar-driven meridional circulation. The solar-driven circulation contributes to increasing the angular momentum of the zonal wind from 15° to the pole at an average rate of $1.2 \times 10^5 \text{ J/m}^2$. From 17° to 53° the average rate of increase is also $1.2 \times 10^5 \text{ J/m}^2$. The tides are able to offset about a third of the increase in this region.

It must be kept in mind that the results of these second order calculations are quite tentative. These calculations are only approximations of non-linear processes and are subject to assumptions such as that concerning the latitudinal dependence of the mean planetary infrared flux. Also, our model cannot be considered complete since the rate of change of angular momentum is not zero at every height and latitude. Part of the problem is due to the fact that the rate of change of angular momentum from the tides and mean meridional circulation is large compared to that from eddy dissipation based on observational estimates of the eddy viscosity. If this eddy dissipation

accurately determines the loss of angular momentum from the jet in the zonal wind, then it must be balanced by a small difference between large quantities, which would be difficult to achieve. It seems more likely that the process which removes angular momentum from the atmosphere through downward transport and frictional transfer to the solid planet is at least comparable to the tides and the mean meridional circulation in the rate of change of angular momentum it generates. Our solar-driven, mean meridional circulation consists of stacked, direct and indirect Hadley cells. It does not transport angular momentum upward throughout the atmosphere so an additional process is required to provide the necessary upward transport. This mean circulation also tends to deplete the angular momentum of the equatorial region so a process to transport angular momentum equatorward is also needed. From our results it appears that the vertical transport of angular momentum by the tides is small, but that the latitudinal transport is significant compared to the transport by the solar-driven circulation.

REFERENCES

- Avdueskii, V.S., N.F. Borodin, V.P. Burtsev, Ya. V. Malkov, M. Ya. Marov, M.K. Rozhdestvenskii, R.S. Romanov, S.S. Sokolov, V.G. Fokin, Z.P. Cheremukhina, and V.I. Shkirina (1976). Automatic Stations Venera 9 and Venera 10: Functioning of descent vehicles and measurement of atmospheric parameters, Cosmic Res., 14, 577-586.
- Bartels, J. (1928). Gezeitenschwingungen der Atmosphäre, Handbuch der Experimentalphysik, 25, 163-210.
- Belton, M., G. Smith, G. Schubert, and A.D. Del Genio (1976). Cloud patterns, waves, and convection in the Venus atmosphere, J. Atmos. Sci., 33, 1394-1417.
- Betz, A.L., M.A. Johnson, R.A. McLaren, and E.C. Sutton (1976). Heterodyne detection of CO₂ emission lines and wind velocities in the atmosphere of Venus, Astrophys. J., 208, L141-L144.
- Betz, A.L., E.C. Sutton, R.A. McLaren, and C.W. McClary (1977). Laser heterodyne spectroscopy, in Proceedings of the Symposium on Planetary Atmospheres, edited by A.V. Jones, pp. 29-33, Royal Society of Canada, Ottawa, Ontario.
- Butler, S.T., and K.A. Small (1963). The excitation of atmospheric oscillations, Proc. Roy. Soc. London, A274, 91-121.
- Chapman, S., and R.S. Lindzen (1970). Atmospheric Tides: Thermal and Gravitational, 200 pp., Gordon and Breach, New York, NY.
- Counselman III, C.C., S.A. Gourevitch, R.W. King, and G.B. Lorient (1980). Zonal and meridional circulation of the lower atmosphere of Venus determined by radio interferometry, J. Geophys. Res., 85, 8026-8030.
- Covey, C.C. (1982). Models of Planetary scale waves in the Venus atmosphere, Ph.D. Thesis, University of California, Los Angeles, CA
- Dickinson, R.E. (1972). Infrared radiative heating and cooling in the Venusian mesosphere. I: Global mean radiative equilibrium, J. Atmos. Sci., 29, 1531-1556.
- Diner, D.J., J. Apt, and L.S. Elson (1982). Comparison of ground-based and spacecraft observations of the infrared emission from Venus: The nature of thermal contrasts, Icarus, 52, 301-319.
- Dobrovolskis, A.R. (1978). The Rotation of Venus, Ph.D. Thesis, Calif. Inst. of Technol., Pasadena, Calif.

- Dolfus, A. (1975). Venus: Evolution of the upper atmosphere clouds, J. Atmos. Sci., 32, 1060-1070.
- Eckart, C. (1960). Hydrodynamics of Oceans and Atmospheres, 290 pp., Pergamon Press, London.
- Elson, L. (1978). Barotropic instability in the upper atmosphere of Venus, Geophys. Res. Lett., 5, 603-605.
- Elson, L.S. (1982). Circulation modeling of the Venusian atmosphere from the cloud tops to 100 km, in preparation.
- Gierasch, P.J. (1975). Meridional circulation and the maintenance of the Venus atmospheric rotation, J. Atmos. Sci., 32, 1038-1044.
- Gold, T., and S. Soter (1971). Atmospheric tides and the 4-day circulation on Venus Icaurs, 14, 16-20.
- Held, I.M., and A.Y. Hou (1980). Nonlinear axially symmetric circulations in a nearly inviscid atmosphere, J. Atmos. Sci., 37, 515-533.
- Hide, R. (1969). Dynamics of the atmospheres of the major planets with an appendix on the viscous boundary layer at the rigid bounding surface of an electrically-conducting rotating fluid in the presence of a magnetic field, J. Atmos. Sci., 26, 841-853.
- Hilsenrath, J., C.W. Beckett, W.S. Benedict, L. Fano, H.J. Hoge, J.F. Masi, R.L. Nuttall, Y.S. Touloukian, and H.W. Woolley (1955). Tables of thermal properties of gases: Tables of thermodynamic and transport properties of air, A, CO₂, CO, H, N, O, steam, National Bureau of Standards Circular 564.
- Hoffman, J.H., V.I. Oyama, and U. von Zahn (1980). Measurements of the Venus lower atmosphere composition: A comparison of results, J. Geophys. Res., 85, 7871-7881.
- Holton, J.R. (1972). An Introduction to Dynamic Meteorology, 319 pp., Academic Press, New York, NY.
- Hoskins, B.J., and A.J. Simmons (1975). A multi-layer spectral model and the semi-implicit method, Quart. J. Roy. Met. Soc., 101, 637-655.
- Ingersoll, A.P., and A.R. Dobrovolskis (1978). Venus' rotation and atmospheric thermal tides, Nature, 275, 37-38.
- Kalnay de Rivas, E. (1973). Numerical models of the circulation of the atmosphere of Venus, J. Atmos. Sci., 31, 763-779.

- Kalnay de Rivas, E. (1975). Further numerical calculations of the circulation of the atmosphere of Venus, J. Atmos. Sci., 32, 1017-1024.
- Kelvin (see Thomson).
- Kirkwood, E., and J. Derome (1977). Some effects of the upper boundary condition and vertical resolution on modeling forced stationary planetary waves, Mon. Wea. Rev., 105, 1239-1251.
- Kliore, A.J., and I.R. Patel (1980). Vertical structure of the atmosphere of Venus from Pioneer Venus orbiter radio occultations, J. Geophys. Res., 85, 7957-7962.
- Kliore, A.J., and I.R. Patel (1982). Thermal structure of the atmosphere of Venus from Pioneer Venus radio occultations, Icarus, 52, 320-334.
- Knollenberg, R.G., and D.M. Hunten (1980). The microphysics of the clouds of Venus: Results of the Pioneer Venus particle size spectrometer experiment, J. Geophys. Res., 85, 8039-8058.
- Leovy, C.B. (1973). Rotation of the upper atmosphere of Venus, J. Atmos. Sci., 30, 1218-1220.
- Leovy, C.B., and R.W. Zurek (1979). Thermal tides and Martian dust storms: Direct evidence for coupling, J. Geophys. Res., 84, 2956-2968.
- Limaye, S.S., and V.E. Suomi (1981). Cloud motions on Venus: Global structure and organization, J. Atmos. Sci., 38, 1220-1235.
- Limaye, S.S., C.J. Grund, and S.P. Burre (1982). Zonal mean circulation at the cloud level on Venus: Spring and Fall 1979 OCPP observations, Icarus, 51, 416-439.
- Lindzen, R.S., (1967). Thermally driven diurnal tide in the atmosphere, Quart J. Roy. Meteorol. Soc., 93, 18-42.
- Lindzen, R.S. (1968). The application of classical atmospheric tidal theory, Proc. Roy. Soc. London, A303, 299-316.
- Lindzen, R.S. (1970). The application and applicability of terrestrial atmospheric tidal theory to Venus and Mars, J. Atmos. Sci., 27, 536-549.
- Lindzen, R.S. (1971). Mathematical problems in the geophysical sciences, Lectures in Applied Mathematics, 14, 293-360.
- Lindzen, R.S., E.S. Batten, and J.W. Kim (1968). Oscillations in atmospheres with tops, Mon. Wea. Rev., 96, 133-140.

- Madala, R.V., S.A. Piacsek, and S.T. Zalesak (1975). A semispectral numerical model for forced, vertically propagating planetary waves. Part 1 - Application of the model to linear diurnal and semidiurnal atmospheric thermal tides, NRL Memorandum Report 3145, Naval Research Laboratory, Washington, D.C.
- Murray, B.C., M.J.S. Belton, G.E. Danielson, M.E. Davies, D. Gault, B. Hapke, B. O'Leary, R.G. Strom, V. Suomi, and N. Trask (1974). Venus: Atmospheric motion and structure from Mariner 10 pictures, Science, 183, 1307-1315.
- Pollack, J.B., O.B. Toon, and R. Boese (1980). Greenhouse models of Venus' high surface temperature, as constrained by Pioneer Venus measurements, J. Geophys. Res., 85, 8223-8231.
- Pollack, J.B. and R.E. Young (1975). Calculations of the radiative and dynamical state of the Venus atmosphere, J. Atmos. Sci., 32, 1025-1037.
- Robert, A., J. Henderson, and C. Turnbull (1972). An implicit time integration scheme for baroclinic models of the atmosphere, Mon. Wea. Rev., 100, 329-335.
- Rossow, W.B. (1983). A general circulation model of a Venus-like atmosphere, J. Atmos. Sci., 40, in press.
- Rossow, W.B., A.D. Del Genio, S.S. Limaye, and L.D. Travis (1980). Cloud morphology and motions from Pioneer Venus images, J. Geophys. Res., 85, 8107-8128.
- Rossow, W.B. and E. Kinsella (1982). Variations of winds on Venus, Bull. Amer. Astr. Soc., 14, 740.
- Rossow, W.B., and G.P. Williams (1979). Large-scale motion in the Venus stratosphere, J. Atmos. Sci., 36, 377-389.
- Schubert, G. (1982). General circulation and the dynamical state of the Venus atmosphere, in Venus, edited by D.M. Hunten, L. Colin, T.M. Donahue, University of Arizona Press, Tucson, Arizona, in press.
- Schubert, G., C. Covey, A. Del Genio, L.S. Elson, G. Keating, A. Seiff, R.E. Young, J. Apt, C.C. Counselman III, A.J. Kliore, S.S. Limaye, H.E. Revercomb, L.A. Sromovsky, V.E. Suomi, F. Taylor, R. Woo, and U. von Zahn (1980). Structure and circulation of the Venus atmosphere, J. Geophys. Res., 85, 8007-8025.
- Seiff, A., D.B. Kirk, R.E. Young, R.C. Blanchard, J.T. Findlay, G.M. Kelly, and S.C. Sommer (1980). Measurements of thermal structure and thermal contrasts in the atmosphere of Venus and related dynamical observations: Results from the four Pioneer Venus probes, J. Geophys. Res., 85, 7903-7933.

- Siebert, M. (1961). Atmospheric tides, in Advances in Geophysics, Vol. 7, pp. 105-182, Academic Press, New York, NY.
- Staniforth, A.N., and R.W. Daley (1977). A finite-element formulation for the vertical discretization of sigma-coordinate primitive equation models, Mon. Wea. Rev., 105, 1108-1118.
- Stone, P.H. (1974). The structure and circulation of the deep Venus atmosphere, J. Atmos. Sci., 31, 1681-1690.
- Suomi, V.E., L.A. Sromovsky, and H.E. Revercomb (1979). Preliminary results of the Pioneer Venus small probe net flux radiometer experiment, Science, 205, 82-85.
- Taylor, F.W., R. Beer, M.T. Chahine, D.J. Diner, L.S. Elson, R.D. Haskins, D.J. McCleese, J.V. Martonchik, P.E. Reichley, S.P. Bradley, J. Delderfield, J.T. Schofield, C.B. Farmer, L. Froidevaux, J. Leung, M.T. Coffey, and J.C. Gille (1980). Structure and meteorology of the middle atmosphere of Venus: Infrared remote sensing from the Pioneer orbiter, J. Geophys. Res., 85, 7963-8006.
- Thomson, W. (later Lord Kelvin), (1882). On the thermodynamic acceleration of the earth's rotation, Proc. Roy. Soc. Edinb., 11, 396-405.
- Tomasko, M.G., L.R. Doose, P.H. Smith, and A.P. Odell (1980a). Measurements of the flux of sunlight in the atmosphere of Venus, J. Geophys. Res., 85, 8167-8186.
- Tomasko, M.G., P.H. Smith, V.E. Suomi, L.A. Sromovsky, H.E. Revercomb, F.W. Taylor, D.J. Martonchik, A. Seiff, R. Boese, J.B. Pollack, A.P. Ingersoll, G. Schubert, and C.C. Covey (1980). The thermal balance of Venus in light of the Pioneer Venus mission, J. Geophys. Res., 85, 8187-8199.
- Toon, D.B., R.P. Turco, and R.C. Whitter (1979). A physical-chemical model of the Venus clouds, Bull. Amer. Astr. Soc., 11, 544.
- Traub, W.A., and N.P. Carleton (1975). Spectroscopic observations of winds on Venus, J. Atmos. Sci., 32, 1045-1059.
- Travis, L.D. (1978). Nature of the atmospheric dynamics on Venus from power spectrum analysis of Mariner 10 images, J. Atmos. Sci., 35, 1584-1595.
- von Zahn, U., K.H. Fricke, D.M. Hunten, D. Krankowsky, K. Mauersberger, and A.O. Nier (1980). The upper atmosphere of Venus during morning conditions, J. Geophys. Res., 85, 7829-7840.

- Woo, R., J.W. Armstrong, and A. Ishimaru (1980). Radio occultation measurements of turbulence in the Venus atmosphere by Pioneer Venus, J. Geophys. Res., 85, 8031-8038.
- Woo, R., J.W. Armstrong, and A.J. Kliore (1982). Small-scale turbulence in the atmosphere of Venus, Icarus, 52, 335-345.
- Woo, R., and A. Ishimaru (1981). Eddy diffusion coefficient for the atmosphere of Venus from radio scintillation measurements, Nature, 289, 383-384.
- Young, A.T. (1975). The clouds of Venus, J. Atmos. Sci., 32, 1125-1132.
- Young, R.E., A. Seiff, and L. Pfister (1981). Modes of dynamical instability in the Venus atmosphere, in An International Conference on the Venus Environment (abstract volume), NASA, Ames Research Center.
- Yung, Y.L., and W.B. DeMore (1982). Photochemistry of the stratosphere of Venus: Implications for atmospheric evolution, Icarus, 51, 199-247.
- Zurek, R.W. (1976). Diurnal tide in the Martian atmosphere, J. Atmos. Res., 33, 321-337.
- Zurek, R.W. (1980). Surface pressure response to elevated tidal heating sources: Comparison of Earth and Mars, J. Atmos. Res., 37, 1132-1136.
- Zurek, R.W. (1981). Inference of dust opacities for the 1977 Martian great dust storms from Viking Lander 1 pressure data, Icarus, 45, 202-215.